DESIGN, CHARACTERIZATION, AND REINFORCEMENT OF MINERALIZED COLLAGEN-GLYCOSAMINOGLYCAN SCAFFOLDS FOR ORTHOPEDIC WOUND REPAIR

BY

DANIEL W. WEISGERBER

DISSERTATION

Submitted in partial fulfillment of the requirements
for the degree of Doctor of Philosophy in Materials Science and Engineering
in the Graduate College of the
University of Illinois at Urbana-Champaign, 2015

Urbana, Illinois

Doctoral Committee:

Professor Brendan Harley, Chair and Director of Research
Professor Paul Braun
Professor Jianjun Cheng
Assistant Professor Cecilia Leal

ABSTRACT

The treatment of craniofacial orthopedic defects remains a challenge due to the large size, complex geometry, and load bearing aspects that often accompany such defects. The typical treatment or correction of craniofacial defects employed during surgical intervention of such injuries often necessitates the use of either autologous or allogenic bone grafts for orthopedic implants as the gold standard. However, this standard of treatment has been plagued with concerns over the size, geometry, donor site morbidity, disease transmission, and availability. To address these concerns, the development of an alternative orthopedic implant biomaterial capable of: (1) flexible design for meeting bone, defect, and patient specific treatment criteria; (2) guiding and supporting cellular specific repair specific to orthopedic defects; (3) demonstrate mechanical competence for surgical implantation and subsequent loading during function. This work outlines the development of a collagen-glycosaminoglycan platform that satisfies these requirements for the treatment of craniofacial defects. Chapter 2 details the fabrication and characterization of the collagen-glycosaminoglycan scaffold biochemical and biophysical properties important for the bioactivity and interaction with target cellular populations. The chapter 3 evaluates the *in vitro* cellular response and subsequent remodeling of a relevant cell population, mesenchymal stem cells, within the collagen-glycosaminoglycan scaffold. Chapter 4 addresses the necessary mechanical reinforcement and subsequent characterization of a multi-scale polycaprolactone-collagen-glycosaminoglycan composite biomaterial for *in vivo* implantation and culture. In chapter 5 the polycaprolactone-collagen-glycosaminoglycan composite was then implanted in a subcritical mandibular ramus defect to affirm the composites *in vivo* efficacy. Finally, chapter 6 evaluated possible alterations in the collagen-glycosaminoglycan scaffold design for enhancing cellular behavior, while chapter 7 expanded upon the multi-compartment collagen-glycosaminoglycan scaffold design for the treatment of craniofacial defects and associated entheses.

To my mother and father, for always supporting me and accepting nothing less than my very best.

ACKNOWLEDGEMENTS

I would like to acknowledge and thank those who have contributed to the work described within this thesis: Dr. Steven Caliari (Chapters 2-3, 7), Douglas Kelkhoff (Chapter 2 and 7), Kevin Earning (Chapter 4), Rebecca Hortensius (Chapters 5 and 6), and Dr. Wheeler and the Wheeler lab group (Chapter 5). My collaborators both at the University of Illinois at Urbana-Champaign and other institutions: Dr. Michael Insana, Dr. Yue Wang, Dr. Mathew Wheeler, Dr. Derek Milner, Dr. Marcello Rubessa, Heather Lopez-Lake, Sammi Lotti, Dr. Mathew Stewart, Kalyn Herzog, Dr. Timothy Miller (UCLA), Dr. Xiaoyan Ren (UCLA), Dr. Justine Lee (UCLA), Dr. Scott Hollister (UMich), Dr. Colleen Flanagan (UMich), Dr. Evelyn Yim (NUS), Marie Cutiongco (NUS), and Tuan Nguyen (NUS). And the training, assistance, and guidance provided by Dr. Mauro Sardela, Dr. Leilei Yin, Dr. Sandra McMasters, Dr. Mathew Bresin, and Karen Doty.

I will never forget all the help and support over the years from my lab colleagues: Dr. Steven Caliari, Emily Gonnerman, Dr. Bhushan Mahadik, Dr. Sunny Choi, Jackie Pence, Dr. Sara Pedron, Dr. Nate Gabrielson, Rebecca Hortensius, Laura Mozdzen, Bill Grier, Dr. Seema Ehsan, and Emily Chen. And the undergraduate research assistants I have mentored: Peter Rapp, Douglas Kelkhoff, and Kevin Erning.

I would like to thank the Material Science and Engineering department and IGERT staff members who on numerous times I have interact with for taking the time out of their busy schedules to help me: Michelle Malloch, Jay Menacher, and Laura Miller. I would especially like to thank my thesis committee members: Dr. Paul Braun, Dr. Jianjun Cheng, Dr. Cecilia Leal, and my adviser Dr. Brendan Harley.

All the work described throughout this thesis was funded at UIUC by: National Science Foundation (NSF) Grant 0965918 IGERT Training the Next Generation of Researchers in Cellular & Molecular

Mechanics and BioNanotechnology; the Chemistry-Biology Interface Training Program NIH NIGMS T32GM070421 (SRC); the Chemical and Biomolecular Engineering Dept. and the Institute for Genomic Biology (BAH) at the University of Illinois at Urbana-Champaign; project S-14-54H was supported by the AO Foundation (Switzerland). This research was carried out in part in the Frederick Seitz Materials Research Laboratory Central Facilities, University of Illinois, which are partially supported by the U.S. Department of Energy under grants DE-FG02-07ER46453 and DE-FG02-07ER46471, and the Microscopy Suite, Imaging Technology Group, Beckman Institute for Advanced Science and Technology, University of Illinois at Urbana-Champaign.

Finally, I would like to thank Mom, Dad, Alan, and Emma for their constant love and support in all my decisions. Love you guys.

TABLE OF CONTENTS

CHAPTER 1

INTRODUCTION AND BACKGROUND TO ORTHOPEDIC BIOMATERIALS

1.1 Introduction to the Anatomy of Bone

The human body is 15 wt% bone with a total of 206 bones subdivided into the appendicular skeleton, pertaining to both the legs and arms containing 126 bones, the axial skeleton, which includes the spine, rib cage, and skull containing 74 bones, and the auditory ossicles, the 6 bones within the ears responsible for transmitting sound [1]. Between these subdivisions of bones, each bone can be classified as a long bone, short bone, flat bone, and irregular bone based upon their geometry and function [1]. There are a total of 90 long bones which are typically illustrated by the femur and tibiae, the largest bones in the legs extending from the hip to the knee and the knee to the ankle respectively, or the phalanges, 3 of which comprise each finger with 2 in the case of the thumb. Of the 30 short bones, common examples include the 8 carpal bones comprising the wrist as well as the 7 tarsal bones that together make up the hind and mid-foot. The skull and rib cage are both comprised of multiple flat bones each of which are representative of the 29 flat bones found in the human body. Finally, the 57 irregular bones are typically depicted as the vertebrae or mandible due to their irregular shape. The sesamoid bones such as the patella in the knee are small independent bones embedded in tendon or muscle, and are typically excluded from the total bone count within the human body.

The two most overt roles bone provides is the protection of our vital organs in the case of the skull and rib cage, and the structural support necessary for locomotion provided by the aptly named musculoskeletal

system. However, bones also serves essential roles in maintaining homeostasis within the body. Aside from adapting and repairing bone, bone resorption and deposition also controls the release and storage of essential ions stored in the bone, including calcium and phosphate. The regulation of these ions remains governed by osteogenic cells, and plays an essential roles in balancing physiological pH in the body as well as other cell processes, such as action potential propagation in neurons via the release of neural transmitters following the influx of calcium via voltage gated ion channels in the axon terminal. Additionally, the bone marrow serves as the site of hematopoiesis, the generation of blood and immune cells within the body.

Each bone is typically comprised of two anatomically distinct types of osseous tissues, an outer cortical bone shell with an inner cancellous bone core. Cortical or compact bone is the denser of the two (<5% porosity) and comprises approximately 80% of all bone mass [1]. The anatomical subunit comprising the cortical bone is the osteon which consists of concentric mineralized collagen lamellae centered on the harversian canal (circa 60 μm in diameter)[2], enclosing the blood vessels and nerves within these canals. Osteogenic cells are embedded within these lamellae in pockets known as lacunae and both communicate with other cells and exchange waste for nutrients from the Harversian canal via channels called canaliculi. In contrast, cancellous bone, also known as trabecular or soft bone, comprises the remaining 20% of all bone mass [1] of all bone and is softer (>30-90% porosity) compared to cortical bone. In the case of cancellous bone, the anatomical osteon subunit is less clear, but has been described as a series of parallel lamellae (circa 500 μm thick) of varying length described as a plate [3]. The ratio of cortical to cancellous is dependent on the bone, such as 1:3 in vertebrae as well as location in that bone 1:1 in the femoral head and 19:1 in the radial diaphysis [1].

The bone extracellular matrix, or the local micro-environment that cells reside in, consists of organic protein constituents, an inorganic mineral phase, and lipids. Of the organic protein constituents in bone,

85-90% consists of the matrix protein collagen type I [1]. The remaining organic protein constituents can be divided into proteins derived exogenously that help guide cellular behavior, such as growth factors and serum-proteins, and a wide range of osteoblast secreted proteins, which include proteoglycans, glycosylated proteins, and osteonectin [1]. Hydroxyapatite calcium phosphate mineral phase and other smaller compounds, such as carbonate and magnesium, account for 35-70% of bone as the inorganic mineral phase of bone.

1.2 *In Utero* and *Ex Utero* Bone Development

During development, new bone formation, also known as osteogenesis, occurs through either intramembranous ossification or endochondral ossification processes [4]. In the case of intramembranous ossification, the mesenchymal tissue is converted to bone, while endochondral ossification involves the conversion of a cartilage intermediate tissue into bone [4].

1.2.1 Intramembranous Ossification

The process of intramembranous ossification, primarily responsible for the development of many of the craniofacial and flat bones found in the skull, first begins with the formation of compact nodules comprised of mesenchymal cells [4]. The bone morphogenetic protein family and the *Cbfa1* gene in mesenchymal cells has been implicated in the differentiation of mesenchymal cells into osteoblasts [4]. Within these nodules, these mesenchymal cells will then expand into capillaries or osteogenic roles, where the latter is responsible for the deposition of an osteoid matrix that binds calcium salts [4]. As the deposition and calcification of osteoid proceeds in needle like projections called spicules, the periosteum membrane is formed by the compact mesenchymal cells surrounding the new bony spicules [4]. Osteoblasts that are trapped within the newly formed bone either undergo apoptosis or differentiate into osteoclasts, while mesenchymal cells bordering the bony spicules and the forming periosteum membrane become osteoblasts to contribute to new bone formation [4].

1.2.2 Endochondral Ossification

In contrast, endochondral ossification is implemented in the formation of the long bones within the body through a series of five stages [4]. In the first stage, mesenchymal cells that are to form a compact nodule are committed to become cartilage cells through paracrine signaling inducing Pax1 and Scleraxis transcription factors, which activate cartilage-specific genes [4]. The subsequent condensation of these cells into a compart nodule and differentiation into chondrocytes, with N-cadherin and N-CAM proteins, and the *SOX9* gene having been identified as having an with important role in this stage of endochondral ossification [4]. The third and fourth stages involves the proliferation of the chondrocytes and their secretion of a cartilage extracellular matrix model before becoming hypertrophic chondrocytes, wherein proliferation is concluded and cellular size increases [4]. Within the fourth stage, these hypertrophic chondrocytes augment the previously secreted cartilage extracellular matrix model with collagen type X, which enables mineralization via calcium carbonate [4]. The fifth and final stage of endochondral ossification involves the blood vessel infiltration, apoptosis of the hypertrophic chondrocytes, and the differentiation of surrounding cellular bodies into osteoblasts with the subsequent deposition of bone by these osteoblasts on the now partially degraded cartilage extracellular matrix [4]. In the case of long bones, this process of endochondral ossification beings at the center of the cartilage extracellular matrix model and expands longitudinally [4]. In order to preserve the potential for new bone formation, the chondrocytes near the end of the cartilage extracellular matrix model proliferate prior to hypertrophy, extending the cartilaginous region [4]. These new cartilaginous regions are referred to as the epiphyseal growth plates, and contain distinct regions of chondrocyte proliferation, chondrocyte maturation, and hypertrophic chondrocytes [4]. The epiphyseal growth plates continue to provide the cartilage extracellular matrix model for new bone formation through this process of endochondral ossification for as long as they are capable of chondrocyte proliferation [4].

1.3 Physiological Aspects of Bone Remodeling and Defect Repair

While bone is capable of providing support during locomotion and biochemical homeostasis, one of the most profound yet often overlooked characteristic is the unique ability of bone to adapt and repair itself in response to its environment using modeling and remodeling processes. The maintenance of bone homeostasis via remodeling is performed to repair damage accumulated at a micron level during physiological function (Figure 1.1) [5]. This remodeling process is achieved through a resorption and deposition cycle lasting 6-7 months. In a similar manner, the repair of small sub-critically sized defects involves bone remodeling following the inflammatory response and stabilization of the defect over a period of months to years [1].

1.3.1 Maintenance of Bone Homeostatic via Remodeling

This cyclic process has been documented with 4 stages consisting of activation, resorption, reversal, and formation. Activation involves the recruitment of monocyte-macrophage osteoclast precursor cells, which proceed to fuse into multi-nucleated preosteoclasts that bind to the organic bone phase creating resorption pockets [1]. During resorption, resorbing osteoclasts release hydrogen ions to mobilize the bone mineral phase and a myriad of matrix degradation proteins dissolving the bone over a period of 2-4 weeks [1]. Following the apoptosis of the multi-nucleated osteoclasts and subsequent completion of resorption, the reversal phase or the transition from resorption to formation is triggered by a series of matrix derived biomolecules and changes in the local strain environment brought about by resorption [1]. Matrix deposition during the formation stage of remodeling occupies the remaining 4-6 months and involves the presence of osteoblasts depositing and mineralizing the bone matrix [1]. During this period of time osteoblasts deposit an unorganized and unmineralized collagen protein matrix, often referred to as woven bone, before being organized and mineralized into the osteon subunit [1]. Following formation, 50-70% of the remaining osteoblasts then either undergo apoptosis, or, if buried within the bone, differentiate into osteocytes joining the canalicular network [1].

Approximately 2-3% of cortical bone is remodeled each year [1]. In a functionally identical process, trabecular bone experiences a higher degree of remodeling, implicating it as the primary source of mineral homeostasis in the body. Changes in bone thickness with age has been attributed to differences in the rate of remodeling in the periosteal or outside surface compared to the endosteal or inside surface of bone [1]. The process of bone repair, commonly referred to as a union, following injury is also similar, but possesses notably different stages related to injury and stabilization. Indirect fracture healing, or the natural physiological healing process in non-operative healing, progresses as the inflammatory response, recruitment of stem cells, generation of a bony callus, revascularization of the callus, callus mineralization and resorption, and finally remodeling [6, 7].

1.3.2 Physiological Repair of Defects

Following the initial trauma, the acute inflammatory response takes place during the first 7 days with the generation and coagulation of hematoma or blood clot at the fracture ends and medulla acting as a template for repair [6]. During this period, inflammatory cells stimulate revascularization and secrete numerous growth factors, such as tumor necrosis factor-α (TNF-α), that regulate cell recruitment and osteogenic differentiation [6]. The recruitment of cells, specifically mesenchymal stem cells (MSCs), to the site and subsequent differentiation is then mediated with a cascade of collagen type I and II matrix production with growth factor signaling, including the transforming growth factor-β (TGF-β) and bone morphoprogenic proteins (BMPs) [6]. Then 7-9 days after injury, a fibrin-rich soft cartilaginous callus is formed between the fracture ends, with sub-periosteal ossification adjacent, to provide a degree of structural support [6]. The subsequent revascularization and neoangiogenesis of the injury site, necessary to provide the nutrients essential for repair, is accomplished through surrounding matrix degradation and the activation of both vascular endothelial growth factor (VEGF) and angiopoietin-dependent cellular pathways [6]. By 14 days after injury, calcification of the previously soft cartilaginous callus occurs as the

responsible chondrocytes become hypertrophic before TNF-α initiates the cascade resulting in its resorption followed by the deposition of woven bone by osteoclasts and osteogenic cells [6]. Finally, after 21-28 days, natural bone formation is achieved through the resorption of the woven bone, instigated by TNF-α, IL-1, and BMPs, by osteoclasts and the deposition of new lamellar bone via osteoblasts in a process similar to remodeling over a period of years [6].

In the case of direct fracture healing of small sub-critical sized defects, surgical intervention is necessary to achieve both anatomical reduction, correction of bone alignment, and stable fixation of the injury to allow either contact or gap healing to restore the function over a period of months to years [6]. Contact healing progresses when the gap between bones is less than 0.01 mm and involves cutting cones headed by osteoblasts that bridge the gap and create cavities that are then filled by bridging osteons [6]. Gap healing occurs within the range of 0.8-1 mm and results in deposition of bone lamella perpendicular to the bone axis, which must undergo additional remodeling into the osteon subunit [6]. It has been observed that strain and loading, Wolff's law, of the injury site can be beneficial to healing kinetics, however, excessive strain or loading can result in delayed union or nonunion [6]. Due to the absence of a fibrous scar at its conclusion, the physiological bone healing processes has been identified as nearly regenerative in nature [6]. However, a plethora of complications have been identified as causing delayed union and nonunion between the fracture ends [7, 8]. Such complications include the age, the existence of co-morbidities such as diabetes, prescribed and non-prescribed drugs in the case of non-steroidal anti-inflammatory drugs and smoking respectively, methods of treatment including anti-coagulation treatments, as well as the critical roles of gap size and reduction in bone fracture [8].

Beyond this critical size limitation, the addition of orthopedic implants during surgical intervention is necessary to promote the union of bones. However, in the case of severe orthopedic trauma involving a large degree of bone loss or complex geometries limitations in the applications of orthopedic implants

remain significant considerations. As such regenerative medicine and tissue engineering solutions have garnered attention as alternatives to the current orthopedic treatments to overcome these limitations.

1.4 A Brief History of Orthopedics

The origin of the word orthopedics can be traced to the word orthopedia original coined by Nicholas Andry at the University of Paris for the treatment of deformities in children in 1741 [9]. It has since evolved into the specialization of treating skeletal deformities in today's medical community. However, the treatment and study of skeletal and musculoskeletal deformities predates 1741 by several centuries. Some of the earliest written accounts addressing the treatment of defects emphasized the significance of reduction or alignment and immobilization by Hippocrates [9]. Later work by historical figures such as Guy de Chauliac (1300-1368) and Leonardo de Vinci (1452-1519) addressed the use of traction for anatomical reduction in treating orthopedic defects by the mechanical leverage of muscle and bone respectively, the latter additionally addressed by Galileo's pupil and physicist Alphonso Giovannni Borelli (1608-1679) [9]. Later, the anatomical structure of bone was introduced with the first known account of bone vascularization, the Harversian canal, by Clopton Havers (1657-1702), and cellular role of osteoblasts in the formation of the osteoid tissue by John Goodsir (1814-1867) [9].

1.5 Treatment Approach for Orthopedic Defects: Reduction, Fixation, and Bone Grafts

Since the 1990s, between 60% and 70% of all injuries involve to the musculoskeletal system, an increase from 23.4 million in the 1990s to 24.8 million today [10]. With even this increase in occurrence, ambulatory visits and prescription drugs for the treatment of musculoskeletal injuries has risen by 85% and 97% respectively [11]. As of 2011, individuals over the age of 65 represent more than half of all musculoskeletal injuries, while these individuals represent only 13% of the total population, with the proportion of the people over 65 projected to increase to 20% by 2030 [11]. While only a subset of the larger musculoskeletal defects, craniofacial defects represent an important target of treatment for

orthopedic surgeons. Craniofacial repair addresses a wide range of defects resulting from birth deformities, such as the cleft lip or cleft palate afflicting 0.17% of all newborns [12, 13], or acute maxillofacial trauma, as in the case of sport activities and traffic accidents that representing 54.4% of such injuries [14].

While orthopedic methods are heavily dependent on the specific injury, the overall orthopedic approach for treating direct fractures remains: anatomical reduction and stable fixation. In the case of fractures, traction, or the anatomical positioning of the fracture ends mechanically, is followed by either open or closed reduction [15]. Stable fixation can occur either internally, in the case of open reduction, with plates and screws or externally, typically in the case of closed reduction, with casts.

Especially pertaining to craniofacial defects, more complicated defects involving geometrically complex bone loss or requiring the addition of bone volume for functional restoration requires a more proactive treatment. In the case of the five most common orthopedic training techniques for craniofacial repair, the cranial or iliac bone to the nasal dorsum, perialar rim graft, lateral canthopexy with full canthal tendon release/mobilization and fixation to orbital rim, osseous genioplasty, and bone graft harvest for orbital floor defects, involve the harvest, placement, alignment, and fixation of the bone graft to fix the targeted defect [16]. While the same treatment principles of traction, reduction, and fixation still hold, addressing such critically sized defects, or defects unable to heal without intervention requires the addition of an orthopedic implant to promote union. Such orthopedic implants can be classified into two general categories, the relatively biologically inert and non-degradable implant, such as titanium or silicon, or the more common gold standard of an autologous or an allogenic bone graft. The autologous bone graft consists of bone harvested from a secondary site within the patient, while the allogenic bone graft involves the implantation of a similarly identical donor bone graft that has been treated to remove any residual cell populations and possible contagions. In both cases limited availability has remained a

constant concern, with autologous bone grafts limited in the amount of bone that can be safely harvested, and allogenic bone grafts limited by donor availability. Additionally, concerns over secondary wound site morbidity from autologous harvesting and allogenic disease transmission remain prominent for these gold standards of orthopedic treatment. As such, regenerative medicine and tissue engineering approaches utilizing a bioactive orthopedic biomaterial implant has garnered attention as an alternative to the use of the autologous and allogenic bone grafts.

1.6 Introduction to Alternative Orthopedic Implant Materials

A majority of orthopedic interventions involve the use of orthopedic implant materials, either biologically inert materials, or more commonly, harvested bone to either replace bone loss or correct defects [16-20]. Even non-osseous related treatments such as ACL reconstruction can employ the use of implant materials or bone harvest for fixation in place of or augmenting interference screws. However, in the case of large defects, harvesting sufficient autologous bone remains impractical requiring the use of allografts to achieve a functional outcome. To avoid autologous bone grafts with associated donor site morbidity and impaired function, allogenic bone grafts have been employed (Figure 1.2). But concerns of allogenic supply and disease transmission still remain prevalent for such allogenic bone grafts. These concerns and limitations over autologous and allogenic bone grafts has spurred the development of biomaterials to replace current implant materials. However, such biomaterials developed as alternatives to the current orthopedic implant, regardless of their classification, must fundamentally be capable of both enabling and enhancing the physiological process in the fields of regenerative medicine and tissue engineering [21]. To accomplish these goals, the regenerative medicine and tissue engineering fields leverage the biochemical, biophysical, and biomolecular material design variables, such as degradation rate, pore size, stiffness, growth factor incorporation, biological motifs, and composition.

Biomaterials designed to replace implant materials can be divided into several categories based upon their role in the physiological process and their composition, these categories generally include biologically inert versus active, degradable or resorbable versus non-degradable, and synthetic versus organic, with growing favor in regenerative medicine and tissue engineering for biologically active and degradable biomaterials capable of influencing the native physiological response as opposed to biologically inert implants. With the development of tissue engineering the significance of both chemical and physical biomaterial properties as well as degradability in guiding the biological response both locally and systemically has been established [22, 23]. Degradable biomaterials designed with such criteria in mind can generally be divided into two broad categories: inorganic and organic biomaterials. Inorganic biomaterials used in tissue engineering can be further categorized into synthetic polymeric biomaterials and ceramic biomaterials. Synthetic biomaterials, with prime examples such as polyethylene glycol (PEG) and poly(lactic acid) (PLA), are flexible in their chemical modification. Ceramics, like tricalcium phosphate and hydroxyapatite, are more commonly used in orthopedic applications due to their physical properties. Organic biomaterials are commonly comprised of both physiologically relevant and naturally occurring proteins and biomolecules, examples ranging from collagen and proteoglycans to silk fibers.

Synthetic biomaterials employed in orthopedic applications are highly favored for the definitive control over the wide range and flexibility of both chemical and physical properties that may be present upon implantation. Outside the fields of regenerative medicine and tissue engineering, synthetic biomaterials, such as poly(L-lactide acid), mixtures of poly(propylene fumarate) and poly(propylene fumarate)-diacrylate, and poly(glycolic acid), have been used to provide viable biodegradable alternatives to metal orthopedic implants, as in the case of interference screws, fixative plates, and FDA approved sutures [24-26]. Within the fields of regenerative medicine and tissue engineering, synthetic biomaterials have been capable of meeting the various design criteria for application across multiple tissues by modulating their stiffness from 10 Pa to 100 kPa [27, 28], variations in microstructure pore size, density, and surface

roughness [29, 30], and the incorporations of different chemistries invoking stimuli dependent responses. The most notable limitation of synthetic biomaterials was their inferior capacity to directly influence cellular behavior and function within regenerative medicine and tissue engineering applications compared to organic biomaterials [31]. However, advances in biology and the biomaterial design has allowed the incorporation of biological motifs and components to increase the inherent bioactivity of these materials without concerns of pathogen transmission and immunogenicity [31]. Examples of the expansive range of biological motifs included in polymeric biomaterial design include the addition of the adhesion promoting RGD (Arg-Gly-Asp amino acid) domain [32], the incorporation of a nano-hydroxiapatite mineral phase in poly(L-lactic acid) composites to better mimic the anatomic bone micro-environment [33], and the inclusion of biomolecules such as growth factors ranging from BMP for bone to VEGF for vascularization [34].

Ceramic biomaterials or bioceramics, almost exclusively calcium phosphate ceramics (CPCs), have been employed in conjunction with orthopedic applications for their excellent resistance to deformation and osteoinductive properties. Numerous calcium based ceramics for the treatment of bone defects are represented most commonly by beta-tricalcium phosphate ($Ca_3(PO_4)_2$; β-TCP) and calcium hydroxyapatite ($Ca_{10}(PO_4)_6(OH)_2$; HA), while others include calcium aluminate ($CaO.Al_2O_3$), beta-calcium pyrophosphate ($Ca_2P_2O_7$), biphasic calcium phosphate (a mixture of HA and β-TCP), calcium carbonate ($CaCO_3$), and amorphous calcium phosphates ($Ca_3(PO_4)_2$) [35-40]. At the micron and nanoscale, the surface roughness, surface charge, crystallinity, grain size, and solubility of ceramic biomaterials are all tunable properties that affect the protein adsorption, subsequent cell adhesion, and ultimately cellular differentiation [39]. At the tissue level, the mechanical properties such as the compressive modulus of ceramic biomaterials are comparable or exceeding cortical bone in the 10 GPa range, with TCP ranges from 20 to 80 GPa depending on the sintering temperature [41]. However, concerns over the inherent pore size, degradation, low ductility, and wear debris represents some of the

difficulties ceramic biomaterials face. Recent work impregnating a β-TCP ceramic with polycaprolactone has shown an improvement in mechanical tolerances [42].

Unlike synthetic and ceramic biomaterials, degradable organic biomaterials have been defined by their native interaction with the physiological environment, with the ability to facilitate cellular processes in regenerative medicine and tissue engineering applications. Examples of naturally derived biomaterials commonly employed in orthopedic applications of regenerative medicine and tissue engineering include chitosan, silk, alginate, fibrin, elastin, laminin, proteoglycans, and collagen based materials and composites [43-46]. The ability of natural polymers to interact with cells, their inherent biocompatible with biocompatible degradation products and low immunogenicity, and ability to closely simulate the native extracellular matrix especially in the case of physiologically relevant matrix proteins such as collagen and fibrin make natural polymers an attractive application [46]. However, in the case of orthopedic implants especially, some natural polymeric biomaterials, with moduli ranging anywhere from 1 kPa to 200 kPa [28, 47, 48], lack the mechanical competence of the target tissue, typically in the 2 MPa to 20 GPa range [49, 50], creating problems during instances of load bearing.

In addition to leveraging the biochemical and biophysical design variables of synthetic, ceramic, and organic biomaterials as a more bioactive treatment approach, the incorporation of biomolecular design considerations has also demonstrated enhanced bioactivity. While such biomolecular components include biological motifs [32], a major avenue of design includes the incorporation and release of proteins, particularly growth factors, into the wound environment to enhance treatment. In particular, growth factors belonging to the bone morphogenetic protein (BMP) family, especially BMP-2, play essential roles in the development, growth, and repair of the skeleton during embryogenesis and extending throughout adulthood [51]. Utilization of growth factors belonging to the BMP family in *in vitro*, *in vivo*, and clinical work has demonstrated bone formation [52-55]. However, complications arising from the use

of growth factors, particularly of the BMP family, have included heterotopic ossification, osteolysis, neurological deficits, and cancer [56-58]. As such, additional work investigating the controlled delivery and release of such biomolecular components is required for safe incorporation in regenerative medicine and tissue engineering biomaterial design.

1.7 Multi-Scale Biomaterial Composites Design: a Solution to a Problem

While all biomaterials possess inherent qualities, a common method for addressing specific deficiencies or augmenting desirable biophysical and biochemical properties is the fabrication of a multi-component multi-scale biomaterial composite. In the case of calcium phosphate ceramics and other bioceramics used in orthopedic applications, the incorporation of natural and synthetic polymeric biomaterials has demonstrated improved protein adsorption and tunable degradation as in chitosan/β-1,3-glucan/calcium phosphate ceramic composite and cellulose/apatite composites [59, 60]. In the case of synthetic and organic biomaterials, the inclusion of a calcium phosphate mineral component like the hydroxyapatite mineralization of silk fibroin hydrogels and agarose gels loaded with either hydroxyapatite or calcium carbonate, greatly increases the osteogenic capacity of the material [40, 61]. Most biomaterial composites are composed of similar scale components typically as polymer-polymer composite biomaterials, as in the case of the collagen-polycaprolactone biomaterial composite developed for controlled insulin release, or more commonly, polymers coated with a nano-crystal hydroxyapatite, such as the chitosan-nano-hydroxyapatite scaffold for osteoblast and mesenchymal stem cell culture [62] [63]. A second approach to composite biomaterial design involves a multi-scale component approach with examples such as a millimeter scale macroporous polycaprolactone construct loaded with growth factors, bone morphoprogenic protein 2 (BMP2) and erythropoietin (EPO) to assist in bioactivity at the cellular level, or a beta-tricalcium phosphate (β-TCP) ceramic with polycaprolactone (PCL) impregnated into the microstructure to improve mechanical ductility [42, 64].

1.8 Collagen-Glycosaminoglycan Scaffolds

Of the natural polymeric biomaterials the collagen and gelatin based scaffold design has shown particular promise for the treatment of a wide range of tissues due to its inherent biophysical properties and immunogenicity. These applications cover a scope of chemically and physically different tissues ranging from soft neural tissue for the treatment of brain and nerve defects in the case of silk-collagen protein constructs [65, 66], to the treatment of cartilage defects [67-69], to muscle tissue [70-72], and to hard bone tissue for the treatment of orthopedic defects [73-75]. Collagen protein is ubiquitous and is found throughout the body in different tissues.The collagen protein family comprises approximately 30% of all protein found in the human body, making it an ideal candidate for extracellular matrix mimetic scaffold design [76, 77]. The collagen-glycosaminoglycan based scaffold design pioneered by Yannas et al in 1989 for the treatment of skin defects has served as a successful template for a range of regenerative medicine and tissue engineering applications [78, 79]. FDA approved, the collagen-glycosaminoglycan scaffold demonstrated a defined chemical composition, tunable pore structure, controlled degradation, and non-angiogenic properties, and was successful in disrupting wound contraction by inhibiting myofibroblast differentiation and activity [78, 80-82]. Additionally, the collagen-glycosaminoglycan scaffold design was later utilized for peripheral nerve regeneration treating a 10 mm gap defect in the rat sciatic nerve and achieving functional repair approaching that of the autograft [83-85]. This scaffold design has since been applied to both osteochondral and orthopedic regenerative medicine and tissue engineering applications [86-90].

As a successful application in both regenerative medicine and tissue engineering, there has been an explosion of studies investigating both the biophysical and biochemical related properties of the collagen-glycosaminoglycan scaffold and their effects on the physiological environment for regenerative medicine and tissue engineering applications. More recent studies performed on this variation of collagen-glycosaminoglycan scaffold design has evaluated the biophysical properties including effect of

lyophilization conditions on pore size [91], the effect of pore size on cell attachment and permeability [92, 93], the mechanical properties and contractile forces exerted by cells [94, 95], and microstructure anisotropy [96, 97]. Similarly, the biochemical properties of collagen-glycosaminoglycan scaffolds pertaining to degradability [98], antigenicity, and immunogenicity [99] have been investigated. Work within this lab has expanded upon this foundation to investigate the application of collagen-glycosaminoglycan scaffolds for cardiatric applications [100] and tendon repair [97, 101], as well as biomolecule incorporation [102, 103], angiogenic processes [104, 105], and variation in proteoglycan composition [106].

1.9 Mineralized Collagen-Glycosaminoglycan Scaffolds

The modification of Yannas et al collagen-glycosaminoglycan scaffold design for orthopedic regenerative medicine and tissue engineering applications has been accomplished with the incorporation of a calcium phosphate mineral phase during fabrication. Studies indicated that it was possible to incorporate a biologically relevant mineral phase by the controlled addition of calcium nitrate tetrahydrate and calcium hydroxide to produce a brushite mineral phase with control over the reaction mass yield via concurrent mapping techniques in the absence of titrants [87, 107]. Using subsequently time dependent and pH controlled hydrolysis steps, it was shown that the brushite mineral phase could be converted from brushite ($CaHPO_4$) to octacalcium phosphate ($Ca_8H_2(PO_4)_6$) to hydroxyapatite [88]. The triple coprecipitation of collagen, glycosaminoglycans, and calcium phosphate has been shown to produce collagen-glycosaminoglycan scaffolds with 0 to 80 wt% mineral phases encompassing the 30 to 70 wt% hydroxyapatite mineral phase often observed in bone [87, 88, 108-112].

Alternative methods of collagen-glycosaminoglycan scaffold mineralization have also included soaking in mineral suspensions such as ammonium sodium phosphate dibasic ($NaNH_4HPO_4$) followed by calcium chloride ($CaCl_2$) or alternatively in simulated body fluid, or the direct addition of calcium phosphate

particles to the collagen-glycosaminoglycan scaffold precursor to incorporate a calcium phosphate mineral phase [113-115]. With various work investigating the effect of mineralization on scaffold biophysical and biochemical properties including facilitation of gene transfection [116-118], growth factor delivery [119-121], mechanics, porosity and pore microstructure, pore size, and matrix production [115]. Additional work has utilized this mineralized collagen-glycosaminoglycan scaffold design for the treatment of osteochondral defects through the development of a multi-compartment scaffold biomaterial [89].

1.10 Overview of Thesis: Motivation, Hypothesis, and Chapter Outline

While bone possesses the remarkable quality of repairing itself to a to such a degree it is considered regenerative, injuries beyond a critical size still result in wounds incapable of physiological repair. Beyond this critical size, surgical intervention employing the gold standard of autologous or allogenic bone grafts is required for functional recovery of the defect. With the growing number of orthopedic interventions compounded by patient specific, complex geometrical constraints, concerns over donor site morbidity in the case of autologous grafts, and allogenic supply and disease transmission in the case of allogenic grafts, has highlighted the need for alternative orthopedic biomaterials. The goal of this work has been the development of one such orthopedic biomaterial for the treatment of complex mandibular and craniofacial defects.

In order to provide a viable alternative to autograft and allografts in the field of orthopedics, a more active biomaterial design capable of facilitating and furthermore instigating the physiological repair processes through biochemical, biophysical, and biomolecular properties, as opposed to the biologically inert materials currently employed. Such active biomaterial design via stimulation and direction of the cellular response through biochemical, biophysical, and biomolecular properties has been the focus of regenerative medicine and tissue engineering efforts. However, supplying the necessary supra-

physiological doses of growth factors to achieve biomolecular stimulation remains a challenge with careful modulation and sustained release of such large dosages. This goal of an orthopedic biomaterial approach will emphasize a biochemical and biophysical material property guided cellular response in the absence of exogenous biomolecule supplementation.

To achieve the treatment of complex mandibular and craniofacial defects in the absence of exogenous biomolecule supplementation, the further development and characterization of the mineralized collagen-glycosaminoglycan design originally developed by Yannas et al and expanded upon by Harley et al was performed. Here we hypothesize that the calcium phosphate mineralized collagen-glycosaminoglycan scaffold is capable of inducing osteogenic cell behavior and mineral deposition through material properties, in the absence of osteogenic supplementation. Furthermore, we hypothesize that the mechanical properties of the mineralized collagen-glycosaminoglycan scaffold can be enhanced for *in vivo* implantation with the incorporation of a polycaprolactone support structure while preserving the innate aforementioned osteogenic potential.

Chapter 2 highlights the flexibility of the mineralized collagen-glycosaminoglycan scaffold in its biophysical and biochemical properties for the treatment of a diverse range of orthopedic defects and patient specific considerations [48]. Here the biochemical and biophysical properties attributed to influencing cellular behavior were evaluated. These biochemical and biophysical properties included the compositional variation in mineral content, the average pore size, elastic modulus in compression, and the permeability.

Chapter 3 investigates the influence of the mineralized collagen-glycosaminoglycan scaffold on a physiologically relevant cell population behavior, specifically evaluating an osteogenic-like phenotype towards the treatment of orthopedic defects [122]. Here mesenchymal stem cells were cultured *in vitro*

over 56 days, with the influence of calcium phosphate mineral content within the collagen-glycosaminoglycan scaffold compared to bone morphogenetic protein 2 and osteogenic media supplemented variations. The metabolic activity, osteogenic gene expression, and matrix remodeling were evaluated on within the collagen-glycosaminoglycan scaffolds.

Chapter 4 evaluates the mechanical reinforcement of previous scaffolds with the fabrication of a multi-scale mineral polycaprolactone-collagen-glycosaminoglycan composite biomaterial for the treatment of load bearing craniofacial orthopedic defects [123]. Here a mechanically competent macro-porous polycaprolactone support construct was impregnated with highly bioactive micro-porous mineralized collagen-glycosaminoglycan matrix. Initial cell attachment was evaluated after 24 h of *in vitro* porcine adipose derived stem cells culture, while differences the bulk elastic moduli and micron-scale pore architecture determined the biophysical properties.

Chapter 5 confirms the *in vivo* efficacy of the multi-scale polycaprolactone-collagen-glycosaminoglycan composite through implantation into a sub-critical mandibular ramus defect within a porcine animal model [124]. Following a 6 week *in vivo* culture, new bone formation in the composite was investigated and compared to the mineralized collagen-glycosaminoglycan scaffold and the polycaprolactone support construct alone. Healing was evaluated through the quantity and relative density of new bone formation.

Chapter 6 investigates compositional alterations to the original mineralized collagen-glycosaminoglycan scaffold with a substitution of heparin as the glycosaminoglycan [125]. Enhancements in bioactivity were evaluated through an *in vitro* culture with porcine adipose derived stem cells over a period of 28 days, with cellular metabolic activity, mineral deposition, and changes in elastic moduli measured as criteria of cellular bioactivity within scaffold variants.

Chapter 7 continues the evaluation of the versatility of the collagen-glycosaminoglycan scaffold through the expansion of the previously developed multi-compartment collagen-glycosaminoglycan scaffold design towards the treatment of entheses within a craniofacial defect [48]. Biochemical and biophysical properties, including pore size, elastic moduli in compression, and permeability, were evaluated within a multi-compartment scaffold containing distinct non-mineral and mineral regions with a gradient interface between.

1.11 Figures

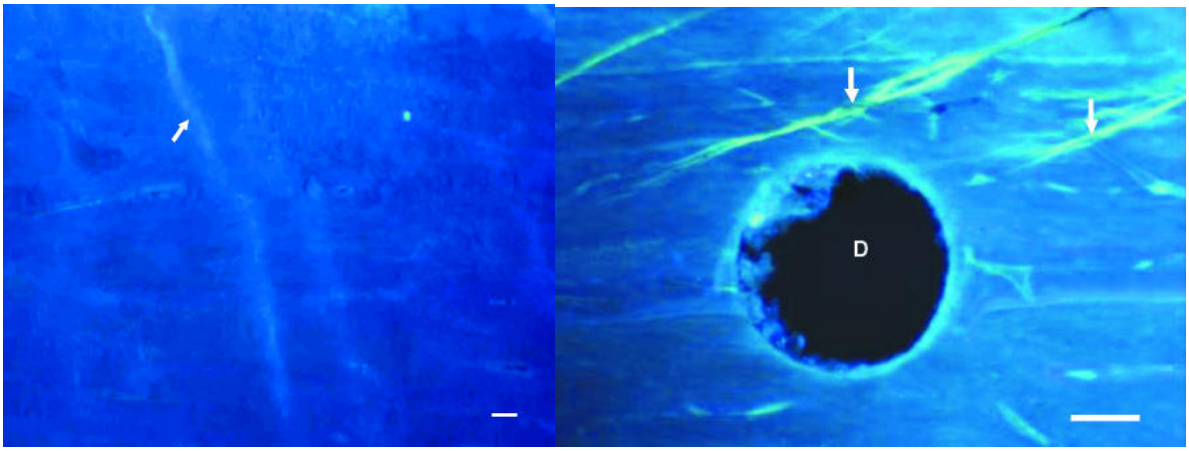

Figure 1.1 Presence of microcracks in bone.

Presence microcracks (identified by right arrows) stained with calcein identified in previous literature [5]. A drill hole was used as a reference point in the right image. The present scale bars were 200 um (left image) and 100 um (right image).

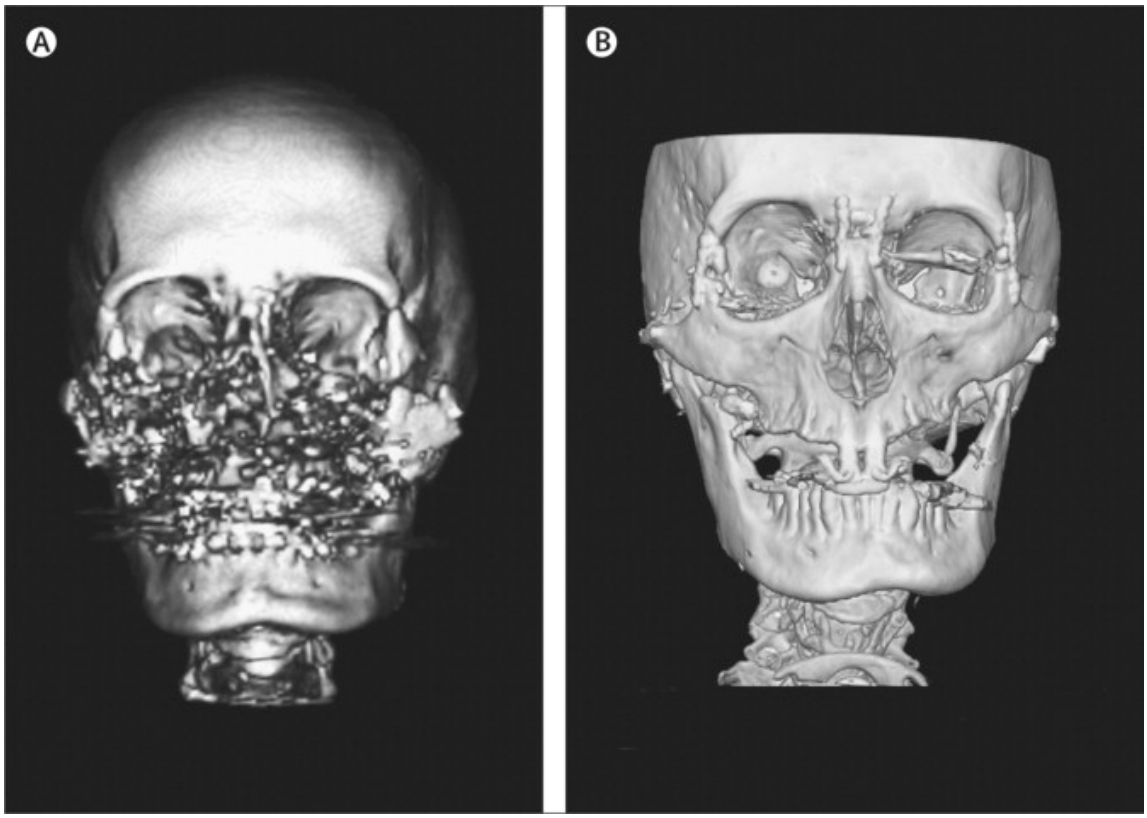

Figure 1.2 Severe craniofacial trauma treated with allograft from a donor.

(A) Severe craniofacial trauma caused by gunshot wound and (B) reconstruction after 3 months [126].

CHAPTER 2

FABRICATION AND CHRACTERIZATION OF THE COLLAGEN-GLYCOSAMINOGLYCAN SCAFFOLD: FLEXIBILITY OF BIOPHYSICAL AND BIOCHEMICAL MATERIAL PROPERTIES AND DESIGN[1]

2.1 Overview

The incorporation of a mineral phase within biomaterials for orthopedic applications has been shown to enhance the osteogenic bioactivity of these minerals scaffolds. Here the incorporation of a calcium phosphate mineral phase into collagen-glycosaminoglycan scaffold design is verified with the resulting alterations in biochemical and biophysical properties being investigated. This chapter investigated two degrees of mineralization (40 wt% and 80 wt%) via a triple co-precipitation and lyophilization method spanning the physiological range of bone mineral (30-75wt%). The hydroxyproline and 1,9-dimethylmehylene blue (DMMB) chemical assays were used to quantify the amount of collagen and glycosaminoglycans, respectively, within the mineralized scaffolds with the remaining mass fraction determining the mineral phase percentage. In both degrees of mineralization, powder x-ray diffraction was used to identify the mineral phase. Additionally, the effect of mineralization on the mechanical

[1] This work is a partial adaption from the study 48. Weisgerber, D.W., et al., *The impact of discrete compartments of a multi-compartment collagen-GAG scaffold on overall construct biophysical properties.* Journal of the mechanical behavior of biomedical materials, 2013. **28**: p. 26-36.. The work presented in Chapter 7 concludes this adaptation from the study 48. Ibid.

properties and microstructure was investigated via the compressive modulus, average pore size, and permeability of the scaffold.

2.2 Introduction

Orthopedic defects remain challenges in regenerative medicine and tissue engineering research due to their large size, complex geometries, and load bearing function. The standard clinical treatment for such critically sized orthopedic defects involves the use of an orthopedic implant, namely an autologous or allogenic bone graft [17, 18, 127]. However, concerns over defect size and volume as well as the donor site pain and morbidity remain for autologous bone grafts, while concerns over disease transmission as well as donor availability for allogenic bone grafts are also predominate [128-131]. These concerns along with the growing prevalence of orthopedic defects resulting from the growing and aging population have sparked the regenerative medicine and tissue engineering communities to investigate orthopedic biomaterial alternatives. Previous orthopedic implants employed clinically are physiologically inert and non-degradable serving only to provide mechanical support with limited osteoconductivity. Prime examples are the titanium hip implant, poly insert, and silicone implants [16]. While these implants support mechanical restoration for load bearing applications they do not support the physiological aspects, such as ion homeostasis and hematopoiesis. However, the lack of physiological function and concerns over loosening, termed aseptic loosening, of the cement failure and resulting wear debris and wear debris have warranted an additional approach to biomaterial design [132-134]. Current regenerative medicine and tissue engineering approaches have taken a more active approach in guiding the physiological wound healing processes through biophysical, biochemical, and biomolecular material properties [21].

This growing paradigm shift toward evaluating tissue engineering biomaterials that actively enhance the physiological wound healing process for a physiologically relevant treatment outcome has prompted biomaterials are evaluated on the biophysical and biochemical properties that influence cellular behavior

[22, 23]. These properties have included material stiffness, necessary in providing support but also the materials influence on cell fate [28], microstructure and surface area as influencing cell attachment, on nutrient and waste exchange [92], and composition especially in the case of orthopedic implants where the role of calcium phosphate minerals has been demonstrated to influence cellular behavior [87].

Within regenerative medicine, biomaterials designed on simulating the extracellular matrix environment, particularly collagen based scaffolds, have shown particular promise [78, 79]. The collagen-glycosaminoglycan scaffold originally crafted for dermal regeneration for burn victims represent one of the many successful applications [78]. Additional studies have evaluated the collagen-glycosaminoglycan scaffold for nerve regeneration [83-85], tendon regeneration [97], and osteochondral regeneration [89]. Additionally, the literature has demonstrated the incorporation of a calcium phosphate mineral phase into the collagen-glycosaminoglycan scaffold for the treatment of orthopedic defects [87, 88].

This work evaluates the fabrication of one such mineralized collagen-glycosaminoglycan scaffold fabricated by the lyophilization of a mineralized collagen-glycosaminoglycan precursor suspension [88]. The lyophilized mineralized collagen-glycosaminoglycan precursor suspension was first fabricated through the controlled triple co-precipitation of collagen, glycosaminoglycan, and calcium phosphate precursor components using a rotor-stator homogenization setup and concurrent mapping techniques to control the calcium phosphate mineral mass yield [87, 107]. The composition with mineral percentage was then evaluated to verify previous work [87, 88, 108, 135]. Then the effect of mineral content and final freezing temperature during lyophilization on the biophysical and biochemical material properties was evaluating including microstructural and mechanical material properties implicated in the bioactivity of orthopedic implants.

2.3 Overview of the Rotor-Stator Homogenization Process

The fabrication of the non-mineralized collagen-glycosaminoglycan (CG) and mineralized collagen-glycosaminoglycan (CGCaP) precursor suspensions was accomplished via the homogenization of collagen, glycosaminoglycans, and mineral components with a rotor-stator. Rotor-stator tissue homogenizers consist of a motor and a probe or generator, which is composed of two parts: the rotor and stator. Here the rotor rotates within the stator between 3,000-60,000 rpm, with the tissue being drawn into the probe through the stator via holes or gaps within the teeth [136]. Larger particulates are then homogenized by mechanical shear and extreme turbulence generated by the rotor-stator. At the micron level, homogenization within the rotor-stator is achieved again by extreme turbulence, but also by the collapse of low-pressure vapor cavities, termed cavitation, and the shear forces generated from the rotor passing the stator [136]. The degree of homogenization and resulting particle size is dictated by the rotor speed and gap between rotor and stator, with smaller particle sizes achieved at faster speeds and smaller gaps. The inherent flexibility of this system allows for the homogenization of various proteins or chemicals into one precursor suspension that can be later used for scaffold fabrication.

2.4 Fabrication of Non-Mineral CG Suspension

The non-mineralized collagen-glycosaminoglycan (CG) suspension was achieved by the homogenization of collagen and glycosaminoglycans via a rotor-stator setup. This was accomplished by homogenization of 0.5% w/v type-I fibrillar collagen isolated from bovine Achilles tendon (Sigma-Aldrich, St. Louis, MO) in 0.05M acetic acid. Then at a ratio of 11.25 collagen:1 glycosaminoglycan, 0.044% w/v chondroitin sulfate isolated from shark cartilage (Sigma-Aldrich, St. Louis, MO) was solubilized in 0.05M acetic acid and added to the homogenized collagen suspension. Following homogenization, the resulting CG suspension was stored at 4°C prior to lyophilization.

2.5 Fabrication of Mineral CGCaP Suspension

Similarly, the mineralized collagen-glycosaminoglycan (CGCaP) suspension was achieved by the triple co-precipitation of collagen, glycosaminoglycan, with a calcium phosphate mineral. The preparation of the precursor suspension proceeded with the homogenization of type-I fibrillar collagen from bovine Achilles tendon (Sigma-Aldrich, St. Louis, MO) and chondroitin sulfate isolated from shark cartilage (Sigma-Aldrich, St. Louis, MO) in the presence of calcium hydroxide ($Ca(OH)_2$; Sigma-Aldrich, St. Louis, MO) and phosphoric acid. The subsequent addition and homogenization of calcium hydroxide and calcium nitrate tetra-hydrate ($Ca(NO_3)_2$ $4H_2O$; Sigma-Aldrich, St. Louis, MO) concluded the triple co-precipitation. The resulting CGCaP suspension was stored at 4°C prior to lyophilization.

The controlled precipitation of the calcium phosphate mineral phase was achieved by a concurrent mapping method previously established [87, 107]. Briefly, control over the mass yield of the calcium phosphate mineral phase was achieved by independently varying the calcium hydroxide to calcium nitrate tetra-hydrate molar ratio and the molarity of the phosphoric acid. In this study, two variations (low and high mineral content) of the molar ratio of the calcium ingredients and the molarity of the phosphoric acid used was derived from the previous work utilizing this triple co-precipitation methodology [87, 88, 108, 135].

2.6 Overview of the Lyophilization Process

Following the fabrication of the precursor suspensions, subsequent lyophilization achieved the 3-dimensional scaffold microstructure employed in this study and throughout all remaining work evaluating the mineralized collagen-glycosaminoglycan scaffold. Lyophilization or freeze drying is the process by which water is removed via freezing and sublimation. Lyophilization represents one of the most common processes for the long term preservation of proteins and accounts for the formulation of approximately 50% of all pharmaceuticals [137]. In the case of biomaterials, lyophilization provides a straightforward

process by which most synthetic and organic polymers can be organized into a 3-dimensional pore structure. Briefly, the biomaterial precursor suspension is cooled until ice crystal nucleation begins with subsequent freezing leading to the growth of the nucleated ice crystals [137]. As the ice crystals grow, the suspension solutes and solid material components of the biomaterials are concentrated at the ice crystal periphery in what is termed “cryoconcentration” [137]. Continued cooling of the precursor solution results in either the eutectic crystallization or vivification of the concentrated solutes [137]. At a temperature below the freezing point of water, the pressure is then reduced by pulling vacuum on the system; if performed correctly, increasing the temperature at a low pressure results in sublimation, the phase transition of water from solid (ice) to vapor (air) avoiding the liquid (water) phase altogether. Removal of the ice crystals results in voids or pores within the resulting matrix, or cake when referring to lyophilization.

For biomaterial fabrication via lyophilization it is essential to note that with various techniques and careful manipulation, ice crystal nucleation and ice crystal growth can be decoupled. This allows for independent control over the pore microstructure via nucleation and pore size via growth kinetics. For the design of biomaterials, and in the particular case of collagen-glycosaminoglycan scaffolds, this allows for the flexible design of unique isotropic or anisotropic pore structures with tunable pore sizes. Examples of such include the alignment of pores in collagen-glycosaminoglycan scaffolds for the treatment of tendon defects [97].

2.7 Non-Mineral and Mineralized Collagen-Glycosaminoglycan Scaffold Fabrication

In the present study, 1 mL of the non-mineral (CG) and mineral (CGCaP) precursor suspensions was pipetted into each of the 6 cylindrical wells (12 mm deep, 13 mm diameter, 1.5 mm thick base) present in a custom polysulfone array mold. Lyophilization was then preformed using a Genesis freeze-dryer (VirTis, Gardener, NY). Briefly, the scaffold precursor suspensions were cooled at a constant rate of

1°C/min to a final freezing temperature of -10°C or -40°C and held at that final freezing temperature for 175 minutes. Sublimation then proceeded at 0°C and 200 mTorr. In the case of the non-mineral CG scaffold a secondary dehydrothermal (DHT) crosslinking step was performed at 105°C and <25 Torr for 24 h in a vacuum oven (Welch, Niles, IL) as previously established [138]. The resulting scaffolds were 12 mm in diameter and 10 mm in height. Subsequent compositional, microstructural, and mechanical analysis was performed on these scaffold specimens.

2.8 Compositional Analysis of the Mineralized Collagen-Glycosaminoglycan Scaffold

In order to demonstrate control over the incorporation of the calcium phosphate mineral phase into the mineralized CGCaP scaffolds, two CGCaP scaffold variations were produce with a high and low mineral wt%. Compositional analysis was achieved using a hydroxyproline assay to measure the concentration of collagen present [139], a 1,9-dimethylmethylene blue (DMMB) assay to determine the amount of sulfated glycosaminoglycan content present [140], and mass subtraction to determine the remaining calcium phosphate mineral phase fraction [87, 88]. Briefly, following lyophilization the dry mass of all samples was measured (n = 4). Subsequent measurement of the collagen content within the scaffold was accomplished by the colorimetric detection and quantification, via a flourometer (Tecan, Männedorf, Switzerland) and comparison to a prepared hydroxyproline standard respectively, of hydroxyproline present within the scaffold digest, digested with 6 M HCl (Sigma-Aldrich, St. Louis, MO) at 110°C for 24 h. Hydroxyproline is derived from the hydroxylation of the amino acid proline and occurs at regular intervals in the collagen amino acid sequence. As such, the total amount of collagen present in each scaffold was determined by a known scaling of the mass of hydroxyproline present within the corresponding digest. The amount of glycosaminoglycan (GAG) present within each scaffold was determined by the formation and isolation, via centrifugation, of the sulfated glycosaminoglycan (GAG)-1,9-dimethylmethylene blue (DMMB) complex (GAG-DMMB) by addition of DMMB to the scaffold digest, digested via proteinase K (Sigma-Aldrich, St. Louis, MO) at 56°C overnight. After removing the

supernatant following centrifugation, the GAG-DMMB complex is re-suspended and colormetrically detected using a flourometer (Tecan, Männedorf, Switzerland) with the resulting quantification and comparison to a prepared chondroitin sulfate standard determining the total amount of GAG present within the scaffold digest and subsequently the scaffold. Because the mineral CGCaP scaffolds were fabricated through the homogenization and lyophilization of only collagen, glycosaminoglycans, and calcium phosphate additives, the remaining fraction of calcium phosphate was determined via mass subtraction: CaP wt% = (total mass – collagen mass – GAG mass)/(total mass) (Figure 2.1).

Visualization of microstructural differences due to the high and low mineral wt% was identified using a JEOL JSM-6060LV Low Vacuum Scanning Electron Microscope (JEOL USA, Peabody, MA). Determination of the calcium phosphate mineral phase was accomplished via powdered x-ray diffraction. Briefly, samples were placed inside a Siemens/Bruker D-5000 diffractometer (Bruker AXS, Madison, WI) with a Cu Kα source and scanned from 2.5° 2θ to 50° 2θ at a rate of 1°/min and an increment of 0.1° 2θ. The mineral phase was then determined from the analysis of the resulting spectra using MDI Jade analysis software (Materials Data Inc., Livermore, CA).

The low mineralized CGCaP scaffold variation was found be composed of 37.8 ± 1.1 wt% collagen, 19.7 ± 0.4 wt% GAG, and 42.6 ± 1.2 wt% CaP mineral (Figure), and are henceforth referred to as the 40 wt% CGCaP scaffold. Similarly, the high mineralized CGCaP scaffold variation was found to be composed of 18.6 ± 3.0 wt% collagen (Figure), 2.9 ± 0.2 wt% GAG, and 78.5 ± 3.0 wt% CaP mineral, and are henceforth referred to as the 80 wt% CGCaP scaffold. In both cases, the composition coincides with the previously described concurrent mapping method and procedures previously outlined [87, 88, 108, 135]. The variation in precursor suspension reflected by the resulting composition of the mineral scaffold highlights ability to produce scaffolds with a defined mineral content spanning the native physiological range of bone, 30-70 wt% [109-112]. This variation in the mineral content was visually observed via

scanning electron microscopy (Figure 2.2). Additionally, the calcium phosphate mineral phase in both 40 wt% and 80 wt% CGCaP scaffolds was found to consist of only brushite ($CaHPO_4$) in agreement with previous work (Figure 2.3), with variation in the peak intensity corresponding to the difference in the quantity of brushite[87, 88]. Additional studies evaluating the calcium phosphate mineral phase in collagen-glycosaminoglycan scaffolds have modification of the brushite phase to octacalcium phosphate to apatite via hydrolysis[87, 88].

2.9 Effect of Composition and Lyophilization Temperature on Pore Microstructure

Changes in the pore structure due to the presence of the calcium phosphate mineral phase was investigated by the comparison of the average pore size at two different final freezing temperatures, -10°C and -40°C. In order to determine the average pore size scaffolds were embedded, sectioned, and stained in accordance to previous work evaluating the pore structure within collagen-glycosaminoglycan scaffolds [91]. Briefly, 6 mm cores of the non-mineral CG and mineral 80 wt% CGCaP scaffolds biopsied (Integra Miltex, York, PA) from their monolithic (12 mm diameter, 10 mm height) counterparts were section in the transverse and longitudinal plane. Both transverse and longitudinal sections were then embedded in glycomethacrylate using a previously described method [91]. Samples were then further sectioned into 5 μm slices, stained with aniline blue (Thermo Fisher Scientific Inc, Waltham, Ma) for collagen, and imaged using an optical microscope (Leica Microsystems, Wetzlar, Germany). A linear intercept macro in Scion Image was then used to calculate both the average pore size and average aspect ratio within each scaffold.

Comparing the non-mineral CG scaffold and mineral CGCaP scaffold exhibited no significant difference in average pore size in the range of 150-160 um. Between the non-mineral CG and mineral CGCaP scaffold, a non-significant average pore size in the range of 150-160 μm was observed (Figure 2.4, Table 2.1). The lack of variation in average pore size between the non-mineral CG and mineral CGCaP

scaffolds is informative and suggests that during lyophilization the concentration of precursor solute, or cryoconcentration during ice crystal growth, did not saturate. Such saturation would force significantly larger struts resulting in a significantly smaller average pore size. This suggests that further alterations in density, through additional protein or calcium phosphate mineral, may be achieved without significant impact to the pore microstructure. Additionally, comparing the non-mineral CG scaffolds between -10°C and -40°C, and the mineral CGCaP scaffolds between -10°C and -40°C also yielded no significant effect of final freezing temperature on average pore size (Figure 2.4, Table 2.1). This is contrary to previous work evaluating the microstructure of collagen-glycosaminoglycan scaffolds [92, 141]. However, the lack of disparity in pore size due to freezing temperature is attributed to the low thermal conductivity of polysulfone, which in effect blunted the difference in freezing kinetics between the two temperatures. Previous studies have already established the significance of freezing kinetics due to cooling rate, freezing temperature, and mold conductivity on pore size [91-93, 141], while this work demonstrates the non-significant impact of calcium phosphate mineral on pore size. As such it is concluded that further manipulation of the freezing kinetics during the fabrication will highlight the flexibility of the lyophilization approach in controlling pore microstructure for mineral scaffold fabrication.

2.10 Effect of Composition on Scaffold Mechanical Characteristics

The effect of the calcium phosphate mineral on the mechanical properties of the collagen-glycosaminoglycan scaffold design was evaluated by the comparison of the non-mineral CG scaffold to the mineral CGCaP scaffold during compression testing. Here scaffolds were compressed to 75% of their total height, 0.75 strain, using a MTS Insight Electromechanical load frame (MTS, Eden Prairie, MN) with a 250 N load cell. In all cases, scaffold height and diameter was recorded using calipers prior to testing. The resulting load vs displacement plots were converted to stress (≡ σ = load/area) vs strain (≡ ε = displacement/height) with the elastic modulus (E), collapse stress (σ_{el}), and collapse strain (ε_{el}) determined

from the linear elastic regime (ε: 0.02-0.12) and the intersection of the linear regression from the elastic regime and collapse plateau respectively (Figure 2.5).

At both final freezing temperatures, -10°C and -40°C, a significant increase ($p < 0.05$) in elastic modulus of the mineral CGCaP scaffold compared to the non-mineral CG scaffolds was observed (Figure 2.6, Table 2.1). Only mineralized scaffold exhibited a significant ($p < 0.05$) change in modulus between the final freezing temperatures, -10°C and -40°C (Figure 2.6, Table 2.1). Here the incorporation of a mineral phase resulted in a two orders of magnitude increase in modulus, however, the relative difference between the mineral CGCaP scaffold and the physiological range of bone (90 MPa – 230 MPa) excludes the current biomaterial from load bearing orthopedic defects [49]. Additionally, both the stress-strain behavior of the non-mineral CG and mineral CGCaP scaffold exhibited the linear elastic, the collapse plateau, and densification regimes characteristic of low-density open-cell foams described by cellular solids theory described in the literature [142]. Because these scaffolds behave as low-density open-cell foams, cellular solids theory can also be used to model the modulus of the material [94, 142]. The collapse strain evaluated for all non-mineral CG and mineral CGCaP scaffolds was approximately 0.1, ranging from 0.07 to 0.14, consistent with previous observations for low-density open-cell foams [94, 142]. The adaptation of the mineral CGCaP scaffold for physiologically relevant orthopedic defects will be addressed through the formation of a biomaterial composite discussed later.

2.11 Effect of Composition on Scaffold Permeability

Finally, as a measure of potential cellular and bimolecular penetration into the scaffold as well as the exchange of cellular waste for nutrients the permeability of the mineral CGCaP scaffold was investigated and compared to that of the non-mineral CG scaffold. In this study the permeability of the scaffold was investigated at various degrees of compression using the constant-head permeability apparatus (Figure 2.7). Briefly, the constant-head permeability apparatus works by measuring the flow of fluid through a

sample under constant pressure, this method is commonly employed in geological studies of soil or rock permeability. In this work, a custom polycarbonate permeability rig was fabricated with variable spacers representing predefined degrees of compression, ε: 0, 0.10, 0.40, and 0.65 (Figure 2.7). The hydrated non-mineral CG or mineral CGCaP scaffold was then placed between two T316 stainless steel mesh discs (0 .0075" wire diameter, 0.009" gaps, TWP Inc, Berkley, CA) with an appropriately sized gasket or grommet preventing leakage. A variable pressure head, ΔP: 1.2", 3.0", or 7"dependent on scaffold variant and degree of compression, was applied. The resulting fluid volume (v, mL) was measured in small volumes with a graduated cylinder against time (t, sec), determining the fluid flow rate (Q = v/t). Using the fluid viscosity (μ), sample thickness (l) and cross-sectional area (A), the permeability (K) of the scaffolds was calculated using Darcy's law [93]:

$$K = \frac{Q \cdot l \cdot \mu}{\Delta P \cdot A}$$

In order to identify changes in scaffold permeability due to the presence of a calcium phosphate mineral phase, compression, final freezing temperature, and cellular solids predictions of the permeability of each scaffold (ε: 0, 0.10, 0.40) was normalized to the identical scaffold unstrained (ε: 0) (Figure 2.8). Between the non-mineral CG and mineral CGCaP scaffold, the mineral scaffold possessed a significantly ($p < 0.05$) higher permeability. This observation was counter to the results predicted by cellular solids theory, which predicted a decrease in permeability with increasing density [142]. Suggesting that the increased fluid flow in the mineral CGCaP scaffold may be due to the inherent mechanical competence and resistance to deformation preserving the highly porous scaffold architecture compared to the non-mineral CG scaffold. Additionally, a significant ($p < 0.05$) decrease in permeability was also observed with the decrease in final freezing temperature, -10°C to -40°C (Figure 2.8), suggesting sensitivity to changes in the average pore size, even the non-significant changes observed (Figure 2.4, Table 2.1). When strained,

the permeability significantly decreased in both the non-mineral CG and mineral CGCaP scaffold corresponding to pore collapse and an increased resistance to fluid flow due to densification, in agreement with cellular solids theory predictions (Figure 2.8) [142].

2.12 Conclusions

This work has evaluated the incorporation of a mineral phase into the collagen-glycosaminoglycan scaffold and the resulting effects on the biophysical material properties encompassing microstructure, mechanics, and permeability (Table 2.1). A variable amount of brushite calcium phosphate mineral ranging from 40 wt% to 80 wt% was incorporated into the collagen-glycosaminoglycan scaffold via a triple co-precipitation and concurrent mapping methods. A non-significant difference in average pore size, circa 160 μm, was observed between the non-mineral CG and mineral CGCaP. Additionally, a non-significant trend in average pore size was observed due to final freezing temperature, this contrast to previous literature is attributed to the mold thermal conductivity blunting the freezing kinetics during lyophilization. A significant increase in the modulus of the collagen-glycosaminoglycan scaffold was observed with the addition of the calcium phosphate mineral phase in accordance to an increase in density predicted by cellular solids theory. Finally, a significant increase in permeability was observed in the mineral CGCaP scaffold compared to the non-mineral CG scaffold, this observation was counter to an increase in density and predictions from cellular solids theory and was attributed to the mechanical competence and resistance to deformation.

2.13 Figures and Tables

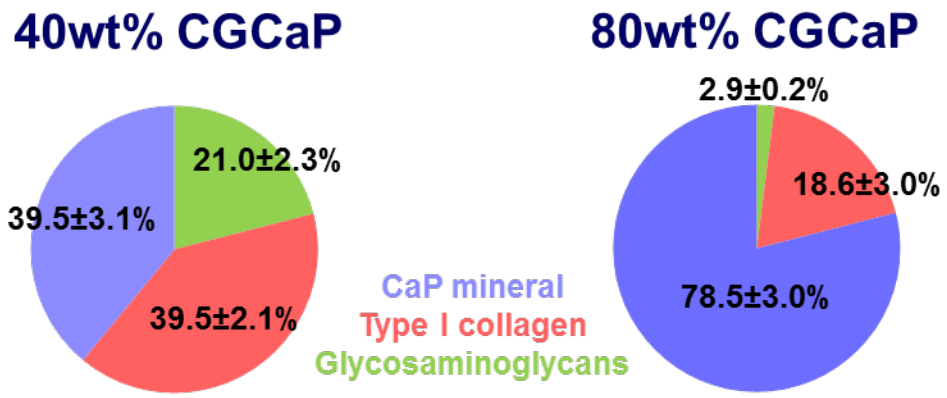

Figure 2.1 The composition of the low (40 wt%) and high (80 wt%) mineralized scaffolds.

Composition was determined via assays evaluating collagen (hydroxyproline assay), glycosaminoglycans (1,9-dimethylmethylene blue), and calcium phosphate (CaP; mass subtraction: CaP wt% = [total mass – collagen mass – glycosaminoglycan mass] / total mass).

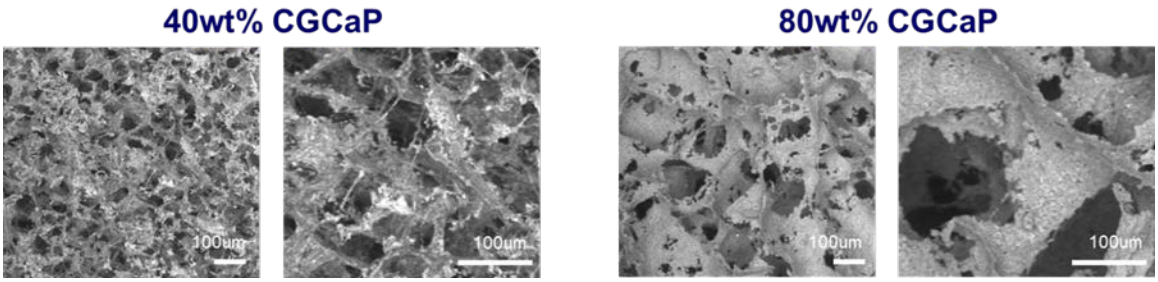

Figure 2.2 SEM visualization of low (40 wt%) and high (80wt%) mineralized scaffolds.

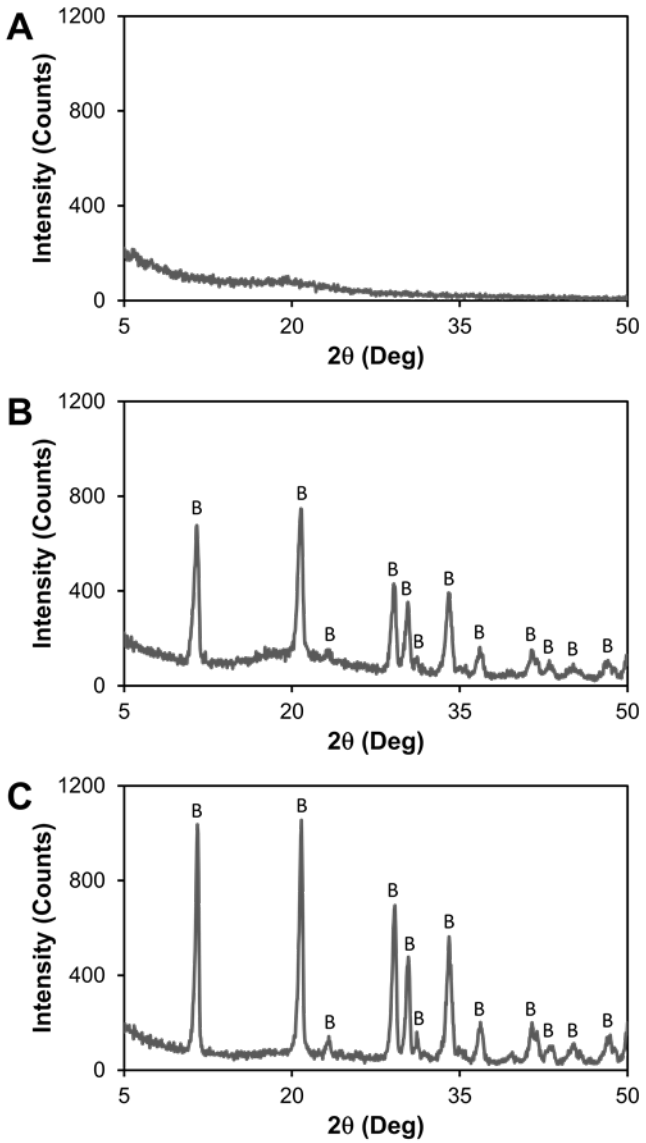

Figure 2.3 The diffraction patterns of scaffolds identifying mineral phase.

Diffraction patterns associated with (A) the non-mineral CG scaffold, (B) the low (40 wt%) mineral CGCaP scaffold, and (C) the high (80 wt%) mineral CGCaP scaffold were determined from powder x-ray diffraction. Analysis of diffraction patterns identified brushite as the calcium phosphate mineral phase.

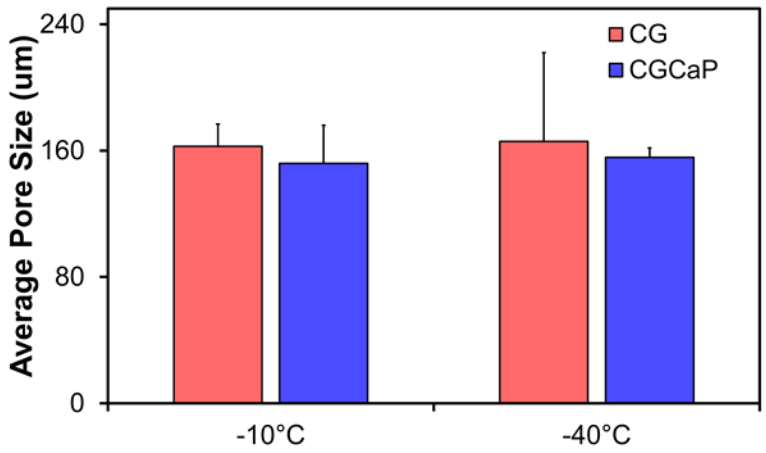

Figure 2.4 The average pore size determined of non-mineral and mineral scaffolds.

Pore size was determined via aniline blue staining of histological sectioning of the non-mineral CG and mineral CGCaP scaffolds that were fabricated at -10°C and -40°C.

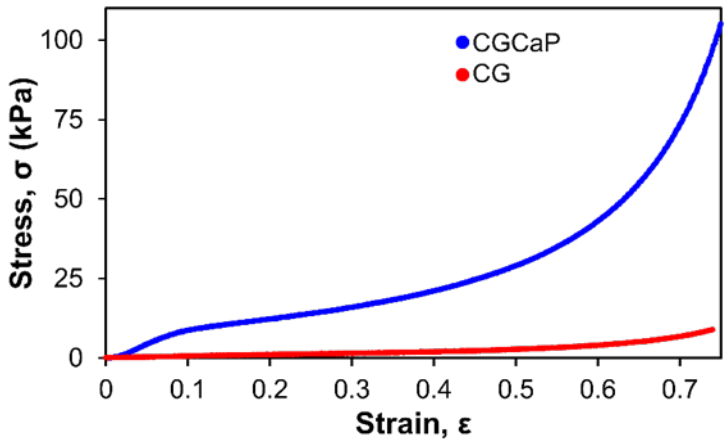

Figure 2.5 The stress-strain behavior of the mineral and non-mineral scaffolds.

As determined in unconfined compression, the stress-strain behavior of the (blue) mineral CGCaP scaffold and the (red) non-mineral CG scaffold. These included the linear elastic (circa 0-0.1 strain), collapse plateau (circa 0.1-0.3 strain), and densification (0.3-0.75 strain) regimes characteristic of low density open cell foams were observed.

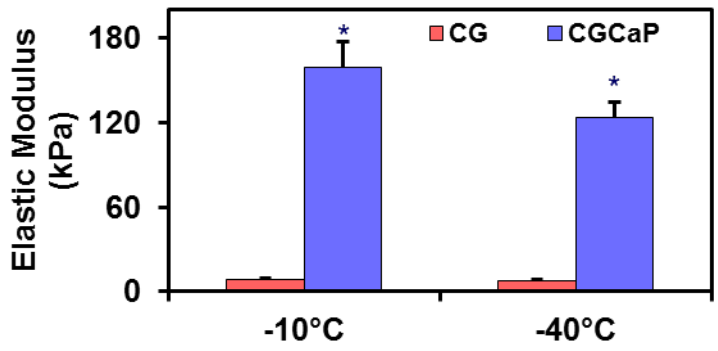

Figure 2.6 The elastic modulus of the non-mineralized collagen-glycosaminoglycan scaffold (red) non-mineral CG scaffold and the (blue) mineral CGCaP scaffolds fabricated via lyophilization with a final freezing temperature of -10°C and -40°C. A significant (*: $p < 0.05$) increase in modulus was observed in the (blue) mineral CGCaP scaffold compared to the (red) non-mineral CG scaffold.

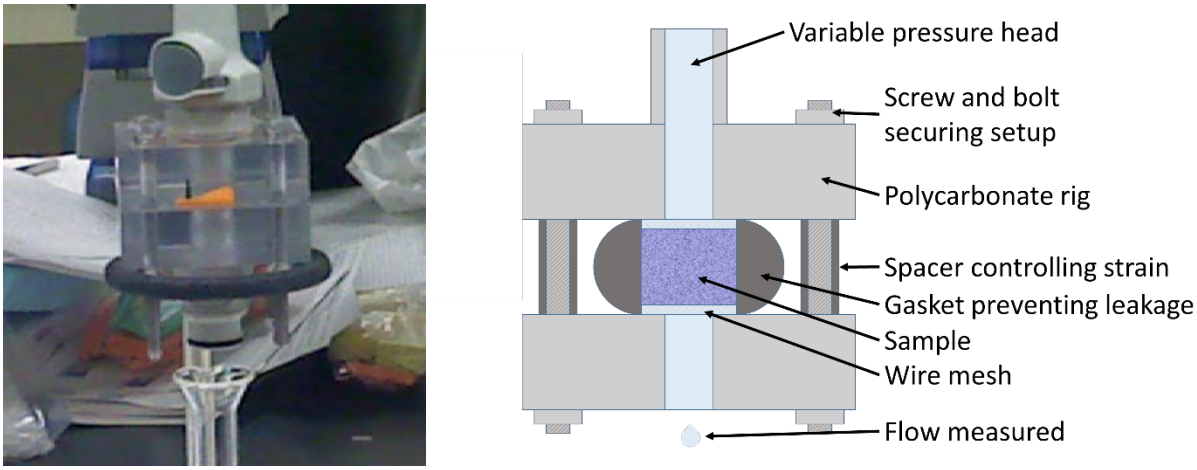

Figure 2.7 Constant head permeability apparatus used to measure permeability.

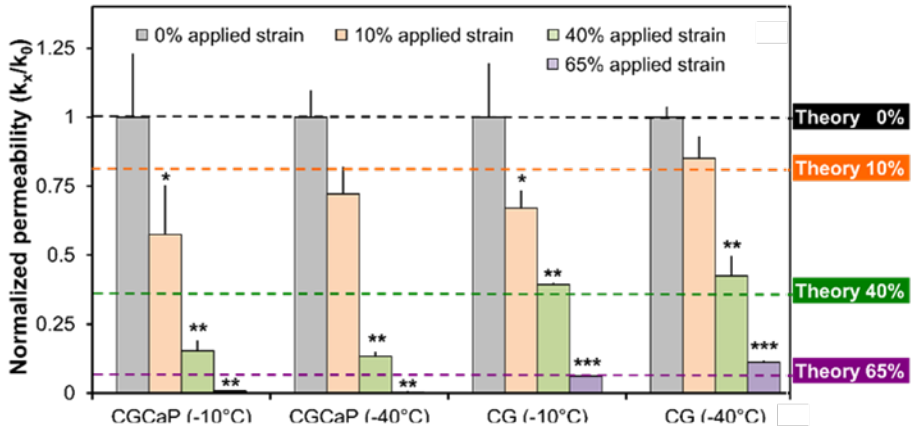

Figure 2.8 Normalized permeability of the mineral and non-mineral scaffolds.

The normalized permeability of non-mineral CG and mineral CGCaP scaffolds fabricated at -10°C and -40°C as measured by a constant head permeability test with cellular solids theory predictions.

Table 2.1 Values of scaffolds measuring microstructure, mechanics, and permeability.

	Scaffold	Non-mineral CG scaffold		Mineral CGCaP scaffold	
	Final Freezing Temperature	-10°C	-40°C	-10°C	-40°C
Microstructure	Average pore size (μm)	163 ± 14	166 ± 56	152 ± 24	156 ± 6
	Average pore aspect ratio	0.92 ± 0.03	0.92 ± 0.03	0.94 ± 0.02	0.95 ± 0.01
Mechanical properties	Elastic modulus (E; kPa)	8.8 ± 1.1	8.1 ± 0.4	159.0 ± 18.3	123.4 ± 11.3
	Collapse strain (ε^*_{el})	0.09 ± 0.06	0.14 ± 0.04	0.09 ± 0.05	0.07 ± 0.03
	Collapse stress (σ^*_{el}; kPa)	0.7 ± 0.4	0.9 ± 0.3	11.2 ± 2.5	7.5 ± 2.0
Permeability	Permeability (m^2)	2.4 ± 0.5 x10^{-8}	1.6 ± 0.1 x10^{-8}	6.1 ± 1.4 x10^{-7}	3.7 ± 0.4 x10^{-7}

Mean pore size and aspect ratios of single compartment CG and 80 wt% CGCaP, and 80 wt% multi-compartment CG-CGCaP (CG, interface, CGCaP regions). Results reported as mean ± STD with histology sections taken from n = 4. Linear elastic moduli (E^*) as well as collapse strain (ε^*_{el}) and stress (σ^*_{el}) of CG and 80 wt% CGCaP. Results reported as a function of final freezing temperature with mean ± STD, n = 6. Permeability of the single-compartment CG and 80 wt% CGCaP scaffolds (ε: 0% strain), mean ± STD, n = 3.

CHAPTER 3

DETERMINATION OF MIENRALIZED COLLAGEN-GLYCOSAMINOGLYCAN SCAFFOLD BIOACTIVITY: ASSESSMENT OF *IN VITRO* CELLULAR BEHAVIOR AND MATRIX DEPOSITION[2]

3.1 Overview

The incorporation of the calcium phosphate mineral phase to the collagen-glycosaminoglycan scaffold design improved the biochemical and biophysical properties of the resulting mineralized collagen-glycosaminoglycan scaffold while maintaining the inherent flexibility in scaffold design. However, in order to assess the effect these biochemical and biophysical properties have on the osteogenic bioactivity of the collagen-glycosaminoglycan scaffold, *in vitro* culture of an appropriate cell population was performed both with and without biomolecule supplementation. During the physiological bone healing process, the recruitment and differentiation of mesenchymal stems cells has been implemented as the major cell population contributing to both bone resorption and deposition [6]. Here human mesenchymal stems cells were seeded onto both non-mineral and mineralized collagen-glycosaminoglycan scaffolds for *in vitro* culture. Bioactivity of the collagen-glycosaminoglycan scaffolds was then assessed via cellular behavior and matrix remodeling metrics. For cellular behavior the metabolic activity and the relative

[2] This work is adapted from the study 122. Weisgerber, D.W., S.R. Caliari, and B.A. Harley, *Mineralized collagen scaffolds induce hMSC osteogenesis and matrix remodeling.* Biomaterials science, 2015. **3**(3): p. 533-42.

mRNA levels associated with osteogenic genes in cells was assessed, while matrix deposition was determined by mineral deposition and changes in scaffold mechanical properties during *in vitro* culture.

3.2 Introduction

As a result of either acute trauma or resection during surgery, orthopedic defects remain particularly challenging targets of regenerative medicine and tissue engineering due to their inherently complex geometry, typically large size, and load bearing function [128-131]. The current standard clinical practice in treating such large critically sized orthopedic defects is the use of either autologous or allogenic bone grafts, however, concerns over the necessary bone volume and shape in addition to the pain and morbidity of the secondary wound site for autologous grafts, as well as the risk of disease transmission and donor availability for allogenic grafts remain a concern for this standard of treatment [143-145]. With the growing population and with more than two million orthopedic surgeries requiring autologous or autogenic bone grafts, the need for regenerative medicine and tissue engineering biomaterial alternatives is growing [146, 147]. However, biomaterials treating the large, geometrically complex, load bearing orthopedic defects must correctly balance biophysical, biochemical, and biomolecular design criteria with the bioactivity of a clinically relevant cell population necessary to produce a physiologically relevant defect repair [148-151].

With the growing need of regenerative medicine and tissue engineering orthopedic biomaterial alternatives a variety of design approaches have been explored, including calcium phosphate mineral constructs [152, 153], synthetic or natural polymeric scaffolds [154, 155], or the polymeric calcium phosphate mineral composites [114, 147, 156, 157]. Due to the inherently variable nature of orthopedic defects dependent on cause, location, and age, orthopedic biomaterials offer a wider degree of tunability allowing for patient specific treatment of such defects. This inherent biomaterial tunability spans biophysical, biochemical, and biomolecular include: morphology, such as fiber alignment [97]; topology,

such as surface roughness [158]; substrate stiffness [28, 159]; inclusion of growth factors such as the bone morphogenetic protein family [160, 161]; full-biomolecule supplementation strategies such as osteogenic media [86, 152, 162]. In the case of media and soluble biomolecular supplementation, the relatively short half-life and diffusive losses of biomolecule supplementation requires repeated supra-physiological supplementation which represents both expensive and complicated clinical treatments with safety concerns arising over the quantity of biomolecules used [147, 163].

Both previous work and literature has evaluated the development of collagen-glycosaminoglycan scaffolds with a range of tunable biophysical and biochemical properties [48, 97, 101] with combinatorial biomolecular supplementation for proliferation and phenotype stability [164, 165]. Particularly, previous work has evaluated a mineralized collagen-glycosaminoglycan scaffold variant for the treatment of orthopedic defects and demonstrated control over the calcium phosphate mineral phase incorporation with defined biophysical and biochemical properties relevant for regenerative medicine and tissue engineering applications.

This work continues the evaluation of the previously described mineralized collagen-glycosaminoglycan scaffold variant for the treatment of orthopedic defects [48], here the *in vitro* efficacy and osteogenic bioactivity is evaluated with both a physiologically and clinically relevant cell population. Here the *in vitro* osteogenic bioactivity of the non-mineral and mineralized collagen-glycosaminoglycan scaffolds with human mesenchymal stem cells was evaluated via metabolic activity, osteogenic gene expression, and matrix deposition metrics both with and without biomolecule supplementation. Specifically, *in vitro* culture was performed in the presence of standard unsupplemented complete mesenchymal stem cell growth media and in the presence of bone morphogenetic protein 2 (BMP2) supplemented complete mesenchymal stem cell growth media and osteogenic media. This approach allowed the separate

evaluation of osteogenic bioactivity contribution due to the calcium phosphate mineral content and the benefits of soluble biomolecule supplementation.

3.3 Materials and Methods

3.3.1 Scaffold Fabrication

In this study both non-mineralized collagen-glycosaminoglycan (CG) and calcium phosphate mineralized collagen-glycosaminoglycan (CGCaP) scaffolds were fabricated from the lyophilization of precursor suspension as previously described. Briefly, the non-mineral CG precursor suspension was fabricated from the homogenization of 0.5% w/v collagen type-I from bovine Achilles tendon (Sigma-Aldrich, St. Louis, MO) and 0.044% w/v chondroitin sulfate from shark cartilage (Sigma-Aldrich, St. Louis, MO) in 0.05M acetic acid. The previously established 40 wt% mineral CGCaP precursor suspension was prepared by homogenizing 1.9% w/v collagen type-I from bovine Achilles tendon (Sigma-Aldrich, St. Louis, MO), 0.044% w/v chondroitin sulfate from shark cartilage (Sigma-Aldrich, St. Louis, MO), calcium hydroxide ($Ca(OH)_2$), and calcium nitrate tetra-hydrate ($Ca(NO_3)_2 \cdot 4H_2O$) in phosphoric acid. Both precursor suspensions were stored at 4°C and degassed prior to use. A custom polysulfone tray (76.2 mm by 76.2 mm, 1.5 mm thick base) was used as a mold with each lyophilized sheet consisting of 23 mL of the appropriate precursor suspension. The lyophilization was performed using a Genesis freeze-dryer (VirTis, Gardener, NY). The precursor suspensions were cooled to a final freezing temperature of -10°C at a constant rate of 1°C/min and held at -10°C for 175 minutes, with sublimation then occurring at 0°C and 200 mTorr. From the resulting 72.6 mm x 72.6 mm non-mineral CG and mineral CGCaP scaffold sheets, individual scaffolds (8 mm diameter, 4 mm thick) were obtained via biopsy punches.

3.3.2 Scaffold Crosslinking

Following lyophilization the non-mineral scaffold underwent a separate dehydrothermal (DHT) crosslinking step, while both non-mineral CG and mineral CGCaP scaffolds were treated with an EDC

crosslinking step. This post fabrication crosslinking steps have been previously demonstrated to influence collagen-glycosaminoglycan scaffold degradation and mechanical properties [94]. As before, the dehydrothermal (DHT) crosslinking was performed at 105°C and <25 Torr for 24 h in a vacuum oven (Welch, Niles, IL). Both non-mineral CG and mineral CGCaP scaffold variants were dehydrated in 100% ethanol and stepwise hydrated in PBS following lyophilization. Hydrated scaffolds were then chemically crosslinked using a 1-ethyl-3-[3-dimethylaminopropyl] carbodiimide hydrochloride (EDC; Sigma-Aldrich, St. Louis, MO) and N-hydroxysulfosuccinimide (NHS; Sigma-Aldrich, St. Louis, MO). EDC and NHS were added in 5:2 molar ratio to moles of carboxylic acid (COOH) side groups present (5:2:1; EDC:NHS:COOH) in the collagen component of the non-mineral CG and mineral CGCaP scaffold [94].

3.3.3 Human Mesenchymal Stem Cell Culture

Human mesenchymal stem cells (hMSCs) were obtained from Lonza (Basel, Switzerland) and cultured in standard T75 flasks at 37°C and 5% CO_2 with complete mesenchymal stem cell growth media comprised of low glucose Dulbecco's modified eagle medium (DMEM), 10% mesenchymal stem cell fetal bovine serum (MSC FBS; Invitrogen, Carlsbad, CA), 1% penicillin-streptomycin (Invitrogen, Carlsbad, CA), and 1% L-glutamine (Invitrogen, Carlsbad, CA). Following expansion, hMSCs were seeded onto the non-mineral CG and mineral CGCaP (8 mm diameter, 4 mm thick) scaffolds using a previously established static seeding method [92]. Briefly, excess liquid from hydrated non-mineral CG and mineral CGCaP scaffolds was blotted away using Kimwipes (Invitrogen, Carlsbad, CA). Then 3.75 $x10^4$ cells were seeded onto one side of the scaffold. After an allowed 15 min for initial cell attachment, scaffolds were flipped over and an additional 3.75 $x10^4$ cells were seeding on the remaining side. The cell laden scaffold was then incubated for 2 h to allow for cell attachment before being submerged into the appropriate cell culture media. Non-mineral CG and mineral CGCaP scaffold *in vitro* hMSC cell culture then proceeded for 56 days at 37°C and 5% CO_2.

3.3.4 Biomolecule Supplementation and Ca / P Ion Release

In order to determine the effect of mineralization on the collagen-glycosaminoglycan scaffold, non-mineral CG and mineral CGCaP scaffolds were seeded with hMSCs and cultured *in vitro* for 56 days with complete mesenchymal growth media. Additionally, enhancement of the mineral CGCaP scaffold osteogenic bioactivity via soluble supplementation was investigated by the *in vitro* culture of hMSCs on mineral CGCaP scaffolds in the presence of either 100 ng/mL bone morphogenetic protein 2 (BMP2; ProSpec, Israel) supplemented complete mesenchymal growth media, or osteogenic media consisting of 50 μM ascorbic acid, 0.1 μM dexamethasone, and 10mM β-glycerophosphate added to complete mesenchymal growth media (Figure 3.1).

Because the presence of calcium and phosphate within the surrounding medium has been documented to influence the behavior of mesenchymal stem cells during in vitro culture, the previously undocumented solubilization and subsequent release of calcium and phosphate from the acellular mineral CGCaP scaffold and acellular non-mineral CG scaffold was quantified using colorimetric assays over a period of 56 days in complete mesenchymal growth media at 37°C and 5% CO_2. Briefly, ion release profiles were determined via Calcium Colorimetric and Phosphate Colorimetric Assay Kits (BioVision, Milpitas, CA). Following the exchange of fresh complete mesenchymal growth media, the removed media was (n = 4 per time point) was stored at 4°C such that all colorimetric analysis was performed together. The colorimetric change in media aliquots was then determined via a Tecan M200 fluorometer (Tecan, Männedorf, Switzerland). The resulting intensity was compared to an appropriate calcium or phosphate standards to determine the total calcium and phosphate ion released.

3.3.5 Measurement of Mesenchymal Stem Cell Metabolic Activity

Cell metabolic activity, specifically the mitochondrial metabolic activity, was assessed using the non-destructive AlamarBlue® assay. The AlamarBlue® assay measures the metabolic activity by the

introduction and uptake of resazurin with the subsequent reduction into the fluorescent byproduct resorufin. A comparison to a prepared cell standard allows the quantification of metabolic activity within the sample. Briefly, all scaffold variants (n = 6) were washed in phosphate buffered saline (PBS) to clear any dead or unattached cells from the scaffold before immersion into 1 mL of the AlamarBlue® assay solution. Scaffolds were cultured in the AlamarBlue® solution for 105 min at 37°C and 5% CO_2 under mild agitation to promote fluid exchange. After incubation in the AlamarBlue® solution, scaffolds were removed and the fluorescent resorufin measured via a F200 spectrophotometer (Tecan) at 540(52)/580(20) nm (excitation/emission). Comparison to an hMSC AlamarBlue® standard was performed with the resulting cellular metabolic activity normalized to that of the initial seeded cell metabolic activity.

3.3.6 Evaluation of Gene Expression within Collagen-Glycosaminoglycan Scaffolds

In order to better determine the effect of mineralization and supplementation on the collagen-glycosaminoglycan scaffold on cell behavior, the gene expression was inferred by the relative expression of messenger ribonucleic acid and, by proxy, the respective gene via real time polymerase chain reaction. In summary, real time polymerase chain reaction, or more commonly qPCR, involves the isolation of messenger ribonucleic acid (mRNA) and its subsequent conversion into complementary deoxyribonucleic acid (cDNA) by the incorporation of reverse transcriptase. Both detection and amplification of the osteogenic genes of interest were accomplished with specific primers. This work utilized the qPCR technique to identify the expression of genes that are associated with: bone sialoprotein (BSP); osteopontin (OPN); run-related transcription factor 2 (RUNX2); collagen type I (COL1A1) for the production of type I collagen; glyceraldehyde 3-phosphate dehydrogenase (GAPDH) as the house keeping gene for normalizing results. Briefly, samples were harvested after 14, 28, and 56 days of *in vitro* culture using a 1% β-mercaptoethanol lysis solution RNA was isolated from the scaffolds and subsequently purified using an RNeasy Plant Mini Kit (Qiagen, Valencia, CA). The resultant mRNA was transcribed

into cDNA via QuantiTect Reverse Transcription Kit (Qiagen, Valencia, CA) and a Bio-Rad S1000 thermal cycler (BioRad, Hercules, CA). Finally, using a QuantiTect SYBR Green PCR Kit (Qiagen, Valencia, CA) and the primer sequences for BSP, OPN, RUNX2, COL1A1, and GAPDH, chosen from the literature and synthesized by Integrated DNA Technologies (Coraville, IA) (Table 3.1), the gene markers were quantified. Results were analyzed using the delta-delta Ct method via Sequence Detection Systems software v2.4 (Applied Biosystems, Carlsbad, CA).

3.3.7 Determination of Mineral Deposition within Collagen-Glycosaminoglycan Scaffolds

Mineral deposition was evaluated through the use of alizarin red histological staining and micro-computed tomography (uCT). Histological deposition of calcium phosphate was performed after 14, 28, and 56 days in culture with day 0 as a control. Briefly, Scaffolds were fixed in 10% formalin (Polyscience Inc, Warrington, PA), processed and embedded in paraffin, before paraffin sectioning which resulted in 5 μm thick transverse sections. Alizarin Red (Sigma-Aldrich, St. Louis, MO) histological staining was then preformed electrostatically staining the calcium phosphate mineral phase red. For non-mineral CG and mineral CGCaP scaffolds with and without supplementation, representative sections of each scaffold were taken with an optical microscope (Leica; Buffalo Grove, IL) with histograms of pixel intensity constructed via Matlab. In the addition to alizarin red histological staining, micro-computed tomography (uCT) was used to assess changes in mineral content of the scaffolds. Briefly, after 14, 28, and 56 days in vitro culture, specimens were fixed in 10% formalin (Polyscience Inc, Warrington, PA), washed in de-ionized water, and lyophilized to remove any liquid from the scaffold. An Xradia MicroXCT-400 was then used to image the 3-dimensional mineral distribution within the scaffold at 25 kEv and 5 watts with 793 projections and a voxel size of 20 μm. The outputted image z-stack was then analyzed via a custom Matlab program via a defined image processing sequence (Figure 3.6) with results reported as mean mineral content as a function of radial position for the entire scaffold.

3.3.8 Changes in Matrix Mechanical Properties within Collagen-Glycosaminoglycan Scaffolds

Finally, the effect of mineralization and biomolecule supplementation on the mechanical properties of collagen-glycosaminoglycan scaffolds *in vitro* over a period of 56 days was evaluated via compression testing. Briefly, using a TA.XTplus Texture Analyzer (StableMicro Systems Ltd., Surrey, UK), the elastic modulus in hydrated unconfined compression of human mesenchymal stem cells (hMSCs)-seeded non-mineral CG and mineral CGCaP scaffolds was evaluated after 14, 28, and 56 days of *in vitro* culture. In order to avoid the strain rate dependent effect of fluid flow within the highly porous collagen-glycosaminoglycan scaffolds, both non-mineral CG and mineral CGCaP scaffolds were compressed at a strain rate of 0.00005 per sec to 0.5 total strain. The elastic modulus was identified from the linear elastic regime of the stress-strain curve as collagen-glycosaminoglycan scaffolds have previously been demonstrated to behave as low-density open cell foams [48, 94, 142]. In addition to the elastic modulus, an estimation of the relative densification ($\rho_{cellular,scaffold}$ /$\rho_{acellular,scaffold}$) of the scaffold due to cellular remodeling was also determined using the established cellular solids theory relationship describing the elastic modulus:

$$\frac{\rho_{cellular,scaffold}}{\rho_{acellular,scaffold}} = \sqrt{\frac{E_{cellular,scaffold}}{E_{acellular,scaffold}}}$$

$$\frac{E_{cellular,scaffold}}{E_{solid,scaffold}} \propto \left(\frac{\rho_{cellular,scaffold}}{\rho_{solid,scaffold}}\right)^2$$

$$\frac{E_{acellular,scaffold}}{E_{solid,scaffold}} \propto \left(\frac{\rho_{acellular,scaffold}}{\rho_{solid,scaffold}}\right)^2$$

Where $\rho_{cellular,scaffold}$ and $\rho_{acellular,scaffold}$ are the densities of the hMSC seeded and unseeded scaffolds respectively, while $E_{cellular,scaffold}$ and $E_{acellular,scaffold}$ are their respective elastic moduli. The associated

$E_{solid,scaffold}$ and $\rho_{solid,scaffold}$, modulus and density respectively, of the solid scaffold and scaling constants as described in cellular solids theory cancelled for the relative densification [94, 135, 142].

3.3.9 Statistical Analysis

Statistical analysis was performed via two-way analysis of variance (ANOVA) tests after which a Tukey-HSD post-hoc test was used. Independent factors included time, scaffold type (CG vs. CGCaP), and treatment (growth media, osteogenic media, BMP-2 supplemented growth media). Mechanical characterization and gene expression experiments used at least $n = 3$ scaffolds per group while metabolic activity and scaffold compositional analyses used $n = 6$ scaffolds per group. Significance was set at $p < 0.5$. Error bars are reported as standard deviation unless otherwise noted.

3.4 Results and Discussion

The resulting ion release profile identified a significant increase in calcium and phosphate ion content within the cell culture media, as early as day 2 for phosphate and day 5 for calcium (Figure 3.2). After 14 days *in vitro* culture, the release of calcium and phosphate reached an asymptote. Based upon the cumulative calcium and phosphate released, the total mineral solubilized corresponded to approximately 80% of the calcium phosphate incorporated during fabrication. An additional evaluation investigating the effect of the mineral CGCaP scaffold chemical crosslinking indicated a burst release of calcium and phosphate during the extensive washing steps, but no change in mineral release rate (Figure 3.3).

A significant increase in metabolic activity by day 56 was observed for the non-mineral CG and mineral CGCaP scaffolds in mesenchymal stem cell growth media, as well as for mineral CGCaP scaffolds supplemented with bone morphogenetic protein 2 (BMP2) and osteogenic media (Figure 3.4). This verified that both the non-mineral CG and mineral CGCaP scaffolds were capable of supporting metabolically activity cell growth regardless of treatment. While the mineral CGCaP scaffolds in

mesenchymal stem cell growth media exhibited a lower initial metabolic activity than those in the non-mineral CG scaffolds, by day 28 the mineral CGCaP scaffolds expressed higher metabolic activity similar metabolic activity that was not significantly different (Figure 3.4). This initial difference in metabolic activity was attributed to the differences in permeability measured previously [48]. Additionally, the osteogenic supplementation in the mineral CGCaP scaffold was observed to have a negative effect on cellular metabolic activity compared to the unsupplemented and bone morphogenetic protein 2 supplemented mesenchymal stem cell growth media. Here it is hypothesized that the comparatively stunted metabolic activity of the mineral CGCaP scaffold supplemented with osteogenic media is due to the early differentiation of the mesenchymal stem cells limiting their metabolic activity and proliferation. This observation is in agreement with previous literature highlighting the tradeoff between cell proliferation and cell phenotype [164, 166-168].

All genes across all scaffolds and treatments were found to increase, with a significant ($p < 0.05$) increase in BSP expression, after 56 days of *in vitro* culture (Figure 3.5). Mineral CGCaP scaffolds supplemented with bone morphogenetic protein 2 exhibited an earlier significant increase in BSP compared to other scaffolds suggesting earlier signs of osteogenic like behavior within the cell population (Figure 3.5). Additionally, a relatively higher expression of BSP and osteopontin was observed in mineral CGCaP scaffolds relative to non-mineral CG scaffolds (Figure 3.5). Besides the earlier expression of BSP in the mineral CGCaP scaffold supplemented with BMP2, mineralized CGCaP scaffolds exhibited little difference in gene expression profiles (Figure 3.5). This suggested that the mineral CGCaP scaffold itself, independent of supplementation, dictates osteogenic cell behavior. The higher expression of COL1A1 may also suggest an increase inclination for collagen deposition within the non-mineral CG and unsupplemented mineral CGCaP scaffolds (Figure 3.5).

Alizarin red histological analysis identified no distinction between mineral CGCaP scaffold treatments, unsupplemented, BMP2 supplemented, and osteogenic supplemented, at all-time points during *in vitro* culture (Figure 3.7, Table 3.2**)**. However, stark differences in mineral content was observed between non-mineral CG and mineral CGCaP scaffolds, with no mineralization observed in the non-mineral CG scaffolds, throughout the course of the study (Figure 3.7, Table 3.2). The more quantitative analysis via micro-computed tomography (μCT) similarly revealed a significantly ($p < 0.0005$) higher degree of mineralization in all hMSC seeded mineral CGCaP scaffold treatment groups compared to the hMSC seeded non-mineral CG scaffolds (Figure 3.8, Figure 3.9, Table 3.2). This suggests that the calcium phosphate mineral content within the mineral CGCaP scaffold plays an important role in the osteogenic potential and subsequent mineral deposition within the collagen-glycosaminoglycan scaffold design. Additionally, within hMSC seeded mineral CGCaP scaffolds, a significant increase in mineral content with culture time was observed within the unsupplemented complete mesenchymal stem cell growth media (day 14 vs 28/56) and the bone morphogenetic protein 2 supplemented complete mesenchymal stem cell growth media (day 14 vs 28 vs 56), while the osteogenic supplemented mineral CGCaP scaffold experienced a significant change in mineral deposition (Figure 3.8, Figure 3.9). The distinct increase or lack of a decrease within the mineral CGCaP scaffolds is counter to the calcium and phosphate release profiles previously investigated. This suggests that the mineral CGCaP scaffold possesses the correct biophysical and biochemical properties to incite osteogenic activity from the mesenchymal stem cell population resulting in scaffold remodeling in the absence of additional physiological cues. Furthermore, the increase in mineral deposition was observed in the absence of supplementation, suggesting that mineral deposition was potentially hampered in the presence of osteogenic supplementation (Figure 3.8, Figure 3.9). In fact, the unsupplemented hMSC seeded mineral CGCaP scaffold exhibited the highest degree of mineralization within the first 28 days, while the BMP-2 supplemented mineral CGCaP scaffolds demonstrated a higher degree of mineral deposition at later time points (Figure 3.8, Figure 3.9).

Again, this identified the mineral CGCaP scaffold without supplementation as capable of the same degree of mineralization as the equivalent biomolecule supplemented mineral CGCaP scaffolds.

An additional radial analysis of the μCT results provided novel information regarding the *in vitro* spatial deposition of new mineral content, and, by proxy, the cell distribution and ingrowth within the mineral CGCaP scaffolds (Figure 3.10). Within all the mineral CGCaP scaffold treatments, new mineral content was located within 1.5 mm of the edge of the 4 mm radial discs (Figure 3.10), while within non-mineral CG scaffolds, no radial variation in mineral content was observed. This is in agreement with the bulk average mineral content assessed previously (Figure 3.10, Figure 3.9 respectively). Under the assumption of uniform solubilization of the calcium phosphate mineral phase within the mineral CGCaP scaffold, the radial differences in mineralization assert a non-uniform matrix remodeling, further emphasizing the need for a biomaterial scaffold design capable of flexible microstructural properties to balance cell penetration and metabolic support via diffusive transport with other biophysical properties such as mechanical robustness. While this work has emphasized the innate osteogenic bioactivity of the mineral CGCaP scaffold in the absence of supplementation, this also provides the unique opportunity for the incorporation of biomolecule supplementation modulating the non-osteogenic aspects of orthopedic defect treatment, such as angiogenesis via vascular endothelial growth factor (VEGF) supplementation. Additionally, the modulation of osteogenic bioactivity through biomaterial properties, as in the case of the mineral CGCaP scaffolds, provides the foundation for the development of a spatially distinct biomaterial design capable of modulating multi-lineage cell specificity via biophysical and biochemical material properties.

The investigation of human mesenchymal stem cells (hMSCs) *in vitro* remodeling in the presence of the non-mineral CG and mineral CGCaP scaffold was expanded upon via the changes in mechanical properties, providing insight into protein and mineral deposition. A significant ($p < 0.05$) difference in modulus between hMSC-seeded non-mineral scaffolds and all hMSC-seeded mineral CGCaP scaffold

treatments was observed after 14, 28, and 56 days *in vitro* culture, while the modulus of all hMSC-seeded mineral CGCaP scaffolds was observed to significantly ($p < 0.05$) increase with time (Figure 3.11, Table 3.2). These observations, between non-mineral and mineral scaffolds with time, mirrors differences in the mineral deposition previously examined (Figure 3.9), which is hypothesized to contribute to the change in mechanical properties. Likewise, no changes in modulus was observed within the non-mineral CG scaffold, suggesting that cellular remodeling did not result in additional extracellular matrix deposition. Additionally, the moduli of control acellular non-mineral CG and mineral CGCaP scaffolds remained unchanged throughout the duration of the *in vitro* culture, demonstrating that crosslinked scaffold mechanical properties were not compromised over this time frame due to degradation (Figure 3.11). A significant ($p < 0.05$) increase in modulus was observed in the mineral CGCaP scaffold supplemented with osteogenic media compared to the unsupplemented mineral CGCaP equivalent (Figure 3.11). This constant increase in modulus in osteogenic media-supplemented mineral CGCaP scaffolds is again evidence of the phenotype vs proliferation trade-off observed in the metabolic activity.

3.5 Influence of Mineralization and Suggested Cellular Cause

In a collaborative effort headed by Justine C. Lee, M.D., Ph.D., Xiaoyan Ren, Ph.D., and Timothy A. Miller, M.D. FACS, at the University of California at Los Angeles (UCLA), additional work has outlined the underlying cellular mechanism involved in the mineral CGCaP scaffolds' inherent osteogenic bioactivity. In this series of studies, non-mineral CG and mineral CGCaP scaffolds were cultured *in vitro* with human mesenchymal stem cells (hMSCs) in the presence of bone morphogenetic protein 2 and, later, osteogenic media to evaluate the effect of mineral content and subsequently crosslinking on the osteogenesis of hMSCs. The resulting biophysical and biochemical properties were determined via quantitative real time polymerase chain reaction (qPCR), western blot analysis of protein activation, histology and immunohistochemistry, and micro-computed tomography (μCT). Initial work via μCT, histology, and immunohistochemistry identified that mineral CGCaP scaffolds were able to promote

osteogenic gene expression and mineralization of hMSCs in the absence of BMP supplementation [169]. Additionally, western blot analysis of the canonical BMP receptor Smad1/5 was consistently phosphorylated in mineral CGCaP scaffolds both with and without BMP2 supplementation, while Smad1/5 phosphorylation in non-mineral CG scaffolds only occurred in the presence of BMP2 supplementation at the periphery of the scaffold [169]. That, coupled with the inverse behavior of ERK1/2, was observed with an increased phosphorylation at day 14 in non-mineral CG scaffolds compared to mineral CGCaP scaffolds, while decreased ERK1/2 phosphorylation was observed at days 14 and 24 in both non-mineral CG and mineral CGCaP scaffolds due to BMP2 stimulation [169]. This suggests that the mineral CGCaP scaffold influences the endogenous production of BMP2 which activates the canonical BMP signaling receptor pathway. An additional study also investigated the hMSC response in mineral CGCaP scaffolds during *in vitro* culture in osteogenic media due to chemical crosslinking via the previously described 1-ethyl-3-[3-dimethylaminopropyl] carbodiimide hydrochloride and N-hydroxysulfosuccinimide with carboxylic acid groups present on collagen [170]. Cell mediated scaffold contraction was observed to result in a significant ($p < 0.05$) degree of contraction compared to their crosslinked counter parts, while the presence of mineralization significantly ($p < 0.05$) decreased contraction to a lesser degree [170]. Interestingly, it was observed via qPCR and μCT that increased contraction in both non-mineral CG and mineral CGCaP scaffolds induced a higher degree of mineralization and osteogenic gene expression [170].

3.6 Conclusions

Biomaterials for bone tissue engineering must be able to instruct cell behavior in the presence of the complex biophysical and biomolecular environments encountered in vivo. While osteogenic media or exogenous BMP-2 supplementation are often used as an essential element of many bone regeneration studies, diffusive loss and rapid degradation are primary concerns of efforts requiring exogenous supplementation. Using a series of collagen-glycosaminoglycan scaffolds, the incorporation of a transient

CaP mineral content was sufficient to enhance hMSC osteogenic differentiation and matrix remodeling in the absence of lineages-specific media supplementation. While osteogenic media and BMP-2 supplementation may enhance the speed or long-term intensity of the response, mineralized CG scaffolds were able to support extensive hMSC osteogenesis, matrix remodeling, and new mineral formation in the absence of lineage specific media.

3.7 Figures and Tables

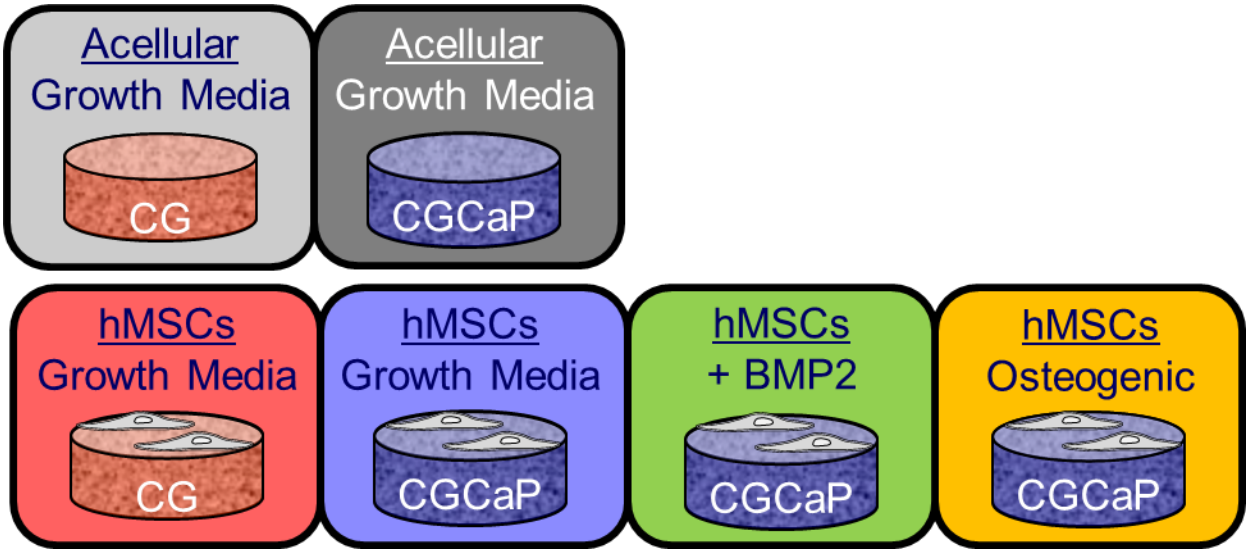

Figure 3.1 The scaffolds and supplementary treatments groups evaluated *in vitro* culture.

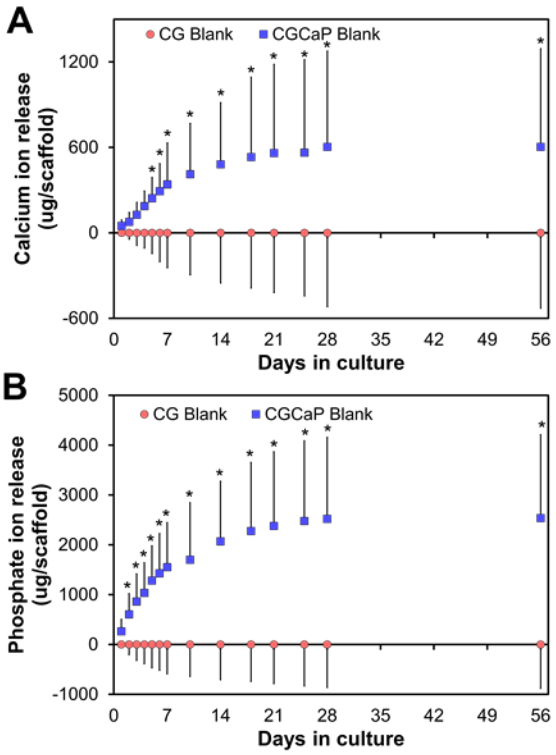

Figure 3.2 Cumulative release of calcium and phosphate from the mineral scaffold.

The cumulative calcium (A) and phosphate (B) ion release profiles for acellular non-mineral CG and mineral CGCaP blank controls under *in vitro* culture conditions for a period of 56 days. Significance (*: $p < 0.05$) between the mineral CGCaP blank and the non-mineral CG blank at the same time point was indicated

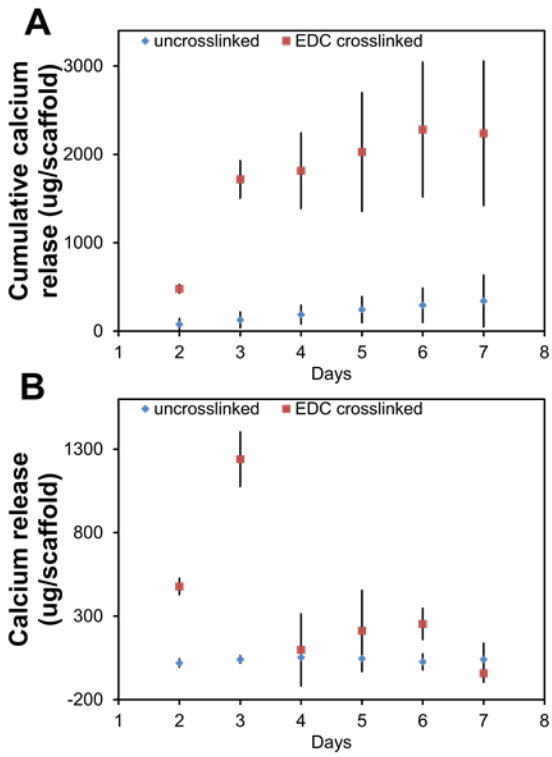

Figure 3.3 Comparison of calcium and phosphate release during crosslinking.

Calcium and phosphate ion release from the mineral scaffolds with and without EDC crosslinking to determine the effect of crosslinking on ion release profiles. Significance (*: $p < 0.05$) between the mineral CGCaP blank and the non-mineral CG blank at the same time point was indicated

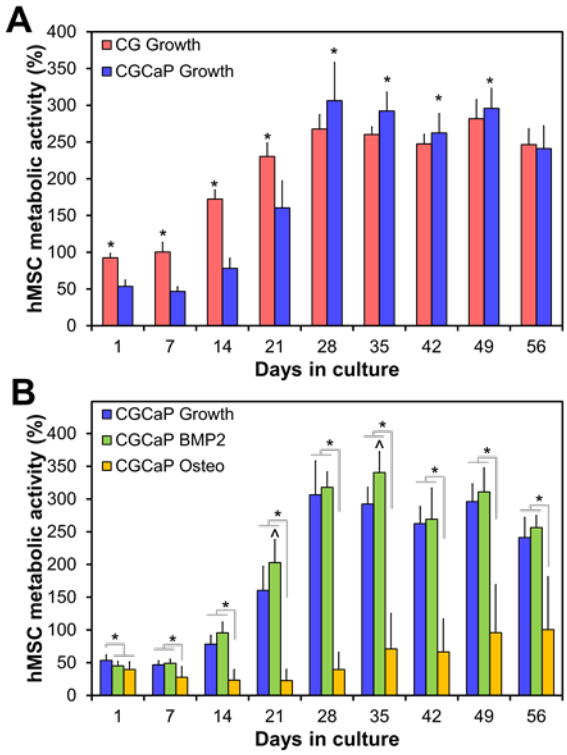

Figure 3.4 The metabolic activity of hMSCs cultured *in vitro*.

The metabolic activity measured during the *in vitro* culture over a period of 56 days. Evaluating differences between (A) the non-mineral CG and mineral CGCaP scaffold cultured with complete mesenchymal stem cell growth media, and (B) the mineral CGCaP scaffold treated with complete stem cell growth media, complete stem cell growth media supplemented with BMP2, and osteogenic media. Significance (*: $p < 0.05$) between indicated groups and significance (^: $p < 0.05$) between all other groups at that time point were identified.

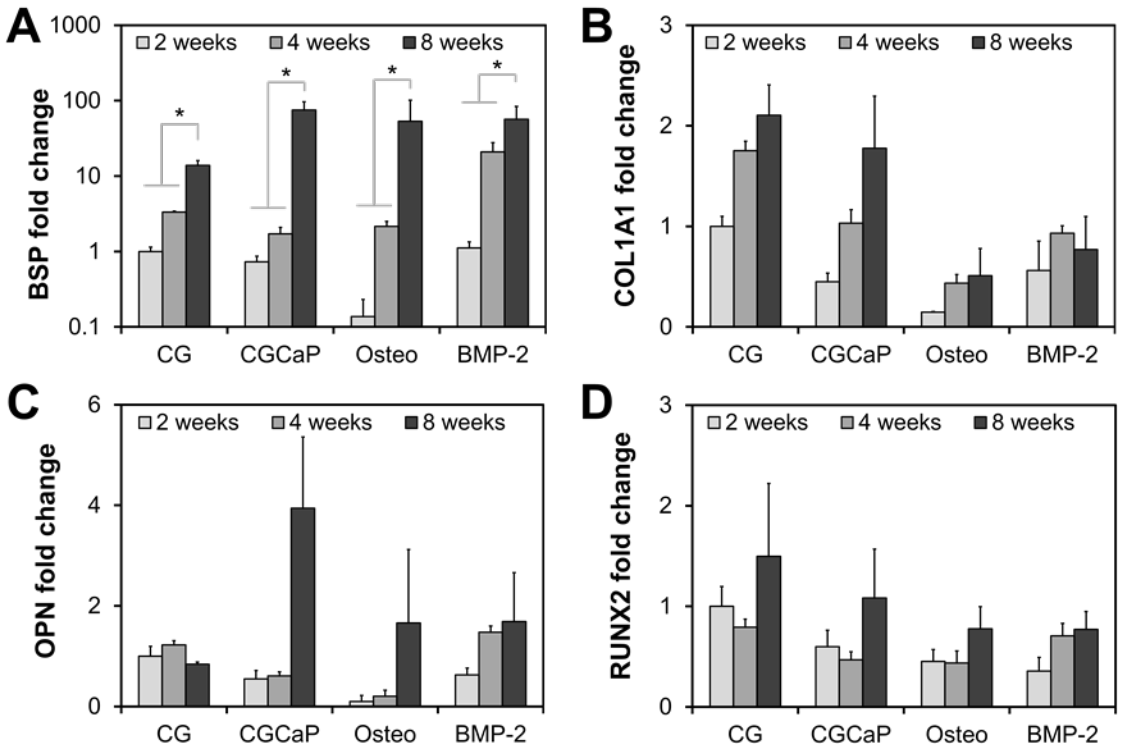

Figure 3.5 Osteogenic genes expressed within mineral and non-mineral scaffolds.

Profiles were obtained via quantitative PCR from *in vitro* culture of human mesenchymal stem cells on non-mineral CG and mineral CGCaP scaffolds with and without supplementation. Significance (*: $p < 0.05$) between indicated groups was identified.

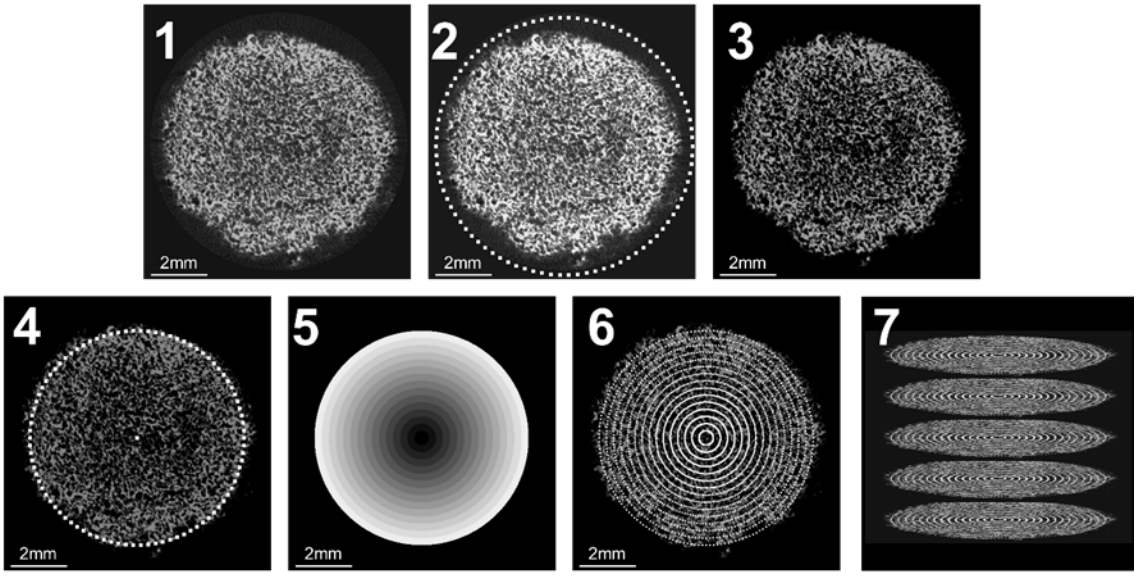

Figure 3.6 Procedure of micro-computed tomographic analysis of mineral deposition.

A step by step procedure indicating the procedure performed in Matlab to analyze the mineral deposition within scaffolds cultured *in vitro* as measured by micro-computed tomography (uCT). Procedure analysis was performed as: (1) selection of a start and end uCT z-stack slice; (2) selection of the entire scaffold and surrounding air; (3) subtraction of the background not selected in step 2; (4) a selection of only the scaffold region; (5) division of the scaffold into radial partitions; (6) analysis of the voxels contained within each radial partition; (7) repeat of this analysis throughout the z-stack, or the uCT volume.

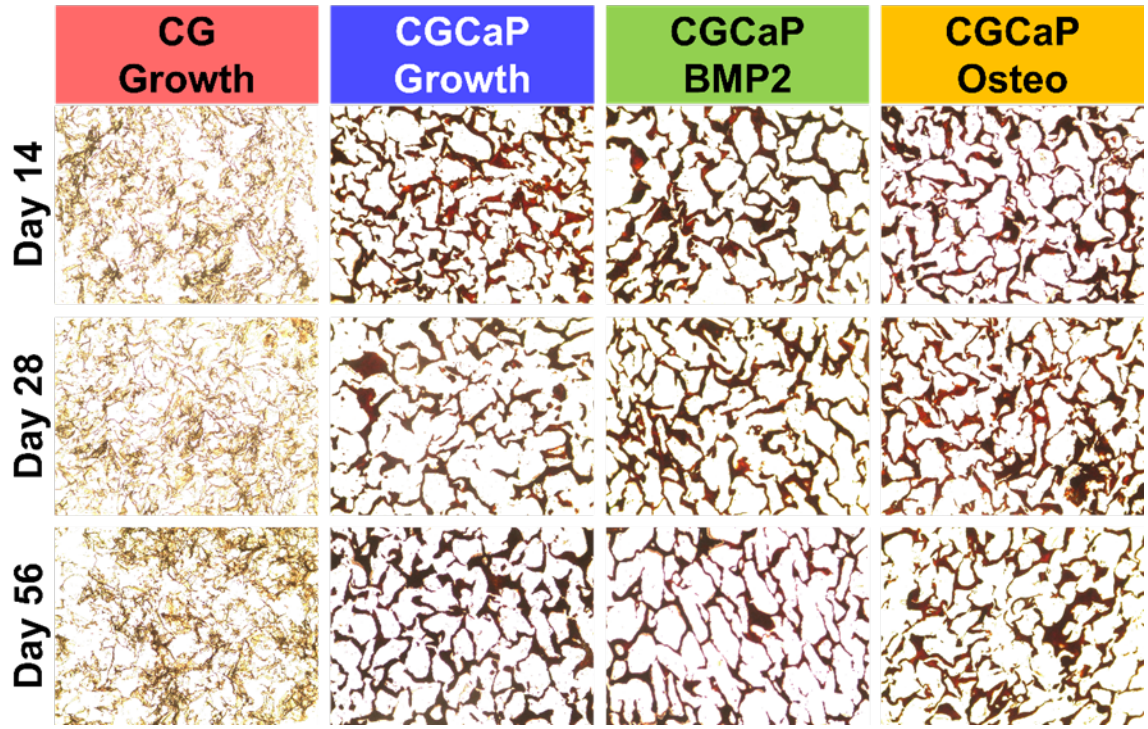

Figure 3.7 Histological staining for mineral content within the scaffolds cultured *in vitro*.

Representative images from the histological alizarin red staining performed on non-mineral CG and mineral CGCaP scaffold cultured *in vitro* with human mesenchymal stem cells to identify any changes within the mineral content.

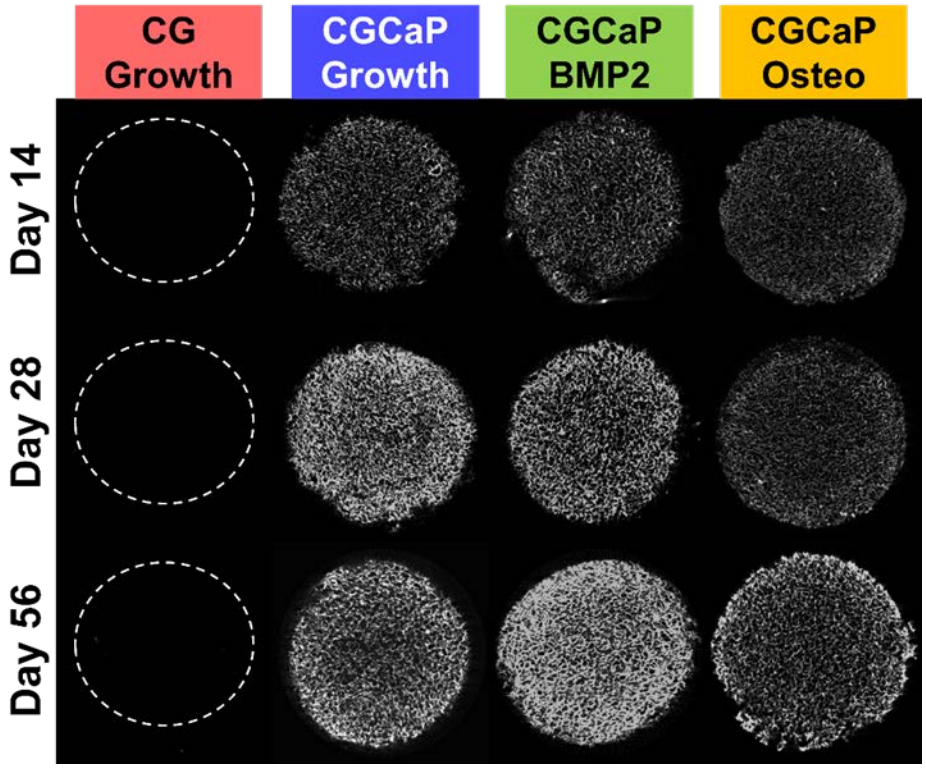

Figure 3.8 Mineral content via micro-computed tomography within scaffolds.

The mineral deposition within the mineral CGCaP and non-mineral CG scaffolds by human mesenchymal stem cells *in vitro* as measured via micro-computed tomography. The non-mineral CG scaffolds were outlined to provide their position in the image.

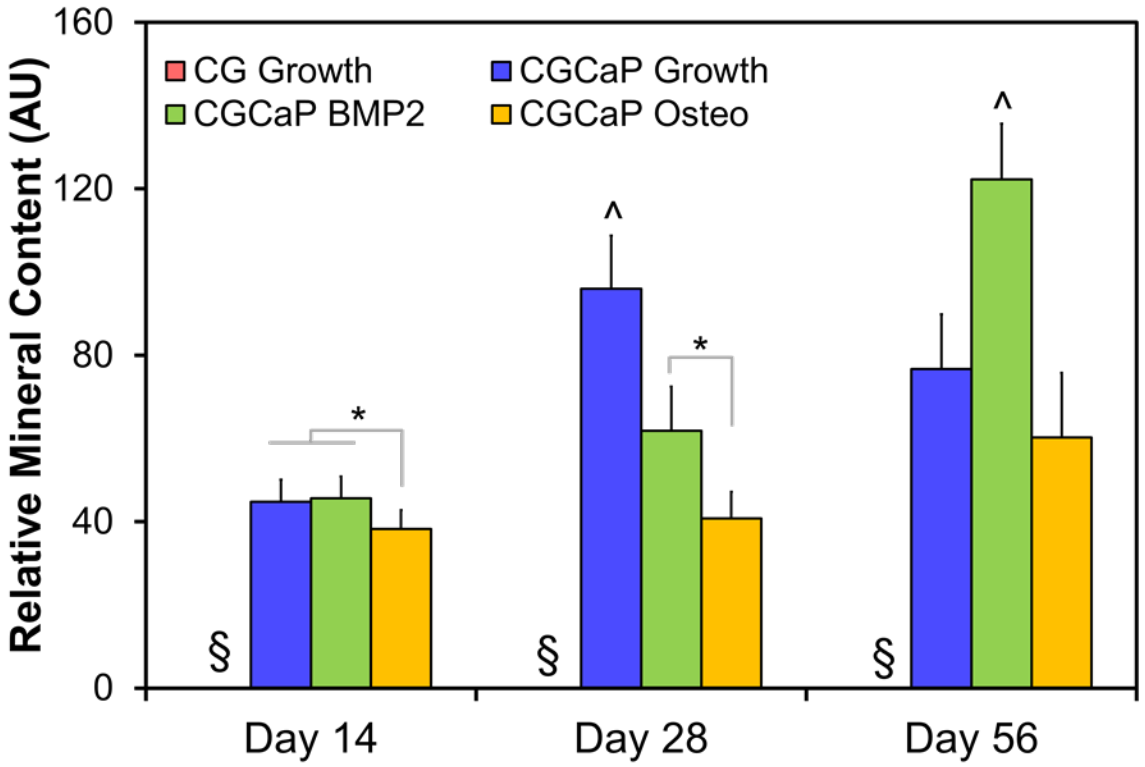

Figure 3.9 The average mineral content within each scaffold as measured via uCT.

Average mineral content was determined via micro-computed tomography. Significance (*: $p < 0.05$) between indicated groups, significance (^: $p < 0.05$) between all other groups at a time point, and significance (§: $p < 0.05$) compared to mineralized CGCaP scaffold variants were identified.

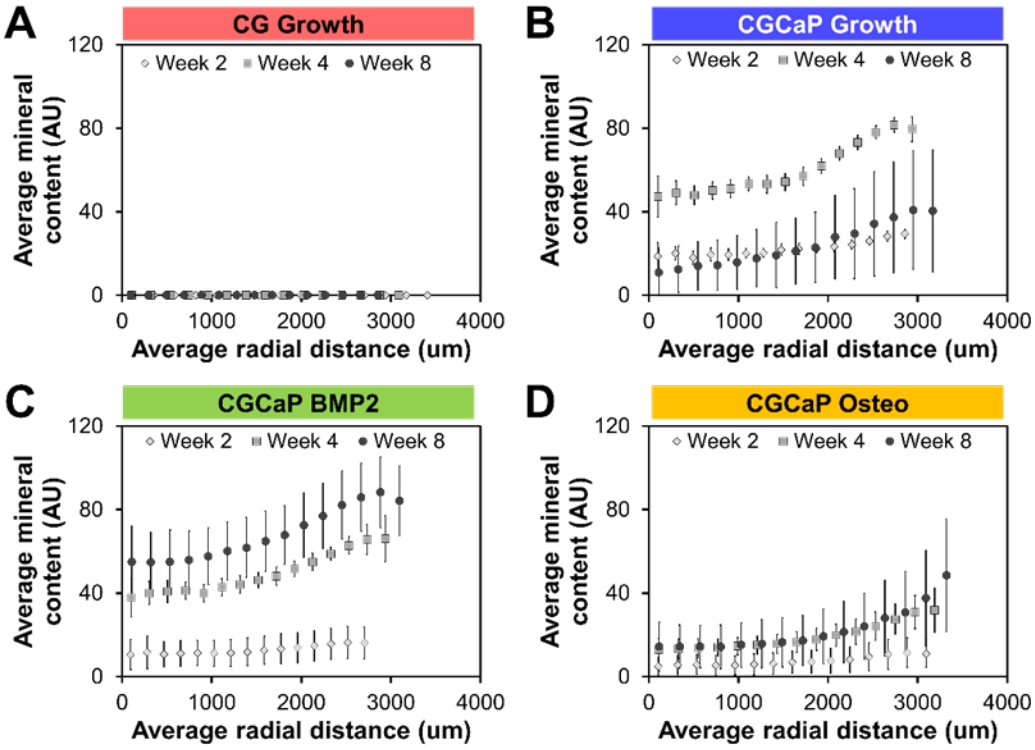

Figure 3.10 A radial analysis of mineral deposition as measured via uCT.

Radial distribution of mineral content as detected via micro-computed tomography in non-mineral CG and mineral CGCaP with and without supplementation during *in vitro* culture of human mesenchymal stem cells. An increase in mineral deposition was associated with both the cellular infiltration and nutrient exchange within the scaffold.

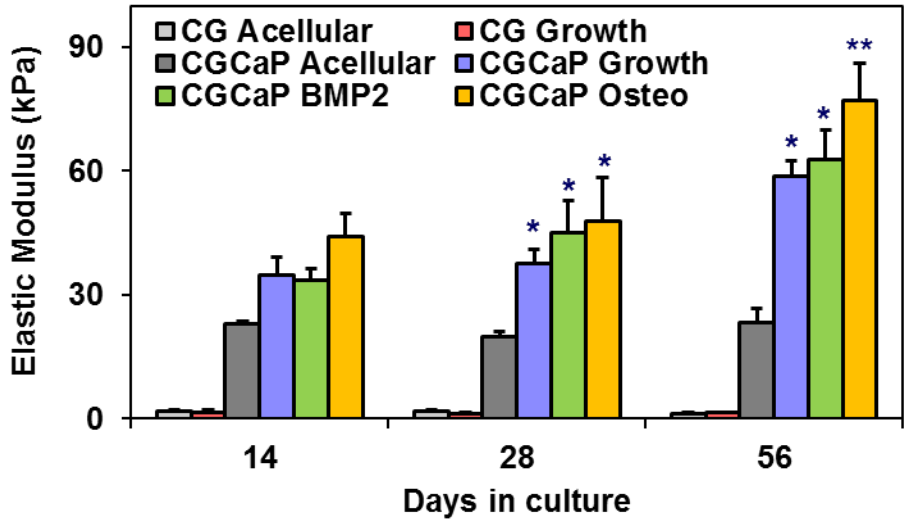

Figure 3.11 Elastic modulus of the mineral and non-mineral scaffolds during *in vitro* culture.

The elastic modulus from non-mineral CG and mineral CGCaP scaffolds with and without supplementation cultured *in vitro* with human mesenchymal stem cells via unconfined hydrated compression. Significant differences compared to the acellular control within scaffold groups at each time point (*: $p < 0.05$) and significant differences compared to all other scaffolds at that time point (**: $P < 0.05$) were observed.

Table 3.1 Primer sequences used in qPCR for gene expression.

Name	Forward	Reverse
COL1A1	CAG CCG CTT CAC CTA CAG C	TTT TGT ATT CAA TCA CTG TCT TGC C
OPN	GCG AGG AGT TGA ATG GTG	CTT GTG GCT GTG GGT TTC
RUNX2	GGTTAATCTCCGCAGGTCACT	CACTGTGCTGAAGAGGCTGTT
BSP	TGCCTTGAGCCTGCTTCC	GCAAAATTAAAGCAGTCTTCATTTTG
GAPDH	CCATGAGAAGTATGACAACAGCC	CCTTCCACGATACCAAAGTTG

Primer sequences used in qPCR for gene expression. Sources were as follows: COL1A1 [171]; OPN [171]; RUNX2 [172]; BSP [173]; GAPDH [174].

Table 3.2 Elastic modulus and estimated denfication of scaffolds as measured during *in vitro* culture.

	Day 14		Day 28		Day 56	
Sample	**Moduli, kPa**	**Est. Dens.**	**Moduli, kPa**	**Est. Dens.**	**Moduli, kPa**	**Est. Dens.**
CG (acellular)	1.83 ± 0.48	---	1.71 ± 0.43	1.00	1.24 ± 0.21	1.00
CG Growth	1.57 ± 0.43	0.93	1.11 ± 0.30	0.81	1.51 ± 0.13	1.10
CGCaP (acellular)	23.00 ± 0.59	---	19.84 ± 1.42	1.00	23.44 ± 3.34	1.00
CGCaP Growth	34.71 ± 4.40	1.23	37.73 ± 3.32	1.38	58.69 ± 3.71	1.58
CGCaP BMP2	33.70 ± 2.73	1.21	45.02 ± 7.72	1.51	62.67 ± 7.27	1.63
CGCaP Osteo	44.16 ± 5.59	1.39	48.00 ± 10.53	1.56	76.95 ± 9.19	1.81

Elastic moduli of non-mineral CG and mineral CGCaP scaffolds both acellular and hMSC seeded without (Growth) and with (bone morphogenetic protein 2: BMP2; osteogenic media: Osteo) supplementation. Estimated densification due to cellular contraction and matrix densification was calculated based on cellular solids theory and the changes in modulus compared to acellular scaffold variants.

CHAPTER 4

ADAPTATION OF THE MINERALIZED COLLAGEN-GLYCOSAMINOGLYCAN SCAFFOLD FOR *IN VIVO* IMPLANTATION: FORMATION OF A MULTI-SCALE BIOMATERIAL COMPOSITE[3]

4.1 Overview

A particular challenge in biomaterial development for treating orthopedic injuries stems from the need to balance bioactive design criteria with the mechanical and geometric constraints governed by the physiological wound environment. Such trade-offs are of particular importance in large craniofacial bone defects which arise from both acute trauma and chronic conditions. Ongoing efforts in our laboratory have demonstrated a mineralized collagen biomaterial that can promote human MSC osteogenesis in the absence of osteogenic media but that possesses suboptimal mechanical properties in regards to use in loaded wound sites. Here we demonstrate a multi-scale composite consisting of a highly bioactive mineralized collage-glycosaminoglycan scaffold with micron-scale porosity and a polycaprolactone support frame (PCL) with millimeter-scale porosity. Fabrication of the composite was performed by impregnating the PCL support frame with the mineral scaffold precursor suspension prior to lyophilization. Here we evaluate the mechanical properties, permeability, and bioactivity of the resulting

[3] This work is adapted from the study 123. Weisgerber, D.W., K. Erning, C. Flanagan, S. Hollister, B.A.C. Harley, *Adaptation of the mineralized collagen-glycosaminoglycan scaffold for in vivo implantation: formation of a multi-scale biomaterial composite*. In preparation, 2015.

composite. Results indicated that the PCL support frame dominates the bulk mechanical response of the composite resulting in a 6000-fold increase in modulus compared to the mineral scaffold alone. Similarly, the incorporation of the mineral scaffold matrix into the composite resulted in a higher specific surface area compared to the PCL support frame alone. The increase in specific surface area within in the collagen-PCL composite also promoted increased initial attachment of porcine adipose derived stem cells versus the PCL construct alone.

4.2 Introduction

Surgical intervention in large and geometrically complex craniofacial defects often necessitates either autologous or allogenic grafts to augment the natural wound healing process. Biomaterial approaches offer an alternative to the autologous implant with the potential to avoid donor site morbidity, alleviate concerns of allogenic supply and disease transmission, and allow real-time production of patient-specific implant geometries [175]. However, to promote physiological repair processes, such biomaterials must maintain their geometry and mechanical competence [176, 177] particularly in the case of load bearing orthopedic injuries [178, 179]. Many injuries, including craniofacial defects, necessitate biomaterials capable of fitting non-trivial geometries to conform to an injury site, but also demonstrate mechanical stability under loading during implantation and routine physiological activity [180]. In all cases, these biomaterials must remain bioactive supporting cellular infiltration, attachment, proliferation, and matrix synthesis.

Recently a range of biodegradable biomaterials have been described that promote pro-osteogenic processes within both the *in vitro* and *in vivo* environments. Here, the combination of organic and naturally derived polymers, such as in the case calcium phosphate mineralized chitosan biomaterials [60, 181-183], have become a commonplace choice due to their ability to mimic the native composition of

bone. While such biomaterials have demonstrated potential to promote osteogenic repair, concerns over ensuring geometric structure and mechanical competence under loading remain at the forefront. In that same spirit, previous and ongoing work within our group has evaluated the efficacy of a calcium phosphate mineralized collagen-glycosaminoglycan scaffold for the treatment of orthopedic injuries. Studies have highlighted the versatility in fabrication of these scaffolds with varied geometric, mechanical, and microstructural properties via freeze drying techniques [48, 97]. *In vitro* studies have likewise demonstrated the ability of the mineralized collagen-glycosaminoglycan scaffold to promote mesenchymal stem cell osteogenic differentiation in the absence of osteogenic media or additional biomolecule supplementation [122]. Interestingly, recent results suggest this mineralized collagen scaffold promotes MSC osteogenesis via activation of endogenous BMP pathways [169, 184]. However, while this effort has demonstrated that the mineralized collagen-glycosaminoglycan matrix can promote pro-osteogenic activities, it has also highlighted the need for identifying strategies to increase the mechanical competence of these implants to meet the needs of *in vivo* applications [48]. And while increasing the relative density of these scaffolds can increase strength, it does so at the cost of reduced nutrient transport and cell penetration within the scaffold [185].

With a critical need in orthopedics for mechanically robust implants that can also be developed to fit patient and injury specific geometries, a variety of three-dimensional printing approaches have recently begun to garner significant attention. Early work by Wagoner Johnson et al., demonstrated the use of 3D-printed hydroxyapatite ceramic scaffolds able to enhance bone ingrowth and healing *in vivo* [186]. Ongoing efforts by Hollister et al. have demonstrated the use of polycaprolactone (PCL) constructs as well as additional control over incorporation of bioactive agents to enhancing biomolecule absorption and release [187, 188], gene transfer [189], and resultant *in vivo* treatment of both cartilage and bone defects [190, 191]. The nature of the PCL construct allows rapid patient customization. After the 3D defect volume is computationally defined, a porous architecture can be designed by iterative addition of a well-

defined unit cell structure to fill the desired shape [192, 193]. Applying principles of mechanics, the deformation and failure modes of the resultant structure can be calculated and refined in order to meet functional requirements. However, the fabrication process and biomechanical stability considerations often limit the porosity of these materials to pores/channels larger than 1mm (3.5mm dia. channels in current PCL constructs for a mandibular repair), resulting in low specific surface areas (surface area/volume) for cell attachment as well as pore sizes well above the 100 – 500 μm range largely believed to be optimal for bone tissue engineering [194, 195]. So while 3D printed biomaterials offer mechanically robust, customizable implants, limits in printed feature size and low specific surface area represent critical dilemmas that must be addressed [196].

This manuscript describes development of a multi-scale biomaterial composite for the treatment of critically sized defects in bone that integrates mineralized collagen scaffolds with high osteogenic potential but suboptimal mechanical properties into 3D-printed PCL constructs with high strength. Multi-scale composites offer unique potential to satisfy multiple, disparate design criteria. Many mechanically efficient structures in nature (*e.g.*, plant stems, porcupine quills, bones) employ multi-scale designs to satisfy mechanical and biological constraints [197]multi-scale , suggesting such designs offer unique advantages for biomaterial design. Here we hypothesize that the combination of a bioactive collagen scaffold with micro-scale porosity with a strong PCL composite with mm-scale porosity will generate a composite with enhanced specific surface area and mechanical properties. We evaluate the average pore size, elastic modulus, permeability, and initial attachment of porcine adipose derived stem cells in multi-scale mineralized polycaprolactone-collagen-glycosaminoglycan (PCL-CGCaP) composite, comparing results to the individual polycaprolactone construct and the mineralized collagen-glycosaminoglycan scaffold alone.

4.3 Materials and Methods

4.3.1 Fabrication of Mineralized Collagen-Glycosaminoglycan Scaffold Precursor Suspension

CGCaP scaffolds were fabricated by lyophilization of a CGCaP precursor suspension as previously described [48, 88]. Briefly, mineralized CGCaP precursor suspension was prepared by homogenizing (1.9 w/v %) bovine type I collagen (Collagen Matrix, Oakland, NJ) and (0.84 w/v %) chondroitin-6-sulfate (Sigma-Aldrich, St. Louis, MO) with calcium salts ($Ca(OH)_2$, $Ca(NO_3)_2 \cdot 4H_2O$, Sigma-Aldrich, St. Louis, MO) in phosphoric acid (Sigma-Aldrich, St. Louis, MO). This CGCaP precursor suspension was stored at 4°C and degassed prior to use. A Genesis freeze-dryer (VisTis, Gardener, NY) was used to lyophilize the precursor suspension in a custom 6 well (11.9 mm diameter, 10 mm height) polysulfone mold. Briefly, the lyophilization consisted of cooling from 20°C to -10°C at a constant rate of 1°C/min with a 2 h hold at -10°C prior to sublimation at 0°C and 200 mTorr.

4.3.2 Fabrication of Polycaprolactone Support Construct

PCL frames were fabricated by selective laser sintering (SLS) of a powder precursor consisting of polycaprolactone and 4 wt% hydroxyapatite. The PCL support frames were 10 mm in height and 11 mm in diameter, the architecture of the frame was defined using a 67% porous 5mm unit cell with 3.5 mm cylindrical pores through each axis (Figure 4.1). Specimen geometry was specified using a custom Interactive Data Language program (IDL, Research Systems, Inc.) with design criteria being stored as a .STL file for fabrication.

4.3.3 Fabrication of Mineralized Collagen-Glycosaminoglycan Scaffold and Mineralized Collagen-Glycosaminoglycan-Polycaprolactone Composite

PCL-CGCaP composites were fabricated by first soaking the PCL frames in the CGCaP precursor suspension for 15 min. Excess CGCaP precursor suspension was removed from the PCL frames via blotting with Kimwipes (Kimberly-Clark, Roswell, GA). Following the degassing of both the wetted PCL

frames and additional CGCaP precursor suspension the two were combined by placing the PCL frame into the previously described custom 6 well polysulfone mold and injecting 1 ml CGCaP precursor suspension into the frame. Composites were fabricated using an identical process conditions as described for creating CGCaP scaffold.

4.3.4 Sterilization and Crosslinking of Specimens for *In Vitro* Culture

All constructs used in the *in vitro* cell cultures underwent an ethanol sterilization with mineral scaffolds and composites undergoing additional cross-linking steps [94, 198]. Briefly, all constructs sterilized by a 24 h soaked in ethanol overnight before being hydrated in sterile PBS for 24 h. Scaffolds and composites were then soaked in a PBS solution of 1-ethyl-3-[3-dimethylaminopropyl] carbodiimide hydrochloride (EDAC, Sigma-Aldrich, St. Louis, MO) and N-hydroxysulfosuccinimide (NHS, Sigma-Aldrich, St. Louis, MO) at a molar ratio of 5:2:1 EADC:NHS:COOH where COOH represents the amount of carboxylic acid present in the collagen [94, 198].

4.3.5 Pore Size Analysis of Specimens.

The visualization of the topology and interface between the PCL support and CGCaP scaffold within the composite was performed using SEM analysis with a JEOL JSM-6060LV Low Vacuum Scanning Electron Microscope (JEOL USA, Peabody, MA). To examine whether the addition of the PCL had any effect on the pore architecture within the composite, pore size analysis of samples was performed via the staining of collagen using aniline blue of samples embedded in a glycomethacrylate (Polysciences Inc., Warrington, PA) [48, 92]. Briefly, whole samples were divided into quarters and soaked in ethanol overnight prior to being stored in glycomethacrylate monomer and catalyst benzoyl peroxide (Polysciences Inc., Warrington, PA) solution for 24 h. Samples were then embedded in glycomethacrylate in both longitudinal and transverse orientations and sectioned into 5 μm slices. Slices were mounted, stained with aniline blue (Thermo Fisher Scientific Inc., Waltham, MA), and imaged with an optical

microscope (Leica Microsystems, Wetzlar, Germany). Subsequent image analysis was performed using a linear intercept method using a custom Matlab program to determine average pore size [91, 199].

4.3.6 Mechanical Behavior of Specimens.

The stress-strain behavior of the PCL frame, CGCaP scaffold, and PCL-CGCaP composite was measured via compressive loading in a TA.XTplus Texture Analyzer (StableMicro Systems Ltd., Surrey, UK) using a 5 kg load cell. Samples were loaded to 4 kg or 50% strain at a rate of 0.01 mm/min. The elastic moduli of each sample (11 mm diameter, 10 mm height) was determined from the linear elastic region of each stress-strain plot.

4.3.7 Permeability of Specimens.

Permeability was measured as previously described [48, 185, 196]. Briefly, axial permeability was assessed with flow through using a custom polycarbonate rig and a constant pressure head (ΔP) of 26.7 cm of de-ionized water. The resulting flow rate (Q) of de-ionized water with viscosity (μ) through a defined cross-sectional area (A) and thickness (l) of each sample (empty chamber, PCL frame, CGCaP scaffold, and PCL-CGCaP composite, n = 3) was measured using a graduated cylinder (10 ± 0.1 mL). Sample permeability (K) was defined via Darcy's law [185]:

$$K = \frac{Q \cdot l \cdot \mu}{\Delta P \cdot A}$$

4.3.8 Porcine Adipose Derived Stem Cell (pASC) Culture and Seeding.

To examine the effect of the CGCaP mineral scaffold on composite bioactivity porcine adipose derived stem cells (gift of Dr. M. Wheeler, Department of Animal Science, UIUC, Urbana, IL) were seeded onto the PCL support and the composite. Porcine adipose derived stem cells were expanded at 37°C and 5%

CO_2 in complete mesenchymal stem cell growth media (low glucose DMEM, 10% MSC FBS and 1% antibiotic-antimycotic). Passage 8 pASCs were seeded onto PCL frames and PCL-CGCaP composites using one of two different seeding methods. Briefly, a previously described static seeding method was used to seed a total of 1.0 $x10^6$ cells onto each sample [97]. Alternatively, samples were soaked in a suspension of 1.0 $x10^6$ cells in complete mesenchymal stem cell growth media for a period of 2 h. Subsequently, all pASC seeded samples were cultured at 37°C and 5% CO_2 in complete mesenchymal stem cell growth media for 24 h.

4.3.9 Measurement of Porcine ASC Metabolic Activity.

The metabolic activity of pASC seeded specimens was quantified via an alamarBlue® assay [200]. Briefly, after 24 h of culture, cell-seeded constructs were incubated in an alamarBlue® solution (Invitrogen) at 37ºC under gentle shaking. The fluorescence of the reduced resazurin byproduct, resorufin, via the metabolically active pASCs was compared to a prepared standard. Using a F200 spectrophotometer (Tecan) the fluorescence was measured at 540(52)/580(20) nm (excitation/ emission). The resulting metabolic activity of each sample (n =6) was normalized to the metabolic activity of a control constructed from the metabolic activity of the number of cells seeded (1.0 $x10^6$ cells).

4.3.10 Statistics Analysis

Statistical analysis was performed via analysis of variance (ANOVA) tests after which a Tukey-HSD post-hoc test was used. Independent factors included the seeding method (static seeding vs cell soak) and scaffold type (PCL frame vs PCL-CGCaP composite). Mechanical and metabolic studies were carried out with n = 6 samples per group, while permeability was carried out with n = 3 samples per group. Significance was set at $p < 0.05$. Error bars are reported as standard deviation unless otherwise stated.

4.4 Results and Discussion

This study has identified a new way to balance the design criteria using a multi-scale composite approach to the development of biomaterials with the development of this PCL-CGCaP composite biomaterial for craniofacial defects. Here we hypothesize that by combining the PCL frame and mineralized CGCaP scaffold into the PCL-CGCaP composite the most favorable properties, increased elastic modulus and increased surface area, will be maintained for future in vivo studies. The impact of incorporating the mineralized CGCaP scaffold into the PCL frame, creating the PCL-CGCaP composite, was determined by measurements of the pore size, mechanics, microstructure, and cell attachment.

In support of our hypothesis, we identified that the incorporation of the mineral CGCaP scaffold into the PCL frame significantly increased the bulk modulus of the material compared to the mineral CGCaP scaffold alone (Figure 4.2). This drastic 6000-fold increase in modulus to 6.8 ± 0.4 MPa approaches the range necessary to mimic *in vivo* cortical bone (90 to 230 MPa) and cancellous bone (2 to 45 MPa) [201]. This change is likely due to the incorporation of the PCL frame acting as the load bearing component. Notably, the increase in mechanical properties in the collagen-PCL composite was achieved without any deleterious changes to the average pore size of the collagen scaffold itself (Figure 4.3). Here, significant decreases in pore size or increased in scaffold density would have significantly impacted specific surface area and nutrient biotransport, which would compromise the bioactivity of the composite [185, 202]. It is further anticipated that this composite architecture will protect the CGCaP matrix within the PCL-CGCaP composite from loads exceeding its yield point, allowing the CGCaP matrix to be tailored specifically to meet requirements regarding cell bioactivity. Previous work has already demonstrated the bioactivity of this matrix and its effect on endogenous BMP2 production [169], integrin activation [203], mechanotransduction [204], and gene expression [122]. So removing the requirement for meeting mechanical constraints offers the potential to further optimize the scaffold solely in the context of driving enhanced MSC osteogenic activity. This finding also suggests a more generic approach to overcome

trade-offs between mechanical robustness and qualities associated with bioactivity via composite design principles [201, 205, 206].

We then examined the effect of the specific surface area of the constructs on construct permeability. In the case of the CGCaP scaffold and PCL-CGCaP composite, a high degree of specific surface area was reflected in the significantly lower permeability compared to the PCL support alone (Figure 4.4). The relatively lower specific surface area and resultant increased permeability in the 3D printed PCL construct has been previously attributed to limitations in feature size (mm-scale, rather than micron-scale, pores) [196]. The significance of specific surface area as a biomaterial design parameter has similarly been addressed [92, 185, 202]. If too low, the specific surface area can severely limit attachment and alter fluid flow within a construct [207], while if too high results in poor infiltration into the construct. Earlier efforts regarding development of collagen-glycosaminoglycan scaffolds have examined the influence in changes in scaffold specific surface area on a range of cellular responses [185]. Importantly these results again suggest it is possible to focus design of the collagen scaffold compartment on structural and bioactivity, rather than mechanical, concerns.

The influence of specific surface area on cell response was then demonstrated via comparison of early metabolic activity metrics for porcine ASCs seeded within the PCL support versus the PCL-CGCaP composite. Here the metabolic activity of pASCs within the PCL support alone was significantly ($p < 0.05$) lower than that within the PCL-CGCaP composite at 24 hours regardless of seeding method tested (Figure 4.5). This observed difference in metabolic activity is likely a function of an increase in initial cell infiltration and attachment as a result of the enhanced specific surface area of the composite. Here the 24 hour timepoint was used both to be consistent with previous work that evaluated the effect of scaffold specific surface area on cell attachment [92], but also because 24 hours offers only a limited period for

any potential proliferation which could affect the results. Interestingly, the static seeding method led to a significant increase in cell attachment compared to the cell soak method in the presence of the increased specific surface area of the PCL-CGCaP composite, suggesting a preferred cell seeding method for future *in vitro* and *in vivo* experiments.

4.5 Conclusions

This work described the development of a multi-scale composite approach for engineering biomaterials for critical-size bone defects. This approach was intended to circumvent the typical design trade-offs found in biomaterials where there is often a tension between optimizing the bioactivity versus mechanical strength of an implant. We report a strategy to create a PCL-CGCaP composite that combines a CGCaP scaffold able to promote MSC osteogenesis in the absence of traditional osteogenic supplementation with a mechanically-robust, patient-customizable PCL support frame generated via 3D-printing. The PCL-CGCaP composite demonstrated a bulk modulus significantly higher than the CGCaP scaffold alone but consistent with the PCL support alone. Similarly, the permeability of the PCL-CGCaP composite was dictated by the CGCaP scaffold compartment. Evaluation of porcine ASC seeded constructs revealed that the increased specific surface area of the composite led to significantly higher overall metabolic activity after 24h consistent with higher ASC attachment rates. In conclusion, the PCL-CGCaP composite was found to be mechanically robust compared to the CGCaP scaffold while maintaining the inherent bioactivity of the CGCaP scaffold and a degree of customizability inherent in its multi-scale composite design.

4.6 Figures and Tables

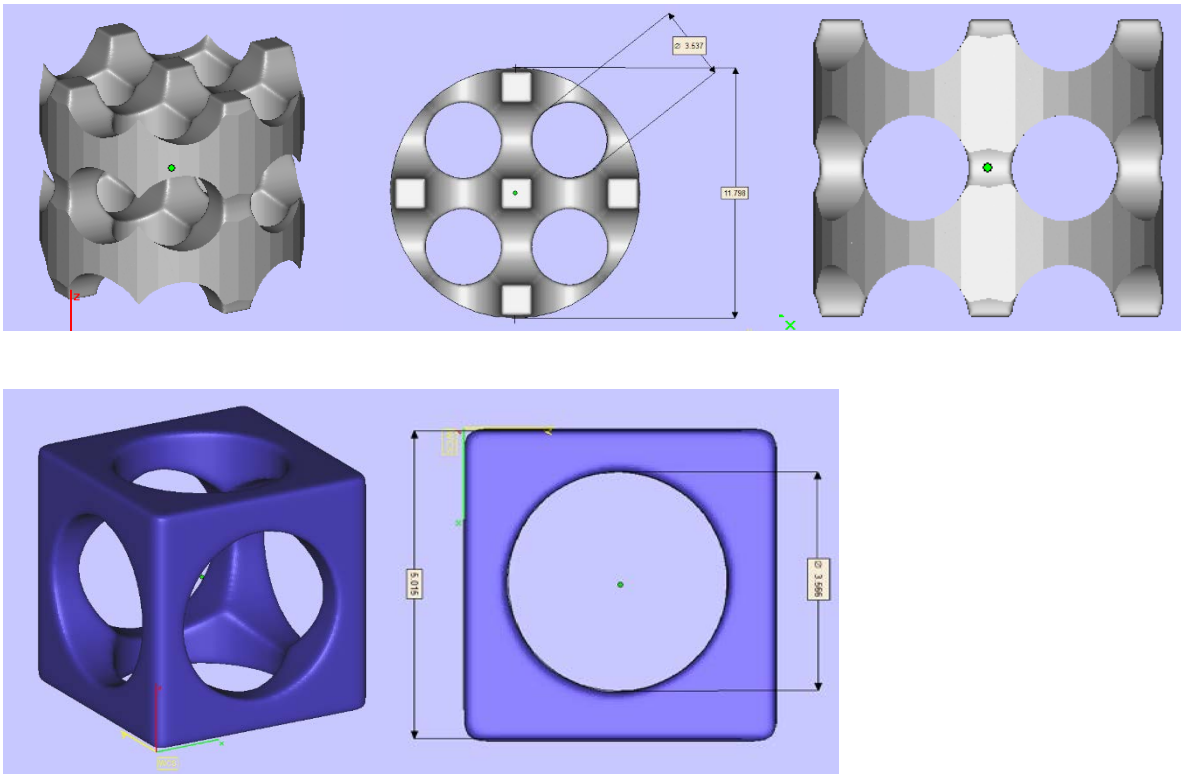

Figure 4.1 Schematic of the polycaprolactone (PCL) support construct and the unit cell.

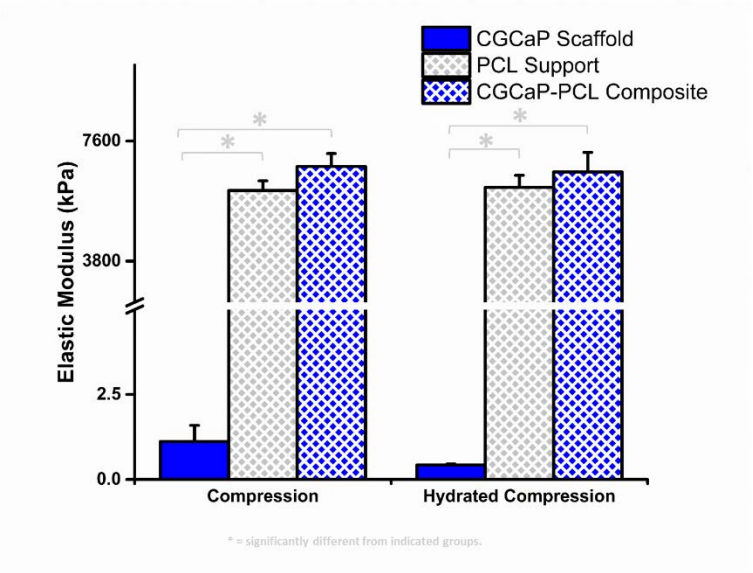

Figure 4.2 Elastic modulus of the scaffold support, and resulting composite.

Compression data comparing the mineralized CGCaP scaffold, PCL support construct, and PCL-CGCaP composite as measured in both dry and hydrated unconfined compression testing. The elastic moduli was determined from the linear elastic regime of the resulting stress-strain behavior measured.

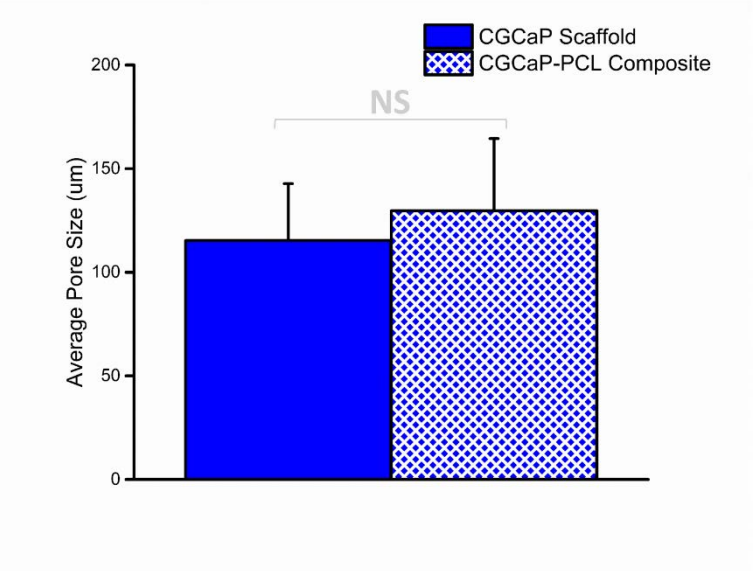

Figure 4.3 Average pore size of the mineral scaffold and the scaffold matrix within the composite.

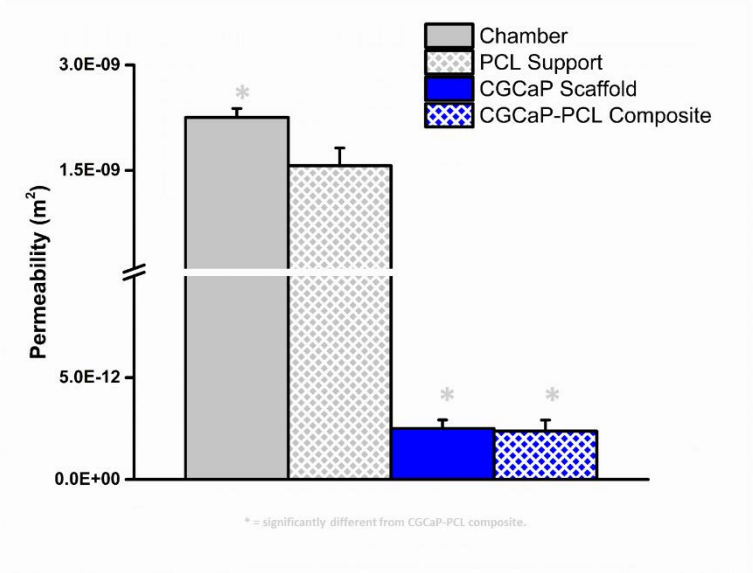

Figure 4.4 Permeability of the support, scaffold, and composite.

The permeability of the empty chamber, PCL support construct, mineral CGCaP scaffold, and PCL-CGCaP composite as measured by a constant head permeability rig. Significance (*: $p < 0.05$) compared to the PCL support construct was indicated. A significant difference between the empty chamber and the PCl support indicates that the PCL support permeability was not limited by the testing apparatus.

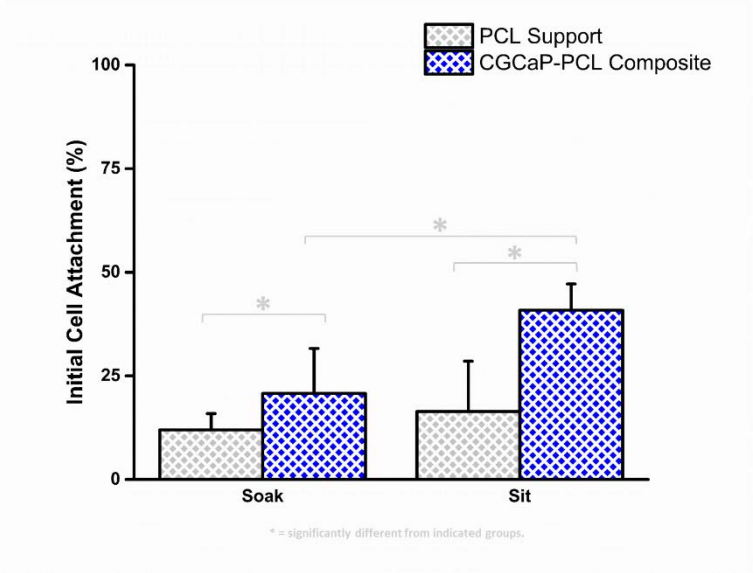

Figure 4.5 The metabolic activity of pACs cultured on the support and the composite.

Here the metabolic activity as measured via AlamarBlue of porcine adipose derived stem cells (pASCs) cultured on the PCL-support and the CGCaP-PCL composite was measured. Two different seeding methodologies, a cell suspension soak and a static cell seeding, were used when seeding the polycaprolactone support construct and the mineral polycaprolactone-collagen-glycosaminoglycan composite. Significance (*: $p < 0.05$) between indicated groups was identified.

CHAPTER 5

IN VIVO IMPLANTATION OF THE MINERAL POLYCAPROLACTONE-COLLAGEN-GLYCOSAMINOGLYCAN COMPOSITE INTO A SUBCRITICAL PORCINE MANDIBULAR RAMUS DEFECT: ASSESSMENT OF *IN VIVO* EFFICACY[4]

5.1 Overview

Initial chapters in this thesis examined the development of the mineralized collagen-glycosaminoglycan scaffold determining the inherent biophysical and biochemical properties, the flexibility in design and fabrication, as well as their effect on the cellular behavior *in vitro*. Further work then evaluated the adaptation of this mineralized collagen-glycosaminoglycan design for *in vivo* implantation by the formation of a mineral polycaprolactone-collagen-glycosaminoglycan composite increasing the inherent mechanical properties. Here we examine the *in vivo* efficacy of the prepared mineral polycaprolactone-collagen-glycosaminoglycan composite as tested in a porcine animal model. Here the mineralized collagen-glycosaminoglycan scaffolds, polycaprolactone support structures, and finally, mineral polycaprolactone-collagen-glycosaminoglycan composites were implanted into a subcritical mandibular

[4] This work is adapted from the study 124. Weisgerber, D.W., R.A. Hortensius, Milner D., Rubessa M., Lopez-Lake H., M. Wheeler, B.A.C. Harley, *In vivo implantation of the mineral polycaprolactone-collagen-glycosaminoglycan composite into a subcritical porcine mandibular ramus defect: assessment of in vivo efficacy*. Ibid. In preparation.

ramus defect with subsequent wound healing being evaluated 6 weeks post-surgery. Metrics used to evaluate the *in vivo* efficacy of these constructs included mineral deposition via micro-computed tomography, bone mineral density via dual energy x-ray absorptiometry, and a histological analysis of the defect location.

5.2 Introduction

Treatment of craniofacial orthopedic defects, resultant from either acute trauma or surgical resection, remains a difficult procedure due to their often large size, complex geometry, and load bearing function. These difficulties arise from the limitations and concerns of the current standard for surgical treatment, namely the autologous and allogenic bone graft. The autologous bone graft, harvested from the patient, is limited by the quantity of bone able to be harvested without compromising donor bone function and the morbidity and pain associated with the donor site [175]. Similarly, the allogenic bone graft offers an alternative with limited availability with concerns over disease transmission [175]. The current focus of regenerative medicine and tissue engineering studies has been the development of degradable biomaterial alternatives capable of invoking and enhancing the native physiological repair processes for the treatment of orthopedic [178, 179], cardiovascular [208, 209], and nerve defects [184, 210]. However, the significance of biophysical and biochemical properties has been established not only for inducing a physiological repair processes, but also for maintaining mechanical competence in complex geometries during implantation and subsequent *in vivo* repair in orthopedic defects [177, 180].

To address the need for maintaining mechanical competence and complex geometries a variety of solutions have been proposed, most involving the formation of a composite biomaterial with individual components addressing either mechanical competence or bioactivity. Examples of such biomaterials include silk hydrogel mechanically reinforced with silk microfibers for cartilage repair [211], and chitosan/β-1,3-glucan/calcium phosphate ceramic for orthopedic defects [60]. Orthopedic biomaterial

composites often simulate the native bone extracellular matrix and consist of a calcium phosphate ceramic, such as beta-tricalcium phosphate ($Ca_3(PO_4)_2$; β-TCP) or calcium hydroxyapatite ($Ca_{10}(PO_4)_6(OH)_2$; HA) influencing mechanical properties and bioactivity [35, 39, 212], with polymeric components, ranging from synthetic polycaprolactone to natural chitosan or silk fibroin [40, 59-61, 64, 187].

Effects described in this thesis has evaluated the *in vitro* efficacy of one such biomaterial composite for the treatment of orthopedic defects that consists of a macro-scale polycaprolactone support construct impregnated with a micro-scale mineralized collagen-glycosaminoglycan matrix [123]. Regenerative medicine and tissue engineering literature has identified the successful *in vitro* and *in vivo* applications of collagen-glycosaminoglycan scaffolds influencing cell bioactivity towards osteochondral [67-69, 89], orthopedic [48, 73-75], cardiatric [100], tendinous [97, 101], muscular [70-72], neurological [65, 66, 83-85], and skin [78, 79] repair, while polycaprolactone has been implemented in numerous orthopedic biomaterial applications [42, 64, 187, 189, 213].

Chapter 5 of this thesis continues the evaluation of the previously developed multi-scale polycaprolactone-collagen-glycosaminoglycan composite with the *in vivo* implantation in a porcine animal model. Here a 10 mm cylindrical sub-critical mandibular ramus defect in male Yorkshire pigs was created and treated with the polycaprolactone support construct, the mineralized collagen-glycosaminoglycan scaffold, and the mineral polycaprolactone-collagen-glycosaminoglycan composite. Efficacy was evaluated after 6 weeks *in vivo* culture, and was based upon new bone volume as well as new bone density as measured by micro-computed tomography and dual x-ray absorptiometry techniques. Additionally, histological analysis also evaluated the efficacy of the biomaterial implants with assessment of new bone mineralization and integration. It is hypothesized that the mineralized collagen-

glycosaminoglycan scaffold and the polycaprolactone-collagen-glycosaminoglycan composite will enhance new bone formation.

5.3 Fabrication of the Collagen-GAG Scaffold, Polycaprolactone Support, and Composite

Fabrication of the polycaprolactone-collagen-glycosaminoglycan (PCL-CGCaP) composite, the mineralized collagen-glycosaminoglycan (CGCaP) scaffold, and the polycaprolactone (PCL) support construct were fabricated as previously described. Briefly, the mineral CGCaP scaffold and matrix precursor suspension was prepared from the 40 wt% mineral CGCaP precursor suspension, fabricated by the homogenization of 1.9% w/v type-I collagen (Collagen Matrix, Oakland, NJ) and 0.84% w/v chondroitin-6-sulfate (Sigma-Aldrich, St. Louis, MO) with calcium hydroxide ($Ca(OH)_2$; Sigma-Aldrich, St. Louis, MO) and calcium nitrate tetra-hydrate ($Ca(NO_3)_2 \cdot 4H_2O$, Sigma-Aldrich, St. Louis, MO) in phosphoric acid (Sigma-Aldrich, St. Louis, MO). Similarly, the PCL support construct was fabricated via the selected laser sintering of 4 wt% hydroxyapatite with construct geometry dictated via an Interactive Data Language program (IDL, Research Systems, Inc.) .STL file, with the same 11 mm diameter, 10 mm height with 3.5 mm cylindrical pores being employed (Figure 4.1). Likewise, the PCL-CGCaP composite was also fabricated by the impregnation of 1 mL of the mineral CGCaP precursor suspension into the PCL support construct following the initial soak of the PCL support construct in the mineral CGCaP precursor suspension. Lyophilization of the mineral CGCaP scaffold and the PCL-CGCaP composite was performed in a 6 well (12 mm diameter, 10 mm height) custom polysulfone array mold with a Genesis freeze-dryer (VisTis, Gardener, NY) at a final freezing temperature of -10°C, a cooling rate of 1°C/min, a 175 min anneal at -10°C, followed by sublimation at 0°C and 200 mTorr.

5.4 Sterilization and Crosslinking of the Scaffold and Composite for *In Vivo* Implantation

Sterilization of all specimens was then performed in 100% ethanol for 24 h, 5 days prior to surgery. Subsequent hydration was accomplished with the step wise addition of sterile phosphate buffered saline over a period of 3 days. Mineral CGCaP scaffolds and PCL-CGCaP composites were then chemically crosslinked via the addition of 1-ethyl-3-[3-dimethylaminopropyl] carbodiimide hydrochloride (EDAC, Sigma-Aldrich, St. Louis, MO) and N-hydroxysulfosuccinimide (NHS, Sigma-Aldrich, St. Louis, MO) in a molar ratio of 5:2:1 (EDAC:NHS:COOH) relative to moles of carboxylic acid (COOH) groups present in collagen. Samples were then stored in sterile phosphate buffered saline at 37°C and 5% CO_2 until *in vivo* implantation.

5.5 Porcine Subcritical Mandibular Ramus Defect Animal Model

In vivo implantation of the CGCaP scaffold, PCL support, and CGCaP-PCL composite specimens was performed on 5 male Yorkshire pigs approximately 6 months of age and weighing between 88.4 and 94.4 kg. Specimens were randomized and implanted into three 10 mm diameter bilateral surgical ramus defects situated on either side of the mandible. In total, 10 of each specimen (CGCaP scaffolds, PCL supports, and CGCaP-PCL composites) were implanted, 2 of each in each pig, with 1 of each on either side of the mandible (Figure 5.1).

5.6 Surgical Methods, *In Vivo* Implantation, and Animal Recovery

The described surgical procedures and associated protocols and facilities were approved by the University of Illinois at Urbana-Champaign Institutional Animal Care and Use committee. Prior to surgery, all pigs received a sedative cocktail (TARK) consisting of Telazol (tiletamine and zolazepam; Pfizer, New York, NY), Atropine (Neogen Corporation, Lexington, KY), Rompun (xylaazine; Lloyd Laboratories,

Shenandoah, IA) and Ketamine (Ketaset®, Fort Dodge Animal Health, Fort Dodge, IA) intramuscularly, then again intravenously via the ear vein canula, as necessary. Additionally, a standard endotracheal administration of 3-5% isoflurane was administered in oxygen as anesthesia during surgery as necessary. The surgical approach first consisted of a single submandibular and retromandibular incision tracing the exterior contour of the mandible. The underlying superficial fat and masseter muscle were then incised and elevated. Then the periosteum was incised and prised, exposing the posterior region of the underlying hemimandible. Utilizing a right-angle surgical drill with a 10 mm (outer diameter) trephine (Stryker, Portage, MI) three bicortical (full thickness) 10 mm diameter cylindrical defects were made to the exposed region of the hemimandible (ramus) (Figure 5.2). Sufficient irrigation with 0.9% physiological saline was provided during drilling to prevent damage to the surrounding tissue during operation. Self-tapping bone screws (Stryker Osteosynthesis Freiburg, Freiburg, Germany) were placed adjacent to each 10 mm defect as a means of localizing the defect after harvest, with the distance between each measured. The PCL support and CGCaP-PCL composite specimens were then press fit into the 10 mm cylindrical defects, while the CGCaP scaffold was fit into the 10 mm defect, rehydrated using 0.9% physiological saline, and anchored at one point to the surrounding mandible using Vetbond (3-M, Minneapolis, MN) (Figure 5.3).

The wound site was closed by suturing the previously described incisions in the periosteum, masseter muscle, superficial fat, and finally the skin using 3-0 Vicryl (Ethicon, Inc, San Angelo, TX) in a three layer continuous stitch with Vetbond additionally applied to the skin layer incision as an auxiliary means of closure. Following surgery, all pigs received a treatment of an antibiotic Excede (1 mL/20 kg; Pfizer, New York, NY) and an analgesia Banamine S (2.2 mg/kg; Schering Plough Animal Health, Summit, NJ). Both during and after surgery each pig was monitored and temperature taken every 15 min until the pig became sternally recumbent. Additionally, both physical and social behavior was evaluated along with any other complication that may have developed twice daily for the first 2 weeks post-surgery. Following

6 weeks, animals were sedated and euthanized, with explants from the mandible cleared of excess tissue (Figure 5.4).

5.7 Analysis of New Bone Formation via Micro-Computed Tomography

Mid-culture assessment and post-harvest quantification of bone fill and relative density within the subcritical 10 mm mandibular ramus defects was evaluated via micro-computed tomography. Prior to harvest, 21 and 28 days *in vivo* culture, animal specimens were sedated and scanned in a Lightspeed 16 slice Helical CT scanner (General Electric, Fairfield, CT). Following harvest, samples were fixed in formalin. Following 5 washes in fresh de-ionized water, samples were then individually scanned in a 50 mL conical tube via an Xradia MicroXCT-400 (Zeiss, Oberkochen, Germany). Scans were performed at 25 kEV and 5 watts with 793 projections and an associated voxel size of 24 μm. An image z-stack was then outputted and analyzed with a custom Matlab (MathWorks, Natick, MA) program (Figure 5.5). Briefly, based upon previous work analyzing mineral deposition within the mineralized collagen-glycosaminoglycan scaffold [122], the axis of the cylindrical defect was traced throughout the image z-stack, an appropriate radius was selected with respect to the cylindrical defect axis, and voxels falling within the specified radius from the cylindrical defect axis were analyzed (Figure 5.6). Depth was calculated with respect to the defect axis with each voxel grouped into radial and angular partitions counting towards the average voxel intensity and number of voxels above the bone threshold. These results were then used to calculate the relative average bone density and the bone fill fraction as a function of radial position or angle from the cylindrical defect axis. Normalization of the average bone density of the defect was performed using the average bone density of the surrounding bone.

Initial analysis during the culture period identified new bone formation (Figure 5.7). From this experiment, no significant differences were observed in the new bone fill fraction between the mineral CGCaP scaffold, the PCL support construct, and the PCL-CGCaP composite (Figure 5.8). This suggests

that the initial impregnation of the PCL support construct within the mineral CGCaP matrix did not compromise the *in vivo* healing potential of the PCL-CGCaP composite compared to the PCL support construct and the mineral CGCaP scaffold alone.

Additionally, a radial analysis of the new bone fill fraction did suggest possible enhancement of bone formation within the center of the defect within the mechanically robust PCL support construct and especially the PCL-CGCaP composite (Figure 5.9). Because some bicortical defects passed through or near the bone marrow, an angular analysis of the new bone formation was performed to identify any potential influence due to the presence of the bone marrow. Angular results did not identify any angular difference in new bone formation that may have been due to the presence of the bone marrow (Figure 5.10).

5.8 Analysis of Bone Mineral Density via Dual X-Ray Absorptiometry

Following micro-computed tomography, bone mineral density of samples was sequentially analyzed via dual x-ray absorptiometry.mineralized collagen Specimens were stored in formalin and washed 4 times in fresh de-ionized water before being individually scanned using a dual x-ray absorptiometry (DXA; Hologic QDR 4500R, Bedford, MA). Within the entire bone sample (global) and an octagonal sub-region (defect) that traced the 10 mm sub-critical defect, the resulting area of the bone specimen (cm^2), bone mineral content (g), and bone mineral density (g/cm^2) were recorded. The bone mineral density of the entire bone sample excluding the defect, or that of the surrounding bone, was calculated by subtracting the global bone mineral content from that of the defect ([global (g) – defect (g)]), and dividing this by the global area of bone specimen by that of the defect ([global (g) – defect (g)]/[global (cm^2) – defect (cm^2)]. For comparison between specimens, the normalized bone mineral density was then taken as the bone mineral density of the defect divided by the bone mineral density of the surrounding bone.

In agreement with new bone fill fraction as measured in micro-computed tomography, there was no significant differences in the bone mineral density observed between the polycaprolactone support construct, mineralized collagen-glycosaminoglycan scaffold, and mineral polycaprolactone-collagen-glycosaminoglycan composite (Figure 5.10). A more direct comparison of the bone mineral density as measured by the dual energy x-ray absorptiometry to the average voxel density and the volume of new bone determined via micro-computed tomography identified no significant differences between the two methods (Figure 5.11).

5.9 Conclusions

This chapter evaluated the *in vivo* implantation of the mineral polycaprolactone-collagen-glycosaminoglycan composite into a sub-critical porcine mandibular ramus defect. Previous work within the literature has established the efficacy of the polycaprolactone support for *in vivo* applications treating both orthopedic and osteochondral defects [64, 190]. Here the mineralized collagen-glycosaminoglycan scaffold and the mineral polycaprolactone-collagen-glycosaminoglycan composite successfully demonstrated equivalent to enhanced healing within a sub-critical defect at early time points. The healing of the sub-critical porcine mandibular ramus defect was determined through new bone formation via micro-computed tomography and bone density via dual energy x-ray absorptiometry. In both cases no significant differences were observed, suggesting that over a period of 6 weeks of *in vivo* culture the mineral polycaprolactone-collagen-glycosaminoglycan composite, mineralized collagen-glycosaminoglycan scaffold, and the polycaprolactone support construct exhibited the same healing. Future endeavors will evaluate the *in vivo* efficacy of the mineral polycaprolactone-collagen-glycosaminoglycan composite in critically sized porcine mandibular defects.

5.10 Figures and Tables

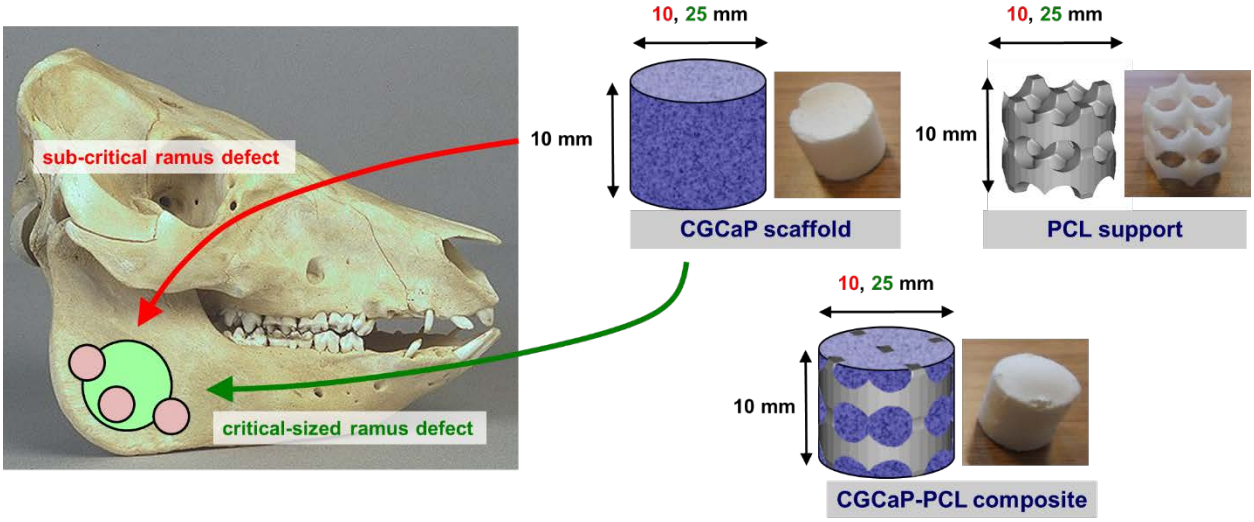

Figure 5.1 Sub-critical and critically sized porcine mandibular ramus defects.

Here the mineralized collagen-glycosaminoglycan scaffold, polycaprolactone support, and mineral polycaprolactone-collagen-glycosaminoglycan composite were implanted into a sub-critical 10 mm defect.

Figure 5.2 Sub-critical defects prior to *in vivo* implantation.

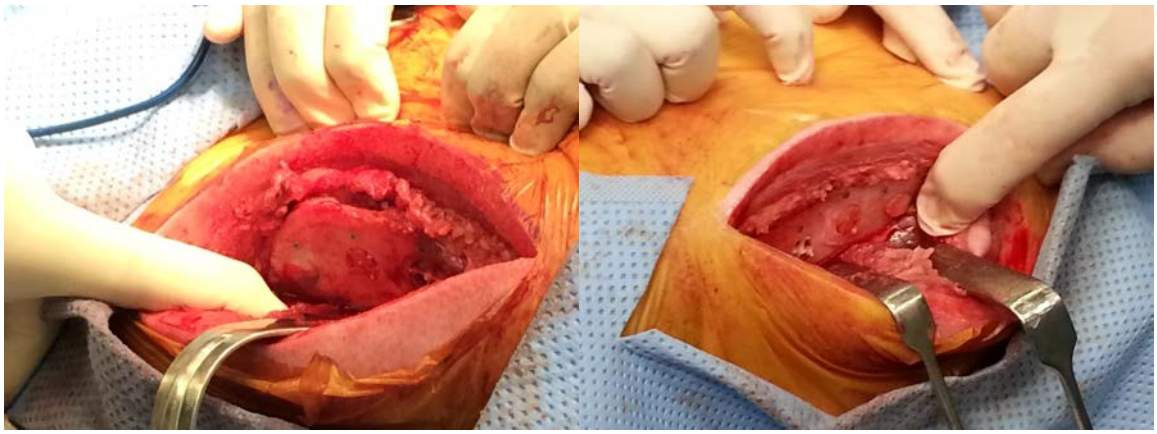

Figure 5.3 Sub-critical defects post-implantation.

Figure 5.4 Explant of the porcine mandible.

The general vicinity of the mineralized collagen-glycosaminoglycan scaffold, polycaprolactone support construct, and mineral polycaprolactone-collagen-glycosaminoglycan composite has been circled with a boney ridge obscuring the self-tapping bone screws traced with a dashed line.

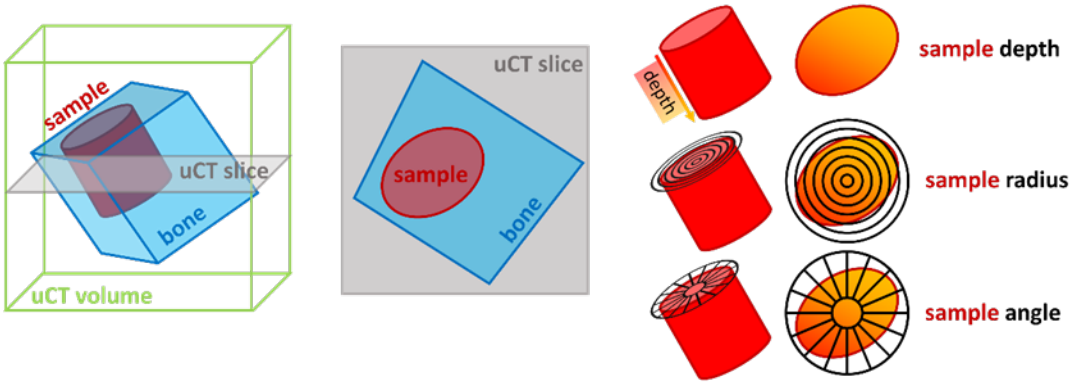

Figure 5.5 Schematic indicating micro-computed tomography analysis.

Each bone sample was scanned with the sample region and orientation identified. Subsequent analysis evaluated the voxel intensity as a function of depth (relative to the sample), radius (relative to the sample axis), and angle (relative to the sample center).

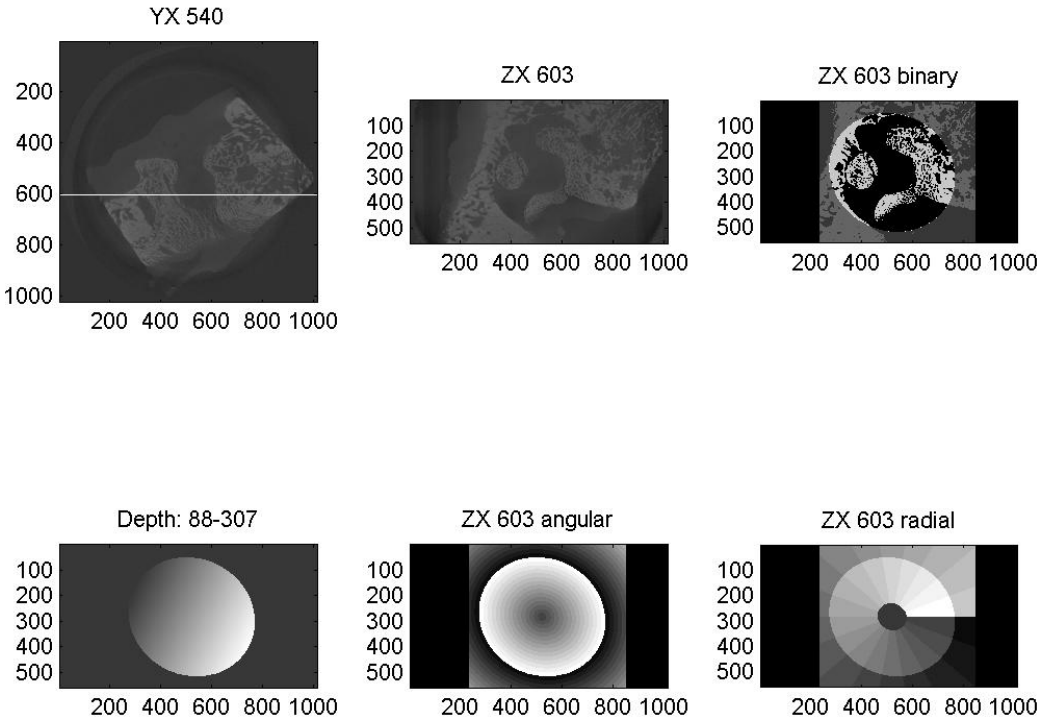

Figure 5.6 Example output of the custom Matlab program analyzing new bone formation.

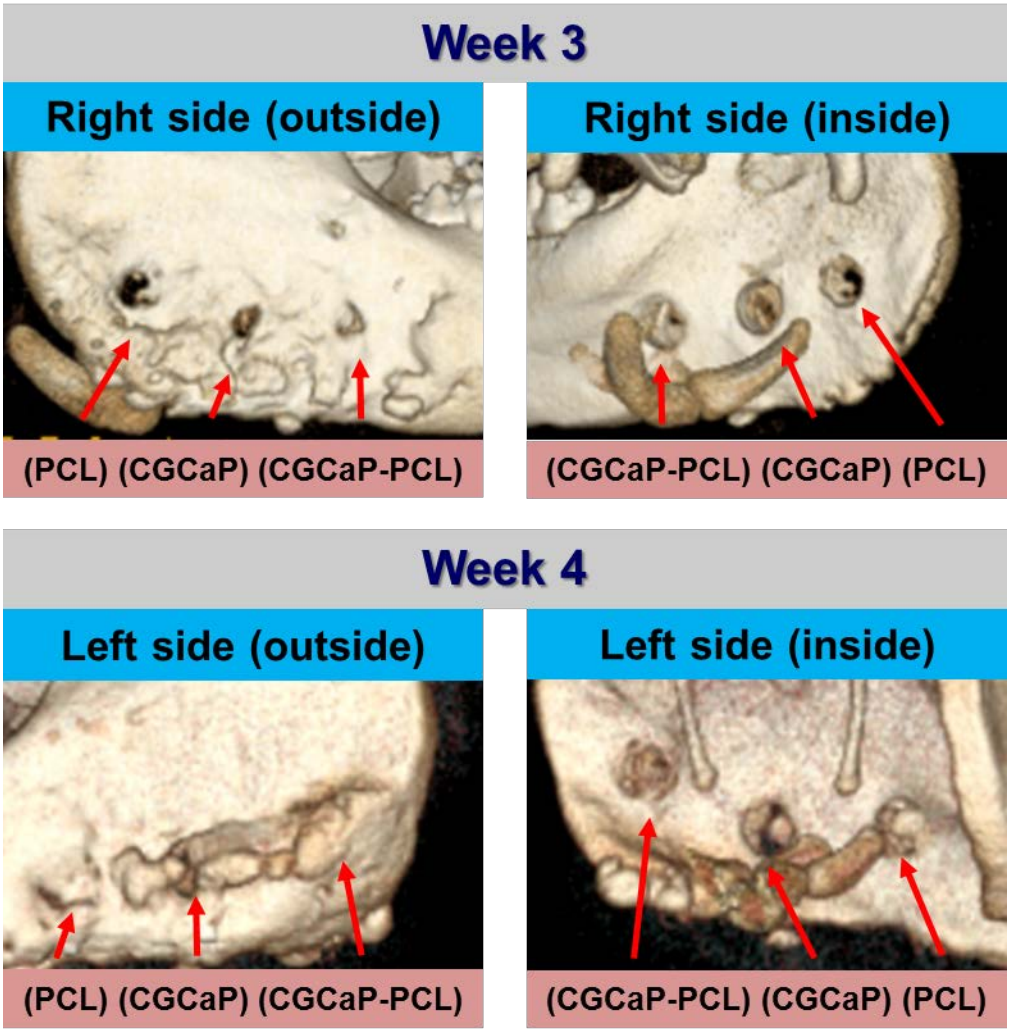

Figure 5.7 Example of micro-computed tomography during *in vivo* culture.

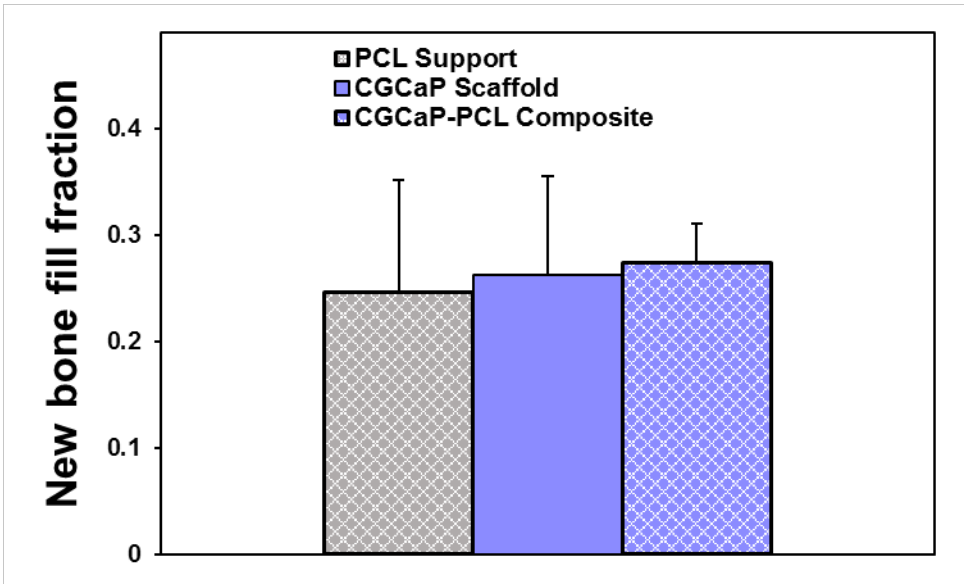

Figure 5.8 Average fill fraction observed within the support, scaffold, and composite.

The PCL support construct, mineralized CGCaP scaffold, and mineralized PCL-CGCaP composite after 42 days of in vivo culture within a sub-critical porcine mandibular ramus defect was determined via micro-computed tomography analysis.

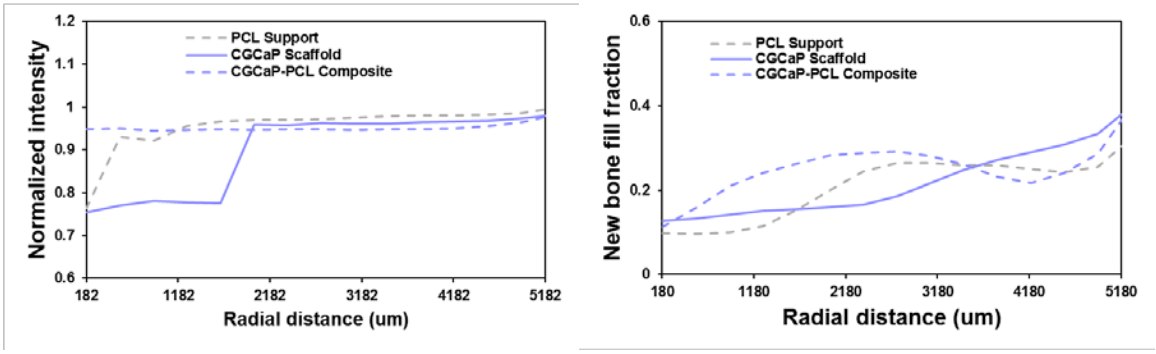

Figure 5.9 Radial analysis of the new bone and density after *in vivo* culture.

A radial analysis performed on the micro-computed tomography results evaluating the new bone formation and density (normalized to surrounding bone) of the PCL support construct, the mineralized CGCaP scaffold, and the mineralized PCL-CGCaP composite.

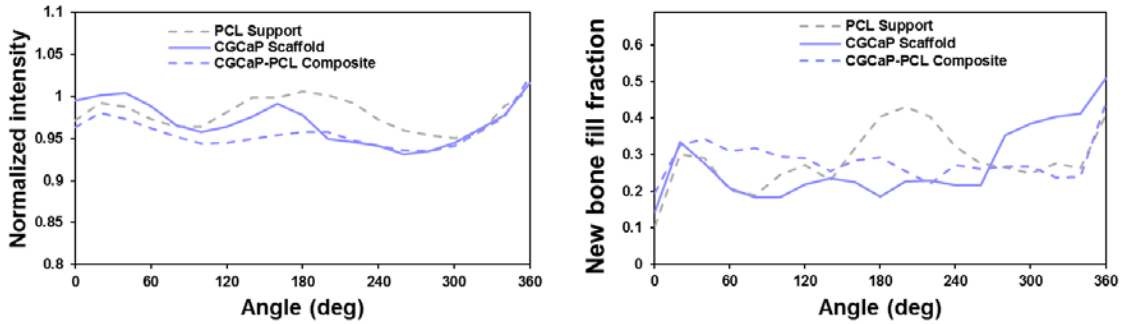

Figure 5.10 Angular an analysis of the new bone and density after *in vivo* culture.

An angular analysis performed on the micro-computed tomography results evaluating the new bone formation and density (normalized to surrounding bone) of the PCL support construct, the mineralized CGCaP scaffold, and the mineralized PCL-CGCaP composite.

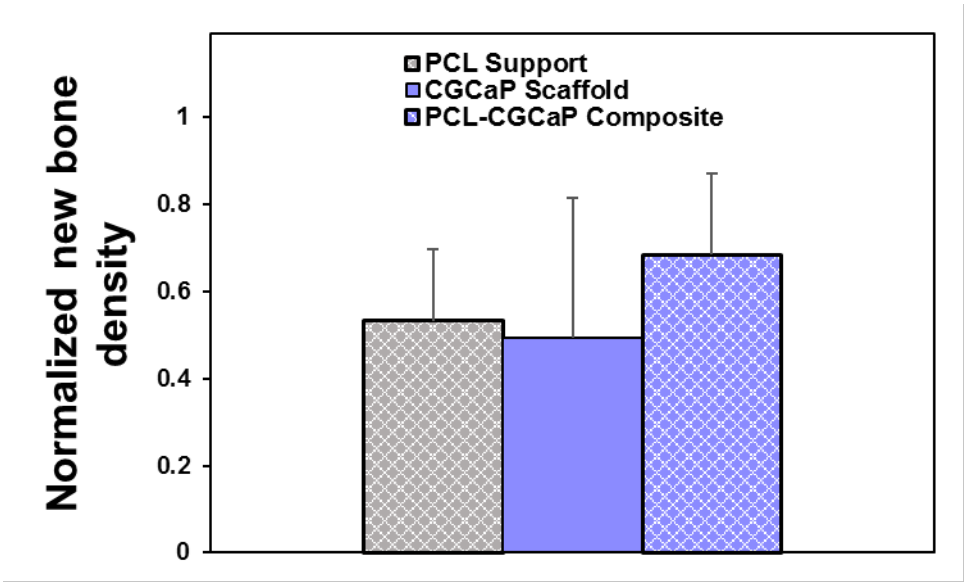

Figure 5.11 Normalized bone mineral density as measured by DXA.

In addition to micro-computed tomography, dual energy x-ray absorptiometry was used to determine the bone mineral density (normalized to surrounding bone) of the PCL support construct, the mineralized CGCaP scaffold, and the mineralized PCL-CGCaP composite.

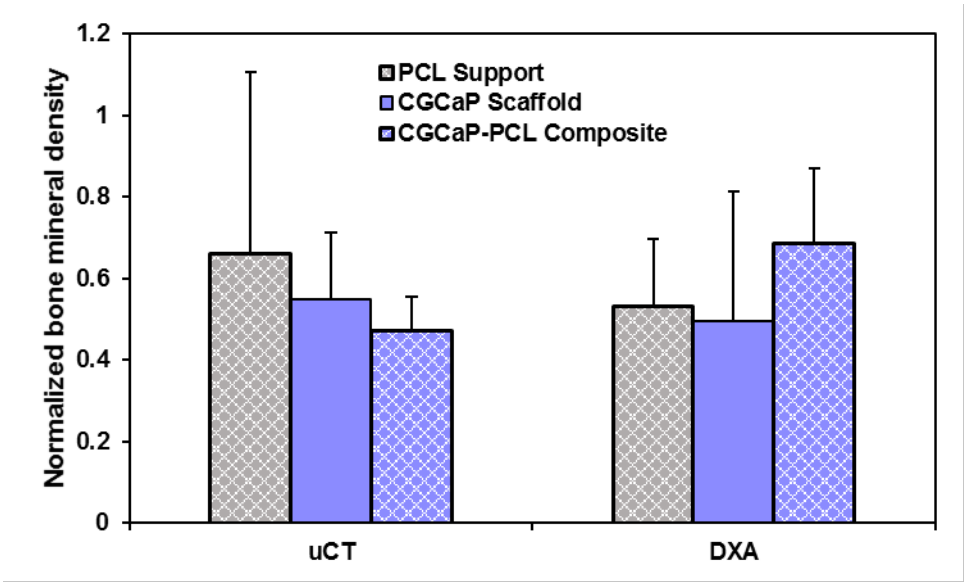

Figure 5.12 A comparison between DXA and uCT results.

In order to directly compare the dual energy x-ray absorptiometry results and the micro-computed tomography results the normalized bone mineral density as measured by dual energy absorptiometry was compared to the product of the normalized bone mineral density and the normalized fill fraction as measured by micro-computed tomography.

CHAPTER 6

ALTERATIONS IN MINERALIZED COLLAGEN-GLYCOSAMINOGLYCAN SCAFFOLD COMPOSITION: EFFECT OF MINERAL ADDITION AND PROTEIN CONSTITUENTS[5]

6.1 Overview

Thus far, this chapters 2 and 3 has previously followed the fabrication and characterization of mineralized collagen-glycosaminoglycan scaffold material properties and bioactivity in the presence of human mesenchymal stem cells. The scaffold design was then adapted for *in vivo* implantation by the formation of a mineral polycaprolactone-collagen-glycosaminoglycan composite with in vivo efficacy verified in a porcine subcritical mandibular ramus defect. Chapter 6, the mineral content and protein composition of the mineralized collagen-glycosaminoglycan scaffold and its potential benefits investigated with the *in vitro* culture of porcine adipose derived stem cells. In this chapter, the effect of a denser non-mineralized collagen-glycosaminoglycan scaffold was compared to the mineralized collagen-glycosaminoglycan scaffold with the glycosaminoglycans employed varying between the standard chondroitin-sulfate

[5] This work is adapted from the study 125. Weisgerber, D.W., R.A. Hortensius, B.A.C. Harley, *Alterations in mineralized collagen-glycosaminoglycan scaffold composition: effect of mineral addition and protein constituents.* Ibid. In preparation.

previously employed in this lab and heparin. Scaffold bioactivity and matrix deposition was investigated *in vitro* over the course of 28 days.

6.2 Introduction

In both regenerative medicine and tissue engineering fields, it has been established that the biophysical, biochemical, and biomolecular biomaterial properties serve essential roles in achieving material bioactivity that is capable of guiding cellular behavior that positively influences or invokes the physiological healing process [22, 23]. For orthopedic biomaterials, especially composites comprised of two or more contributing constituents, the material properties governing the bioactivity are heavily influenced by individual constituent properties. Examples of such constituent influences include the increased degradation and ductility of calcium phosphate ceramic biomaterials with the incorporation of a polymeric phase [42], or the fiber reinforcement of both natural and synthetic polymeric biomaterials [214, 215]. Biomolecular alterations have similarly garnered much attention in the form of soluble supplementation or biomolecule tethering [164, 170, 216].

One approach for influencing the bioactivity of biomaterials has been the incorporation of heparin as a biochemical regulator of biomolecules [217]. While its physiological function is poorly understood, heparin has been identified as influencing the retention and binding of multiple growth factors throughout the body [218-220], and has been employed clinically for its anticoagulation and anti-inflammatory properties [221]. The influence of heparin on biomolecule retention due to electrostatic interactions has been attributed to its relatively high degree of negative charge compared to other glycosaminoglycans, as well as its amino acid sequencing for biomolecule binding affinity [222, 223].

One such application of heparin in biomaterial design has been the exchange of chondroitin sulfate for heparin in collagen-glycosaminoglycan scaffolds. The collagen-glycosaminoglycan biomaterial design has been successfully employed for the treatment of a variety of tissue defects ranging from cartilage [67-69, 89], to bone [48, 73-75], to tendon [97, 101], muscular [70-72], and skin [78, 79]. Previous work has investigated the benefits imparted by the incorporation of heparin into the anisotropic collagen-glycosaminoglycan scaffold design for treating tendon defects [106]. However, the effect of heparin within a mineralized collagen-glycosaminoglycan scaffold variant for orthopedic applications has not been investigated.

An additional application of incorporating heparin into the collagen-glycosaminoglycan scaffold is the potential sequestration of osteogenic growth factors such as bone morphogenetic protein 2 (BMP2). Collaborative work has previously established an endogenous BMP2 feedback loop in mesenchymal stem cells seeded onto the mineralized collagen-glycosaminoglycan scaffold [169]. Literature work has identified the complexation and sequestration of BMP2 with heparin [224]. Combined with the endogenous production of BMP2, the mineralized collagen-heparin scaffolds offers the possibility of stable sequestration, potentially prolonging the BMP2 feedback loop identified with mesenchymal stem cells. However, previous literature has suggested that the addition of heparin introduces inhibitory effects on osteogenic activity via soluble BMP2 supplementation *in vitro* [225], necessitating the investigation of the interaction between heparin and the endogenous BMP2 feedback loop observed within the mineralized collagen-glycosaminoglycan scaffold.

This work further investigates the benefits of heparin incorporation in the collagen-glycosaminoglycan scaffold design for orthopedic applications. Here, within the mineralized collagen-glycosaminoglycan scaffold previously described [48, 87, 88, 122], chondroitin-sulfate was exchanged for heparin and the resultant bioactivity was assessed. *In vitro* culture of porcine adipose derived stem cells was investigated

in the presence of non-mineral and mineralized collagen-glycosaminoglycan scaffolds fabricated with either chondroitin-sulfate or heparin. Changes in the metabolic activity, mineral deposition, and changes in modulus were evaluated over the course of the 28 day *in vitro* culture as metrics of scaffold bioactivity.

6.3 Fabrication of Non-Mineralized Collagen-Glycosaminoglycan Precursor Suspensions

In this study a denser non-mineralized collagen-glycosaminoglycan and the previous mineralized collagen-glycosaminoglycan precursor suspensions were fabricated using previously described methods with alternating glycosaminoglycan content. In the case of the non-mineralized collagen-glycosaminoglycan precursor, 2.0% w/v type-I fibrillar collagen isolated from bovine Achilles tendon (Sigma-Aldrich, St. Louis, MO) was homogenized with 0.176% w/v glycosaminoglycan isolated from shark cartilage (Sigma-Aldrich, St. Louis, MO), with a ratio of 11.25:1 collagen:glycosaminoglycan, in 0.05M acetic acid (Sigma-Aldrich, St. Louis, MO). The non-mineralized collagen-chondroitin sulfate (Col:CS) scaffold was fabricated using chondroitin sulfate isolated from shark cartilage (Sigma-Aldrich, St. Louis, MO) as the glycosaminoglycan during fabrication, while the non-mineralized collagen-heparin (Col:HA) was fabricated using heparin as the glycosaminoglycan during fabrication.

6.4 Fabrication of Mineralized Collagen-Glycosaminoglycan Precursor Suspensions

The mineralized collagen-glycosaminoglycan precursor suspensions were fabricated as the previously described 40 wt% mineral CGCaP precursor suspension. Briefly, 1.9% w/v type-I collagen (Collagen Matrix, Oakland, NJ), 0.044% w/v glycosaminoglycan, calcium hydroxide ($Ca(OH)_2$, Sigma-Aldrich, St. Louis, MO), and calcium nitrate tetra-hydrate ($Ca(NO_3)_2 \cdot 4H_2O$, Sigma-Aldrich, St. Louis, MO) were homogenized in phosphoric acid (Sigma-Aldrich, St. Louis, MO). As with the non-mineral Col:CS and Col:HA scaffolds, the mineralized collagen-chondroitin sulfate (Col:CS:CaP) and mineralized collagen-

heparin (Col:HA:CaP) were fabricated with the addition of chondroitin sulfate isolated from shark cartilage (Sigma-Aldrich, St. Louis, MO) and heparin (Sigma-Aldrich, St. Louis, MO) during homogenization respectively.

6.5 Fabrication of Non-Mineral and Mineral Scaffolds via Lyophilization

All Col:CS, Col:HA, Col:CS:CaP, and Col:HA:CaP scaffold variants were lyophilized from 23 mL of the corresponding precursor suspensions using a custom polyfulfone tray (76.2 mm by 76.2 mm, 1.5 mm thick base). Lyophilization proceeded with a 1°C/min cooling from 20°C to a final freezing temperature -10°C, a 175 min hold at -10°C, with sublimation then occurring at 0°C and 200 mTorr. Scaffolds were then obtained from each 72.6 mm x 72.6 mm x 4 mm sheets via biopsy punches for cellular bioactivity (6 mm diameter, 4 mm thick) and mechanical (12 mm diameter, 4 mm thick) analysis.

6.6 Visualization of Chondroitin Sulfate and Heparin Scaffolds

Differences in microstructure was observed via scanning electron microstructure. Specimens were sliced vertically and oriented for imaging the transverse plane using a JEOL JSM-6060LV Low Vacuum Scanning Electron Microscope (JEOL USA, Peabody, MA). Qualitatively, no differences in scaffold microstructure were observed between chondroitin sulfate and heparin scaffolds (Figure 6.1).

6.7 Sterilization and Crosslinking of Scaffolds for *In Vitro* Culture

Non-mineral Col:CS and Col:HA scaffolds were dehydrothermally crosslinked in a vacuum oven (Welch, Niles, IL) for 24 h at 105°C and <25 Torr. All scaffold variants were then sterilized in 100% ethanol and stepwise hydrated in sterile phosphate buffered saline at 37°C and 5% CO_2 before being chemically crosslinked. Chemical crosslinking was performed via 1-ethyl-3-[3-dimethylaminopropyl] carbodiimide hydrochloride (EDC; Sigma-Aldrich, St. Louis, MO) and N-hydroxysulfosuccinimide (NHS; Sigma-

Aldrich, St. Louis, MO) chemistry added at a 5:2:1 (EDC:NHS:COOH) molar ratio to the moles of caroboxylic acid groups (COOH) present on collagen.

6.8 *In Vitro* Culture of Porcine Adipose Derived Stem Cells

To determine the effect of mineral and glycosaminoglycans on the osteogenic potential of the mineralized collagen-glycosaminoglycan scaffold was investigated *in vitro* with porcine adipose derived stem cells (pASCs) courtesy of Dr. M. Wheeler (Department of Animal Science, University of Illinois at Urbana-Champaign, Urbana, IL). Briefly, pASCs were cultured in complete mesenchymal stem cell growth media, low glucose Dulbecco's modified eagle medium (DMEM), 10% mesenchymal stem cell fetal bovine serum (MSC FBS; Invitrogen, Carlsbad, CA), 1% antibiotic-antimycotic (Invitrogen, Carlsbad, CA) at 37°C and 5% CO_2. At passage 8, pASCs were seeded onto Col:CS, Col:HA, Col:CS:CaP, Col:HA:CaP scaffolds using a previously established static seeding method wherein 3.5 $x10^6$ pASCs were seeded onto each side of the disc with 15 min allotted for attachment between. After an additional 2 h for attachment, complete mesenchymal stem cell growth media was added and scaffolds were cultured *in vitro* at 37°C and 5% CO_2 over a period of 28 days.

6.9 Evaluation of Cellular Metabolic Activity during *In Vitro* Culture

The effect on bioactivity of the mineral and glycosaminoglycan content within the collagen-glycosaminoglycan scaffolds was assessed by the metabolic activity of pASCs cultured in vitro via the non-destructive AlamarBlue® assay. Briefly, *in vitro* pASCs cultured scaffolds were rinsed of dead or unattached cells in phosphate buffered saline and then cultured in 1 mL AlamarBlue® assay solution at 37°C and 5% CO_2 under gentle agitation. The metabolic activity of the pASCs within the scaffold was measured via the uptake and subsequent conversion of resazurin within the cell into resorufin, the fluorescent byproduct. Quantification of resorufin was then measured via a F200 spectrophotometer (Tecan, Männedorf, Switzerland) at the excitation/emission of 540(52)/580(20) nm. The results were then

reported as the metabolic activity normalized to that of the number of cells originally seeded, 0.75 $x10^6$ cells.

Across all scaffold variants, non-mineral vs mineral and chondroitin vs heparin, a significant ($p < 0.05$) increase in the metabolic activity was observed over the 28 day in vitro culture (Figure 6.2). This result agrees with previous work identifying that the collagen-glycosaminoglycan scaffold supports cell proliferation and healthy metabolic activity in the presence of a calcium phosphate mineral phase and either heparin or chondroitin sulfate [106, 122]. The presence of the calcium phosphate mineral phase was observed to induce a significantly ($p < 0.05$) lower metabolic activity over the first 14 days in vitro before inducing a significantly ($p < 0.05$) higher degree of metabolic activity by day 28 (Figure 6.2). This observation precisely coincides with an earlier observation in which 0.5 wt% non-mineral CG scaffolds possessed a significantly higher degree of human mesenchymal stem cell metabolic activity than the mineral CGCaP scaffolds until day 28 at which point the mineral CGCaP scaffold possessed a higher degree of metabolic activity [122]. This strongly suggests that the mineralized collagen-glycosaminoglycan scaffold induces a degree of phenotype differentiation within the first 28 days in the absence of soluble supplementation independent of stem cell line and scaffold density [122, 169, 170]. In evaluating the effect of glycosaminoglycan (chondroitin sulfate vs heparin) non-mineral heparin scaffolds exhibited a significantly ($p < 0.05$) higher metabolic activity as early as day 3 and as late as day 28 (Figure 6.2), while mineral heparin scaffolds only possessed a significantly ($p < 0.05$) higher degree of activity between days 7 and 14 (Figure 6.2). This is in agreement with previous work that has identified a positive effect of heparin on the cellular metabolic activity of equine tenocytes in a highly aligned collagen-glycosaminoglycan scaffold aimed at the repair of tendon defects [106]. However, this positive effect was modulated in the presence of the calcium phosphate mineral phase within the mineral CGCaP scaffolds, blunting this observed difference by day 28 (Figure 6.2).

6.10 Evaluation of Mineral Deposition during *In Vitro* Culture

The effect of mineral and glycosaminoglycan content on collagen-glycosaminoglycan scaffold bioactivity was also assessed by the in vitro deposition of mineral content as measured via micro-computed tomography (μCT). Briefly, after 1, 7, 14, and 28 days of *in vitro* pASC culture all scaffold variants were transferred into fresh deionized water and immediately flash frozen in liquid nitrogen to stop all cellular activity and preserve mineral deposition. Subsequent lyophilization was performed at a final freezing temperature of -10°C on a precooled shelf with sublimation at 0°C and 200 mTorr to remove any liquid constituents. Samples were then scanned in an Xradia MicroXCT-400 (Zeiss, Oberkochen, Germany) at 25 kEV and 5 watts with 793 projections and an associated voxel size of 31 μm. The resulting z-stacks were then analyzed using a custom Matlab (MathWorks, Natick, MA) program assessing radial intensity through the height of the sample (Figure 6.3).

The analysis of the resulting data indicated a significant ($p < 0.05$) degree of mineralization in the mineral Col:CS:CaP and Col:HA:CaP scaffolds over the 28 day *in vitro* culture, while the non-mineral Col:CS and Col:HA indicated a lesser degree of significant ($p < 0.05$) mineral deposition (Figure 6.4). Within the mineral Col:CS:CaP scaffolds a significant ($p < 0.05$) increase in mineral was observed by day 28, significantly ($p < 0.05$) higher than Col:CS, Col:HA, and Col:HA:CaP at that time point (Figure 6.4). Mineralization of the 2% w/v non-mineral Col:CS scaffolds seeded with pASCs suggests either a cell specific or density specific response compared to previous work evaluating the mineral deposition of a 0.5% w/v non-mineral Col:CS scaffold seeded with human mesenchymal stem cells [122]. Literature has suggested that alterations in substrate stiffness can modulate the cellular response, particularly in regards to differentiation [28]. In both the non-mineral and mineral scaffolds the addition of heparin (Col:CS vs Col:HA; Col:CS:CaP vs Col:HA:CaP) corresponded to no significant change in the observed mineral deposition (Figure 6.4). While the incorporation of heparin was observed to increase in metabolic activity of porcine adipose derived stem cells up to day 28 (Figure 6.2). This initial increase in metabolic activity

did not correspond to an increase in mineral deposition observed. As suggested previously, this discrepancy between metabolic activity and mineral deposition highlights the tradeoff between cell proliferation and cell phenotype observed within the collagen-glycosaminoglycan scaffold, previously between unsupplemented and osteogenic supplemented mineralized collagen-glycosaminoglycan scaffolds [122].

6.11 Evaluation of Matrix Mechanics during *In Vitro* Culture

Finally, the quantitative changes in scaffold mechanical properties was used as a qualitative measure of *in vitro* porcine adipose derived stem cell remodeling within all collagen-glycosaminoglycan variants. Col:CS, Col:HA, Col:CS:CaP, and Col:HA:CaP *in vitro* were tested in unconfined hydrated compression with the elastic modulus determined from the measured stress-strain behavior. Briefly, *in vitro* mechanical samples (12 mm diameter, 4 mm thick) were removed after 1, 7, 14, and 28 days of *in vitro* pASC culture at 37°C and 5% CO_2 and kept in sterile phosphate buffer saline while undergoing compression. Hydrated unconfined compression tests were performed via a TA.XTplus Texture Analyzer (StableMicro Systems Ltd., Surrey, UK) with a 1 kg load cell at a strain rate of 0.01 mm/min to 0.75 strain. Pure phosphate buffered saline controls were performed under identical conditions in the absence of a specimen as a blank control. The force-displacement due to the blank control was then subtracted from the hydrated specimen force-displacement in order to determine the specimen stress-strain behavior alone. The elastic modulus was then determined from the linear elastic regime of the resulting stress-strain curve.

The mineralized collagen-glycosaminoglyan scaffold variants (Col:CS:CaP and Col:HA:CaP) possessed a significantly ($p < 0.05$) higher modulus compared to their non-mineral counterparts (Col:CS and Col:HA respectively) (Figure 6.5). The incorporation of a mineral component to the collagen-glycosaminoglycan scaffold significantly increased the modulus of the resultant scaffold. This result agrees with previous

work that has investigated the mechanical properties [48]. Additionally, altering the glycosaminoglycan component from chondroitin sulfate to heparin did not significantly affect the modulus of non-mineral (Col:CS vs Col:HA) and mineral (Col:CS:CaP vs Col:HA:CaP) scaffolds after 28 days of *in vitro* porcine adipose derived stem cell culture (Figure 6.5). The lack of difference between the mineral (Col:CS:CaP vs Col:HA:CaP) scaffolds is in agreement with the lack of difference observed due to mineral deposition, suggesting that the reinforcement due to cellular remodeling was unaffected by the presence of the heparin in the Col:HA:CaP scaffold (Figure 6.5).

6.12 Conclusions

The incorporation of heparin was observed to positively influence the metabolic activity of the non-mineral scaffolds throughout the study in agreement with previous work [226], and increase the metabolic activity through day 21 within the mineral scaffold. Previously observed differences between non-mineral and mineralized collagen-glycosaminoglycan scaffolds were also reaffirmed with the *in vitro* culture of porcine adipose derived stem cells. The incorporation of heparin had no effect on mineral deposition or mechanics within the compared to the chondroitin sulfate counterpart. As such, the incorporation of heparin was concluded to not interfere with the osteogenic bioactivity of the mineralized collagen-glycosaminoglycan scaffold. In agreement with previous work, the mineralized collagen-glycosaminoglycan scaffolds exhibited a significant increase in the mineral deposition and modulus over the culture period, with no change in the non-mineralized variants. Finally, previous inhibitory effects identified with heparin were not observed to negatively affect the osteogenic potential of the porcine adipose derived stem cells in mineral deposition or modulus within this chapter.

6.13 Figures and Tables

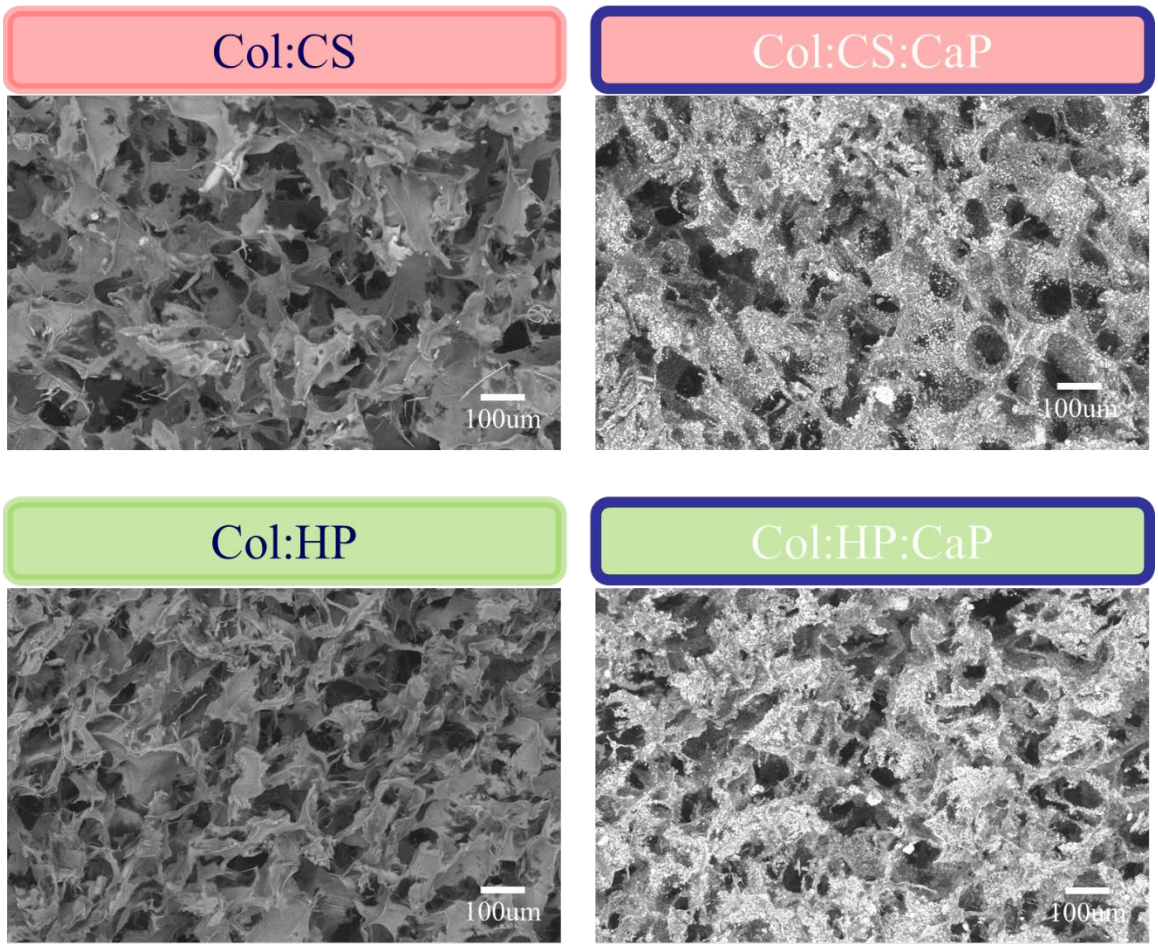

Figure 6.1 Microstructural differences between heparin and chondroitin sulfate scaffolds.

Microstructural differences between non-mineralized (Col:CS vs Col:HP) and mineralized (Col:CS:CaP vs Col:HP:CaP) as observed via scanning electron microscopy. Qualitatively, no differences were observed between the two glycosaminoglycans (heparin vs chondroitin sulfate) used during fabrication.

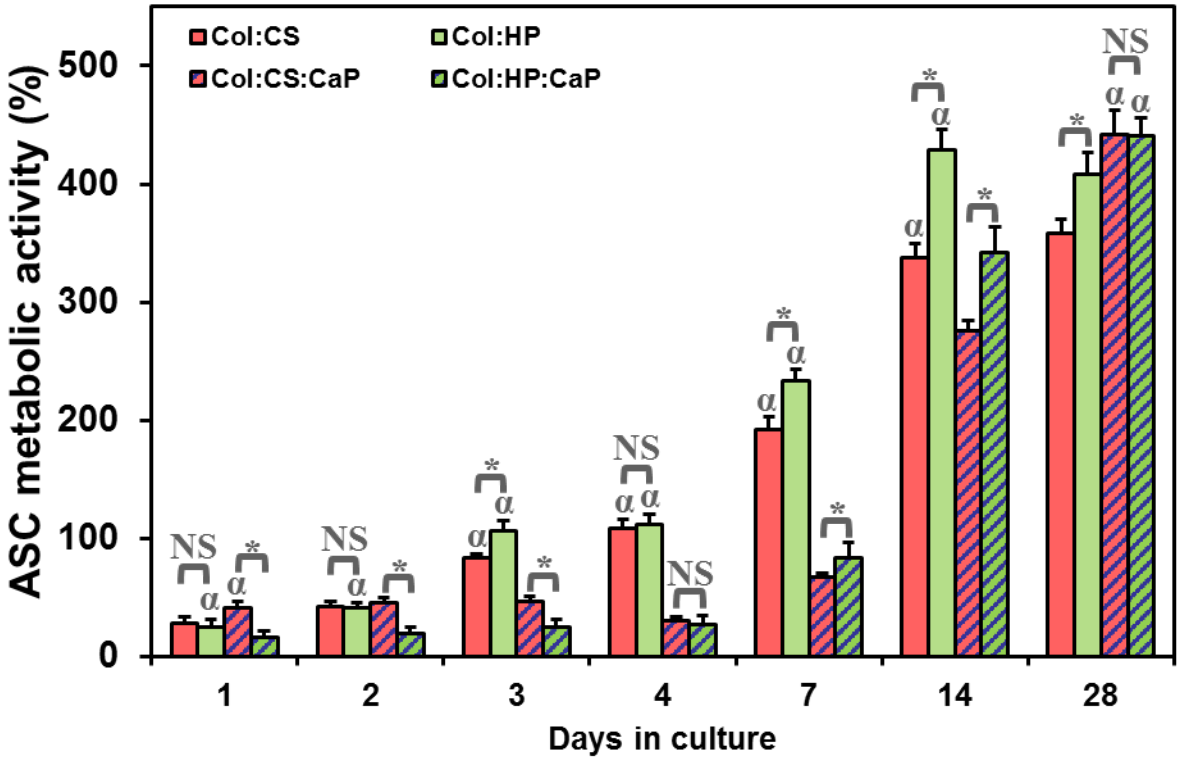

Figure 6.2 Metabolic activity of ASCs cultured on chondroitin sulfate and heparin scaffolds.

The metabolic activity of porcine adipose derived stem cells (ASCs) cultured on non-mineralized and mineralized scaffolds containing either chondroitin sulfate or heparin over a period of 28 days was determined via an AlamarBlue assay. Significance (*: $p < 0.05$) between indicated groups and significance (α: $p < 0.05$) between corresponding glycosaminoglycan (Col:CS vs Col:CS:CaP; Col:HP vs Col:HP:CaP) at each time point was indicated.

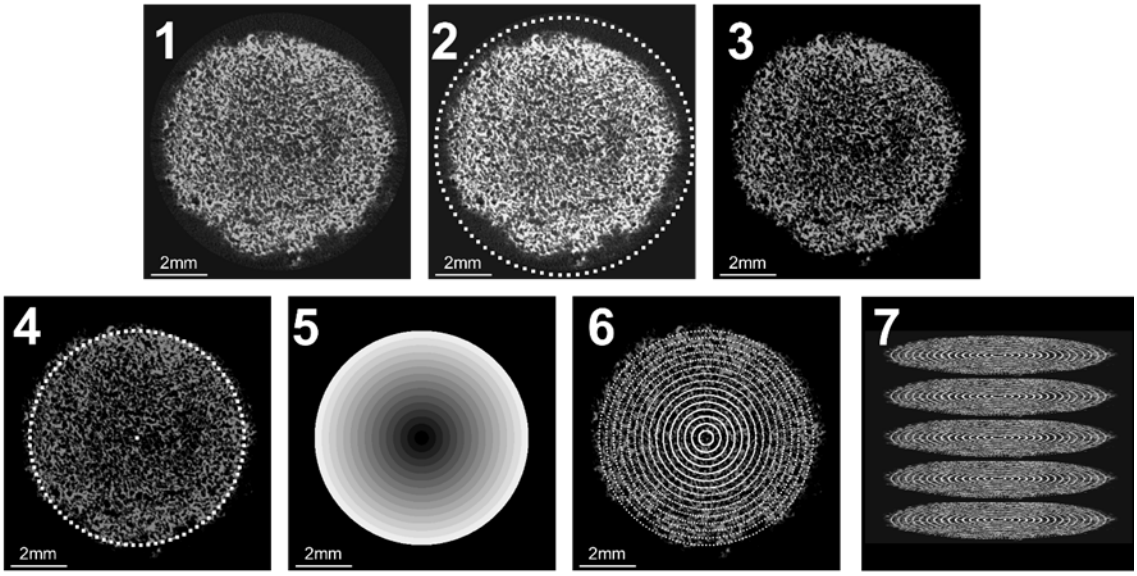

Figure 6.3 Procedure of micro-computed tomographic analysis of mineral deposition.

A step by step procedure indicating the procedure performed in Matlab to analyze the mineral deposition within scaffolds cultured *in vitro* as measured by micro-computed tomography (uCT). Procedure analysis was performed as: (1) selection of a start and end uCT z-stack slice; (2) selection of the entire scaffold and surrounding air; (3) subtraction of the background not selected in step 2; (4) a selection of only the scaffold region; (5) division of the scaffold into radial partitions; (6) analysis of the voxels contained within each radial partition; (7) repeat of this analysis throughout the z-stack, or the uCT volume.

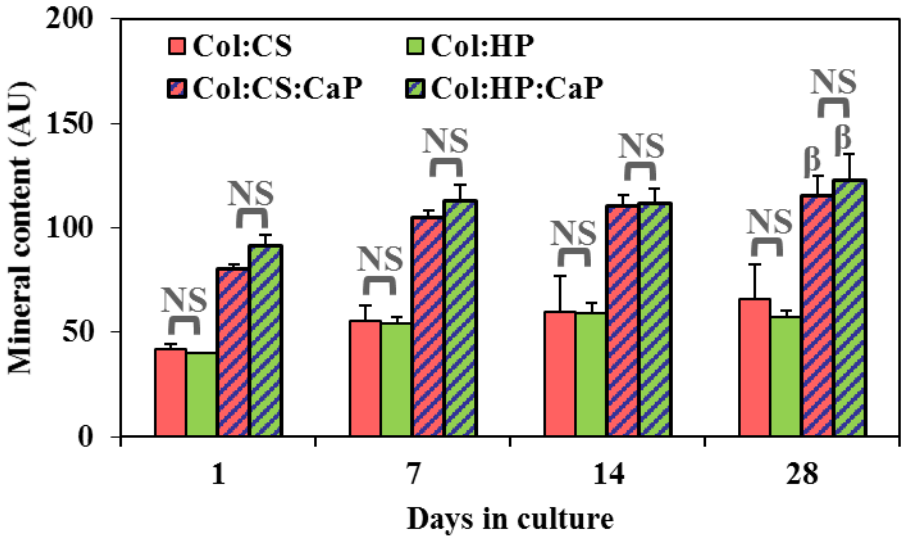

Figure 6.4 *In vitro* mineral deposition observed in chondroitin sulfate and heparin scaffolds.

Mineral deposition of porcine adipose derived stem cells (ASCs) cultured on non-mineralized and mineralized scaffolds containing either chondroitin sulfate or heparin over a period of 28 days was determined via micro-computed tomography. Significance (*: $p < 0.05$) between indicated groups and significance (β: $p < 0.05$) of a single group between days 1 and 28 was indicated.

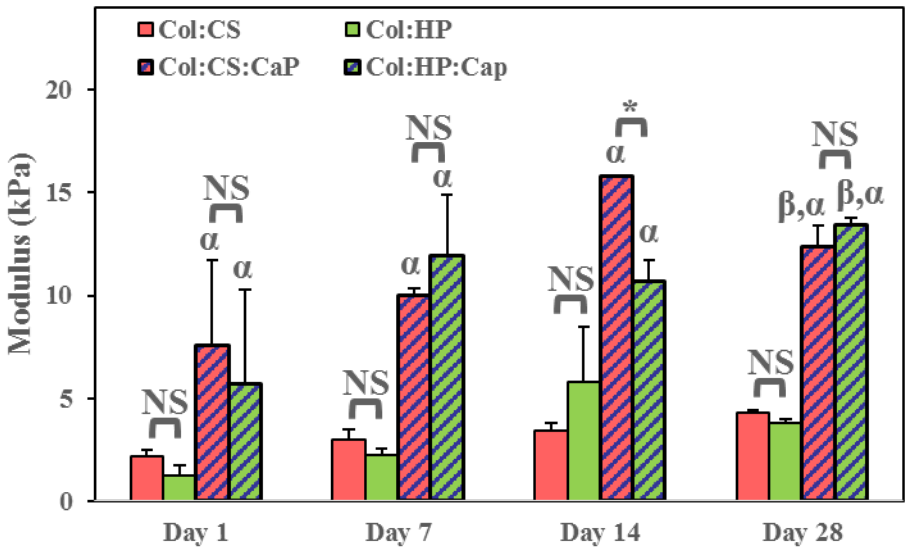

Figure 6.5 Elastic moduli of heparin or chondroitin sulfate scaffolds cultured with pASCs.

The elastic moduli of non-mineralized and mineralized scaffolds containing either chondroitin sulfate or heparin cultured with porcine adipose derived stem cells (ASCs) over a period of 28 days was determined in hydrated unconfined compression. Significance (*: $p < 0.05$) between indicated groups, significance (β: $p < 0.05$) of a single group between days 1 and 28, and significance (α: $p < 0.05$) between corresponding glycosaminoglycan (Col:CS vs Col:CS:CaP; Col:HP vs Col:HP:CaP) at each time poin was indicated.

CHAPTER 7

MULTI-COMPARTMENT SCAFFOLDS FOR TREATING BONE-LIGAMENT AND BONE-TENDON INTERFACES: SCAFFOLD DESIGN AND FABRICATION[6]

7.1 Overview

Previous chapters have considered monolithic non-mineral and mineralized collagen-glycosaminoglycan scaffolds for the treatment of orthopedic defects within various bones. However, many orthopedic defects either occur at or encompass the enthesis or the junction between bone and connective tissues, such as tendon or ligament. Chapter 7 of this thesis details the continued development of a multi-compartment collagen-glycosaminoglycan scaffold fabricated via a liquid phase co-synthesis technique for the treatment of orthopedic defects involving bone. Work described in this chapter combines a liquid phase co-synthesis technique to create a multi-compartment scaffold with graded mineral content, then the use of visualization via scanning electron microscopy and histological methods to assess the properties and performance of the graded materials. Additionally, the bulk mechanical properties and the local strain environment during compression were assessed in unconfined compression.

---

[6] This work is a partial adaption from the study 48. Weisgerber, D.W., et al., *The impact of discrete compartments of a multi-compartment collagen-GAG scaffold on overall construct biophysical properties.* Journal of the mechanical behavior of biomedical materials, 2013. **28**: p. 26-36. The work in Chapter 2 concludes this adaptation from the study ibid.

7.2 Introduction

In addition to the native complexities associated with recapitulating complex geometries and load bearing capacities, the difficulty in applying regenerative medicine and tissue engineering approaches is compounded by the spatial heterogeneity often encompassed by orthopedic injuries around the enthesis, or the insertion site between bone and connective tissues [227]. Some of the more common orthopedic injuries occurring at or encompassing the enthesis include tears in the anterior cruciate ligament (ACL) essential for knee alignment and function, or osteoarthritis with damage to the articular cartilage responsible for providing smooth and painless movement in joints [228, 229]. Mechanically, the enthesis between bone and tendon provides the anatomical solution to the complex physiological junction between two mechanically distinct tissues ($E_{bone} \sim 10^2 E_{tendon}$) by an equally complex interfacial zone comprised of spatially graded biochemical and microstructural components [227, 230]. The enthesis remains a common site of injury despite its complex yet efficient design, treatment of more than seventy five thousand injuries occurring at the enthesis in the United States alone remains a difficult challenge motivated by the high degree of re-failure rates after surgical intervention [231-238]. The need for regenerative medicine and tissue engineering solutions have driven the search for multi-compartment biomaterials capable of spatially guiding cellular differentiation and bioactivity towards physiologically relevant repair in each compartment at the enthesis.

While the clinical relevance of spatially distinct multi-compartment biomaterials remains dominate, the approach and characterization of such multi-compartment biomaterials remains a critical point of interest. To address these approaches, a range of biomaterial fabrication strategies include sequential dipping in mineralized solutions [239], stereolithographic and 3D-printing approaches [144, 240, 241], and the layering of hydrogel constructs [242, 243]. Previous literature has investigated the development of the collagen-glycosaminoglycan scaffolds for the treatment of injuries occurring at the dermis, peripheral nerves, cartilage, and tendon [78, 85, 97, 98], as well as the development of the mineralized collagen-

glycosaminoglycan scaffold for the treatment of orthopedic injuries [87, 88, 108, 135]. This chapter will focus on the development and characterization of a non-mineral to mineral multi-compartment collagen-glycosaminoglycan scaffold for the treatment of orthopedic injuries occurring at the enthesis.

Previous work has described the application of a liquid phase co-synthesis technique layering distinct non-mineral and mineral precursor suspensions and subsequent lyophilization to produce a highly porous (>95%) collagen-glycosaminoglycan scaffold with distinct non-mineral and mineral compartments with a gradient interface between the two for the treatment of osteochondral tissue engineering applications [89, 90]. However, none of these works examined how this fabrication process directly affected local structural and biophysical properties of the composite scaffold. The goal of this chapter was to evaluate the fabrication and characterization of microstructure, mechanical, and permeability properties of one such non-mineral to mineral multi-compartment collagen-glycosaminoglycan scaffold for the future development of *in vivo* and *in vitro* studies.

7.3 Preparation of Non-Mineral and Mineral Precursor Suspensions

Here the multi-compartment collagen-glycosaminoglycan scaffold consisted of a two compartments, non-mineral and mineral, mimicking the physiological enthesis between bone and either tendon or ligament. Here the previously described non-mineral and mineral suspensions were layered via a liquid phase co-synthesis technique previously described [89]. For comparison, monolithic non-mineral and mineralized collagen-glycosaminoglycan scaffolds were also fabricated in addition to the multi-compartment collagen-glycosaminoglycan scaffold.

As before, the non-mineralized collagen-glycosaminoglycan (CG) precursor suspension was fabricated from the homogenization of collagen and glycosaminoglycans. Briefly, type-I fibrillar collagen isolated from bovine Achilles tendon (Sigma-Aldrich, St. Louis, MO) and chondroitin sulfate isolated from shark

cartilage (Sigma-Aldrich, St. Louis, MO) was homogenized in 0.05 M acetic acid (Sigma-Aldrich, St. Louis, MO). This suspension was stored at 4°C and degassed prior to use in non-mineral CG and the multi-compartment scaffold lyophilization.

Additionally, the mineralized collagen-glycosaminoglycan (CGCaP) suspension was fabricated from the co-precipitation of collagen, glycosaminoglycans, and a calcium phosphate mineral phase as previously described. An 80 wt% mineralized collagen-glycosaminoglycan (CGCaP) precursor suspension was fabricated from the homogenization of type-I fibrillar collagen from bovine Achilles tendon (Sigma-Aldrich, St. Louis, MO), chondroitin sulfate isolated from shark cartilage (Sigma-Aldrich, St. Louis, MO), calcium hydroxide ($Ca(OH)_2$; Sigma-Aldrich, St. Louis, MO) and calcium nitrate tetra-hydrate ($Ca(NO_3)_2\ 4H_2O$; Sigma-Aldrich, St. Louis, MO) in phosphoric acid (Sigma-Aldrich, St. Louis, MO). Control over the calcium phosphate mineral phase mass yield was achieved through concurrent mapping technique dictating the calcium hydroxide to calcium nitrate tetra-hydrate molar ratio and phosphoric acid molarity [87, 107]. Similar to the non-mineral CG precursor suspension, the mineral precursor suspension was stored at 4°C and degassed prior to use in mineral CGCaP and the multi-compartment scaffold lyophilization.

7.4 Fabrication of Non-Mineral and Mineralized Collagen-Glycosaminoglycan Scaffolds

Monolithic non-mineral CG and mineral CGCaP scaffolds were fabricated from the lyophilization of the corresponding CG and CGCaP precursor suspensions. Briefly, 1 mL of the non-mineral CG and mineral CGCaP precursor suspensions were pipetted into each well of a custom polysulfone 6 well array mold (12 mm deep, 13 mm diameter, 1.5 mm thick base). Lyophilization consisted of a constant cooling rate of 1°C/min to a final freezing temperature of either -10°C or -40°C, a 175 min anneal at the final freezing temperature, and sublimation at 0°C and 200 mTorr in a Genesis freeze-dryer (VirTis, Gardener, NY).

For the monolithic non-mineral CGCaP scaffolds an extra 24 h dehydrothermal crosslinking step was performed in a vacuum oven (Welch, Niles, IL) at 105°C and <25 Torr.

7.5 Fabrication of the Non-Mineral Mineral Multi-Compartment Collagen-GAG Scaffold

The non-mineral mineral multi-compartment (CG-CGCaP) scaffold was fabricated by the liquid phase co-synthesis of a 1:1 ratio of non-mineral CG precursor suspension and mineral CGCaP precursor suspension. To start 0.5 mL of the mineral CGCaP precursor suspension was pipetted into the custom 6 well polysulfone array mold (12 mm deep, 13 mm diameter, 1.5 mm thick base). An additional 0.5 mL non-mineral CG precursor suspension was then carefully pipetted with only minimal disruption to the surface of the previously pipetted mineral CGCaP precursor suspension. A period of 20 min was then allotted for the inter-diffusion of the two precursor suspensions. The relative viscosity of the suspensions slowed the inter-diffusion creating distinct non-mineral CG and mineral CGCaP compartments with an interface between the two. Subsequent lyophilization proceeded in a Genesis freeze-dryer (VirTis, Gardener, NY) with a constant cooling rate of 1°C/min to a final freezing temperature of either -10°C or -40°C, a 175 min anneal at the final freezing temperature, and sublimation at 0°C and 200 mTorr.

7.6 Evaluation of Multi-Compartment Scaffold Microstructure

Initial verification of the multi-compartment CG-CGCaP scaffold was performed via visualization using scanning electron microscopy (SEM) and histological analysis to determine the localization of the mineral phase and the average pore size within each scaffold. The scanning electron microscopy of the interface utilized a JEOL JSM-6060LV Low Vacuum Scanning Electron Microscope (JEOL USA, Peabody, MA). Histological analysis proceeded as previously described with 6 mm cores biopsied (Integra Miltex, York, PA) from the multi-compartment CG-CGCaP scaffold and sectioned either transverse or longitudinal. These sections were then embedded in glycomethacrylate (Polysciences Inc., Warrington, PA) with

histological sectioning into 5 μm thick slices oriented in the transverse or longitudinal planes. Aniline blue (Thermo Fisher Scientific Inc, Waltham, Ma) staining then enabled the imaging of collagen struts in each section via an optical microscope (Thermo Fisher Scientific Inc, Waltham, Ma). Identification of the average pore size was accomplished from a linear intercept macro within Scion Image.

Scanning electron microscopy clearly identified the non-mineral CG and mineral CGCaP compartments within the multi-compartment CG-CGCaP scaffold and the resulting interface between the two (Figure 7.1). A qualitative investigation of the image revealed no apparent voids or points of delamination that would jeopardize scaffold integrity. The resulting average pore size of the multi-compartment scaffold was compared to the monolithic non-mineral CG and mineral CGCaP scaffold variations previously fabricated under identical conditions (Figure 2.4, Table 2.1). Within the multi-compartment CG-CGCaP, a significant ($p < 0.05$) decrease in the average pore size was observed from the non-mineral CG compartment, across the interface, and finally in the mineral CGCaP compartment was observed at a final freezing temperature of -10°C (Figure 7.2, Table 7.1). An identical non-significant trend in average pore size was also observed between the non-mineral CG, interface, and mineral CGCaP scaffold fabricated at a final freezing temperature of -40°C (Figure 7.2, Table 7.1). This apparent difference in average pore size between the non-mineral CG and mineral CGCaP compartments in the multi-compartment CG-CGCaP scaffold suggests a difference in freezing rate between the two, with the non-mineral CG compartment freezing at a slower rate. Such a difference in freezing rate is attributed to the different internal heat transfer coefficients between the non-mineral CG and mineral CGCaP precursor suspensions. Previous work with monolithic scaffold variants has identified the internal heat transfer due to the mold as dictating pore microstructure, these results suggest that the relative precursor suspension ordering within the multi-compartment CG-CGCaP scaffold significantly affects the pore microstructure. Additionally, a significant difference was observed between the non-mineral CG compartment and the monolithic non-mineral CG scaffold (Figure 7.2, Table 7.1). Here the significantly higher average pore

size in the non-mineral CG compartment can again be attributed to the slower freezing rate due to the presence of the mineral CGCaP precursor suspension and its associated internal heat transfer coefficient. This highlights the importance of both the precursor suspension and the mold internal heat transfer coefficients in multi-compartment scaffold design. In agreement with these conclusions, no significant difference in average pore size was observed between the mineral CGCaP compartment and the monolithic mineral CGCaP scaffold, as identical freezing kinetics was experienced in both situations (Figure 7.2, Table 7.1).

7.7 Quantification of Multi-Compartment Scaffold Interface via Micro-Computed Tomography

Although the interface between the non-mineral CG and mineral CGCaP compartments in the multi-compartment CG-CGCaP scaffold was previously observed via scanning electron microscopy, the width of the interface was quantified via micro-computed tomography (μCT). Micro computed tomography was performed at 25 kEv and 5 watts on a Xradia MicroXCT-400 (Xradia, Pleasanton, CA) with 1021 projections and a voxel size of 20 μm. An analysis of the voxel intensity and localization of the mineral content was performed via a custom Matlab (MathWorks, Natick, MA) program. The area of interest, 7.56 mm x 7.56 mm bounded by the surface of the multi-compartment CG-CGCaP scaffold, was selected (Figure 7.3). This square area of interest was then partitioned into 225 equally sized sections, 25 x 25 voxels, 0.25 mm^2, and the average intensity calculated within each partition. This process was then repeated throughout the image z-stack resulting in the 225 section profiles of the average intensity versus z-position, or depth. The monolithic non-mineral CG and mineral CGCaP compartment intensities were determined from the top and bottom images within the sample z-stack respectively. Image slices possessing an intensity between the monolithic non-mineral CG and mineral CGCaP mean intensities ± 3 standard deviations were taken to be part of the interfacial region.

Here visualization of the non-mineral to mineral multi-compartment CG-CGCaP scaffold was accomplished by scanning electron microscopy (Figure 7.1). Qualitative analysis of the scans clearly differentiated the individual non-mineral CG and mineral CGCaP compartment by the difference in intensity due to the presence of the mineral content. Additionally, the interface was identified as the junction between the non-mineral CG and mineral CGCaP compartments. No apparent delamination or defects, such as voids, that may act as stress concentrators and result in the mechanical failure were identified from the scan (Figure 7.1). An in depth quantitative analysis of the non-mineral to mineral multi-compartment CG-CGCaP scaffold interface was performed via micro-computed tomography (Figure 7.4). Here 225 intensity profiles were followed through the sample thickness (Figure 7.5). The average intensity of the non-mineral CG and mineral CGCaP compartments were clearly identified, with the interfacial region between the two possessing an average intensity lying between the average intensity ± 3 standard deviations of these two (Figure 7.5). Knowing the image slice location within the image z-stack, or depth within the scaffold, allows a quantification of the interface width. This analysis has identified an interfacial region of 1.9 ± 0.7 mm. This interfacial region was controlled by the degree of inter-diffusion allowed during fabrication, which in the multi-compartment scaffold fabricated by the liquid phase co-synthesis methodology can be tuned for an appropriately sized interfacial region.

7.8 Mechanical Properties of Multi-Compartment Scaffolds

The mechanical properties of the non-mineral to mineral multi-compartment CG-CGCaP scaffold was appraised via the determination of modulus following lyophilization at a final freezing temperature of -10°C and -40°C. This appraisal of the multi-compartment CG-CGCaP modulus was accomplished via unconfined compression with a MTS Insight Electromechanical load frame (MTS, Eden Prairie, MN). Unconfined compression to 0.75 strain at a rate of 1 mm/sec was performed with a 250 N load cell. Stress-strain profiles were then calculated from the resulting load-displacement via specimen height and diameter recorded via calipers prior to testing. The elastic modulus, collapse stress, and collapse strain

were then determined from the stress-strain behavior based on the low density cellular solids model. The resulting moduli were then compared to the equivalent monolithic scaffold counterparts (Figure 2.5, Table 2.1).

As in the monolithic non-mineral CG and 80 wt% mineral CGCaP scaffolds, the non-mineral to mineral multi-compartment CG-CGCaP scaffold was observed to possess the linear elastic, collapse plateau, and densification regimes observed in low density open cell foams according to cellular solids theory [142]. Statistical significance ($p < 0.05$) was observed between the monolithic non-mineral CG and mineral CGCaP scaffolds and the non-mineral to mineral multi-compartment CG-CGCaP scaffold for specimens lyophilized at a final freezing temperature of -10°C (Figure 7.6). However, no significance was detected between the monolithic non-mineral CG and non-mineral mineral multi-compartment CG-CGCaP scaffold lyophilized at -40°C (Figure 7.6). Statistic differences ($p < 0.05$) in collapse strain reflected the significant differences observed in the elastic modulus (Table 7.1). All variations were observed to possess similar collapse strains within the regime 0.07-0.14, an observation consistent with cellular solids predictions and previous results (Table 7.1) [94, 142].

7.9 Conclusions

This work evaluated the fabrication of a non-mineral mineral CG-CGCaP multi-compartment scaffold for the treatment of enthesis for orthopedic interface repair. The average pore size was observed to decrease with increasing density from the non-mineral CG compartment to the mineral CGCaP compartment. Additionally, the mechanical properties and permeability of the non-mineral mineral CG-CGCaP multi-compartment scaffold reflected those of the limiting compartment, the softer non-mineral CG compartment in both cases.

7.10 Figures and Tables

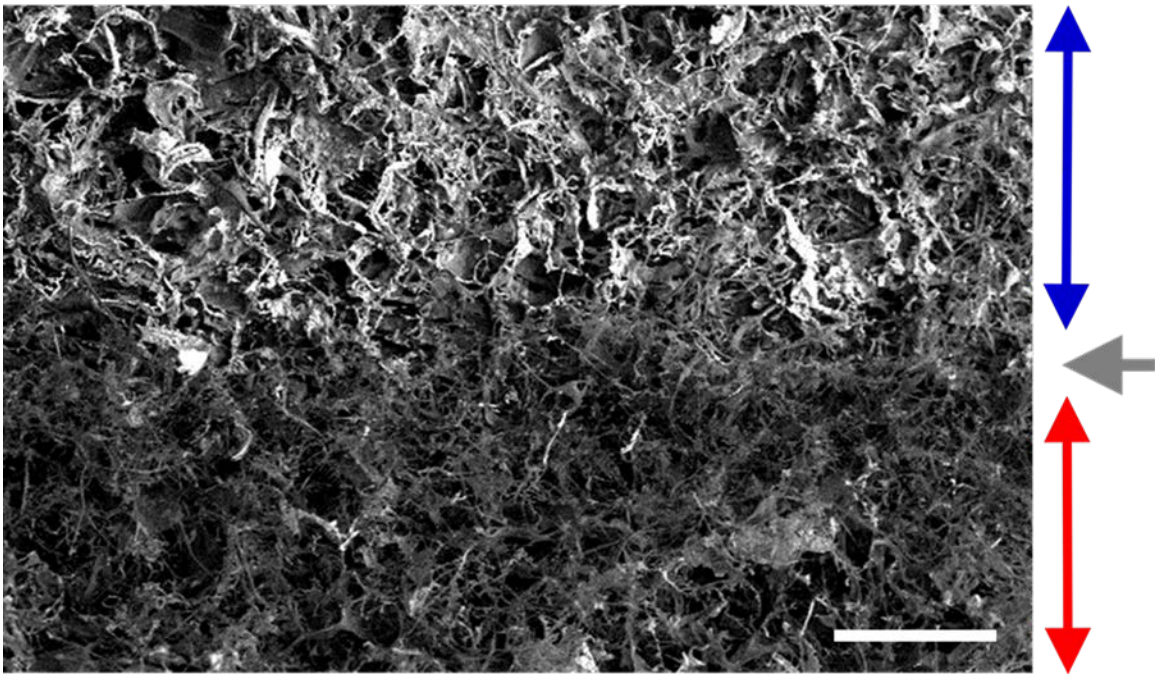

Figure 7.1 Visualization of the multi-compartment scaffold interface.

Visualization of the interface (grey arrow) between the non-mineral CG (red arrow) and mineral CGCaP (blue arrow) compartments within the CG-CGCaP multi-compartment scaffold as measured by scanning electron microscopy. Scale bar: 1mm.

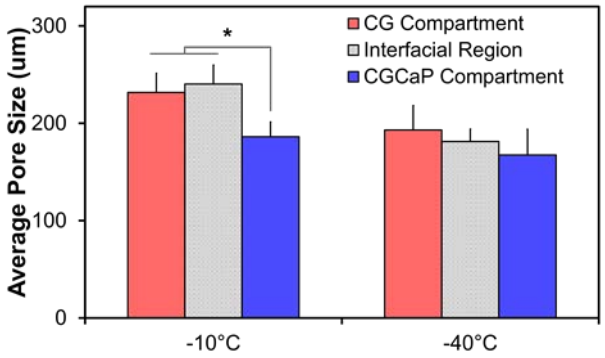

Figure 7.2 The average pore size within the multi-compartment scaffold.

The average pore size within multi-compartment scaffold divided into the CG compartment region, the interface, and the mineral CGCaP region. Pore size was determined via alanine staining of the collagen struts and a linear intercept macro. Scaffolds were fabricated at -10°C and -40°C.

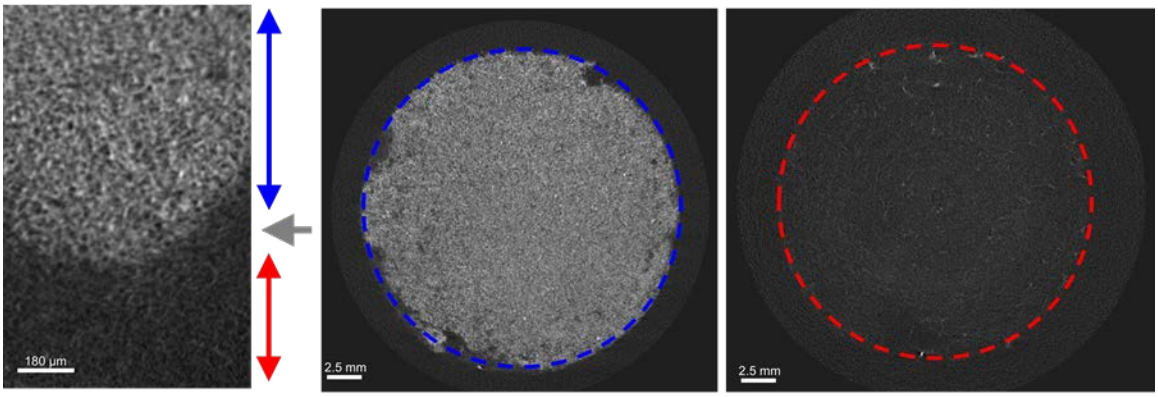

Figure 7.3 uCT with cross sections of the multi-compartment scaffold.

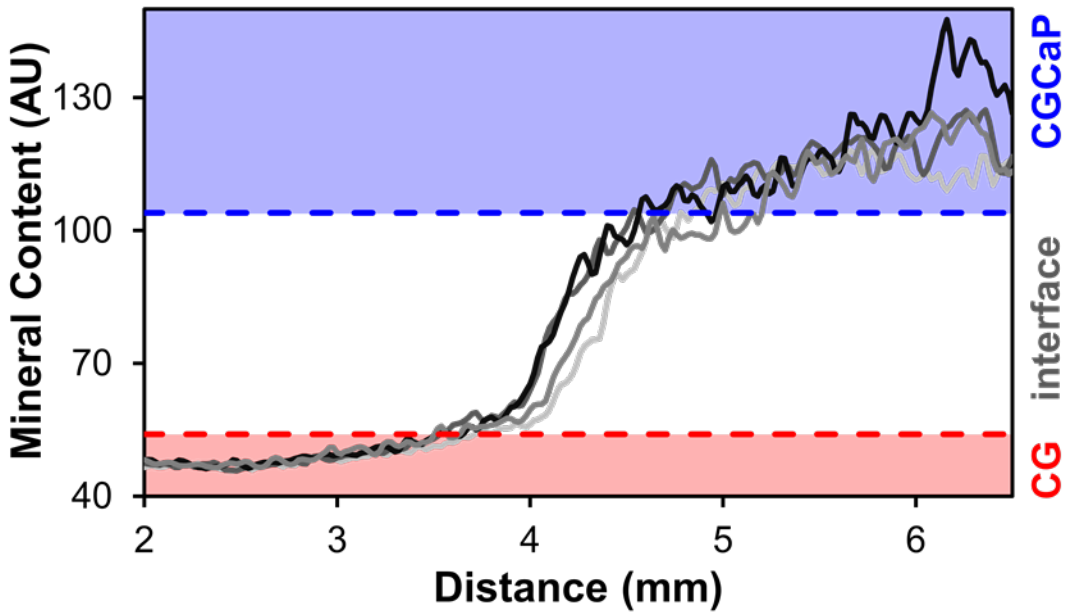

Figure 7.4 Average uCT intensity profiles across the multi-compartment scaffold interface.

Four representative average intensity profiles as a function of distance through the multi-compartment CG-CGCaP scaffold. Mineral content associated with individual non-mineral CG and mineral CGCaP compartments are representative by the red and blue regions present respectively.

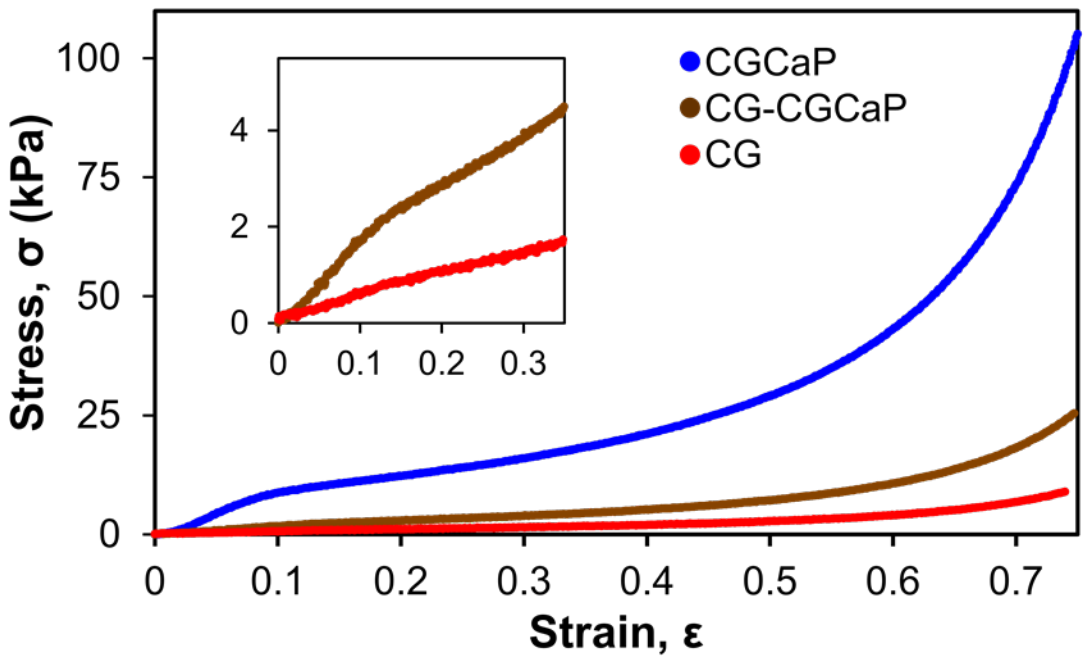

Figure 7.5 Multi-compartment scaffold stress-strain profiles observed during compression.

The stress-strain profiles of the non-mineral CG-CGCaP multi-compartment scaffold compared to the monolithic non-mineral CG and mineral CGCaP scaffolds in unconfined compression.

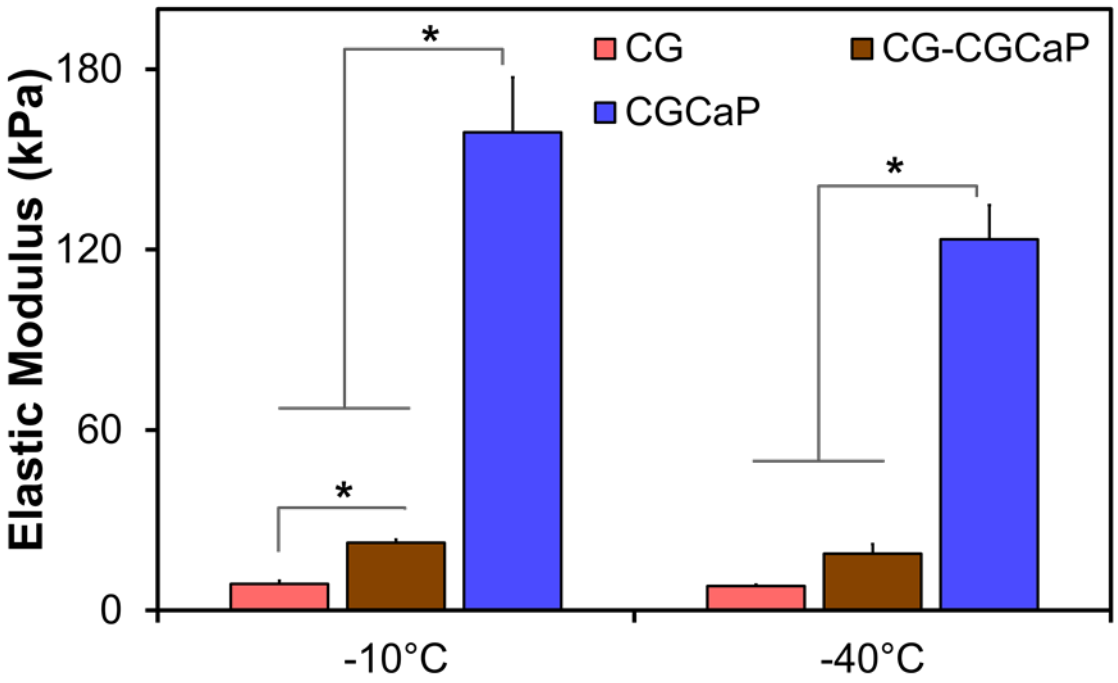

Figure 7.6 Elastic moduli of the multi-compartment scaffold.

The elastic moduli were determined from the linear elastic regime of the stress-strain profiles of the multi-compartment CG-CGCaP scaffold, the non-mineralized CG scaffold, and the mineralized CGCaP scaffold as measured in unconfined compression. With significance (*: $p < 0.05$) indicated between groups.

Table 7.1 Values for microstructure and mechanics of the multi-compartment scaffold.

	Multi-compartment CG-CGCaP scaffold					
Final freezing temperature	**-10°C**			**-40°C**		
	CG	**Inter**	**CGCaP**	**CG**	**Inter**	**CGCaP**
Average pore size (um)	232 ± 20	240 ± 19	186 ± 15	193 ± 25	181 ± 13	167 ± 26
Average pore aspect ratio	0.93 ± 0.02	0.94 ± 0.02	0.95 ± 0.02	0.94 ± 0.02	0.92 ± 0.04	0.93 ± 0.02
Elastic modulus (E; kPa)	22.5 ± 1.1			18.9 ± 3.2		
Collapse strain (ε^*_{el})	0.11 ± 0.04			0.13 ± 0.02		
Collapse stress (σ^*_{el}; kPa)	2.1 ± 0.8			2.1 ± 0.2		

Table 7.2 Values for microstructure and mechanics of the non-mineral and mineral scaffold.

	Non-mineral CG scaffold		**Mineral CGCaP scaffold**	
Final Freezing Temperature	**-10°C**	**-40°C**	**-10°C**	**-40°C**
Average pore size (μm)	163 ± 14	166 ± 56	152 ± 24	156 ± 6
Average pore aspect ratio	0.92 ± 0.03	0.92 ± 0.03	0.94 ± 0.02	0.95 ± 0.01
Elastic modulus (E; kPa)	8.8 ± 1.1	8.1 ± 0.4	159.0 ± 18.3	123.4 ± 11.3
Collapse strain (ε^*_{el})	0.09 ± 0.06	0.14 ± 0.04	0.09 ± 0.05	0.07 ± 0.03
Collapse stress (σ^*_{el}; kPa)	0.7 ± 0.4	0.9 ± 0.3	11.2 ± 2.5	7.5 ± 2.0

CHAPTER 8

SUMMARY AND FUTURE OPPORTUNITIES

8.1 Summary

This work has provided knowledge of the characterization and manipulation of the biochemical and biophysical properties of a mineralized collagen-glycosaminoglycan scaffold for the treatment of craniofacial orthopedic defects. For such injuries requiring surgical intervention, the current gold standard of treatment involves the use of either an autograft or allograft implant. However, concerns over autograft donor site morbidity, pain, and availability, along with concerns over allograft disease transmission and availability represent limitations in this field.

Following an overview of the physiological aspects and tissue engineering treatment of bone, chapter 2 highlighted the ability of the mineralized collagen-glycosaminoglycan scaffold to remain flexible in its biophysical and biochemical properties for meeting the treatment criteria imposed by both different orthopedic defects and patient specific considerations. Here the biochemical and biophysical properties implicated in influencing cellular behavior were evaluated. The amount of mineral content (40 wt% - 80 wt%) was varied within the physiological range (35 wt% - 70 wt%), with the corresponding micron-scale porous microstructure, moduli under compression, and permeability determined.

Chapter 3 evaluated the ability of the mineralized collagen-glycosaminoglycan scaffold to influence cellular behavior towards a functionally relevant physiological wound healing outcome only by the biochemical and biophysical material properties in the absence of biomolecule supplementation. Here the influence of the mineralized collagen-glycosaminoglycan scaffold on the primary stem cell population, mesenchymal stem cells, associated with the physiological bone healing process was evaluated over a 56

day *in vitro* culture period. Cellular health and activity within the collagen-glycosaminoglycan scaffolds was measured via cellular metabolic activity, while the expression of osteogenic genes was investigated with qPCR, and cellular remodeling reflected in temporal changes in mineral deposition via μCT and elastic moduli under hydrated unconfined compression.

Chapter 4 addressed the mechanical reinforcement of the mineralized collagen-glycosaminoglycan scaffold for the treatment of load bearing craniofacial defects through the development of a multi-scale mineral polycaprolactone-collagen-glycosaminoglycan composite biomaterial. Here a mechanically competent macro-porous polycaprolactone support construct was impregnated with highly bioactive micro-porous mineralized collagen-glycosaminoglycan matrix. The biophysical material properties, including the bulk elastic moduli under compression and micron-scale pore architecture, were evaluated, while initial bioactivity was demonstrated over a 24 h *in vitro* culture of an animal model inspired porcine adipose derived stem cell culture.

Chapter 5 confirmed the *in vivo* efficacy of the multi-scale polycaprolactone-collagen-glycosaminoglycan composite in a 6 week sub-critical mandibular ramus defect with a porcine animal model. Here both the mineralized collagen-glycosaminoglycan scaffold and the mineral polycaprolactone-collagen-glycosaminoglycan composite was identified to have no deleterious effect on a sub-critical mandibular ramus defect compared to the previously established polycaprolactone support construct. The evaluation of new bone formation via μCT and new bone density via DXA were used as criteria to evaluate this initial *in vivo* efficacy.

Chapter 6 evaluated the compositional flexibility of the mineralized collagen-glycosaminoglycan scaffold with the incorporation of a heparin alternative glycosaminoglycan as opposed to chondroitin sulfate. Here

the *in vitro* consequences of heparin on adipose derived stem cells was identified to promote early cellular metabolic activity compared to chondroitin sulfate.

Chapter 7 further expanded upon the previously developed multi-compartment collagen-glycosaminoglycan scaffold design for the treatment of craniofacial defects and supporting entheses by evaluating the biochemical and biophysical properties that have been identified as influencing *in vitro* and *in vivo* bioactivity. The incorporation of two distinct non-mineral and mineral compartments with a gradient interface was verified using SEM and μCT techniques, while identifying the pore microstructure and limiting compartments for mechanical properties and permeability.

Within the context of the regenerative medicine and tissue engineering, the treatment of orthopedic defects, specifically craniofacial defects, requires: (1) the flexibility in design for meeting bone, defect, and patient specific criteria; (2) guiding and supporting orthopedic repair and remodeling both *in vitro* and *in vivo*; (3) the demonstration of mechanical competence for surgical implantation and subsequent loading during *in vivo* culture. This work has demonstrated the ability of the mineralized collagen-glycosaminoglycan scaffold to meet all of these criteria. Chapters 2, 6, and 7 highlighted the flexibility of the collagen-glycosaminoglycan scaffold design. Chapter 3 identified the influence of the collagen-glycosaminoglycan scaffold biophysical and biochemical properties on mesenchymal stem cells, while chapters 4 and 5 addressed the successful reinforcement and *in vivo* implantation of the polycaprolactone-collagen-glycosaminoglycan composite biomaterial.

8.2 Outstanding Questions and Future Opportunities

The work summarized within chapters 2 through 7 has established the efficacy of the mineralized collagen-glycosaminoglycan scaffold in influencing cellular behavior via biophysical and biochemical

properties in the absence of biomolecular supplementation towards the treatment of orthopedic defects. Additionally, this work has outlined the development and *in vivo* efficacy of a multi-scale mineralized polycaprolactone-collagen-glycosaminoglycan composite for sub-critical craniofacial defects. However, future work continuing the investigation of the mineralized collagen-glycosaminoglycan platform has yet to investigate further grow factor integration, possible immunomodulatory effects, and the long-term and critical-size repair potential for craniofacial defects.

Chapter 3 and 4 established that the mineralized collagen-glycosaminoglycan scaffold and multi-scale polycaprolactone-collagen-glycosaminoglycan composite were capable of guiding cellular behavior towards an osteogenic-like phenotype in the absence of growth factor supplementation. With collaborative work elucidating an endogenous bone morphogenetic protein (BMP) feedback loop being responsible for described cellular influence. However, while not necessary, the incorporation of growth factors, such as vascular endothelial growth factor (VEGF), may serve to enhance the innate bioactivity, by enhancing early vasculogenesis. This avenue of biomolecular design represents an opportunity for the controlled tethering and subsequent release of growth factors enhancing not only the osteogenic potential, but other aspects of the physiological repair process.

Chapter 5 affirmed the *in vivo* efficacy of the mineral polycaprolactone-collagen-glycosaminoglycan composite in a sub-critical porcine mandibular ramus defect. In this study the mineral polycaprolactone-collagen-glycosaminoglycan composite and mineralized collagen-glycosaminoglycan scaffold demonstrated equivalent healing potential compared to the previously established polycaprolactone support construct for the treatment of orthopedic defects. However, a critical-size and long term assessment of *in vivo* efficacy represents the next step in biomaterial development.

Chapter 6 evaluated the potential use of heparin as an alternative glycosaminoglycan within the mineralized collagen-glycosaminoglycan scaffold design. While the chapter presented early metabolic

enhancement as a possible benefit, the effect of heparin incorporation on bone morphogenetic protein 2 sequestration and the endogenous feedback loop activation has not been investigated. This represents a potential avenue of future work evaluating the role of heparin in the mineralized scaffold variants by influencing cellular behavior through the modulation of growth factor presentation.

Finally, Chapter 7 investigated the development of a multi-compartment collagen-glycosaminoglycan scaffold for the treatment of entheses that may be involved in craniofacial defects. Additional efforts within the lab have evaluated the mechanical reinforcement of the interface and the potential for spatial differentiation along the interface of the multi-compartment scaffold. However, opportunities yet remain for the *in vivo* implantation of such scaffolds into a large animal model for treating craniofacial defects involving the enthesis.

APPENDIX A

CUSTOM MATLAB CODE WRITTEN FOR DATA ANALYSIS

A.1 Average Pore Size Analysis of Histological Samples

```
close all
clear
clc

list_input=dir;
list_output=cell(1, 1);
list_output(1) = [];
for i = 3: length(list_input)
   input_string = getfield(list_input(i), 'name');
   if ~isempty(input_string)
      if sum(input_string(length(input_string) - 3:length(input_string)) == '.tif') == 4
         list_output{length(list_output) + 1} = input_string;
      end
   end
end

for ii=1:length(list_output);

   ii
   filename=list_output{ii};

   image=imread(filename);

   SETleft=0;
   SETwidth=1;
   SETtop=0;
   SETheight=1;
   AspectRatio=1;
   scale=867;

   width=round(size(image,2)*SETwidth);
   top=round(size(image,1)*SETtop);
   height=round(size(image,1)*SETheight);
```

```
left=round(size(image,2)*SETleft);

MLxSTART=left+1;
MLxEND=left+width;
MLySTART=top+1;
MLyEND=top+height;

image=image(MLySTART:MLyEND,MLxSTART:MLxEND);

if size(gray,3)==3
   gray=double(0.3*image(:,:,1)+0.59*image(:,:,2)+0.11*image(:,:,3));
else
   gray=image;
end
gray=round(double(gray));
gray=abs(255-gray);

clear image

val=0:255;
feq=0*ones(1,256);
trigger=0;
for i=0:255
 feq(i+1)=sum(sum(gray==i));
end
for oo=(val(feq==max(feq))+1):256
   if feq(oo)<=max(feq)/2 && trigger==0
      trigger=1;
      HWHM=oo-(val(feq==max(feq))+1);
   end
end
threshold=val(feq==max(feq))+2.548*HWHM/3*12;

clear feq val trigger HWHM

binary=gray;
binary(binary<threshold)=0;
binary(binary>=threshold)=255;

binary=abs(255-binary);

clear gray
```

```
if width<height
   MinDim=width;
else
   MinDim=height;
end
ThetaStep=pi/36;

rUser1=0*ones(36,1);
rUser2=rUser1;

for j=0:1:35

   LineSum=0;
   Intercepts=0;
   x1=left;
   y1=top;
   Theta=j*ThetaStep;
   nx=10*sin(Theta)*width/height;
   ny=10*abs(cos(Theta));
   for i=0:1:nx
      if Theta==0
         x1=left;
         x2=x1+width;
      else
         x1=left+(width*i/(nx+1))+width/(2*(nx+1));
         x2=x1+(height*cos(Theta)/sin(Theta));
      end
      y2=top+height;
      if x2>=left+width
         x2=left+width;
         y2=y1+(x2-x1)*sin(Theta)/cos(Theta);
      elseif x2<left
         x2=left;
         if Theta>pi/2
            y2=y1+(x2-x1)*sin(Theta)/cos(Theta);
         end
      end
      plength=sqrt((x2-x1)^2+((y2-y1)/AspectRatio)^2);
      valx=x1;
      valy=y1;
      dx=(x2-x1)/plength;
      dy=(y2-y1)/plength;
      switchh=true;
```

```
    if plength>=MinDim
       LineSum=LineSum+(plength/scale);
       for k=0:1:plength
          if round(y1+k*dy+1)<=size(binary,1) && round(x1+k*dx+1)<=size(binary,2)
             if binary(round(y1+k*dy+1),round(x1+k*dx+1))>0
                indicator=true;
             else
                indicator=false;
             end
          end
          if switchh==true && indicator==true
             Intercepts=Intercepts+1;
             switchh=false;
          end
          if indicator==false
             switchh=true;
          end
       end
    end
end
for i=1:1:ny
    if Theta<=pi/2
       x1=left;
       x2=left+width;
    else
       x1=left+width;
       x2=left;
    end
    y1=top+height*i/(ny+1);
    y2=y1+(width*sin(Theta)/abs(cos(Theta)));
    if y2>top+height
       y2=top+height;
       x2=x1+((y2-y1)*cos(Theta)/sin(Theta));
    end
    plength=sqrt((x2-x1)^2+((y2-y1)/AspectRatio)^2);
    valx=x1;
    valy=y1;
    dx=(x2-x1)/plength;
    dy=(y2-y1)/plength;
    switchh=true;
    if plength>=MinDim
       LineSum=LineSum+(plength/scale);
       for k=0:1:plength
```

```
            if round(y1+k*dy+1)<=size(binary,1) && round(x1+k*dx+1)<=size(binary,2)
               if binary(round(y1+k*dy+1),round(x1+k*dx+1))>0
                  indicator=true;
               else
                  indicator=false;
               end
            end
            if switchh==true && indicator==true
               Intercepts=Intercepts+1;
               switchh=false;
            end
            if indicator==false
               switchh=true;
            end
         end
      end
   end
   IntLength=LineSum/Intercepts;
   rUser1(j+1)=180*Theta/pi;
   rUser2(j+1)=IntLength*1000;
end
maxdim=0;
for i=1:1:36
   if rUser2(i)>maxdim
      maxdim=rUser2(i);
   end
end
width1=400;
height1=400;
pscale=0.8*(width1+height1)/(2*maxdim);
for i=1:1:36
   dx1=pscale*0.5*rUser2(i)*cos(rUser1(i)*pi/180);
   dy1=pscale*0.5*rUser2(i)*sin(rUser1(i)*pi/180);
   if i<36
      dx2=pscale*0.5*rUser2(i+1)*cos(rUser1(i+1)*pi/180);
      dy2=pscale*0.5*rUser2(i+1)*sin(rUser1(i+1)*pi/180);
   else
      dx2=-pscale*0.5*rUser2(1)*cos(rUser1(1)*pi/180);
      dy2=-pscale*0.5*rUser2(1)*sin(rUser1(1)*pi/180);
   end
end
n=36;
sumX=0;
```

```
    sumY=0;
    sumZ=0;
    sumXY=0;
    sumYZ=0;
    sumXZ=0;
    sumZsqr=0;
    sumXsqr=0;
    for i=1:1:n
        Y=1/((rUser2(i)/2)^2);
        X=cos(2*pi*rUser1(i)/180);
        Z=sin(2*pi*rUser1(i)/180);
        sumX=sumX+X;
        sumY=sumY+Y;
        sumZ=sumZ+Z;
        sumXY=sumXY+X*Y;
        sumYZ=sumYZ+Y*Z;
        sumXZ=sumXZ+X*Z;
        sumZsqr=sumZsqr+Z^2;
        sumXsqr=sumXsqr+X^2;
    end
    C1=((sumXY*sumZsqr)-(sumXZ*sumYZ))/((sumXsqr*sumZsqr)-sumXZ^2);
    C2=((sumYZ*sumXsqr)-(sumXY*sumXZ))/((sumXsqr*sumZsqr)-sumXZ^2);
    C0=(sumY/n)-C1*(sumX/n)-C2*(sumZ/n);
    a=1/sqrt(C0+sqrt(C1^2+C2^2));
    b=sqrt(sqrt(C1^2+C2^2)/(C0*sqrt(C1^2+C2^2)+C2^2-C1^2));
    d=1.5*2*sqrt((a^2+b^2)/2);

    results(ii+1,:)={filename,threshold,C1,C2,C0,a,b,a/b,d};

end

results(1,:)={'filename','threshold','C1','C2','C0','a','b','pore aspect ratio','diameter'};

time=clock;

xlswrite(['PoreSizeAnalysis_' int2str(time(1)) '_' int2str(time(2)) '_' int2str(time(3)) '_' int2str(time(4)) '_'
int2str(time(5))],results);
```

A.2 Analysis of Mineral Deposition by Human Mesenchymal Stem Cells during *In Vitro* Culture via Micro-Computed Tomography

```
close all
clear
clc

%%% INGREDIENTS %%%

slices = 15; % Max is 225.
voxel = 16; % Voxel size in um.

filename = 'W4RG_Tomo_AreaA_Recon_Export';
filestart = 180;
fileend = 325;

%%% MAKE MATRIX %%%

time = clock;
time_label = ['_' int2str(time(1)) '_' int2str(time(2)) '_' int2str(time(3)) '_' int2str(time(4)) '_'
int2str(time(5)) '_' int2str(time(6))];

for i = filestart:fileend
   if i<10
      file = [filename '000' int2str(i)];
   elseif i<100
      file = [filename '00' int2str(i)];
   elseif i<1000
      file = [filename '0' int2str(i)];
   else
      file = [filename int2str(i)];
   end
   image = imread(file,'tif');
   if i==filestart
      matrix=0.*ones(size(image,1),size(image,2),fileend-filestart+1);
      matrix(:,:,i-filestart+1)=image(:,:,1);
   else
      matrix(:,:,i-filestart+1)=image(:,:,1);
   end
   disp([int2str(i-filestart) '/' int2str(fileend-filestart)]);
```

```
end
clear image file i

%%% DEFINING CIRCULAR LOGIC %%%

north=[];
south=[];
east=[];
west=[];
for z = 1:size(matrix,3)
   count = 1;
   crust = 0;
   while crust == 0
         if sum(matrix(count,:,z)~=0)>0
            crust = 1;
            if isempty(north)
               north = count;
            else
               north = mean([north count]);
            end
         end
      count = count+1;
   end
   count = size(matrix,1);
   crust = 0;
   while crust == 0
         if sum(matrix(count,:,z)~=0)>0
            crust = 1;
            if isempty(south)
               south = count;
            else
               south = mean([south count]);
            end
         end
      count = count-1;
   end
   count = 1;
   crust = 0;
   while crust == 0
      if sum(matrix(:,count,z)~=0)>0
         crust = 1;
         if isempty(west)
            west = count;
```

```
        else
            west = mean([west count]);
        end
    end
    count = count+1;
  end
  count = size(matrix,2);
  crust = 0;
  while crust == 0
    if sum(matrix(:,count,z)~=0)>0
        crust = 1;
        if isempty(east)
            east = count;
        else
            east = mean([east count]);
        end
    end
    count = count-1;
  end
end
center = [round(mean([north south])) round(mean([west east]))];
radius = max([center(1)-north south-center(1) center(2)-west east-center(2)]);
image = ceil(0.8.*matrix(:,:,round(size(matrix,3)/2)));
remember = image;
count = 3;
crust = 0;
while crust == 0
  if center(1)+count<=size(image,1) && center(1)-count>=1 && center(2)+count<=size(image,2) &&
center(2)-count>=1
    crust = 1;
    image(center(1)-count:center(1)+count,center(2)-count:center(2)+count)=255;
  else
    count=count-1;
  end
end
count = 3;
crust = 0;
vector = [center(1)-north south-center(1) center(2)-west east-center(2)];
while crust == 0
  if center(1)+radius+count<=size(image,1) && center(1)-radius-count>=1 &&
center(2)+radius+count<=size(image,2) && center(2)-radius-count>=1
    crust = 1;
    for theta = 0:2*pi()/180:2*pi()
```

```
        x = round(radius*cos(theta));
        y = round(radius*sin(theta));
        image(center(1)+y-count:center(1)+y+count,center(2)+x-count:center(2)+x+count)=255;
      end
   elseif count > 0
      count = count-1;
   elseif count == 0 && length(vector)>1
      count = 3;
      vector(vector == max(vector)) = [];
      radius = max(vector);
      disp('STATUS: Decreased radius.');
   else
      crust = 1;
      disp('ERROR: Radius is too big.');
   end
end
condition = 'no';
while ~strcmp(condition,'yes')
   close all;
   figure;
   imshow(image, [0 255]);
   condition = input('Is ths correct (yes or no): ','s');
   if strcmp(condition,'no')
      condition = input('What is wrong (center or radius): ','s');
      if strcmp(condition,'center')
         disp(['Current center is: ' int2str(center(1)) ',' int2str(center(2))]);
         disp(['Current radius is: ' int2str(radius)]);
         center(1) = input('Please input new row (y,1) coordinate for center: ');
         center(2) = input('Please input new column (x,2) coordinate for center: ');
      elseif strcmp(condition,'radius')
         disp(['Current center is: ' int2str(center(1)) ',' int2str(center(2))]);
         disp(['Current radius is: ' int2str(radius)]);
         radius = input('Please input new radius: ');
      end
      image = ceil(0.8.*matrix(:,:,round(size(matrix,3)/2)));
      count = 3;
      crust = 0;
      while crust == 0
         if center(1)+count<=size(image,1) && center(1)-count>=1 && center(2)+count<=size(image,2)
&& center(2)-count>=1
            crust = 1;
            image(center(1)-count:center(1)+count,center(2)-count:center(2)+count)=255;
         else
```

```
            count=count-1;
         end
      end
      count = 3;
      crust = 0;
      while crust == 0
         if center(1)+radius+count<=size(image,1) && center(1)-radius-count>=1 &&
center(2)+radius+count<=size(image,2) && center(2)-radius-count>=1
            crust = 1;
            for theta = 0:2*pi()/90:2*pi()
               x = round(radius*cos(theta));
               y = round(radius*sin(theta));
               image(center(1)+y-count:center(1)+y+count,center(2)+x-count:center(2)+x+count)=255;
            end
         elseif count > 0
            count = count-1;
         elseif count == 0
            count = 3;
            radius = input('Radius is too big. Please input new radius: ');
         end
      end
   end
end
imwrite(image,[filename '_center_and_radius_C' time_label],'gif');
clear count y x image theta crust condition vector north south east west

%%% CLEARING THE AIR %%%

air = cell(1,2);
airzone = 0.*matrix(:,:,round(size(matrix,3)/2));
for y = 1:size(airzone,1)
   for x = 1:size(airzone,2)
      if sqrt((y-center(1))^2+(x-center(2))^2)>radius
         airzone(y,x) = 1;
      end
   end
end
image = matrix(:,:,round(size(matrix,3)/2));
air{1,1} = max(max(image(airzone>0)));
air{1,2}='max';
image = image - air{1,1};
image(image<0) = 0;
```

```
disp(['Background removed: ' int2str(sum(sum(image(airzone>0)==0))) ' out of '
int2str(sum(sum(airzone==1)))]);
histogram = zeros(1,256);
count = 3;
crust = 0;
while crust == 0
   if center(1)+radius+count<=size(image,1) && center(1)-radius-count>=1 &&
center(2)+radius+count<=size(image,2) && center(2)-radius-count>=1
      crust = 1;
      for theta = 0:2*pi()/90:2*pi()
         x = round(radius*cos(theta));
         y = round(radius*sin(theta));
         image(center(1)+y-count:center(1)+y+count,center(2)+x-count:center(2)+x+count)=255;
      end
   elseif count > 0
      count = count-1;
   else
      crust = 1;
   end
end
close all
figure;
imshow(image, [0 255]);
condition = 'no';
while ~strcmp(condition,'yes')
   disp(['Current background value: ' int2str(air{1,1})]);
   condition = input('Is this correct (yes or no): ','s');
   if strcmp(condition,'no')
      image = matrix(:,:,round(size(matrix,3)/2));
      condition = input('Set air as (max, mean, custom): ','s');
      if strcmp(condition,'max')
         air{1,1} = max(max(image(airzone>0)));
         air{1,2} = 'max';
      elseif strcmp(condition,'mean')
         air{1,1} = mean(mean(image(airzone>0)));
         air{1,2} = 'mean';
      elseif strcmp(condition,'custom')
         for z = 0:255
            histogram(z+1) = sum(sum(image==z));
         end
         figure;
         plot(0:255,histogram);
         air{1,1} = input('Please input new background value: ');
```

```
        air{1,2} = 'custom';
    end
    image = image - air{1,1};
    image(image<0) = 0;
    disp(['Background removed: ' int2str(sum(sum(image(airzone>0)==0))) ' out of '
int2str(sum(sum(airzone==1)))]);
    count = 3;
    crust = 0;
    while crust == 0
        if center(1)+radius+count<=size(image,1) && center(1)-radius-count>=1 &&
center(2)+radius+count<=size(image,2) && center(2)-radius-count>=1
            crust = 1;
            for theta = 0:2*pi()/90:2*pi()
                x = round(radius*cos(theta));
                y = round(radius*sin(theta));
                image(center(1)+y-count:center(1)+y+count,center(2)+x-count:center(2)+x+count)=255;
            end
        elseif count > 0
            count = count-1;
        else
            crust = 1;
        end
    end
    close all
    figure;
    imshow(image,[0 255]);
  end
end
imwrite(image,[filename '_threshold_post_C' time_label],'gif');
image = matrix(:,:,round(size(matrix,3)/2));
image = image - air{1,1};
imwrite(image,[filename '_threshold_post' time_label],'gif');
if strcmp(air{1,2},'max')
  for z = 1:size(matrix,3)
    temporary = matrix(:,:,z);
    temporary = temporary-max(max(temporary(airzone==1)));
    matrix(:,:,z)=temporary;
  end
elseif strcmp(air{1,2},'mean')
  temporary = matrix(:,:,z);
  temporary = temporary-mean(mean(temporary(airzone==1)));
  matrix(:,:,z)=temporary;
elseif strcmp(air{1,2},'custom')
```

```
   matrix=matrix-air{1,1};
end
matrix(matrix<0) = 0;
clear crust count image y x theta histogram z condition temporary airzone

%%% REDO CIRCULAR LOGIC %%%

condition = input('Would you like to alter the radius prior to partitioning (yes or no): ','s');
if strcmp(condition,'yes')

   image = ceil(0.8.*matrix(:,:,round(size(matrix,3)/2)));
   count = 3;
   crust = 0;
   while crust == 0
      if center(1)+radius+count<=size(image,1) && center(1)-radius-count>=1 &&
center(2)+radius+count<=size(image,2) && center(2)-radius-count>=1
         crust = 1;
         for theta = 0:2*pi()/90:2*pi()
            x = round(radius*cos(theta));
            y = round(radius*sin(theta));
            image(center(1)+y-count:center(1)+y+count,center(2)+x-count:center(2)+x+count)=255;
         end
      elseif count > 0
         count = count-1;
      else
         crust = 1;
      end
   end

   condition = 'no';
   contrast = 0;
   while ~strcmp(condition,'yes')
      close all;
      figure;
      imshow(image, [0 255]);
      condition = input('Is ths correct (yes or no): ','s');
      if strcmp(condition,'no')
         condition = input('What is wrong (center, radius, or contrast): ','s');
         if strcmp(condition,'center')
            disp(['Current center is: ' int2str(center(1)) ',' int2str(center(2))]);
            disp(['Current radius is: ' int2str(radius)]);
            center(1) = input('Please input new row (y,1) coordinate for center: ');
            center(2) = input('Please input new column (x,2) coordinate for center: ');
```

```
        elseif strcmp(condition,'radius')
            disp(['Current center is: ' int2str(center(1)) ',' int2str(center(2))]);
            disp(['Current radius is: ' int2str(radius)]);
            radius = input('Please input new radius: ');
        elseif strcmp(condition,'contrast')
            contrast = 1;
        end
        if contrast == 1
            image = remember;
        else
            image = ceil(0.8.*matrix(:,:,round(size(matrix,3)/2)));
        end
        count = 3;
        crust = 0;
        while crust == 0
            if center(1)+count<=size(image,1) && center(1)-count>=1 &&
center(2)+count<=size(image,2) && center(2)-count>=1
                crust = 1;
                image(center(1)-count:center(1)+count,center(2)-count:center(2)+count)=255;
            else
                count=count-1;
            end
        end
        count = 3;
        crust = 0;
        while crust == 0
            if center(1)+radius+count<=size(image,1) && center(1)-radius-count>=1 &&
center(2)+radius+count<=size(image,2) && center(2)-radius-count>=1
                crust = 1;
                for theta = 0:2*pi()/90:2*pi()
                    x = round(radius*cos(theta));
                    y = round(radius*sin(theta));
                    image(center(1)+y-count:center(1)+y+count,center(2)+x-count:center(2)+x+count)=255;
                end
            elseif count > 0
                count = count-1;
            elseif count == 0
                count = 3;
                radius = input('Radius is too big. Please input new radius: ');
            end
        end
    end
end
```

```
   imwrite(image,[filename '_center_and_radius_C' time_label],'gif');
end

%%% TANGENTIAL PIE SLICING %%%

if slices > radius
   slices = radius;
end
zones = zeros(size(matrix,1),size(matrix,2),slices);
for y = 1:size(matrix,1)
   for x = 1:size(matrix,2)
      if sqrt((y-center(1))^2+(x-center(2))^2)<radius
         for z = 1:slices
            if sqrt((y-center(1))^2+(x-center(2))^2)>=(z-1)*radius/slices && sqrt((y-center(1))^2+(x-
center(2))^2)<z*radius/slices
               zones(y,x,z)=1;
               break
            end
         end
      end
   end
end
image = zeros(size(zones,1),size(zones,2));
for z = 1:slices
   image = image+zones(:,:,z)*round((z-1)*255/slices);
end
figure;
imshow(image,[0 255]);
imwrite(image,[filename '_slices' time_label],'gif');

image = round(0.8*matrix(:,:,round(size(matrix,3)/2)));
for z = 1:slices
   count = 1;
   crust = 0;
   filling = z/slices*radius;
   while crust == 0;
      if center(1)+filling+count<=size(image,1) && center(1)-filling-count>=1 &&
center(2)+filling+count<=size(image,2) && center(2)-filling-count>=1
         crust = 1;
         for theta = 0:2*pi()/180:2*pi()
            x = round(filling*cos(theta));
            y = round(filling*sin(theta));
            image(center(1)+y-count:center(1)+y+count,center(2)+x-count:center(2)+x+count)=255;
```

```
            end
        elseif count>0
            count = count+1;
        else
            crust = 1;
            disp(['ERROR IN CREATING ' filename '_slices_overlay']);
        end
    end
end
figure;
imshow(image,[0 255]);
imwrite(image,[filename '_slices_overlay' time_label],'gif');

clear z image y x filling crust theta count

%%% PREPARING THE PIE PAN %%%

excel = cell(size(matrix,3)+4,size(zones,3)+2);
excel{4,1} = 'File Name:';
excel{4,2} = 'Stack Distance:';
excel{3,2} = 'Radial Distance:';
for z = 1:slices
    excel{2,2+z} = ['Slice #' int2str(z)];
    excel{3,2+z} = [int2str((z-1)*radius/slices*voxel) '-' int2str(z*radius/slices*voxel) ' um'];
end
for z = filestart:filestart+size(matrix,3)-1
    if z<10
        excel{5+z-filestart,1} = [filename '000' int2str(z)];
    elseif z<100
        excel{5+z-filestart,1} = [filename '00' int2str(z)];
    elseif z<1000
        excel{5+z-filestart,1} = [filename '0' int2str(z)];
    else
        excel{5+z-filestart,1} = [filename int2str(z)];
    end
    excel{5+z-filestart,2} = [int2str((z-filestart)*voxel) ' um'];
end

%%% BAKING THE SLICED PIE %%%

for y = 1:size(matrix,3)
    for x = 1:size(zones,3)
        temporary=matrix(:,:,y).*zones(:,:,x)+zones(:,:,x)-1;
```

```
      excel{4+y,2+x}=mean(temporary(temporary>=0));
   end
end
excel{1,2}=['Variables: filename = ' filename '; filestart = ' int2str(filestart) '; fileend = ' int2str(fileend) '; slices = ' int2str(slices) '; air setting = ' air{1,2} '; air threshold = ' int2str(air{1,1}) 'center = [' int2str(center(1)) ',' int2str(center(2)) ']; radius = ' int2str(radius) ' pixels'];
time=clock;
excel{1,1}=['Time: Year = ' int2str(time(1)) '; Month = ' int2str(time(2)) '; Day = ' int2str(time(3)) '; Hour = ' int2str(time(4)) '; Minute = ' int2str(time(5)) '; Second = ' int2str(time(6))];
if slices+2<225
   xlswrite(['IMAGE_DENSITY_' int2str(time(1)) '_' int2str(time(2)) '_' int2str(time(3)) '_' int2str(time(4)) '_' int2str(time(5)) '_' int2str(time(6))],excel,1);
end
load gong;
wavplay(y,Fs);
```

A.3 Analysis of New Bone Formation in Sub-Critical Porcine Mandibular Ramus Defects during *In Vivo* Culture

```
close all
clear
clc

%%% Settings %%%

filename = input('Please input the file name without the file number (ie
pig1390_R3_Tomo_AreaA_recon2_Export0001 inputs pig1390_R3_Tomo_AreaA_recon2_Export): ','s');
filestart = input('Please input the file number associated with the first file (ie 0230 is added as 230): ');
fileend = input('Please input the file number associated with the last file (ie 0832 maybe added as 832): ');
type = input('Please input the file extension (jpeg, tif, gif, etc): ','s');
version = 'fff.1440.09092015';
font = input('Please input font for identification of ROI (2 is recommeneded): ');
parts = input('Please input the number of radial partitions (15 is recommended): ');
angles = input('Please input the number of angular partitions (18 is recommended): ');
voxel = input('Please input the voxel size in um: ');
bit_d = input('Please input the image bit depth (8 is typical): ');

%%% Select plane %%%

i = round((fileend+filestart)/2);
if i<10
   file = [filename '000' int2str(i)];
elseif i<100
   file = [filename '00' int2str(i)];
elseif i<1000
   file = [filename '0' int2str(i)];
else
   file = [filename int2str(i)];
end
image = imread(file,type);
y_size = size(image,1);
x_size = size(image,2);
z_size = fileend-filestart+1;
y_end = size(image,1);
x_end = size(image,2);
y_start = 1;
x_start = 1;
```

```
z_start = 1;
z_end = fileend-filestart+1;
YX = zeros(size(image,1),size(image,2),2);
YX(:,:,1) = image(:,:,1);
ZY = zeros(fileend-filestart+1,size(image,1),2);
ZX = zeros(fileend-filestart+1,size(image,2),2);
clear image i

for i = filestart:fileend
   if i<10
      file = [filename '000' int2str(i)];
   elseif i<100
      file = [filename '00' int2str(i)];
   elseif i<1000
      file = [filename '0' int2str(i)];
   else
      file = [filename int2str(i)];
   end
   image = imread(file,type);
   ZX(i-filestart+1,:,1) = image(round(size(image,1)/2),:,1);
   ZY(i-filestart+1,:,1) = rot90(image(:,round(size(image,2)/2),1));
   clear image
end
clear file i
ref = round(0.8*YX(:,:,1));

figure(1);
subplot(1,3,1);
subimage(YX(:,:,1),[0 2^bit_d-1]);
title('YX plane');
subplot(1,3,2);
subimage(ZY(:,:,1),[0 2^bit_d-1]);
title('ZY plane');
subplot(1,3,3);
subimage(ZX(:,:,1),[0 2^bit_d-1]);
title('ZX plane');
saveas(1,[filename '_planes.jpg']);
shg;

answer = 'figure';
while ~strcmp(answer,'yes')
   plane = input('Please select a plane to perform analysis on (YX, ZY, or ZX): ','s');
```

```
    if strcmp(answer,'figure')
        figure(2);
        answer = 'no';
    end
    if strcmp(plane,'YX')
        imshow(YX(:,:,1),[0 2^bit_d-1]);
        shg;
        answer = input('Is this correct the correct plane (yes or no): ','s');
    elseif strcmp(plane,'ZY')
        imshow(ZY(:,:,1),[0 2^bit_d-1]);
        shg;
        answer = input('Is this correct the correct plane (yes or no): ','s');
    elseif strcmp(plane,'ZX')
        imshow(ZX(:,:,1),[0 2^bit_d-1]);
        shg;
        answer = input('Is this correct the correct plane (yes or no): ','s');
    end
end
saveas(2,[filename '_planeselected.jpg']);
close all


%%%%%%%%%%%%%%%%%%%%%%%%%%%%%
%%% ALL CODING FOR ZY PLANE %%
%%%%%%%%%%%%%%%%%%%%%%%%%%%%%

%%% Select start and end %%%

if strcmp(plane,'ZY')

    figure(1);
    answer = 'no';
    while ~strcmp(answer,'yes')
        for i = filestart:fileend
            if i<10
                file = [filename '000' int2str(i)];
            elseif i<100
                file = [filename '00' int2str(i)];
            elseif i<1000
                file = [filename '0' int2str(i)];
            else
                file = [filename int2str(i)];
            end
```

```
        image = imread(file,type);
        ZY(i-filestart+1,:,1) = rot90(image(:,x_start,1));
        clear image file i
    end
    i = round((filestart+fileend)/2);
    if i<10
        file = [filename '000' int2str(i)];
    elseif i<100
        file = [filename '00' int2str(i)];
    elseif i<1000
        file = [filename '0' int2str(i)];
    else
        file = [filename int2str(i)];
    end
    image = imread(file,type);
    ref = image(:,:,1);
    clear image file i

    if x_start-font<1
        ref(:,x_start:x_start+2*font,1) = 2^bit_d-1;
    elseif x_start+font>x_size
        ref(:,x_start-2*font:x_start,1) = 2^bit_d-1;
    else
        ref(:,x_start-font:x_start+font,1) = 2^bit_d-1;
    end
    subplot(1,2,1);
    subimage(ref,[0 2^bit_d-1]);
    title('XY reference');
    subplot(1,2,2);
    subimage(ZY(:,:,1),[0 2^bit_d-1]);
    shg;
    title(['First image ' int2str(x_start)]);
    answer = input('Is this the image to start analysis on (yes or no): ','s');
    if strcmp(answer,'no')
        x_start = input(['Please select a new image to start analysis on (1 to ' int2str(x_end) '): ']);
    elseif strcmp(answer,'yes')
        saveas(1,[filename '_firstimage.jpg']);
    end
end
answer = 'no';
while ~strcmp(answer,'yes')
    for i = filestart:fileend
        if i<10
```

```
            file = [filename '000' int2str(i)];
        elseif i<100
            file = [filename '00' int2str(i)];
        elseif i<1000
            file = [filename '0' int2str(i)];
        else
            file = [filename int2str(i)];
        end
        image = imread(file,type);
        x_size = size(image,2);
        ZY(i-filestart+1,:,2) = rot90(image(:,x_end,1));
        clear image file i ref
    end
    ref = round(0.8*YX(:,:,1));
    if x_end-font<1
        ref(:,x_end:x_end+2*font,1) = 2^bit_d-1;
    elseif x_end+font>x_size
        ref(:,x_end-2*font:x_end,1) = 2^bit_d-1;
    else
        ref(:,x_end-font:x_end+font,1) = 2^bit_d-1;
    end
    subplot(1,2,1);
    subimage(ref,[0 2^bit_d-1]);
    title('XY reference');
    subplot(1,2,2);
    subimage(ZY(:,:,2),[0 2^bit_d-1]);
    title(['Last image ' int2str(x_end)]);
    shg;
    answer = input('Is this the image to end analysis on (yes or no): ','s');
    if strcmp(answer,'no')
        x_end = input(['Please select a new image to end analysis on (' int2str(x_start+1) ' to '
int2str(x_size) '): ']);
    elseif strcmp(answer,'yes')
        saveas(1,[filename '_lastimage.jpg']);
    end
end

close all
clear ref


%%% Select radius and center %%%
```

```
for i = filestart:fileend
   if i<10
      file = [filename '000' int2str(i)];
   elseif i<100
      file = [filename '00' int2str(i)];
   elseif i<1000
      file = [filename '0' int2str(i)];
   else
      file = [filename int2str(i)];
   end
   image = imread(file,type);
   ZY(i-filestart+1,:,1) = rot90(round(0.8*image(:,x_start,1)));
   ZY(i-filestart+1,:,2) = rot90(round(0.8*image(:,x_end,1)));
   clear image file i
end
center = zeros(x_size,2);
center(x_start,1) = round(size(ZY,1)/2);%%
center(x_start,2) = round(size(ZY,2)/2);%%
radius = round((sqrt(center(x_start,1)^2+center(x_start,2)^2))/2);
answer = 'no';
figure(1);
while ~strcmp(answer,'yes')
   for theta = 0:2*pi()/180:2*pi()
      y = round(radius*cos(theta))+center(x_start,2);
      z = round(radius*sin(theta))+center(x_start,1);
      if y < 1
         y = 1;
      elseif y>y_size
         y = y_size;
      end
      if z<1
         z = 1;
      elseif z>z_size
         z = z_size;
      end
      if y-font<1
         if z-font<1
            ZY(z:z+2*font,y:y+2*font,1) = 2^bit_d-1;
         elseif z+font>size(ZY,1)
            ZY(z-2*font:z,y:y+2*font,1) = 2^bit_d-1;
         else
            ZY(z-font:z+font,y:y+2*font,1) = 2^bit_d-1;
         end
```

```
    elseif y+font>size(ZY,2)
        if z-font<1
            ZY(z:z+2*font,y-2*font:y,1) = 2^bit_d-1;
        elseif z+font>size(ZY,1)
            ZY(z-2*font:z,y-2*font:y,1) = 2^bit_d-1;
        else
            ZY(z-font:z+font,y-2*font:y,1) = 2^bit_d-1;
        end
    else
        if z-font<1
            ZY(z:z+2*font,y-font:y+font,1) = 2^bit_d-1;
        elseif z+font>size(ZY,1)
            ZY(z-2*font:z,y-font:y+font,1) = 2^bit_d-1;
        else
            ZY(z-font:z+font,y-font:y+font,1,1) = 2^bit_d-1;
        end
    end
end
subplot(1,2,1);
imshow(ZY(:,:,1),[0 2^bit_d-1]);
title('First image');
subplot(1,2,2);
imshow(ZY(:,:,2),[0 2^bit_d-1]);
title('Last image');
shg;
answer = input('Is this correct (yes or no): ','s');
if strcmp(answer,'no')
    answer = input('What is wrong (center or radius): ','s');
    if strcmp(answer,'center')
        disp(['Current center is: ' int2str(center(x_start,1)) ',' int2str(center(x_start,2))]);
        disp(['Current radius is: ' int2str(radius) ' (' int2str(round(radius*voxel/1000)) ' mm)']);
        center(x_start,1) = input('Please input new row (z,1) coordinate for the center: ');
        center(x_start,2) = input('Please input new column (y,2) coordinate for the center: ');
    elseif strcmp(answer,'radius')
        disp(['Current center is: ' int2str(center(x_start,1)) ',' int2str(center(x_start,2))]);
        disp(['Current radius is: ' int2str(radius) ' (' int2str(round(radius*voxel/1000)) ' mm)']);
        radius = input('Please input new radius: ');
    end
    for i = filestart:fileend
        if i<10
            file = [filename '000' int2str(i)];
        elseif i<100
            file = [filename '00' int2str(i)];
```

```
        elseif i<1000
            file = [filename '0' int2str(i)];
        else
            file = [filename int2str(i)];
        end
        image = imread(file,type);
        ZY(i-filestart+1,:,1) = rot90(round(0.8*image(:,x_start,1)));
        clear image file i
    end

  end
end
answer = 'no';
if center(x_end,1)==0 && center(x_end,2)==0%%
  center(:,1) = center(x_start,1);%%
  center(:,2) = center(x_start,2);%%
end%%
while ~strcmp(answer,'yes')
  for theta = 0:2*pi()/180:2*pi()
    y = round(radius*cos(theta))+center(x_end,2);
    z = round(radius*sin(theta))+center(x_end,1);
    if y < 1
        y = 1;
    elseif y>y_size
        y = y_size;
    end
    if z<1
        z = 1;
    elseif z>z_size
        z = z_size;
    end
    if y-font<1
        if z-font<1
            ZY(z:z+2*font,y:y+2*font,2) = 2^bit_d-1;
        elseif z+font>size(ZY,1)
            ZY(z-2*font:z,y:y+2*font,2) = 2^bit_d-1;
        else
            ZY(z-font:z+font,y:y+2*font,2) = 2^bit_d-1;
        end
    elseif y+font>size(ZY,2)
        if z-font<1
            ZY(z:z+2*font,y-2*font:y,2) = 2^bit_d-1;
        elseif z+font>size(ZY,1)
```

```
            ZY(z-2*font:z,y-2*font:y,2) = 2^bit_d-1;
        else
            ZY(z-font:z+font,y-2*font:y,2) = 2^bit_d-1;
        end
    else
        if z-font<1
            ZY(z:z+2*font,y-font:y+font,2) = 2^bit_d-1;
        elseif z+font>size(ZY,1)
            ZY(z-2*font:z,y-font:y+font,2) = 2^bit_d-1;
        else
            ZY(z-font:z+font,y-font:y+font,2) = 2^bit_d-1;
        end
    end
end
subplot(1,2,2);
imshow(ZY(:,:,2),[0 2^bit_d-1]);
title('Last image');
shg;
answer = input('Is this correct (yes or no): ','s');
if strcmp(answer,'no')
    answer = input('What is wrong (center or radius): ','s');
    if strcmp(answer,'center')
        disp(['Current center is: ' int2str(center(x_end,1)) ',' int2str(center(x_end,2))]);
        disp(['Current radius is: ' int2str(radius) ' (' int2str(round(radius*voxel/1000)) ' mm)']);
        center(x_end,1) = input('Please input new row (z,1) coordinate for the center: ');
        center(x_end,2) = input('Please input new column (y,2) coordinate for the center: ');
    elseif strcmp(answer,'radius')
        disp(['Current center is: ' int2str(center(x_end,1)) ',' int2str(center(x_end,2))]);
        disp(['Current radius is: ' int2str(radius) ' (' int2str(round(radius*voxel/1000)) ' mm)']);
        radius = input('Please input new radius: ');
    end
    for i = filestart:fileend
        if i<10
            file = [filename '000' int2str(i)];
        elseif i<100
            file = [filename '00' int2str(i)];
        elseif i<1000
            file = [filename '0' int2str(i)];
        else
            file = [filename int2str(i)];
        end
        image = imread(file,type);
        ZY(i-filestart+1,:,2) = rot90(round(0.8*image(:,x_end,1)));
```

```
        clear image file i
      end
   end
end
saveas(1,[filename '_ROI1.jpg']);
close all

%%% Shifting ROI %%%

answer = 'no';
while ~strcmp(answer,'yes')
   z_change = (center(x_end,1)-center(x_start,1))/(x_end-x_start);
   y_change = (center(x_end,2)-center(x_start,2))/(x_end-x_start);
   x_change = 1;
   for x = 1:x_start-1
      center(x,1) = center(x_start,1)-round(z_change*(x_start-x));
      center(x,2) = center(x_start,2)-round(y_change*(x_start-x));
   end
   for x = x_start+1:x_end-1
      center(x,1) = center(x_start,1)+round(z_change*(x-x_start));
      center(x,2) = center(x_start,2)+round(y_change*(x-x_start));
   end
   for x = x_end+1:x_size
      center(x,1) = center(x_end,1)+round(z_change*(x-x_end));
      center(x,2) = center(x_end,2)+round(y_change*(x-x_end));
   end
   a = x_end-x_start;%%
   b = center(x_end,2)-center(x_start,2);%%
   c = center(x_end,1)-center(x_start,1);%%
   count = 1;
   figure(3);
   for x = x_start:round((x_end-x_start)/5):x_end
      for i = filestart:fileend
         if i<10
            file = [filename '000' int2str(i)];
         elseif i<100
            file = [filename '00' int2str(i)];
         elseif i<1000
            file = [filename '0' int2str(i)];
         else
            file = [filename int2str(i)];
         end
         image = imread(file,type);
```

```
   ZY(i-filestart+1,:,1) = rot90(round(0.8*image(:,x,1)));
   clear image file i
end
for y = 1:y_size
   for z = 1:z_size
      xo = x-x_start;%%
      yo = y-center(x_start,2);%%
      zo = z-center(x_start,1);%%
      t = acos((a*xo+b*yo+c*zo)/sqrt(a^2+b^2+c^2)/sqrt(xo^2+yo^2+zo^2));%%
      r = sqrt(xo^2+yo^2+zo^2)*sin(t);%%
      h = sqrt(xo^2+yo^2+zo^2)*cos(t);%%

      if round(r)==radius && h>=0 && h<=sqrt(a^2+b^2+c^2)
         if z-font<1
            if y-font<1
               ZY(z:z+2*font,y:y+2*font) = 2^bit_d-1;
            elseif y+font>y_size
               ZY(z:z+2*font,y-2*font:y) = 2^bit_d-1;
            else
               ZY(z:z+2*font,y-font:y+font) = 2^bit_d-1;
            end
         elseif z+font>z_size
            if y-font<1
               ZY(z-2*font:z,y:y+2*font) = 2^bit_d-1;
            elseif y+font>y_size
               ZY(z-2*font:z,y-2*font:y) = 2^bit_d-1;
            else
               ZY(z-2*font:z,y-font:y+font) = 2^bit_d-1;
            end
         else
            if y-font<1
               ZY(z-font:z+font,y:y+2*font) = 2^bit_d-1;
            elseif y+font>y_size
               ZY(z-font:z+font,y-2*font:y) = 2^bit_d-1;
            else
               ZY(z-font:z+font,y-font:y+font) = 2^bit_d-1;
            end
         end
      end
   end
end
subplot(2,3,count);
imshow(ZY(:,:,1),[0 2^bit_d-1]);
```

```
        title(['Image ' int2str(x)]);
        count = count+1;
    end
    shg;
    answer = input('Is this ROI correct for all images displaed (yes or no): ','s');
    if strcmp(answer,'no')
        answer = input('What is wrong (radius, center): ','s');
        if strcmp(answer,'radius')
            disp(['First image center is: ' int2str(center(x_start,1)) ',' int2str(center(x_start,2))]);
            disp(['Last image center is: ' int2str(center(x_end,1)) ',' int2str(center(x_end,2))]);
            disp(['Current radius is: ' int2str(radius) ' (' int2str(round(radius*voxel/1000)) ' mm)']);
            radius = input('Please input a new radius: ');
        elseif strcmp(answer,'center')
            disp(['First center is: ' int2str(center(x_start,1)) ',' int2str(center(x_start,2))]);
            disp(['Current radius is: ' int2str(radius)]);
            center(x_start,1) = input('Please input a new row (z,1) for the first image center: ');
            center(x_start,2) = input('Please input a new column (y,2) for the first image center: ');
            disp(['Last image center is: ' int2str(center(x_end,1)) ',' int2str(center(x_end,2))]);
            disp(['Current radius is: ' int2str(radius) ' (' int2str(round(radius*voxel/1000)) ' mm)']);
            center(x_end,1) = input('Please input a new row (z,1) for the last image center: ');
            center(x_end,2) = input('Please input a new column (y,2) for the last image center: ');
        end
    elseif strcmp(answer,'yes')
        saveas(3,[filename '_ROI2.jpg']);
        ostart = ['x' int2str(x_start) ',y' int2str(center(x_start,2)) ',z' int2str(center(x_start,1))];
        oend = ['x' int2str(x_end) ',y' int2str(center(x_end,2)) ',z' int2str(center(x_end,1))];
    else
        disp('Invalid input');
    end
    close all
end
o_start = x_start;
o_end = x_end;

%%% Threshold %%%

ZY = zeros(z_size,y_size,1);
threshold_in = zeros(1,2^bit_d);
threshold_all = zeros(1,2^bit_d);
for x = x_start:round((x_end-x_start)/5):x_end
    for i = filestart:fileend
        if i<10
            file = [filename '000' int2str(i)];
```

```
        elseif i<100
            file = [filename '00' int2str(i)];
        elseif i<1000
            file = [filename '0' int2str(i)];
        else
            file = [filename int2str(i)];
        end
        image = imread(file,type);
        ZY(i-filestart+1,:,1) = rot90(round(image(:,x,1)));
        clear image file i
    end
    for y = 1:y_size
        for z = 1:z_size
            threshold_all(1,ZY(z,y)+1) = threshold_all(1,ZY(z,y)+1)+1;

            xo = x-x_start;%%
            yo = y-center(x_start,2);%%
            zo = z-center(x_start,1);%%
            t = acos((a*xo+b*yo+c*zo)/sqrt(a^2+b^2+c^2)/sqrt(xo^2+yo^2+zo^2));%%
            r = sqrt(xo^2+yo^2+zo^2)*sin(t);%%
            h = sqrt(xo^2+yo^2+zo^2)*cos(t);%%

            if round(r)==radius && h>=0 && h<=sqrt(a^2+b^2+c^2)
                threshold_in(1,ZY(z,y)+1) = threshold_in(1,ZY(z,y)+1)+1;
            end
        end
    end
end

answer = 'no';
while ~strcmp(answer,'yes')
    figure(1);
    subplot(1,2,1);
    plot(0:2^bit_d-1,threshold_all)
    title('Histogram');
    subplot(1,2,2);
    plot(0:2^bit_d-1,threshold_in);
    title('ROI histogram');
    threshold = input(['Please select a threshold value (0 to ' int2str(2^bit_d-1) '): ']);
    figure(2)
    count = 1;
    for x = x_start:x_end-x_start:x_end
        for i = filestart:fileend
```

```
            if i<10
                file = [filename '000' int2str(i)];
            elseif i<100
                file = [filename '00' int2str(i)];
            elseif i<1000
                file = [filename '0' int2str(i)];
            else
                file = [filename int2str(i)];
            end
            image = imread(file,type);
            ZY(i-filestart+1,:,1) = rot90(round(image(:,x,1)));
            clear image file i
        end
        subplot(2,2,count);
        subimage(ZY,[0 2^bit_d-1]);
        title(['ZY' int2str(x)]);
        ZY(ZY<threshold) = 0;
        ZY(ZY>=threshold) = 2^bit_d-1;
        subplot(2,2,count+1);
        subimage(ZY,[0 2^bit_d-1]);
        title(['ZY' int2str(x) ' binary']);
        count = count+2;
    end
    answer = input('Is this threshold value correct (yes or no): ','s');
    if strcmp(answer,'yes')
        saveas(1,[filename '_threshold.jpg']);
        saveas(2,[filename '_binary1.jpg']);
    end
    close all
end

answer = 'no';
while ~strcmp(answer,'yes')
    count = 1;
    figure(1);
    for x = x_start:round((x_end-x_start)/5):x_end
        for i = filestart:fileend
            if i<10
                file = [filename '000' int2str(i)];
            elseif i<100
                file = [filename '00' int2str(i)];
            elseif i<1000
                file = [filename '0' int2str(i)];
```

```
            else
               file = [filename int2str(i)];
            end
            image = imread(file,type);
            ZY(i-filestart+1,:,1) = rot90(round(image(:,x,1)));
            clear image file i
        end
        subplot(2,3,count);
        ZY(ZY<threshold) = 0;
        ZY(ZY>=threshold) = 2^bit_d-1;
        subimage(ZY,[0 2^bit_d-1]);
        title(['ZY' int2str(x) ' binary']);
        count = count+1;
    end
    answer = input('Is this threshold value correct throughout the depth (yes or no): ','s');
    if strcmp(answer,'yes')
        saveas(1,[filename '_binary2.jpg']);
    elseif strcmp(answer,'no')
        figure(2);
        subplot(1,2,1);
        plot(threshold_all,0:2^bit_d-1)
        title('Histogram');
        subplot(1,2,2);
        plot(threshold_in,0:2^bit_d-1);
        title('ROI histogram');
        threshold = input(['Please select a threshold value (0 to ' int2str(2^bit_d-1) '): ']);
    end
    close all
end
clear count x ZY threshold_all threshold_in x y z xt yt zt xtt ytt ztt r d

%%% Trimming %%%

c_start = x_start;
c_end = x_end;
answer = 'no';
while ~strcmp(answer,'yes')
    YX = zeros(y_size,x_size,3);
    ZY = zeros(z_size,y_size,3);
    ZX = zeros(z_size,x_size,3);
    for i = filestart:fileend
        if i<10
            file = [filename '000' int2str(i)];
```

```
    elseif i<100
        file = [filename '00' int2str(i)];
    elseif i<1000
        file = [filename '0' int2str(i)];
    else
        file = [filename int2str(i)];
    end
    image = imread(file,type);
    ZY(i-filestart+1,:,1) = rot90(image(:,x_start,1));
    ZY(i-filestart+1,:,2) = rot90(image(:,round((x_start+x_end)/2),1));
    ZY(i-filestart+1,:,3) = rot90(image(:,x_end,1));
    ZX(i-filestart+1,:,1) = image(y_start,:,1);
    ZX(i-filestart+1,:,2) = image(round((y_start+y_end)/2),:,1);
    ZX(i-filestart+1,:,3) = image(y_end,:,1);
    clear image file i
end
count = 1;
for i = round(z_start:(z_end-z_start)/2:z_end)
    if i<10
        file = [filename '000' int2str(i)];
    elseif i<100
        file = [filename '00' int2str(i)];
    elseif i<1000
        file = [filename '0' int2str(i)];
    else
        file = [filename int2str(i)];
    end
    image = imread(file,type);
    YX(:,:,count) = image(:,:,1);
    count = count+1;
    clear image file i
end
image = YX(:,:,2);
YX(:,:,2) = YX(:,:,3);
YX(:,:,3) = image;
clear count image

a = c_end-c_start;
b = center(c_end,2)-center(c_start,2);
c = center(c_end,1)-center(c_start,1);

count = 0;
for z = round(z_start:(z_end-z_start)/2:z_end)
```

```
count = count+1;
for x = 1:x_size
   if center(x,2)-font<1
      if x-font<1
         YX(center(x,2):center(x,2)+2*font,x:x+2*font,count) = 2^bit_d-1;
      elseif x+font>x_size
         YX(center(x,2):center(x,2)+2*font,x-2*font:x,count) = 2^bit_d-1;
      else
         YX(center(x,2):center(x,2)+2*font,x-font:x+font,count) = 2^bit_d-1;
      end
   elseif center(x,2)+font>y_size
      if x-font<1
         YX(center(x,2)-2*font:center(x,2),x:x+2*font,count) = 2^bit_d-1;
      elseif x+font>x_size
         YX(center(x,2)-2*font:center(x,2),x-2*font:x,count) = 2^bit_d-1;
      else
         YX(center(x,2)-2*font:center(x,2),x-font:x+font,count) = 2^bit_d-1;
      end
   else
      if x-font<1
         YX(center(x,2)-font:center(x,2)+font,x:x+2*font,count) = 2^bit_d-1;
      elseif x+font>x_size
         YX(center(x,2)-font:center(x,2)+font,x-2*font:x,count) = 2^bit_d-1;
      else
         YX(center(x,2)-font:center(x,2)+font,x-font:x+font,count) = 2^bit_d-1;
      end
   end
   for y = 1:y_size

      xo = x-c_start;%%
      yo = y-center(c_start,2);%%
      zo = z-center(c_start,1);%%
      t = acos((a*xo+b*yo+c*zo)/sqrt(a^2+b^2+c^2)/sqrt(xo^2+yo^2+zo^2));%%
      r = sqrt(xo^2+yo^2+zo^2)*sin(t);%%
      h = sqrt(xo^2+yo^2+zo^2)*cos(t);%%

      if round(r)==radius && h>=0 && h<=sqrt(a^2+b^2+c^2)
         YX(y,x,count) = 2^bit_d-1;
      elseif round(r)>radius || h<=0 || h>sqrt(a^2+b^2+c^2)
         YX(y,x,count) = round(0.5*YX(y,x,count));
      end
   end
end
```

```
end

count = 0;
for y = round(y_start:(y_end-y_start)/2:y_end)
   count = count+1;
   for x = 1:x_size
      if center(x,1)-font<1
         if x-font<1
            ZX(center(x,1):center(x,1)+2*font,x:x+2*font,count) = 2^bit_d-1;
         elseif x+font>x_size
            ZX(center(x,1):center(x,1)+2*font,x-2*font:x,count) = 2^bit_d-1;
         else
            ZX(center(x,1):center(x,1)+2*font,x-font:x+font,count) = 2^bit_d-1;
         end
      elseif center(x,1)+font>z_size
         if x-font<1
            ZX(center(x,1)-2*font:center(x,1),x:x+2*font,count) = 2^bit_d-1;
         elseif x+font>x_size
            ZX(center(x,1)-2*font:center(x,1),x-2*font:x,count) = 2^bit_d-1;
         else
            ZX(center(x,1)-2*font:center(x,1),x-font:x+font,count) = 2^bit_d-1;
         end
      else
         if x-font<1
            ZX(center(x,1)-font:center(x,1)+font,x:x+2*font,count) = 2^bit_d-1;
         elseif x+font>x_size
            ZX(center(x,1)-font:center(x,1)+font,x-2*font:x,count) = 2^bit_d-1;
         else
            ZX(center(x,1)-font:center(x,1)+font,x-font:x+font,count) = 2^bit_d-1;
         end
      end
      for z = 1:z_size

         xo = x-c_start;%%
         yo = y-center(c_start,2);%%
         zo = z-center(c_start,1);%%
         t = acos((a*xo+b*yo+c*zo)/sqrt(a^2+b^2+c^2)/sqrt(xo^2+yo^2+zo^2));%%
         r = sqrt(xo^2+yo^2+zo^2)*sin(t);%%
         h = sqrt(xo^2+yo^2+zo^2)*cos(t);%%

         if round(r)==radius && h>=0 && h<=sqrt(a^2+b^2+c^2)
            ZX(z,x,count) = 2^bit_d-1;
         elseif round(r)>radius || h<=0 || h>sqrt(a^2+b^2+c^2)
```

```
            ZX(z,x,count) = round(0.5*ZX(z,x,count));
        end
    end
end

count = 0;
for x = round(x_start:(x_end-x_start)/2:x_end)
    count = count+1;
    if center(x,1)-font<1
        if center(x,2)-font<1
            ZY(center(x,1):center(x,1)+2*font,center(x,2):center(x,2)+2*font,count) = 2^bit_d-1;
        elseif center(x,2)+font>y_size
            ZY(center(x,1):center(x,1)+2*font,center(x,2)-2*font:center(x,2),count) = 2^bit_d-1;
        else
            ZY(center(x,1):center(x,1)+2*font,center(x,2)-font:center(x,2)+font,count) = 2^bit_d-1;
        end
    elseif center(x,1)+font>z_size
        if center(x,2)-font<1
            ZY(center(x,1)-2*font:center(x,1),center(x,2):center(x,2)+2*font,count) = 2^bit_d-1;
        elseif center(x,2)+font>y_size
            ZY(center(x,1)-2*font:center(x,1),center(x,2)-2*font:center(x,2),count) = 2^bit_d-1;
        else
            ZY(center(x,1)-2*font:center(x,1),center(x,2)-font:center(x,2)+font,count) = 2^bit_d-1;
        end
    else
        if center(x,2)-font<1
            ZY(center(x,1)-font:center(x,1)+font,center(x,2):center(x,2)+2*font,count) = 2^bit_d-1;
        elseif center(x,2)+font>y_size
            ZY(center(x,1)-font:center(x,1)+font,center(x,2)-2*font:center(x,2),count) = 2^bit_d-1;
        else
            ZY(center(x,1)-font:center(x,1)+font,center(x,2)-font:center(x,2)+font,count) = 2^bit_d-1;
        end
    end
    for y = 1:y_size
        for z = 1:z_size

            xo = x-c_start;%%
            yo = y-center(c_start,2);%%
            zo = z-center(c_start,1);%%
            t = acos((a*xo+b*yo+c*zo)/sqrt(a^2+b^2+c^2)/sqrt(xo^2+yo^2+zo^2));%%
            r = sqrt(xo^2+yo^2+zo^2)*sin(t);%%
            h = sqrt(xo^2+yo^2+zo^2)*cos(t);%%
```

```
            if round(r)==radius && h>=0 && h<=sqrt(a^2+b^2+c^2)
                ZY(z,y,count) = 2^bit_d-1;
            elseif round(r)>radius || h<=0 || h>sqrt(a^2+b^2+c^2)
                ZY(z,y,count) = round(0.5*ZY(z,y,count));
            end
        end
    end
end

for x = x_start:x_end-x_start:x_end
    if x-font<1
        YX(:,x:x+2*font,:) = 2^bit_d-1;
        ZX(:,x:x+2*font,:) = 2^bit_d-1;
    elseif x+font>x_size
        YX(:,x-2*font:x,:) = 2^bit_d-1;
        ZX(:,x-2*font:x,:) = 2^bit_d-1;
    else
        YX(:,x-font:x+font,:) = 2^bit_d-1;
        ZX(:,x-font:x+font,:) = 2^bit_d-1;
    end
end
for y = y_start:y_end-y_start:y_end
    if y-font<1
        YX(y:y+2*font,:,:) = 2^bit_d-1;
        ZY(:,y:y+2*font,:) = 2^bit_d-1;
    elseif y+font>y_size
        YX(y-2*font:y,:,:) = 2^bit_d-1;
        ZY(:,y-2*font:y,:) = 2^bit_d-1;
    else
        YX(y-font:y+font,:,:) = 2^bit_d-1;
        ZY(:,y-font:y+font,:) = 2^bit_d-1;
    end
end
for z = z_start:z_end-z_start:z_end
    if z-font<1
        ZY(z:z+2*font,:,:) = 2^bit_d-1;
        ZX(z:z+2*font,:,:) = 2^bit_d-1;
    elseif z+font>z_size
        ZY(z-2*font:z,:,:) = 2^bit_d-1;
        ZX(z-2*font:z,:,:) = 2^bit_d-1;
    else
        ZY(z-font:z+font,:,:) = 2^bit_d-1;
```

```
        ZX(z-font:z+font,:,:) = 2^bit_d-1;
    end
end

figure(1);
subplot(1,3,1);
subimage(ZX(:,:,1),[0 2^bit_d-1]);
title(['ZX ' int2str(y_start)]);
subplot(1,3,2);
subimage(ZX(:,:,2),[0 2^bit_d-1]);
title(['ZX ' int2str(round((y_end+y_start)/2))]);
subplot(1,3,3);
subimage(ZX(:,:,3),[0 2^bit_d-1]);
title(['ZX ' int2str(y_end)]);
figure(2);
subplot(1,3,1);
subimage(ZY(:,:,1),[0 2^bit_d-1]);
title(['ZY ' int2str(x_start)]);
subplot(1,3,2);
subimage(ZY(:,:,2),[0 2^bit_d-1]);
title(['ZY ' int2str(round((x_end+x_start)/2))]);
subplot(1,3,3);
subimage(ZY(:,:,3),[0 2^bit_d-1]);
title(['ZY ' int2str(x_end)]);
figure(3);
subplot(1,3,1);
subimage(YX(:,:,1),[0 2^bit_d-1]);
title(['YX ' int2str(z_start)]);
subplot(1,3,2);
subimage(YX(:,:,2),[0 2^bit_d-1]);
title(['YX ' int2str(round((z_end+z_start)/2))]);
subplot(1,3,3);
subimage(YX(:,:,3),[0 2^bit_d-1]);
title(['YX ' int2str(z_end)]);

answer = input('Is this correct (yes or no): ','s');
if strcmp(answer,'yes')
    saveas(1,[filename '_trimZX.jpg']);
    saveas(2,[filename '_trimZY.jpg']);
    saveas(3,[filename '_trimYX.jpg']);
elseif strcmp(answer,'no')
    answer = input('Change ROI cutoff (x) (yes or no): ','s');
    if strcmp(answer,'yes')
```

```
        disp(['Current ROI start (x): ' int2str(c_start)]);
        disp(['Current ROI end (x): ' int2str(c_end)]);
        c_start = input(['Input a new ROI start (1 to ' int2str(x_size) '): ']);
        c_end = input(['Input a new ROI end ' int2str(c_start+1) ' to ' int2str(x_size) '): ']);
      end
      answer = input('Change (x,y,z) scan ranges (yes or no): ','s');
      if strcmp(answer,'yes')
        disp(['Current x start: ' int2str(x_start)]);
        disp(['Current x end: ' int2str(x_end)]);
        x_start = input(['Input x start (1 to ' int2str(x_size) '): ']);
        x_end = input(['Input x end (' int2str(x_start+1) ' to ' int2str(x_size) '): ']);
        disp(['Current y start: ' int2str(y_start)]);
        disp(['Current y end: ' int2str(y_end)]);
        y_start = input(['Input y start (1 to ' int2str(y_size) '): ']);
        y_end = input(['Input y end (' int2str(y_start+1) ' to ' int2str(y_size) '): ']);
        disp(['Current z start: ' int2str(z_start)]);
        disp(['Current z end: ' int2str(z_end)]);
        z_start = input(['Input z start (1 to ' int2str(z_size) '): ']);
        z_end = input(['Input z end (' int2str(z_start+1) ' to ' int2str(z_size) '): ']);
      end
      answer = 'no';
    else
      disp('Invalid input.');
    end
end
close all

%%% Data analysis %%%

disp('Starting data analysis.');
a = c_end-c_start;
b = center(c_end,2)-center(c_start,2);
c = center(c_end,1)-center(c_start,1);
d = ceil(sqrt(a^2+b^2+c^2));

radial_data = zeros(d+1,2*parts,4);
angular_data = zeros(d+1,2*angles+1,4);
inside_data = zeros(d+1,1,4);
outside_data = zeros(d+1,1,4);

stopwatch_count = 0;
stopwatch_sum = 0;
```

```
for x = x_start:x_end
   stopwatch_start = clock;
   view = zeros(z_size,y_size,5);
   for i = filestart:fileend
      if i<10
         file = [filename '000' int2str(i)];
      elseif i<100
         file = [filename '00' int2str(i)];
      elseif i<1000
         file = [filename '0' int2str(i)];
      else
         file = [filename int2str(i)];
      end
      image = imread(file,type);
      ZY(i-filestart+1,:,1) = rot90(image(:,x,1));
      if i==round((filestart+fileend)/2)
         YX = image(:,:,1);
      end
      clear image file i
   end
   view(:,:,1) = ZY(:,:,1);
   view(:,:,3) = view(:,:,3)-1;
   for y = y_start:y_end
      for z = z_start:z_end

         xo = x-c_start;%%
         yo = y-center(c_start,2);%%
         zo = z-center(c_start,1);%%
         t = acos((a*xo+b*yo+c*zo)/sqrt(a^2+b^2+c^2)/sqrt(xo^2+yo^2+zo^2));%%
         r = sqrt(xo^2+yo^2+zo^2)*sin(t);%%
         h = sqrt(xo^2+yo^2+zo^2)*cos(t);%%

         p = atan2(z-center(x,1),y-center(x,2));%%
         if p<0
            p = 2*pi+p;
         end

         dd = round(h);
         rr = ceil(r/(radius/parts));
         pp = ceil(p/2/pi*angles);

         if r>0 && r<=radius && h>=0 && h<=sqrt(a^2+b^2+c^2) %inside ROI
```

```
    view(z,y,3) = dd;
    view(z,y,4) = 55+round(rr*200/parts);

    inside_data(dd+1,1,1) = inside_data(dd+1,1,1)+ZY(z,y);
    inside_data(dd+1,1,2) = inside_data(dd+1,1,2)+1;

    radial_data(dd+1,rr,1) = radial_data(dd+1,rr,1)+ZY(z,y);
    radial_data(dd+1,rr,2) = radial_data(dd+1,rr,2)+1;

    if r<=radius/sqrt(angles+1)
       angular_data(dd+1,1,1) = angular_data(dd+1,1,1)+ZY(z,y);
       angular_data(dd+1,1,2) = angular_data(dd+1,1,2)+1;
       view(z,y,5) = 55;
    else
       angular_data(dd+1,pp+1,1) = angular_data(dd+1,pp+1,1)+ZY(z,y);
       angular_data(dd+1,pp+1,2) = angular_data(dd+1,pp+1,2)+1;
       view(z,y,5) = 55+round(pp*200/angles);
    end

    if ZY(z,y)>=threshold
       radial_data(dd+1,rr,3) = radial_data(dd+1,rr,3)+ZY(z,y);
       radial_data(dd+1,rr,4) = radial_data(dd+1,rr,4)+1;
       inside_data(dd+1,1,4) = inside_data(dd+1,1,4)+1;
       inside_data(dd+1,1,3) = inside_data(dd+1,1,3)+ZY(z,y);
       if r<=radius/sqrt(angles+1)
          angular_data(dd+1,1,3) = angular_data(dd+1,1,3)+ZY(z,y);
          angular_data(dd+1,1,4) = angular_data(dd+1,1,4)+1;
       else
          angular_data(dd+1,pp+1,3) = angular_data(dd+1,pp+1,3)+ZY(z,y);
          angular_data(dd+1,pp+1,4) = angular_data(dd+1,pp+1,4)+1;
       end
       view(z,y,2) = 200;
    end

    if round(r)==radius
       view(z,y,2) = 255;
    end

elseif r>radius && h>=0 && h<=sqrt(a^2+b^2+c^2) && ceil(r/(radius/parts))<=2*parts

    view(z,y,4) = round(ceil((r-radius)/(radius/parts))*200/parts);
    view(z,y,5) = round(pp*200/angles);
    radial_data(dd+1,rr,1) = radial_data(dd+1,rr,1)+ZY(z,y);
```

```
            radial_data(dd+1,rr,2) = radial_data(dd+1,rr,2)+1;
            outside_data(dd+1,1,1) = outside_data(dd+1,1,1)+ZY(z,y);
            outside_data(dd+1,1,2) = outside_data(dd+1,1,2)+1;
            angular_data(dd+1,pp+angles,1) = angular_data(dd+1,pp+angles,1)+ZY(z,y);
            angular_data(dd+1,pp+angles,2) = angular_data(dd+1,pp+angles,2)+1;

            if ZY(z,y)>=threshold
               view(z,y,2) = 100;
               radial_data(dd+1,rr,3) = radial_data(dd+1,rr,3)+ZY(z,y);
               radial_data(dd+1,rr,4) = radial_data(dd+1,rr,4)+1;
               outside_data(dd+1,1,3) = outside_data(dd+1,1,3)+ZY(z,y);
               outside_data(dd+1,1,4) = outside_data(dd+1,1,4)+1;
               angular_data(dd+1,pp+angles,3) = angular_data(dd+1,pp+angles,3)+ZY(z,y);
               angular_data(dd+1,pp+angles,4) = angular_data(dd+1,pp+angles,4)+1;
            else
               view(z,y,2) = 55;
            end
         end
      end
   end
end

matrix = view(:,:,3);
if max(max(matrix))>=0
   value = [min(min(matrix(matrix>-1))) max(max(matrix))];
   matrix = matrix-min(min(matrix(matrix>-1)));
   matrix(matrix<0) = 0;
   matrix = round(matrix/max(max(matrix))*200)+55;
   view(:,:,3) = matrix;
else
   view(:,:,3) = 0;
   value = [0 0];
end
clear matrix

if x-font<1
   YX(:,x:x+2*font) = 2^bit_d-1;
elseif x+font>x_size
   YX(:,x-2*font:x) = 2^bit_d-1;
else
   YX(:,x-font:x+font) = 2^bit_d-1;
end
figure(x);
subplot(2,3,1);
```

```
        subimage(YX,[0 2^bit_d-1]);
        title(['YX ' int2str(round((filestart+fileend)/2))]);
        subplot(2,3,2);
        subimage(view(:,:,1),[0 2^bit_d-1]);
        title(['ZY ' int2str(x)]);
        subplot(2,3,3);
        subimage(view(:,:,2),[0 255]);
        title(['ZY ' int2str(x) ' binary']);
        subplot(2,3,4);
        subimage(view(:,:,3),[0 255]);
        title(['Depth: ' int2str(value(1)*voxel) '-' int2str(value(2)*voxel) ' um']);
        subplot(2,3,5);
        subimage(view(:,:,4),[0 255]);
        title(['ZY ' int2str(x) ' radial']);
        subplot(2,3,6);
        subimage(view(:,:,5),[0 255]);
        title(['ZY ' int2str(x) ' angular']);
        saveas(x,[filename '_result' int2str(x) '.jpg']);
        close all

        stopwatch_end = clock;
        stopwatch_sum = stopwatch_sum+stopwatch_end(6)-stopwatch_start(6)+stopwatch_end(5)*60-
stopwatch_start(5)*60+stopwatch_end(4)*3600-stopwatch_start(4)*3600;
        stopwatch_count = stopwatch_count+1;
        hh = floor((x_end-x)*stopwatch_sum/stopwatch_count/3600);
        mm = floor(((x_end-x)*stopwatch_sum/stopwatch_count-hh*3600)/60);
        ss = (x_end-x)*stopwatch_sum/stopwatch_count-hh*3600-mm*60;
        disp(['Approximate time remaining: ' int2str(hh) 'h ' int2str(mm) 'm ' int2str(ss) 's (status: ' int2str(x-
x_start+1) '/' int2str(x_end-x_start+1) ')'])
    end

    %%% Data write %%%

    disp('Generating excel file.');
    data_radial = cell(d+1+3,2*parts+3,3);
    data_angular = cell(d+1+3,2*angles+1+3,3);

    for k = 1:3
        data_radial{3,3,k} = 'Depth (um):';
        data_angular{3,3,k} = 'Depth (um):';
        for j = 1:d+1
            data_radial{j+3,3,k} = (j-1)*voxel;
            data_angular{j+3,3,k} = (j-1)*voxel;
```

```
    end
end

data_radial{3,1,1} = 'Outside average intensity:';
data_angular{3,1,1} = 'Outside average intensity:';
for j = 1:d+1
    data_radial{j+3,1,1} = outside_data(j,1,1)/outside_data(j,1,2);
    data_angular{j+3,1,1} = outside_data(j,1,1)/outside_data(j,1,2);
end

data_radial{3,2,1} = 'Inside average intensity:';
data_angular{3,2,1} = 'Inside average intensity:';
for j = 1:d+1
    data_radial{j+3,2,1} = inside_data(j,1,1)/inside_data(j,1,2);
    data_angular{j+3,2,1} = inside_data(j,1,1)/inside_data(j,1,2);
end

data_radial{3,1,2} = 'Outside average >threshold intensity:';
data_angular{3,1,2} = 'Outside average >threshold intensity:';
for j = 1:d+1
    data_radial{j+3,1,2} = outside_data(j,1,3)/outside_data(j,1,4);
    data_angular{j+3,1,2} = outside_data(j,1,3)/outside_data(j,1,4);
end

data_radial{3,2,2} = 'Inside average >threshold intensity:';
data_angular{3,2,2} = 'Inside average >threshold intensity:';
for j = 1:d+1
    data_radial{j+3,2,2} = inside_data(j,1,3)/inside_data(j,1,4);
    data_angular{j+3,2,2} = inside_data(j,1,3)/inside_data(j,1,4);
end

data_radial{3,1,3} = 'Outside fill fraction:';
data_angular{3,1,3} = 'Outside fill fraction:';
for j = 1:d+1
    data_radial{j+3,1,3} = outside_data(j,1,4)/outside_data(j,1,2);
    data_angular{j+3,1,3} = outside_data(j,1,4)/outside_data(j,1,2);
end

data_radial{3,2,3} = 'Inside fill fraction:';
data_angular{3,2,3} = 'Inside fill fraction:';
for j = 1:d+1
    data_radial{j+3,2,3} = inside_data(j,1,4)/inside_data(j,1,2);
    data_angular{j+3,2,3} = inside_data(j,1,4)/inside_data(j,1,2);
```

```
    end

    for i = 1:parts
        for k = 1:3
            data_radial{2,i+3,k} = ['Inside partition ' int2str(i)];
            data_radial{3,i+3,k} = [int2str((i-1)*radius/parts*voxel) ' to ' int2str(i*radius/parts*voxel) ' um'];
            data_radial{2,i+3+parts,k} = ['Outside partition ' int2str(i)];
            data_radial{3,i+3+parts,k} = [int2str((i-1)*radius/parts*voxel) ' to ' int2str(i*radius/parts*voxel) '
um'];
        end
    end
    for i = 1:2*parts
        for j = 1:d+1
            data_radial{j+3,i+3,1} = radial_data(j,i,1)/radial_data(j,i,2);
            data_radial{j+3,i+3,2} = radial_data(j,i,3)/radial_data(j,i,4);
            data_radial{j+3,i+3,3} = radial_data(j,i,4)/radial_data(j,i,2);
        end
    end

    for k = 1:3
        data_angular{2,4,k} = 'Center partition:';
        data_angular{3,4,k} =  ['0 to ' int2str(radius/sqrt(angles+1)) ' um'];
        for i = 1:angles
            data_angular{2,i+4,k} = ['Inside angle ' int2str(i)];
            data_angular{3,i+4,k} = [int2str((i-1)*360/angles) ' to ' int2str((i)*360/angles) ' deg'];
            data_angular{2,i+4+angles,k} = ['Outside angle ' int2str(i)];
            data_angular{3,i+4+angles,k} = [int2str((i-1)*360/angles) ' to ' int2str((i)*360/angles) ' deg'];
        end
    end
    for j = 1:d+1
        data_angular{j+3,4,1} = angular_data(j,1,1)/angular_data(j,1,2);
        data_angular{j+3,4,2} = angular_data(j,1,3)/angular_data(j,1,4);
        data_angular{j+3,4,3} = angular_data(j,1,4)/angular_data(j,1,2);
        for i = 1:2*angles
            data_angular{j+3,i+4,1} = angular_data(j,i+1,1)/angular_data(j,i+1,2);
            data_angular{j+3,i+4,2} = angular_data(j,i+1,3)/angular_data(j,i+1,4);
            data_angular{j+3,i+4,3} = angular_data(j,i+1,4)/angular_data(j,i+1,2);
        end
    end

    data_radial{1,1,1} = 'RADIAL (average intensity)';
    data_radial{1,1,2} = 'RADIAL (average >threshold intensity)';
    data_radial{1,1,3} = 'RADIAL (fill fraction)';
```

```
data_angular{1,1,1} = 'ANGULAR (average intensity)';
data_angular{1,1,2} = 'ANGULAR (average >threshold intensity)';
data_angular{1,1,3} = 'ANGULAR (fill fraction)';

history = cell(6,10,1);
history{1,1,1} = 'HISTORY';
history{1,3,1} = 'filename: ';
history{1,4,1} = filename;
history{1,5,1} = 'filestart: ';
history{1,6,1} = filestart;
history{1,7,1} = 'fileend: ';
history{1,8,1} = fileend;
history{1,9,1} = 'version: ';
history{1,10,1} = version;

history{2,1,1} = 'x_start:';
history{2,2,1} = x_start;
history{2,3,1} = 'x_end: ';
history{2,4,1} = x_end;
history{2,5,1} = 'x_change: ';
history{2,6,1} = x_change;
history{2,7,1} = 'x:[c_start,c_end]: ';
history{2,8,1} = ['[' int2str(c_start) ',' int2str(c_end) ']'];
history{2,9,1} = 'x_size: ';
history{2,10,1} = x_size;

history{3,1,1} = 'y_start: ';
history{3,2,1} = y_start;
history{3,3,1} = 'y_end: ';
history{3,4,1} = y_end;
history{3,5,1} = 'y_change: ';
history{3,6,1} = y_change;
history{3,7,1} = 'y:[c_start,c_end]: ';
%       history{3,8,1} = ['[' int2str(c_start) ',' int2str(c_end) ']'];
history{3,9,1} = 'y_size: ';
history{3,10,1} = y_size;

history{4,1,1} = 'z_start: ';
history{4,2,1} = z_start;
history{4,3,1} = 'z_end: ';
history{4,4,1} = z_end;
history{4,5,1} = 'z_change: ';
history{4,6,1} = z_change;
```

```
    history{4,7,1} = 'z:[c_start,c_end]: ';
    %       history{4,8,1} = ['[' int2str(c_start) ',' int2str(c_end) ']'];
    history{4,9,1} = 'z_size: ';
    history{4,10,1} = z_size;

    history{5,1,1} = 'threshold: ';
    history{5,2,1} = threshold;
    history{5,3,1} = 'radius: ';
    history{5,4,1} = radius;
    history{5,5,1} = 'type: ';
    history{5,6,1} = type;
    history{5,7,1} = 'parts: ';
    history{5,8,1} = parts;
    history{5,9,1} = 'angles: ';
    history{5,10,1} = angles;

    history{6,1,1} = 'voxel: ';
    history{6,2,1} = voxel;
    history{6,3,1} = 'bit depth: ';
    history{6,4,1} = bit_d;
    history{6,5,1} = 'plane: ';
    history{6,6,1} = plane;
    history{6,7,1} = 'start coordinates: ';
    history{6,8,1} = o_start;
    history{6,9,1} = 'end coordinates: ';
    history{6,10,1} = o_end;

    time = clock;
    data_name = [filename(1:12) '_' int2str(time(2)) int2str(time(3)) int2str(time(1)) '_' int2str(time(4))
int2str(time(5))];
    xlswrite(data_name,data_radial(:,:,1),1);
    xlswrite(data_name,data_radial(:,:,2),2);
    xlswrite(data_name,data_radial(:,:,3),3);
    xlswrite(data_name,data_angular(:,:,1),4);
    xlswrite(data_name,data_angular(:,:,2),5);
    xlswrite(data_name,data_angular(:,:,3),6);
    xlswrite(data_name,history(:,:,1),7);
    raw_name = [filename(1:5) '_RAWDATA_' int2str(time(2)) int2str(time(3)) int2str(time(1)) '_'
int2str(time(4)) int2str(time(5))];
    xlswrite(raw_name,radial_data(:,:,1),1);
    xlswrite(raw_name,radial_data(:,:,2),2);
    xlswrite(raw_name,radial_data(:,:,3),3);
    xlswrite(raw_name,radial_data(:,:,4),4);
```

```
    xlswrite(raw_name,angular_data(:,:,1),5);
    xlswrite(raw_name,angular_data(:,:,2),6);
    xlswrite(raw_name,angular_data(:,:,3),7);
    xlswrite(raw_name,angular_data(:,:,4),8);
    xlswrite(raw_name,[inside_data(:,:,1) inside_data(:,:,2) inside_data(:,:,3) inside_data(:,:,4)],9);
    xlswrite(raw_name,[outside_data(:,:,1) outside_data(:,:,2) outside_data(:,:,3) outside_data(:,:,4)],10);

    %%%%%%%%%%%%%%%%%%%%%%%%%%%%%
    %%% ALL CODING FOR ZX PLANE %%
    %%%%%%%%%%%%%%%%%%%%%%%%%%%%%

    %%% Select start and end %%%

elseif strcmp(plane,'ZX')

    figure(1);
    answer = 'no';
    while ~strcmp(answer,'yes')
        for i = filestart:fileend
            if i<10
                file = [filename '000' int2str(i)];
            elseif i<100
                file = [filename '00' int2str(i)];
            elseif i<1000
                file = [filename '0' int2str(i)];
            else
                file = [filename int2str(i)];
            end
            image = imread(file,type);
            ZX(i-filestart+1,:,1) = image(y_start,:,1);
            clear image file i
        end
        i = round((filestart+fileend)/2);
        if i<10
            file = [filename '000' int2str(i)];
        elseif i<100
            file = [filename '00' int2str(i)];
        elseif i<1000
            file = [filename '0' int2str(i)];
        else
            file = [filename int2str(i)];
        end
        image = imread(file,type);
```

```
    ref = round(0.8*image(:,:,1));
    clear image file i

    if y_start-font<1
       ref(y_start:y_start+2*font,:,1) = 2^bit_d-1;
    elseif y_start+font>y_size
       ref(y_start-2*font:y_start,:,1) = 2^bit_d-1;
    else
       ref(y_start-font:y_start+font,:,1) = 2^bit_d-1;
    end
    subplot(1,2,1);
    subimage(ref,[0 2^bit_d-1]);
    title('XY reference');
    subplot(1,2,2);
    subimage(ZX(:,:,1),[0 2^bit_d-1]);
    shg;
    title(['First image ' int2str(y_start)]);
    answer = input('Is this the image to start analysis on (yes or no): ','s');
    if strcmp(answer,'no')
       y_start = input(['Please select a new image to start analysis on (1 to ' int2str(y_end) '): ']);
    elseif strcmp(answer,'yes')
       saveas(1,[filename '_firstimage.jpg']);
    end
end
answer = 'no';
while ~strcmp(answer,'yes')
    for i = filestart:fileend
       if i<10
          file = [filename '000' int2str(i)];
       elseif i<100
          file = [filename '00' int2str(i)];
       elseif i<1000
          file = [filename '0' int2str(i)];
       else
          file = [filename int2str(i)];
       end
       image = imread(file,type);
       ZX(i-filestart+1,:,2) = image(y_end,:,1);
       clear image file i ref
    end
    i = round((filestart+fileend)/2);
    if i<10
       file = [filename '000' int2str(i)];
```

```
        elseif i<100
            file = [filename '00' int2str(i)];
        elseif i<1000
            file = [filename '0' int2str(i)];
        else
            file = [filename int2str(i)];
        end
        image = imread(file,type);
        ref = round(0.8*image(:,:,1));
        clear image file i

        if y_end-font<1
            ref(y_end:y_end+2*font,:,1) = 2^bit_d-1;
        elseif y_end+font>y_size
            ref(y_end-2*font:y_end,:,1) = 2^bit_d-1;
        else
            ref(y_end-font:y_end+font,:,1) = 2^bit_d-1;
        end
        subplot(1,2,1);
        subimage(ref,[0 2^bit_d-1]);
        title('XY reference');
        subplot(1,2,2);
        subimage(ZX(:,:,2),[0 2^bit_d-1]);
        title(['Last image ' int2str(y_end)]);
        shg;
        answer = input('Is this the image to end analysis on (yes or no): ','s');
        if strcmp(answer,'no')
            y_end = input(['Please select a new image to end analysis on (' int2str(y_start+1) ' to '
int2str(y_size) '): ']);
        elseif strcmp(answer,'yes')
            saveas(1,[filename '_lastimage.jpg']);
        end
    end

    close all
    clear ref


    %%% Select radius and center %%%

    for i = filestart:fileend
        if i<10
            file = [filename '000' int2str(i)];
```

```
    elseif i<100
        file = [filename '00' int2str(i)];
    elseif i<1000
        file = [filename '0' int2str(i)];
    else
        file = [filename int2str(i)];
    end
    image = imread(file,type);
    ZX(i-filestart+1,:,1) = rot90(round(0.8*image(y_start,:,1)));
    ZX(i-filestart+1,:,2) = rot90(round(0.8*image(y_end,:,1)));
    clear image file i
end
center = zeros(y_size,2);
center(y_start,1) = round(size(ZX,1)/2);%%
center(y_start,2) = round(size(ZX,2)/2);%%
radius = round((sqrt(center(y_start,1)^2+center(y_start,2)^2))/2);
answer = 'no';
figure(1);
while ~strcmp(answer,'yes')
    for theta = 0:2*pi()/180:2*pi()
        x = round(radius*cos(theta))+center(y_start,2);
        z = round(radius*sin(theta))+center(y_start,1);
        if x < 1
            x = 1;
        elseif x>x_size
            x = x_size;
        end
        if z<1
            z = 1;
        elseif z>z_size
            z = z_size;
        end
        if x-font<1
            if z-font<1
                ZX(z:z+2*font,x:x+2*font,1) = 2^bit_d-1;
            elseif z+font>size(ZX,1)
                ZX(z-2*font:z,x:x+2*font,1) = 2^bit_d-1;
            else
                ZX(z-font:z+font,x:x+2*font,1) = 2^bit_d-1;
            end
        elseif x+font>size(ZX,2)
            if z-font<1
                ZX(z:z+2*font,x-2*font:x,1) = 2^bit_d-1;
```

```
      elseif z+font>size(ZX,1)
         ZX(z-2*font:z,x-2*font:x,1) = 2^bit_d-1;
      else
         ZX(z-font:z+font,x-2*font:x,1) = 2^bit_d-1;
      end
   else
      if z-font<1
         ZX(z:z+2*font,x-font:x+font,1) = 2^bit_d-1;
      elseif z+font>size(ZX,1)
         ZX(z-2*font:z,x-font:x+font,1) = 2^bit_d-1;
      else
         ZX(z-font:z+font,x-font:x+font,1,1) = 2^bit_d-1;
      end
   end
end
subplot(1,2,1);
imshow(ZX(:,:,1),[0 2^bit_d-1]);
title('First image');
subplot(1,2,2);
imshow(ZX(:,:,2),[0 2^bit_d-1]);
title('Last image');
shg;
answer = input('Is this correct (yes or no): ','s');
if strcmp(answer,'no')
   answer = input('What is wrong (center or radius): ','s');
   if strcmp(answer,'center')
      disp(['Current center is: ' int2str(center(y_start,1)) ',' int2str(center(y_start,2))]);
      disp(['Current radius is: ' int2str(radius) ' (' int2str(round(radius*voxel/1000)) ' mm)']);
      center(y_start,1) = input('Please input new row (z,1) coordinate for the center: ');
      center(y_start,2) = input('Please input new column (y,2) coordinate for the center: ');
   elseif strcmp(answer,'radius')
      disp(['Current center is: ' int2str(center(y_start,1)) ',' int2str(center(y_start,2))]);
      disp(['Current radius is: ' int2str(radius) ' (' int2str(round(radius*voxel/1000)) ' mm)']);
      radius = input('Please input new radius: ');
   end
   for i = filestart:fileend
      if i<10
         file = [filename '000' int2str(i)];
      elseif i<100
         file = [filename '00' int2str(i)];
      elseif i<1000
         file = [filename '0' int2str(i)];
      else
```

```
            file = [filename int2str(i)];
        end
        image = imread(file,type);
        ZX(i-filestart+1,:,1) = round(0.8*image(y_start,:,1));
        clear image file i
    end

  end
end
answer = 'no';
if center(y_end,1)==0 && center(y_end,2)==0%%
  center(:,1) = center(y_start,1);%%
  center(:,2) = center(y_start,2);%%
end%%
while ~strcmp(answer,'yes')
  for theta = 0:2*pi()/180:2*pi()
    x = round(radius*cos(theta))+center(y_end,2);
    z = round(radius*sin(theta))+center(y_end,1);
    if x < 1
      x = 1;
    elseif x>x_size
      x = x_size;
    end
    if z<1
      z = 1;
    elseif z>z_size
      z = z_size;
    end
    if x-font<1
      if z-font<1
        ZX(z:z+2*font,x:x+2*font,2) = 2^bit_d-1;
      elseif z+font>size(ZX,1)
        ZX(z-2*font:z,x:x+2*font,2) = 2^bit_d-1;
      else
        ZX(z-font:z+font,x:x+2*font,2) = 2^bit_d-1;
      end
    elseif x+font>size(ZX,2)
      if z-font<1
        ZX(z:z+2*font,x-2*font:x,2) = 2^bit_d-1;
      elseif z+font>size(ZX,1)
        ZX(z-2*font:z,x-2*font:x,2) = 2^bit_d-1;
      else
        ZX(z-font:z+font,x-2*font:x,2) = 2^bit_d-1;
```

```
        end
    else
        if z-font<1
            ZX(z:z+2*font,x-font:x+font,2) = 2^bit_d-1;
        elseif z+font>size(ZX,1)
            ZX(z-2*font:z,x-font:x+font,2) = 2^bit_d-1;
        else
            ZX(z-font:z+font,x-font:x+font,2) = 2^bit_d-1;
        end
    end
end
subplot(1,2,2);
imshow(ZX(:,:,2),[0 2^bit_d-1]);
title('Last image');
shg;
answer = input('Is this correct (yes or no): ','s');
if strcmp(answer,'no')
    answer = input('What is wrong (center or radius): ','s');
    if strcmp(answer,'center')
        disp(['Current center is: ' int2str(center(y_end,1)) ',' int2str(center(y_end,2))]);
        disp(['Current radius is: ' int2str(radius) ' (' int2str(round(radius*voxel/1000)) ' mm)']);
        center(y_end,1) = input('Please input new row (z,1) coordinate for the center: ');
        center(y_end,2) = input('Please input new column (y,2) coordinate for the center: ');
    elseif strcmp(answer,'radius')
        disp(['Current center is: ' int2str(center(y_end,1)) ',' int2str(center(y_end,2))]);
        disp(['Current radius is: ' int2str(radius) ' (' int2str(round(radius*voxel/1000)) ' mm)']);
        radius = input('Please input new radius: ');
    end
    for i = filestart:fileend
        if i<10
            file = [filename '000' int2str(i)];
        elseif i<100
            file = [filename '00' int2str(i)];
        elseif i<1000
            file = [filename '0' int2str(i)];
        else
            file = [filename int2str(i)];
        end
        image = imread(file,type);
        ZX(i-filestart+1,:,2) = round(0.8*image(y_end,:,1));
        clear image file i
    end
end
```

```
end
saveas(1,[filename '_ROI1.jpg']);
close all

%%% Shifting ROI %%%

answer = 'no';
while ~strcmp(answer,'yes')
   z_change = (center(y_end,1)-center(y_start,1))/(y_end-y_start);
   x_change = (center(y_end,2)-center(y_start,2))/(y_end-y_start);
   y_change = 1;
   for y = 1:y_start-1
      center(y,1) = center(y_start,1)-round(z_change*(y_start-y));
      center(y,2) = center(y_start,2)-round(x_change*(y_start-y));
   end
   for y = y_start+1:y_end-1
      center(y,1) = center(y_start,1)+round(z_change*(y-y_start));
      center(y,2) = center(y_start,2)+round(x_change*(y-y_start));
   end
   for y = y_end+1:y_size
      center(y,1) = center(y_end,1)+round(z_change*(y-y_end));
      center(y,2) = center(y_end,2)+round(x_change*(y-y_end));
   end
   b = y_end-y_start;%%
   a = center(y_end,2)-center(y_start,2);%%
   c = center(y_end,1)-center(y_start,1);%%
   count = 1;
   figure(3);
   for y = y_start:round((y_end-y_start)/5):y_end
      for i = filestart:fileend
         if i<10
            file = [filename '000' int2str(i)];
         elseif i<100
            file = [filename '00' int2str(i)];
         elseif i<1000
            file = [filename '0' int2str(i)];
         else
            file = [filename int2str(i)];
         end
         image = imread(file,type);
         ZX(i-filestart+1,:,1) = round(0.8*image(y,:,1));
         clear image file i
      end
```

```
    for x = 1:x_size
        for z = 1:z_size
            yo = y-y_start;%%
            xo = x-center(y_start,2);%%
            zo = z-center(y_start,1);%%
            t = acos((a*xo+b*yo+c*zo)/sqrt(a^2+b^2+c^2)/sqrt(xo^2+yo^2+zo^2));%%
            r = sqrt(xo^2+yo^2+zo^2)*sin(t);%%
            h = sqrt(xo^2+yo^2+zo^2)*cos(t);%%

            if round(r)==radius && h>=0 && h<=sqrt(a^2+b^2+c^2)
                if z-font<1
                    if y-font<1
                        ZX(z:z+2*font,x:x+2*font) = 2^bit_d-1;
                    elseif x+font>x_size
                        ZX(z:z+2*font,x-2*font:x) = 2^bit_d-1;
                    else
                        ZX(z:z+2*font,x-font:x+font) = 2^bit_d-1;
                    end
                elseif z+font>z_size
                    if x-font<1
                        ZX(z-2*font:z,x:x+2*font) = 2^bit_d-1;
                    elseif x+font>x_size
                        ZX(z-2*font:z,x-2*font:x) = 2^bit_d-1;
                    else
                        ZX(z-2*font:z,x-font:x+font) = 2^bit_d-1;
                    end
                else
                    if x-font<1
                        ZX(z-font:z+font,x:x+2*font) = 2^bit_d-1;
                    elseif x+font>x_size
                        ZX(z-font:z+font,x-2*font:x) = 2^bit_d-1;
                    else
                        ZX(z-font:z+font,x-font:x+font) = 2^bit_d-1;
                    end
                end
            end
        end
    end
    subplot(2,3,count);
    imshow(ZX(:,:,1),[0 2^bit_d-1]);
    title(['Image ' int2str(y)]);
    count = count+1;
end
```

```
    shg;
    answer = input('Is this ROI correct for all images displaed (yes or no): ','s');
    if strcmp(answer,'no')
        answer = input('What is wrong (radius, center): ','s');
        if strcmp(answer,'radius')
            disp(['First image center is: ' int2str(center(y_start,1)) ',' int2str(center(y_start,2))]);
            disp(['Last image center is: ' int2str(center(y_end,1)) ',' int2str(center(y_end,2))]);
            disp(['Current radius is: ' int2str(radius) ' (' int2str(round(radius*voxel/1000)) ' mm)']);
            radius = input('Please input a new radius: ');
        elseif strcmp(answer,'center')
            disp(['First center is: ' int2str(center(y_start,1)) ',' int2str(center(y_start,2))]);
            disp(['Current radius is: ' int2str(radius)]);
            center(y_start,1) = input('Please input a new row (z,1) for the first image center: ');
            center(y_start,2) = input('Please input a new column (x,2) for the first image center: ');
            disp(['Last image center is: ' int2str(center(y_end,1)) ',' int2str(center(y_end,2))]);
            disp(['Current radius is: ' int2str(radius) ' (' int2str(round(radius*voxel/1000)) ' mm)']);
            center(y_end,1) = input('Please input a new row (z,1) for the last image center: ');
            center(y_end,2) = input('Please input a new column (x,2) for the last image center: ');
        end
    elseif strcmp(answer,'yes')
        saveas(3,[filename '_ROI2.jpg']);
        o_start = ['x' int2str(center(y_start,2)) ',y' int2str(y_start) ',z' int2str(center(y_start,1))];
        o_end = ['x' int2str(center(y_end,2)) ',y' int2str(y_end) ',z' int2str(center(y_end,1))];
    else
        disp('Invalid input');
    end
    close all
end

%%% Threshold %%%

ZX = zeros(z_size,x_size,1);
threshold_in = zeros(1,2^bit_d);
threshold_all = zeros(1,2^bit_d);
for y = round(y_start:(y_end-y_start)/5:y_end)
    for i = filestart:fileend
        if i<10
            file = [filename '000' int2str(i)];
        elseif i<100
            file = [filename '00' int2str(i)];
        elseif i<1000
            file = [filename '0' int2str(i)];
        else
```

```
            file = [filename int2str(i)];
        end
        image = imread(file,type);
        ZX(i-filestart+1,:,1) = round(image(y,:,1));
        clear image file i
    end
    for x = 1:x_size
        for z = 1:z_size
            threshold_all(1,ZX(z,x)+1) = threshold_all(1,ZX(z,x)+1)+1;

            yo = y-y_start;%%
            xo = x-center(y_start,2);%%
            zo = z-center(y_start,1);%%
            t = acos((a*xo+b*yo+c*zo)/sqrt(a^2+b^2+c^2)/sqrt(xo^2+yo^2+zo^2));%%
            r = sqrt(xo^2+yo^2+zo^2)*sin(t);%%
            h = sqrt(xo^2+yo^2+zo^2)*cos(t);%%

            if round(r)==radius && h>=0 && h<=sqrt(a^2+b^2+c^2)
                threshold_in(1,ZX(z,x)+1) = threshold_in(1,ZX(z,x)+1)+1;
            end
        end
    end
end

answer = 'no';
while ~strcmp(answer,'yes')
    figure(1);
    subplot(1,2,1);
    plot(0:2^bit_d-1,threshold_all)
    title('Histogram');
    subplot(1,2,2);
    plot(0:2^bit_d-1,threshold_in);
    title('ROI histogram');
    threshold = input(['Please select a threshold value (0 to ' int2str(2^bit_d-1) '): ']);
    figure(2)
    count = 1;
    for y = y_start:y_end-y_start:y_end
        for i = filestart:fileend
            if i<10
                file = [filename '000' int2str(i)];
            elseif i<100
                file = [filename '00' int2str(i)];
            elseif i<1000
```

```
            file = [filename '0' int2str(i)];
        else
            file = [filename int2str(i)];
        end
        image = imread(file,type);
        ZX(i-filestart+1,:,1) = round(image(y,:,1));
        clear image file i
    end
    subplot(2,2,count);
    subimage(ZX,[0 2^bit_d-1]);
    title(['ZX' int2str(y)]);
    ZX(ZX<threshold) = 0;
    ZX(ZX>=threshold) = 2^bit_d-1;
    subplot(2,2,count+1);
    subimage(ZX,[0 2^bit_d-1]);
    title(['ZX' int2str(y) ' binary']);
    count = count+2;
  end
  answer = input('Is this threshold value correct (yes or no): ','s');
  if strcmp(answer,'yes')
    saveas(1,[filename '_threshold.jpg']);
    saveas(2,[filename '_binary1.jpg']);
  end
  close all
end

answer = 'no';
while ~strcmp(answer,'yes')
  count = 1;
  figure(1);
  for y = round(y_start:(y_end-y_start)/5:y_end)
    for i = filestart:fileend
      if i<10
        file = [filename '000' int2str(i)];
      elseif i<100
        file = [filename '00' int2str(i)];
      elseif i<1000
        file = [filename '0' int2str(i)];
      else
        file = [filename int2str(i)];
      end
      image = imread(file,type);
      ZX(i-filestart+1,:,1) = round(image(y,:,1));
```

```
        clear image file i
    end
    subplot(2,3,count);
    ZX(ZX<threshold) = 0;
    ZX(ZX>=threshold) = 2^bit_d-1;
    subimage(ZX,[0 2^bit_d-1]);
    title(['ZX' int2str(y) ' binary']);
    count = count+1;
  end
  answer = input('Is this threshold value correct throughout the depth (yes or no): ','s');
  if strcmp(answer,'yes')
    saveas(1,[filename '_binary2.jpg']);
  elseif strcmp(answer,'no')
    figure(2);
    subplot(1,2,1);
    plot(threshold_all,0:2^bit_d-1)
    title('Histogram');
    subplot(1,2,2);
    plot(threshold_in,0:2^bit_d-1);
    title('ROI histogram');
    threshold = input(['Please select a threshold value (0 to ' int2str(2^bit_d-1) '): ']);
  end
  close all
end
clear count x ZY threshold_all threshold_in x y z xt yt zt xtt ytt ztt r d

%%% Trimming %%%

c_start = y_start;
c_end = y_end;
answer = 'no';
while ~strcmp(answer,'yes')
  YX = zeros(y_size,x_size,3);
  ZY = zeros(z_size,y_size,3);
  ZX = zeros(z_size,x_size,3);
  for i = filestart:fileend
    if i<10
      file = [filename '000' int2str(i)];
    elseif i<100
      file = [filename '00' int2str(i)];
    elseif i<1000
      file = [filename '0' int2str(i)];
    else
```

```
        file = [filename int2str(i)];
    end
    image = imread(file,type);
    ZY(i-filestart+1,:,1) = rot90(image(:,x_start,1));
    ZY(i-filestart+1,:,2) = rot90(image(:,round((x_start+x_end)/2),1));
    ZY(i-filestart+1,:,3) = rot90(image(:,x_end,1));
    ZX(i-filestart+1,:,1) = image(y_start,:,1);
    ZX(i-filestart+1,:,2) = image(round((y_start+y_end)/2),:,1);
    ZX(i-filestart+1,:,3) = image(y_end,:,1);
    clear image file i
end
count = 1;
for i = round(z_start:(z_end-z_start)/2:z_end)
    if i<10
        file = [filename '000' int2str(i)];
    elseif i<100
        file = [filename '00' int2str(i)];
    elseif i<1000
        file = [filename '0' int2str(i)];
    else
        file = [filename int2str(i)];
    end
    image = imread(file,type);
    YX(:,:,count) = image(:,:,1);
    count = count+1;
    clear image file i
end
image = YX(:,:,2);
YX(:,:,2) = YX(:,:,3);
YX(:,:,3) = image;
clear count image

b = c_end-c_start;
a = center(c_end,2)-center(c_start,2);
c = center(c_end,1)-center(c_start,1);

count = 1;
for z = round(z_start:(z_end-z_start)/2:z_end)
    for y = 1:y_size
        if center(y,2)-font<1
            if y-font<1
                YX(y:y+2*font,center(y,2):center(y,2)+2*font,count) = 2^bit_d-1;
            elseif y+font>y_size
```

```
            YX(y-2*font:y,center(y,2):center(y,2)+2*font,count) = 2^bit_d-1;
        else
            YX(y-font:y+font,center(y,2):center(y,2)+2*font,count) = 2^bit_d-1;
        end
    elseif center(y,2)+font>x_size
        if y-font<1
            YX(y:y+2*font,center(y,2)-2*font:center(y,2),count) = 2^bit_d-1;
        elseif y+font>y_size
            YX(y-2*font:y,center(y,2)-2*font:center(y,2),count) = 2^bit_d-1;
        else
            YX(y-font:y+font,center(y,2)-2*font:center(y,2),count) = 2^bit_d-1;
        end
    else
        if y-font<1
            YX(y:y+2*font,center(y,2)-font:center(y,2)+font,count) = 2^bit_d-1;
        elseif y+font>y_size
            YX(y-2*font:y,center(y,2)-font:center(y,2)+font,count) = 2^bit_d-1;
        else
            YX(y-font:y+font,center(y,2)-font:center(y,2)+font,count) = 2^bit_d-1;
        end
    end
    for x = 1:x_size

        yo = y-c_start;%%
        xo = x-center(c_start,2);%%
        zo = z-center(c_start,1);%%
        t = acos((a*xo+b*yo+c*zo)/sqrt(a^2+b^2+c^2)/sqrt(xo^2+yo^2+zo^2));%%
        r = sqrt(xo^2+yo^2+zo^2)*sin(t);%%
        h = sqrt(xo^2+yo^2+zo^2)*cos(t);%%

        if round(r)==radius && h>=0 && h<=sqrt(a^2+b^2+c^2)
            YX(y,x,count) = 2^bit_d-1;
        elseif round(r)>radius || h<=0 || h>sqrt(a^2+b^2+c^2)
            YX(y,x,count) = round(0.5*YX(y,x,count));
        end
    end
  end
  count = count+1;
end

count = 1;
for y = round(y_start:(y_end-y_start)/2:y_end)
```

```
if center(y,1)-font<1
   if center(y,2)-font<1
      ZX(center(y,1):center(y,1)+2*font,center(y,2):center(y,2)+2*font,count) = 2^bit_d-1;
   elseif center(y,2)+font>x_size
      ZX(center(y,1):center(y,1)+2*font,center(y,2)-2*font:center(y,2),count) = 2^bit_d-1;
   else
      ZX(center(y,1):center(y,1)+2*font,center(y,2)-font:center(y,2)+font,count) = 2^bit_d-1;
   end
elseif center(y,1)+font>z_size
   if center(y,2)-font<1
      ZX(center(y,1)-2*font:center(y,1),center(y,2):center(y,2)+2*font,count) = 2^bit_d-1;
   elseif center(y,2)+font>x_size
      ZX(center(y,1)-2*font:center(y,1),center(y,2)-2*font:center(y,2),count) = 2^bit_d-1;
   else
      ZX(center(y,1)-2*font:center(y,1),center(y,2)-font:center(y,2)+font,count) = 2^bit_d-1;
   end
else
   if center(y,2)-font<1
      ZX(center(y,1)-font:center(y,1)+font,center(y,2):center(y,2)+2*font,count) = 2^bit_d-1;
   elseif center(y,2)+font>x_size
      ZX(center(y,1)-font:center(y,1)+font,center(y,2)-2*font:center(y,2),count) = 2^bit_d-1;
   else
      ZX(center(y,1)-font:center(y,1)+font,center(y,2)-font:center(y,2)+font,count) = 2^bit_d-1;
   end
end
for x = 1:x_size
   for z = 1:z_size

      yo = y-c_start;%%
      xo = x-center(c_start,2);%%
      zo = z-center(c_start,1);%%
      t = acos((a*xo+b*yo+c*zo)/sqrt(a^2+b^2+c^2)/sqrt(xo^2+yo^2+zo^2));%%
      r = sqrt(xo^2+yo^2+zo^2)*sin(t);%%
      h = sqrt(xo^2+yo^2+zo^2)*cos(t);%%

      if round(r)==radius && h>=0 && h<=sqrt(a^2+b^2+c^2)
         ZX(z,x,count) = 2^bit_d-1;
      elseif round(r)>radius || h<=0 || h>sqrt(a^2+b^2+c^2)
         ZX(z,x,count) = round(0.5*ZX(z,x,count));
      end
   end
end
count = count+1;
```

```
end

count = 1;
for x = round(x_start:(x_end-x_start)/2:x_end)
   for y = 1:y_size
      if center(y,1)-font<1
         if y-font<1
            ZY(center(y,1):center(y,1)+2*font,y:y+2*font,count) = 2^bit_d-1;
         elseif y+font>y_size
            ZY(center(y,1):center(y,1)+2*font,y-2*font:y,count) = 2^bit_d-1;
         else
            ZY(center(y,1):center(y,1)+2*font,y-font:y+font,count) = 2^bit_d-1;
         end
      elseif center(y,1)+font>z_size
         if y-font<1
            ZY(center(y,1)-2*font:center(y,1),y:y+2*font,count) = 2^bit_d-1;
         elseif y+font>y_size
            ZY(center(y,1)-2*font:center(y,1),y-2*font:y,count) = 2^bit_d-1;
         else
            ZY(center(y,1)-2*font:center(y,1),y-font:y+font,count) = 2^bit_d-1;
         end
      else
         if y-font<1
            ZY(center(y,1)-font:center(y,1)+font,y:y+2*font,count) = 2^bit_d-1;
         elseif y+font>y_size
            ZY(center(y,1)-font:center(y,1)+font,y-2*font:y,count) = 2^bit_d-1;
         else
            ZY(center(y,1)-font:center(y,1)+font,y-font:y+font,count) = 2^bit_d-1;
         end
      end

      for z = 1:z_size

         yo = y-c_start;%%
         xo = x-center(c_start,2);%%
         zo = z-center(c_start,1);%%
         t = acos((a*xo+b*yo+c*zo)/sqrt(a^2+b^2+c^2)/sqrt(xo^2+yo^2+zo^2));%%
         r = sqrt(xo^2+yo^2+zo^2)*sin(t);%%
         h = sqrt(xo^2+yo^2+zo^2)*cos(t);%%

         if round(r)==radius && h>=0 && h<=sqrt(a^2+b^2+c^2)
            ZY(z,y,count) = 2^bit_d-1;
         elseif round(r)>radius || h<=0 || h>sqrt(a^2+b^2+c^2)
```

```
            ZY(z,y,count) = round(0.5*ZY(z,y,count));
        end

    end
  end
  count = count+1;
end

for x = x_start:x_end-x_start:x_end
  if x-font<1
    YX(:,x:x+2*font,:) = 2^bit_d-1;
    ZX(:,x:x+2*font,:) = 2^bit_d-1;
  elseif x+font>x_size
    YX(:,x-2*font:x,:) = 2^bit_d-1;
    ZX(:,x-2*font:x,:) = 2^bit_d-1;
  else
    YX(:,x-font:x+font,:) = 2^bit_d-1;
    ZX(:,x-font:x+font,:) = 2^bit_d-1;
  end
end
for y = y_start:y_end-y_start:y_end
  if y-font<1
    YX(y:y+2*font,:,:) = 2^bit_d-1;
    ZY(:,y:y+2*font,:) = 2^bit_d-1;
  elseif y+font>y_size
    YX(y-2*font:y,:,:) = 2^bit_d-1;
    ZY(:,y-2*font:y,:) = 2^bit_d-1;
  else
    YX(y-font:y+font,:,:) = 2^bit_d-1;
    ZY(:,y-font:y+font,:) = 2^bit_d-1;
  end
end
for z = z_start:z_end-z_start:z_end
  if z-font<1
    ZY(z:z+2*font,:,:) = 2^bit_d-1;
    ZX(z:z+2*font,:,:) = 2^bit_d-1;
  elseif z+font>z_size
    ZY(z-2*font:z,:,:) = 2^bit_d-1;
    ZX(z-2*font:z,:,:) = 2^bit_d-1;
  else
    ZY(z-font:z+font,:,:) = 2^bit_d-1;
    ZX(z-font:z+font,:,:) = 2^bit_d-1;
  end
```

```
end

figure(1);
subplot(1,3,1);
subimage(ZX(:,:,1),[0 2^bit_d-1]);
title(['ZX ' int2str(y_start)]);
subplot(1,3,2);
subimage(ZX(:,:,2),[0 2^bit_d-1]);
title(['ZX ' int2str(round((y_end+y_start)/2))]);
subplot(1,3,3);
subimage(ZX(:,:,3),[0 2^bit_d-1]);
title(['ZX ' int2str(y_end)]);
figure(2);
subplot(1,3,1);
subimage(ZY(:,:,1),[0 2^bit_d-1]);
title(['ZY ' int2str(x_start)]);
subplot(1,3,2);
subimage(ZY(:,:,2),[0 2^bit_d-1]);
title(['ZY ' int2str(round((x_end+x_start)/2))]);
subplot(1,3,3);
subimage(ZY(:,:,3),[0 2^bit_d-1]);
title(['ZY ' int2str(x_end)]);
figure(3);
subplot(1,3,1);
subimage(YX(:,:,1),[0 2^bit_d-1]);
title(['YX ' int2str(z_start)]);
subplot(1,3,2);
subimage(YX(:,:,2),[0 2^bit_d-1]);
title(['YX ' int2str(round((z_end+z_start)/2))]);
subplot(1,3,3);
subimage(YX(:,:,3),[0 2^bit_d-1]);
title(['YX ' int2str(z_end)]);

answer = input('Is this correct (yes or no): ','s');
if strcmp(answer,'yes')
   saveas(1,[filename '_trimZX.jpg']);
   saveas(2,[filename '_trimZY.jpg']);
   saveas(3,[filename '_trimYX.jpg']);
elseif strcmp(answer,'no')
   answer = input('Change ROI cutoff (y) (yes or no): ','s');
   if strcmp(answer,'yes')
      disp(['Current ROI start (y): ' int2str(c_start)]);
      disp(['Current ROI end (y): ' int2str(c_end)]);
```

```
        c_start = input(['Input a new ROI start (1 to ' int2str(y_size) '): ']);
        c_end = input(['Input a new ROI end ' int2str(c_start+1) ' to ' int2str(y_size) '): ']);
      end
      answer = input('Change (x,y,z) scan ranges (yes or no): ','s');
      if strcmp(answer,'yes')
        disp(['Current x start: ' int2str(x_start)]);
        disp(['Current x end: ' int2str(x_end)]);
        x_start = input(['Input x start (1 to ' int2str(x_size) '): ']);
        x_end = input(['Input x end (' int2str(x_start+1) ' to ' int2str(x_size) '): ']);
        disp(['Current y start: ' int2str(y_start)]);
        disp(['Current y end: ' int2str(y_end)]);
        y_start = input(['Input y start (1 to ' int2str(y_size) '): ']);
        y_end = input(['Input y end (' int2str(y_start+1) ' to ' int2str(y_size) '): ']);
        disp(['Current z start: ' int2str(z_start)]);
        disp(['Current z end: ' int2str(z_end)]);
        z_start = input(['Input z start (1 to ' int2str(z_size) '): ']);
        z_end = input(['Input z end (' int2str(z_start+1) ' to ' int2str(z_size) '): ']);
      end
      answer = 'no';
    else
      disp('Invalid input.');
    end
end
close all

%%% Data analysis %%%

disp('Starting data analysis.');
b = c_end-c_start;
a = center(c_end,2)-center(c_start,2);
c = center(c_end,1)-center(c_start,1);
d = ceil(sqrt(a^2+b^2+c^2));

radial_data = zeros(d+1,2*parts,4);
angular_data = zeros(d+1,2*angles+1,4);
inside_data = zeros(d+1,1,4);
outside_data = zeros(d+1,1,4);

stopwatch_count = 0;
stopwatch_sum = 0;

for y = y_start:y_end
    stopwatch_start = clock;
```

```
view = zeros(z_size,x_size,5);
for i = filestart:fileend
   if i<10
      file = [filename '000' int2str(i)];
   elseif i<100
      file = [filename '00' int2str(i)];
   elseif i<1000
      file = [filename '0' int2str(i)];
   else
      file = [filename int2str(i)];
   end
   image = imread(file,type);
   ZX(i-filestart+1,:,1) = image(y,:,1);
   if i==round((filestart+fileend)/2)
      YX = image(:,:,1);
   end
   clear image file i
end
view(:,:,1) = ZX(:,:,1);
view(:,:,3) = view(:,:,3)-1;
for x = x_start:x_end
   for z = z_start:z_end

      yo = y-c_start;%%
      xo = x-center(c_start,2);%%
      zo = z-center(c_start,1);%%
      t = acos((a*xo+b*yo+c*zo)/sqrt(a^2+b^2+c^2)/sqrt(xo^2+yo^2+zo^2));%%
      r = sqrt(xo^2+yo^2+zo^2)*sin(t);%%
      h = sqrt(xo^2+yo^2+zo^2)*cos(t);%%

      p = atan2(z-center(y,1),x-center(y,2));%%
      if p<0
         p = 2*pi+p;
      end

      dd = round(h);
      rr = ceil(r/(radius/parts));
      pp = ceil(p/2/pi*angles);

      if r>0 && r<=radius && h>=0 && h<=sqrt(a^2+b^2+c^2) %inside ROI

         view(z,x,3) = dd;
         view(z,x,4) = 55+round(rr*200/parts);
```

```
    inside_data(dd+1,1,1) = inside_data(dd+1,1,1)+ZX(z,x);
    inside_data(dd+1,1,2) = inside_data(dd+1,1,2)+1;

    radial_data(dd+1,rr,1) = radial_data(dd+1,rr,1)+ZX(z,x);
    radial_data(dd+1,rr,2) = radial_data(dd+1,rr,2)+1;

    if r<=radius/sqrt(angles+1)
       angular_data(dd+1,1,1) = angular_data(dd+1,1,1)+ZX(z,x);
       angular_data(dd+1,1,2) = angular_data(dd+1,1,2)+1;
       view(z,x,5) = 55;
    else
       angular_data(dd+1,pp+1,1) = angular_data(dd+1,pp+1,1)+ZX(z,x);
       angular_data(dd+1,pp+1,2) = angular_data(dd+1,pp+1,2)+1;
       view(z,x,5) = 55+round(pp*200/angles);
    end

    if ZX(z,x)>=threshold
       radial_data(dd+1,rr,3) = radial_data(dd+1,rr,3)+ZX(z,x);
       radial_data(dd+1,rr,4) = radial_data(dd+1,rr,4)+1;
       inside_data(dd+1,1,4) = inside_data(dd+1,1,4)+1;
       inside_data(dd+1,1,3) = inside_data(dd+1,1,3)+ZX(z,x);
       if r<=radius/sqrt(angles+1)
          angular_data(dd+1,1,3) = angular_data(dd+1,1,3)+ZX(z,x);
          angular_data(dd+1,1,4) = angular_data(dd+1,1,4)+1;
       else
          angular_data(dd+1,pp+1,3) = angular_data(dd+1,pp+1,3)+ZX(z,x);
          angular_data(dd+1,pp+1,4) = angular_data(dd+1,pp+1,4)+1;
       end
       view(z,x,2) = 200;
    end

    if round(r)==radius
       view(z,x,2) = 255;
    end

elseif r>radius && h>=0 && h<=sqrt(a^2+b^2+c^2) && ceil(r/(radius/parts))<=2*parts

    view(z,x,4) = round(ceil((r-radius)/(radius/parts))*200/parts);
    view(z,x,5) = round(pp*200/angles);
    radial_data(dd+1,rr,1) = radial_data(dd+1,rr,1)+ZX(z,x);
    radial_data(dd+1,rr,2) = radial_data(dd+1,rr,2)+1;
    outside_data(dd+1,1,1) = outside_data(dd+1,1,1)+ZX(z,x);
```

```
            outside_data(dd+1,1,2) = outside_data(dd+1,1,2)+1;
            angular_data(dd+1,pp+angles,1) = angular_data(dd+1,pp+angles,1)+ZX(z,x);
            angular_data(dd+1,pp+angles,2) = angular_data(dd+1,pp+angles,2)+1;

            if ZX(z,x)>=threshold
               view(z,x,2) = 100;
               radial_data(dd+1,rr,3) = radial_data(dd+1,rr,3)+ZX(z,x);
               radial_data(dd+1,rr,4) = radial_data(dd+1,rr,4)+1;
               outside_data(dd+1,1,3) = outside_data(dd+1,1,3)+ZX(z,x);
               outside_data(dd+1,1,4) = outside_data(dd+1,1,4)+1;
               angular_data(dd+1,pp+angles,3) = angular_data(dd+1,pp+angles,3)+ZX(z,x);
               angular_data(dd+1,pp+angles,4) = angular_data(dd+1,pp+angles,4)+1;
            else
               view(z,x,2) = 55;
            end
         end
      end
   end
end

matrix = view(:,:,3);
if max(max(matrix))>=0
   value = [min(min(matrix(matrix>-1))) max(max(matrix))];
   matrix = matrix-min(min(matrix(matrix>-1)));
   matrix(matrix<0) = 0;
   matrix = round(matrix/max(max(matrix))*200)+55;
   view(:,:,3) = matrix;
else
   view(:,:,3) = 0;
   value = [0 0];
end
clear matrix

if y-font<1
   YX(y:y+2*font,:) = 2^bit_d-1;
elseif y+font>y_size
   YX(y-2*font:y,:) = 2^bit_d-1;
else
   YX(y-font:y+font,:) = 2^bit_d-1;
end
figure(y);
subplot(2,3,1);
subimage(YX,[0 2^bit_d-1]);
title(['YX ' int2str(round((filestart+fileend)/2))]);
```

```
        subplot(2,3,2);
        subimage(view(:,:,1),[0 2^bit_d-1]);
        title(['ZX ' int2str(y)]);
        subplot(2,3,3);
        subimage(view(:,:,2),[0 255]);
        title(['ZX ' int2str(y) ' binary']);
        subplot(2,3,4);
        subimage(view(:,:,3),[0 255]);
        title(['Depth: ' int2str(value(1)) '-' int2str(value(2))]);
        subplot(2,3,5);
        subimage(view(:,:,4),[0 255]);
        title(['ZX ' int2str(y) ' angular']);
        subplot(2,3,6);
        subimage(view(:,:,5),[0 255]);
        title(['ZX ' int2str(y) ' radial']);
        saveas(y,[filename '_result' int2str(y) '.jpg']);
        close all

        stopwatch_end = clock;
        stopwatch_sum = stopwatch_sum+stopwatch_end(6)-stopwatch_start(6)+stopwatch_end(5)*60-
stopwatch_start(5)*60+stopwatch_end(4)*3600-stopwatch_start(4)*3600;
        stopwatch_count = stopwatch_count+1;
        hh = floor((y_end-y)*stopwatch_sum/stopwatch_count/3600);
        mm = floor(((y_end-y)*stopwatch_sum/stopwatch_count-hh*3600)/60);
        ss = (y_end-y)*stopwatch_sum/stopwatch_count-hh*3600-mm*60;
        disp(['Approximate time remaining: ' int2str(hh) 'h ' int2str(mm) 'm ' int2str(ss) 's (status: ' int2str(y-
y_start+1) '/' int2str(y_end-y_start+1) ')'])
    end

    %%% Data write %%%

    disp('Generating excel file.');
    data_radial = cell(d+1+3,2*parts+3,3);
    data_angular = cell(d+1+3,2*angles+1+3,3);

    for k = 1:3
        data_radial{3,3,k} = 'Depth (um):';
        data_angular{3,3,k} = 'Depth (um):';
        for j = 1:d+1
            data_radial{j+3,3,k} = (j-1)*voxel;
            data_angular{j+3,3,k} = (j-1)*voxel;
        end
    end
```

```
data_radial{3,1,1} = 'Outside average intensity:';
data_angular{3,1,1} = 'Outside average intensity:';
for j = 1:d+1
   data_radial{j+3,1,1} = outside_data(j,1,1)/outside_data(j,1,2);
   data_angular{j+3,1,1} = outside_data(j,1,1)/outside_data(j,1,2);
end

data_radial{3,2,1} = 'Inside average intensity:';
data_angular{3,2,1} = 'Inside average intensity:';
for j = 1:d+1
   data_radial{j+3,2,1} = inside_data(j,1,1)/inside_data(j,1,2);
   data_angular{j+3,2,1} = inside_data(j,1,1)/inside_data(j,1,2);
end

data_radial{3,1,2} = 'Outside average >threshold intensity:';
data_angular{3,1,2} = 'Outside average >threshold intensity:';
for j = 1:d+1
   data_radial{j+3,1,2} = outside_data(j,1,3)/outside_data(j,1,4);
   data_angular{j+3,1,2} = outside_data(j,1,3)/outside_data(j,1,4);
end

data_radial{3,2,2} = 'Inside average >threshold intensity:';
data_angular{3,2,2} = 'Inside average >threshold intensity:';
for j = 1:d+1
   data_radial{j+3,2,2} = inside_data(j,1,3)/inside_data(j,1,4);
   data_angular{j+3,2,2} = inside_data(j,1,3)/inside_data(j,1,4);
end

data_radial{3,1,3} = 'Outside fill fraction:';
data_angular{3,1,3} = 'Outside fill fraction:';
for j = 1:d+1
   data_radial{j+3,1,3} = outside_data(j,1,4)/outside_data(j,1,2);
   data_angular{j+3,1,3} = outside_data(j,1,4)/outside_data(j,1,2);
end

data_radial{3,2,3} = 'Inside fill fraction:';
data_angular{3,2,3} = 'Inside fill fraction:';
for j = 1:d+1
   data_radial{j+3,2,3} = inside_data(j,1,4)/inside_data(j,1,2);
   data_angular{j+3,2,3} = inside_data(j,1,4)/inside_data(j,1,2);
end
```

```
    for i = 1:parts
        for k = 1:3
            data_radial{2,i+3,k} = ['Inside partition ' int2str(i)];
            data_radial{3,i+3,k} = [int2str((i-1)*radius/parts*voxel) ' to ' int2str(i*radius/parts*voxel) ' um'];
            data_radial{2,i+3+parts,k} = ['Outside partition ' int2str(i)];
            data_radial{3,i+3+parts,k} = [int2str((i-1)*radius/parts*voxel) ' to ' int2str(i*radius/parts*voxel) '
um'];
        end
    end
    for i = 1:2*parts
        for j = 1:d+1
            data_radial{j+3,i+3,1} = radial_data(j,i,1)/radial_data(j,i,2);
            data_radial{j+3,i+3,2} = radial_data(j,i,3)/radial_data(j,i,4);
            data_radial{j+3,i+3,3} = radial_data(j,i,4)/radial_data(j,i,2);
        end
    end

    for k = 1:3
        data_angular{2,4,k} = 'Center partition:';
        data_angular{3,4,k} =  ['0 to ' int2str(radius/sqrt(angles+1)) ' um'];
        for i = 1:angles
            data_angular{2,i+4,k} = ['Inside angle ' int2str(i)];
            data_angular{3,i+4,k} = [int2str((i-1)*360/angles) ' to ' int2str((i)*360/angles) ' deg'];
            data_angular{2,i+4+angles,k} = ['Outside angle ' int2str(i)];
            data_angular{3,i+4+angles,k} = [int2str((i-1)*360/angles) ' to ' int2str((i)*360/angles) ' deg'];
        end
    end
    for j = 1:d+1
        data_angular{j+3,4,1} = angular_data(j,1,1)/angular_data(j,1,2);
        data_angular{j+3,4,2} = angular_data(j,1,3)/angular_data(j,1,4);
        data_angular{j+3,4,3} = angular_data(j,1,4)/angular_data(j,1,2);
        for i = 1:2*angles
            data_angular{j+3,i+4,1} = angular_data(j,i+1,1)/angular_data(j,i+1,2);
            data_angular{j+3,i+4,2} = angular_data(j,i+1,3)/angular_data(j,i+1,4);
            data_angular{j+3,i+4,3} = angular_data(j,i+1,4)/angular_data(j,i+1,2);
        end
    end

    data_radial{1,1,1} = 'RADIAL (average intensity)';
    data_radial{1,1,2} = 'RADIAL (average >threshold intensity)';
    data_radial{1,1,3} = 'RADIAL (fill fraction)';
    data_angular{1,1,1} = 'ANGULAR (average intensity)';
    data_angular{1,1,2} = 'ANGULAR (average >threshold intensity)';
```

```
data_angular{1,1,3} = 'ANGULAR (fill fraction)';

history = cell(6,10,1);
history{1,1,1} = 'HISTORY';
history{1,3,1} = 'filename: ';
history{1,4,1} = filename;
history{1,5,1} = 'filestart: ';
history{1,6,1} = filestart;
history{1,7,1} = 'fileend: ';
history{1,8,1} = fileend;
history{1,9,1} = 'version: ';
history{1,10,1} = version;

history{2,1,1} = 'x_start:';
history{2,2,1} = x_start;
history{2,3,1} = 'x_end: ';
history{2,4,1} = x_end;
history{2,5,1} = 'x_change: ';
history{2,6,1} = x_change;
history{2,7,1} = 'x:[c_start,c_end]: ';
%       history{2,8,1} = ['[' int2str(c_start) ',' int2str(c_end) ']'];
history{2,9,1} = 'x_size: ';
history{2,10,1} = x_size;

history{3,1,1} = 'y_start: ';
history{3,2,1} = y_start;
history{3,3,1} = 'y_end: ';
history{3,4,1} = y_end;
history{3,5,1} = 'y_change: ';
history{3,6,1} = y_change;
history{3,7,1} = 'y:[c_start,c_end]: ';
history{3,8,1} = ['[' int2str(c_start) ',' int2str(c_end) ']'];
history{3,9,1} = 'y_size: ';
history{3,10,1} = y_size;

history{4,1,1} = 'z_start: ';
history{4,2,1} = z_start;
history{4,3,1} = 'z_end: ';
history{4,4,1} = z_end;
history{4,5,1} = 'z_change: ';
history{4,6,1} = z_change;
history{4,7,1} = 'z:[c_start,c_end]: ';
%       history{4,8,1} = ['[' int2str(c_start) ',' int2str(c_end) ']'];
```

```
    history{4,9,1} = 'z_size: ';
    history{4,10,1} = z_size;

    history{5,1,1} = 'threshold: ';
    history{5,2,1} = threshold;
    history{5,3,1} = 'radius: ';
    history{5,4,1} = radius;
    history{5,5,1} = 'type: ';
    history{5,6,1} = type;
    history{5,7,1} = 'parts: ';
    history{5,8,1} = parts;
    history{5,9,1} = 'angles: ';
    history{5,10,1} = angles;

    history{6,1,1} = 'voxel: ';
    history{6,2,1} = voxel;
    history{6,3,1} = 'bit depth: ';
    history{6,4,1} = bit_d;
    history{6,5,1} = 'plane: ';
    history{6,6,1} = plane;
    history{6,7,1} = 'start coordinates: ';
    history{6,8,1} = o_start;
    history{6,9,1} = 'end coordinates: ';
    history{6,10,1} = o_end;

    time = clock;
    data_name = [filename(1:11) '_' int2str(time(2)) int2str(time(3)) int2str(time(1)) '_' int2str(time(4))
int2str(time(5))];
    xlswrite(data_name,data_radial(:,:,1),1);
    xlswrite(data_name,data_radial(:,:,2),2);
    xlswrite(data_name,data_radial(:,:,3),3);
    xlswrite(data_name,data_angular(:,:,1),4);
    xlswrite(data_name,data_angular(:,:,2),5);
    xlswrite(data_name,data_angular(:,:,3),6);
    xlswrite(data_name,history(:,:,1),7);

    raw_name = [filename(1:5) '_RAWDATA_' int2str(time(2)) int2str(time(3)) int2str(time(1)) '_'
int2str(time(4)) int2str(time(5))];
    xlswrite(raw_name,radial_data(:,:,1),1);
    xlswrite(raw_name,radial_data(:,:,2),2);
    xlswrite(raw_name,radial_data(:,:,3),3);
    xlswrite(raw_name,radial_data(:,:,4),4);
    xlswrite(raw_name,angular_data(:,:,1),5);
```

```
    xlswrite(raw_name,angular_data(:,:,2),6);
    xlswrite(raw_name,angular_data(:,:,3),7);
    xlswrite(raw_name,angular_data(:,:,4),8);
    xlswrite(raw_name,[inside_data(:,:,1) inside_data(:,:,2) inside_data(:,:,3) inside_data(:,:,4)],9);
    xlswrite(raw_name,[outside_data(:,:,1) outside_data(:,:,2) outside_data(:,:,3) outside_data(:,:,4)],10);
end

load gong;
wavplay(y,Fs);
```

APPENDIX B

PROCEDURES AND PROTOCOLS FOR SCAFFOLD FABRICATION, CHARACTERIZATION, AND CELL CULTURE

B.1 Fabrication of Non-Mineralized Precursor Suspension

B.1.1 Reference

Yannas, I.; Lee, E.; Orgill, D.; Skrabut, E.; Murphy, G. Synthesis and characterization of a model extracellular matrix that induces partial regeneration of adult mammalian skin. *Proc Natl Acad Sci U S A* **1989**, 86 (3), 933-7.

O'Brien, F.; Harley, B.; Yannas, I.; Gibson, L. Influence of freezing rate on pore structure in freeze-dried collagen-GAG scaffold. *Biomaterials* **2004**, 25 (6), 1077-86.

B.1.2 Supplies

- Dry Collagen (Cat. No. C9879, Sigma Aldrich)
- Chondroitin-6-Sulfate (Cat. No. C4384, Sigma Aldrich)
- Glacial Acetic Acid (Cat. No. 71251, Sigma Aldrich)
- De-Ionized Water

B.1.3 Equipment

- Balance
- Jacketed Cooling Vessel

- Blender
- Pipette
- 25mL Conical Tube

B.1.4 Procedure

1. Setup the jacketed vessel, setting the water temperature to 4°C.

2. Add 0.87 mL glacial acetic acid to 300 mL of de-ionized water to make a solution of 0.05 M acetic acid.

3. Add 1.5g of Collagen to the jacketed vessel. Then add 250mL of the 0.05 M acetic acid solution to the Collagen. Set the blender to 15,000 rpm for 30min, so that the collagen is submerged prior to hydration.

4. Measure out 0.133 g of Chondroitin-6-Sulfate and add it to 50mL of the 0.05 M acetic acid solution in a beaker. Then mix the buffer and the Chondroitin (GAG Solution), using a magnetic stirring bar, until fully dissolved.

5. Set the blender to 15,000rpm and blend the Collagen made in step 3 for 60min.

6. Add the GAG Solution prepared in step 4 to the Collagen Solution prepared in step 3 while mixing at 15,000 rpm. In between each addition, take care to prevent any clumping of the collagen/GAG with a spatula. With the additional volume, the slurry will mix better.

7. Blend this GAG / Hydrated Collagen Solution at 15,000rpm for 30min.

8. Stores the slurry for 18-22hrs at 2-8°C.

B.1.5 Notes

- Solution expires 3 months after manufacture.
- When mixing Phosphoric Acid with De-Ionized Water, never add water to acid.

B.2 Preparation of Phosphoric Acid-Calcium Hydroxide Buffer Solution

B.2.1 Reference

Process Record No. PR OM-001 Preparation of 0.1456M Phosphoric Acid/0.037M Calcium Hydroxide, BioUetikon and OrthoMimetics.

B.2.2 Supplies

- 5.904mL of 85% Phosphoric Acid (Cat. No. P5811, Sigma Aldrich)
- 570mL De-IonizedWater
- 1.644g Calcium Hydroxide (Cat. No. 31219, Sigma Aldrich)

B.2.3 Equipment

- Balance
- Glass Beaker
- pH Meter
- Magnetic Stirrer (Recommended)
- 0.2μm filter (For Sterilization)
- Sterile bottle (For Sterilization)

B.2.4 Procedure

2. Add 5.904mL of 85% Phosphoric Acid to 570mL De-Ionized Water in a glass beaker and stir thoroughly.

3. Add 1.644g Calcium Hydroxide to the Phosphoric Acid solution and stir until fully dissolved and no visible particulates can be seen. A magnetic stirrer is recommended.

4. Using De-Ionized Water, bring the Phosphoric Acid solution to the intend volume of 600mL if needed.

5. Use a pH meter to check the final pH of the solution. It is recommended to be between 2.0-2.4.

B.2.5 Notes

- Solution expires 3 months after manufacture.
- When mixing Phosphoric Acid with De-Ionized Water, never add water to acid.

B.3 Fabrication of Mineralized Precursor Suspension

B.3.1 Reference

Process Record No. PR OM-004 Preparation of Mineralized Slurry, BioUetikon and OrthoMimetics.

B.3.2 Supplies

- 0.1456M Phosphoric Acid / 0.037M Calcium Hydroxide Buffer Solution
- Dry Collagen (Cat. No. C9879, Sigma Aldrich)
- Chondroitin-6-Sulfate (Cat. No. C4384, Sigma Aldrich)
- Calcium Hydroxide (Cat. No. 31219, Sigma Aldrich)
- Calcium Nitrate Tetrahydrate (Cat. No. 31218, Sigma Aldrich)
- De-Ionized Water

B.3.3 Equipment

- Balance
- Jacketed Cooling Vessel
- Blender
- Pipette
- 25mL Conical Tube

B.3.4 Procedure

9. Setup the jacketed vessel, setting the water temperature to 4°C.

10. Add 5.7966g of Collagen to the jacketed vessel. Then add 242.12mL of Phosphate Acid / Calcium Hydroxide buffer to the Collagen. Set the blender to 15,000 rpm for 30min, so that the collagen is submerged prior to hydration. Allow the collagen to hydrate for 18-22hrs in the cooled jacketed vessel at 4°C. This mixture will become very viscous and difficult to blend.

11. Measure out 2.515g of Chondroitin-6-Sulfate and add it to 42.94mL of Phosphate Acid / Calcium Hydroxide Buffer in a beaker. Then mix the buffer and the Chondroitin (GAG Solution), using a magnetic stirring bar, until fully dissolved.

12. Measure out 1.92g of Calcium Hydroxide and 1.17g of Calcium Nitrate Tetrahydrate and place both in a 25mL Conical Tube. Add 15mL of De-Ionized Water to the 25mL Conical Tube using a pipette. Then mix (vortex/shake) the solution to suspend the salts in the De-Ionized Water.

13. Set the blender to 15,000rpm and blend the Hydrated Collagen made in step 2 for 60min.

14. Add the GAG Solution prepared in step 3 to the Hydrated Collagen Solution prepared in step 3 in 8mL steps while mixing at 15,000 rpm. In between each 8mL step, take care to prevent any clumping of the collagen/GAG with a spatula. With the additional volume, the slurry will mix better.

15. Blend this GAG / Hydrated Collagen Solution at 15,000rpm for 30min.

16. Blend the Collagen / GAG mixture at 200-800rpm while adding the salts to maximize dispersion. Using a pipette, add the salt solution at a rate of 8mL/min to the Collagen / GAG mixture, allowing time for blending after each volume. Then blend the slurry at 15,000rpm for 30min.

17. Stores the slurry for 18-22hrs at 2-8°C.

B.3.5 Notes

- Do not use the slurry immediately after manufacturing.
- Prior to use, the slurry must be blended to ensure proper mixing.
- Do not mix the GAG Solution too aggressively to prevent separation.
- When adding the Salts Solution to the GAG / Hydrated Collagen Solution be prepared for foaming.
- Carefully wash all equipment (rotor-stator, mixing flasks, and moulds) carefully and thoroughly to prevent any cross contamination.

B.4 Hydroxyproline Assay for Collagen Content

B.4.1 References

Chapter 16: Determination of Collagen Content, Concentration, and Sub-types in Kidney Tissue

Chrishan S. Samuel

Methods in Molecular Biology, vol. 466: Kidney Research

B.4.2 Materials

- Chloramines T (Sigma-Aldrich, 857319-5G, $20.20)
- Sodium Acetate Anhydrous (Sigma-Aldrich, 236500-25G, $28.80)
- Tri-Sodium Citrate $2H_2O$ (?)
- Citric Acid (Sigma-Aldrich, 251275-5G, $24.10)
- 4-(Dimethylamino)benzaldehyde (a.k.a. DMAB) (Sigma-Aldrich, 39070-50G, $46.30)
- HCl (Sigma-Aldrich, 84428-100ML, $32.30)
- Strong Base (NaOH) (Sigma-Aldrich, 221465-25G, $27.40)
- DI H_2O
- Hydroxyproline (Sigma-Aldrich, H5877-250MG, $18.40)
- Isopropanol (Sigma-Aldrich, 190764-500ML, $32.60)

B.4.3 Procedure

1. With the exception of the Chloramine T Solution and the Acetate Citrate Buffer, all solutions should be prepared the day of the assay for best possible freshness.

2. Prepare the Chloramines T Solution by dissolving Chloramine T in DI H_2O to yield a 7g/100mL solution. It can be stored up to 2 week at 4^oC in the dark.

3. Prepare an Acetate Citrate Buffer (pH 6.0 per 100mL) by dissolving 3.44g Sodium Acetate Anhydrous, 3.75g Tri-Sodium Citrate $2H_2O$, and 0.55g Citric Acid in 38.5mL of Isopropyl Alcohol and DI H_2O. It can be stored at 4^oC for 6 months.

4. Prepare an Oxidation Buffer by combining 1:4 Chloarmine T Solution with Acetate Citrate Buffer. It is recommened that 1mL Chloramine T solution and 4mL Acetate Citrate Buffer be used.

5. Prepare Ehrlich's reagent by combining 2.0g para-dimethylaminobenzaldehyde in 3.0mL 60% perchloric acid. This can be stored up to 2 weeks at 4^oC in the dark.

6. Prepare an Analytical Isopropanol agent by combining 3:13 Ehrlich's reagent with Isopropanol. The solution will be yellow in color.

7. Prepare a 6-8mm diameter scaffold punch.

8. Accurately measure the dry weight of the sample.

9. Place the sample in a 1mL Reacta-Vial. A regular plastic cap can be used to seal the vial. A second larger glass jar can be used as secondary containment during the hydrolysis (Step 9).

10. Submerge the samples in 0.4-0.5mL 6M HCl prior to being hydrolyzed at 110^{o}C for 24hrs in the oven. For larger vials, 1-2mL 6M HCl can be used.

11. Cool samples to 4^{o}C in the fume hood and fridge.

12. Neutralize the 6M HCl used for the hydrolysis.
    a. It is suggested to prepare and use a stock 6M NaOH solution.

13. Double the volume of each sample using a stock solution of 0.2M HCl.

14. Assay each sample in either duplicates, triplicates, or quadruplicates. Add 10uL sample (in 0.1M HCl) to 90uL DI H_2O. (Total of 100uL).

15. Prepare the standard curve by adding: 0uL, 2 uL, 4 uL, 6 uL, 8 uL, and 10 uL 1mg/mL Hydroxyproline (in 0.1M HCl) and adjusting to a total volume of 100uL with DI H_2O.

16. Steps 17-23 are time sensitive and should be done as soon as possible. Steps 15-17 must be done within 4min. Steps 18-19 need to be done within another 4min.

17. Add 200uL Isopropanol to all samples.

18. Add 100uL Oxidation Buffer to all samples (total volume now 0.4mL).

19. Vortex all samples and allow them to stand at room temperature for 4±0.5min.

20. Add 1.3mL Analytical Isopropanol reagent to all samples (total volume now 1.7mL).

21. Place all samples into a water bath pre-set to 60^{o}C for 25min.

22. Cool samples at 4^{o}C for 5-10min.

23. Add 3.3mL Isopropanol to all samples (total volume 5mL).

24. Pipette samples into a clear plastic 96 well plate for use in the spectrometer.

25. Calibrate spectrometer using the blank sample (0uL Hydroxyproline in 0.1M HCl). Obtain absorbance at 558nm. From this a standard curve can be generated.

B.4.4 Operation of the spectrometer

1. Turn on the computer, if not already on. This seriously takes roughly 20min, if the computer is still running slow, you could open the task manager and close McAfee applications.

2. Turn on the spectrometer, the tray will automatically eject (a second time) when it is completely turned on and ready to be used.

3. Open the program Gen5 located on the desktop.

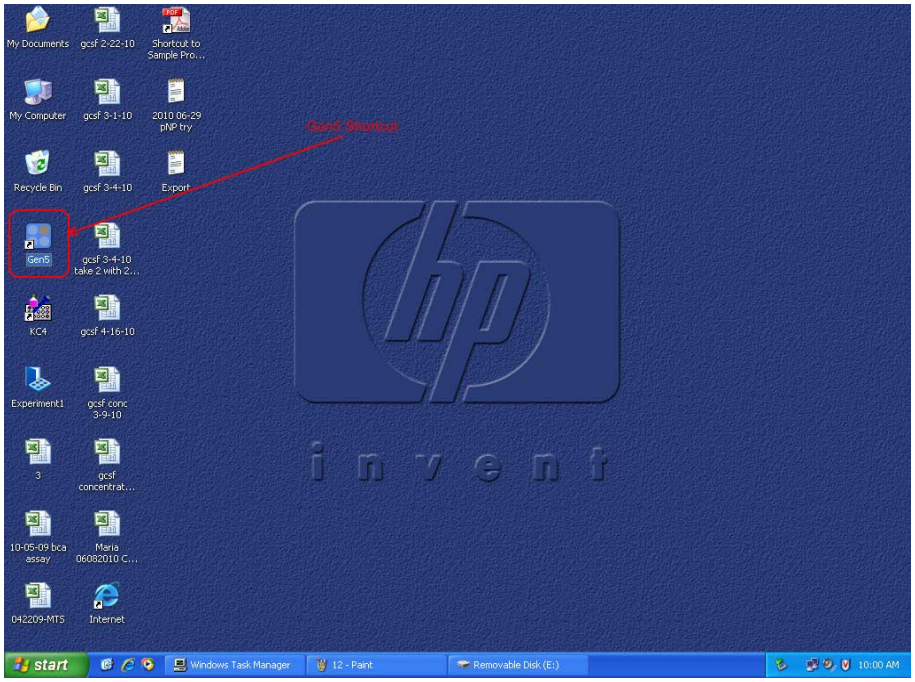

4. Under ‘Open A Recent Item’ and ‘Protocols” click on the ‘Harley_HOPro_Assay_1.prt’ or just select under ‘Create a New Item’ an ‘Experiment’.

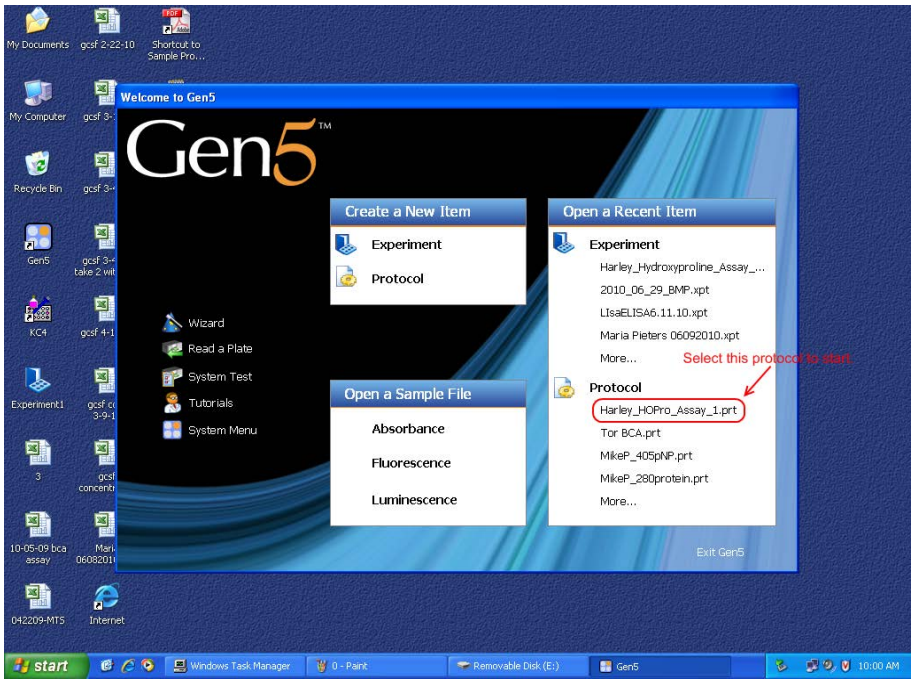

5. On the next screen, under ‘File’ click ‘New Experiment…’.

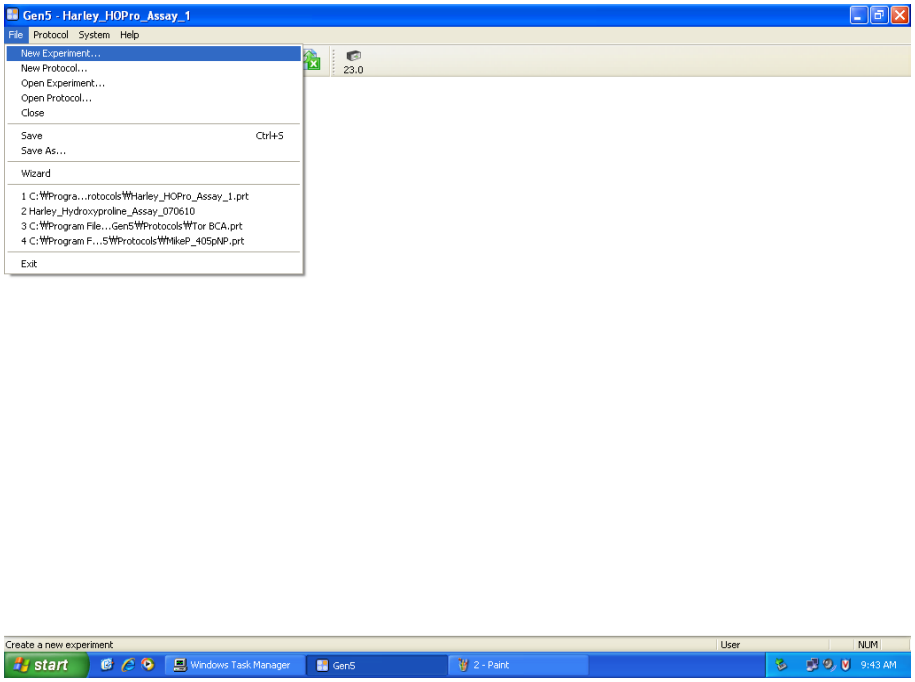

6. Select ‘Harley_HOPro_Assay_1.prt’ and click ‘Ok’.

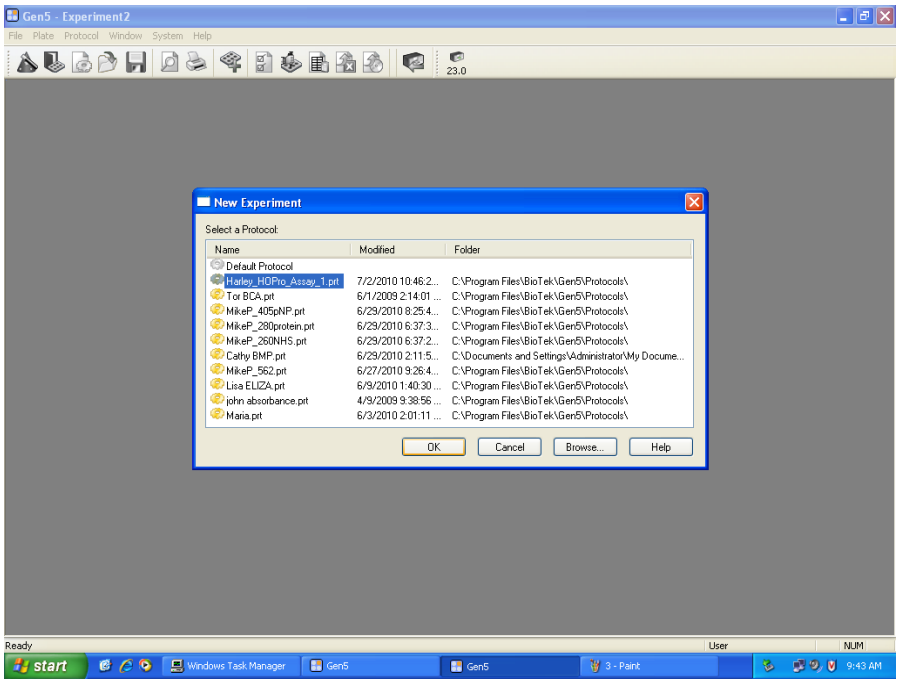

7. Once loaded, under ‘Plate’ click ‘Read’.

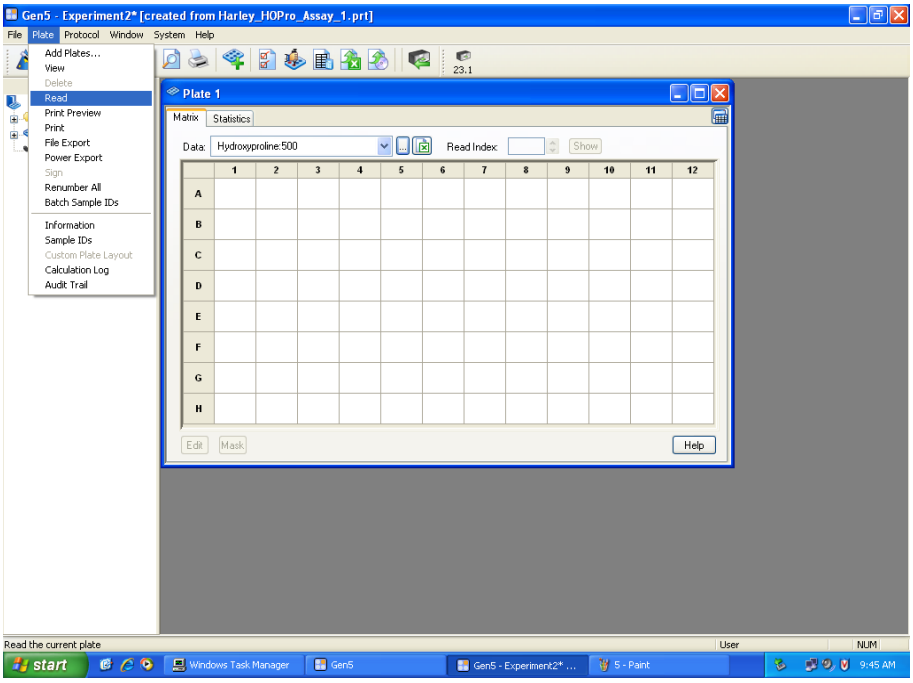

8. Enter any desired information to identify the experiment and click ‘Read’.

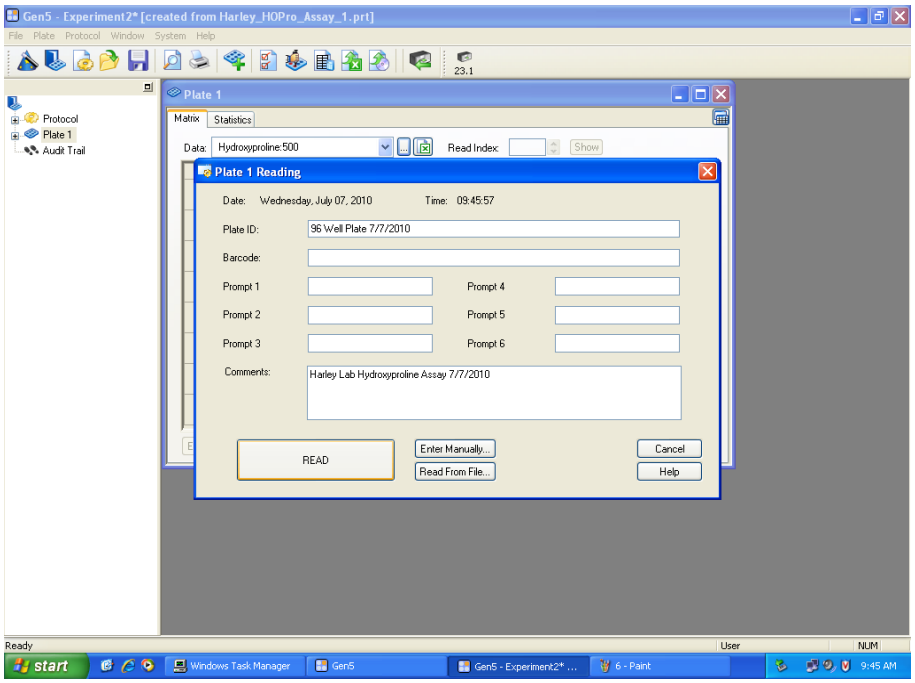

9. You will now be prompted to place the 96 well plate onto the carrier and then press ‘Ok’.

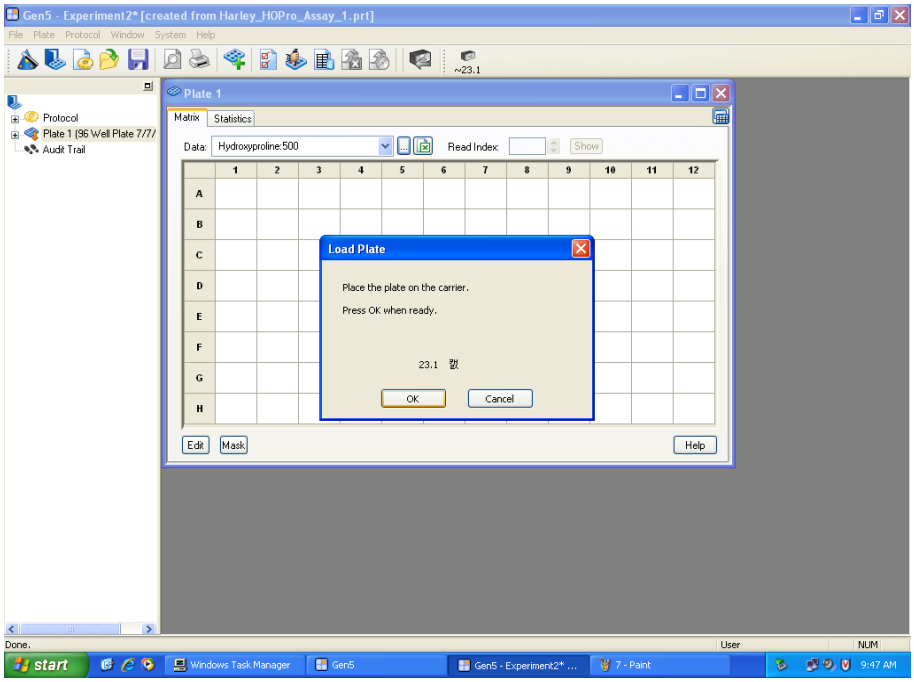

10. The experiment will automatically start. It will take about 10min to complete.

11. Upon completion, the data being displayed will default to ‘Hydroxyproline 500’ which corresponds to 500nm absorption measurement.

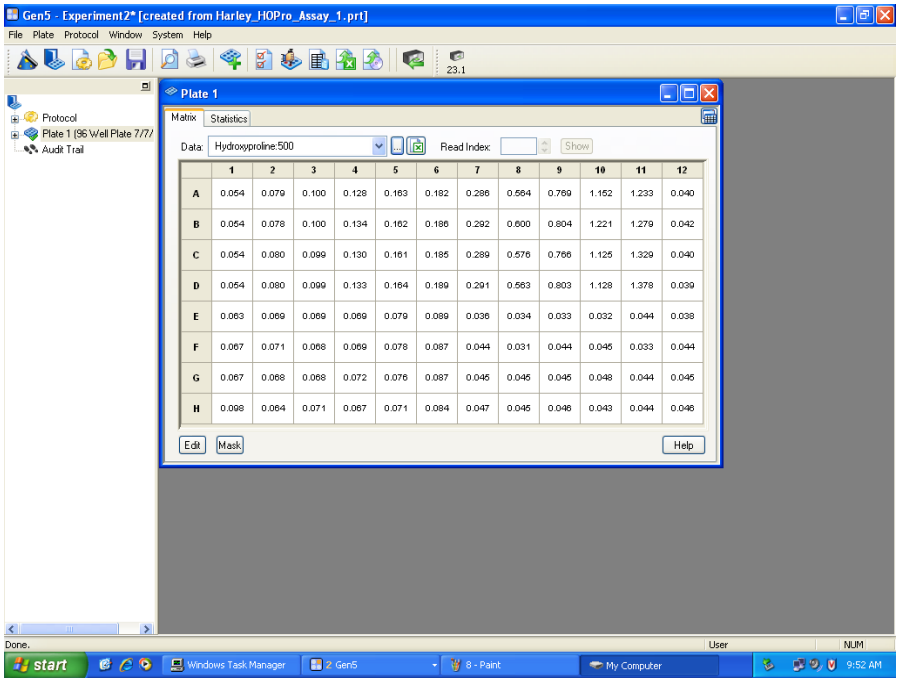

12. The data being displayed can be changed by using the drop down list.

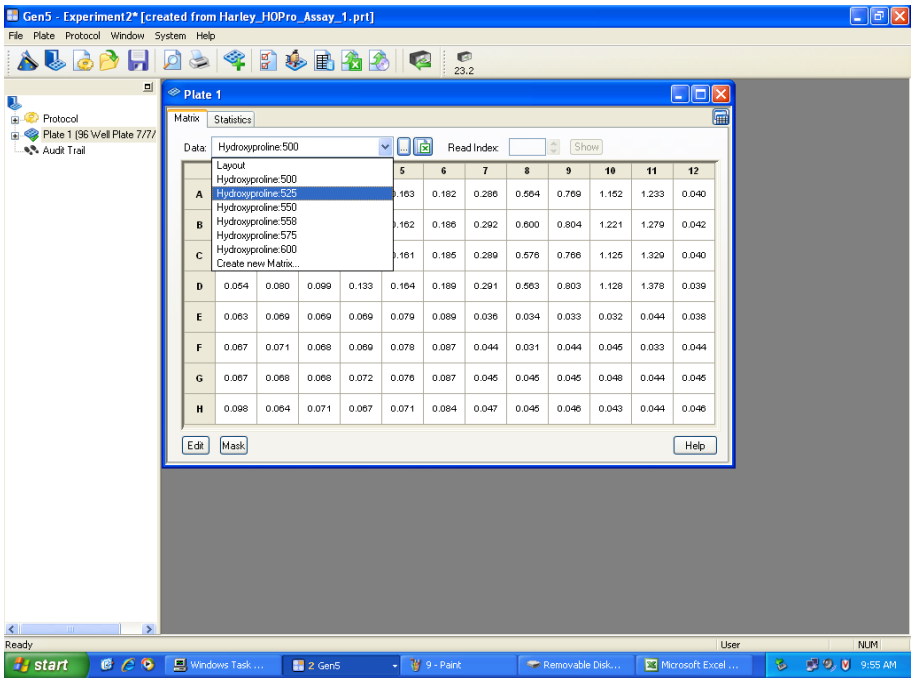

13. This data can be exported to excel by clicking on the green excel button located next to the drop down list.

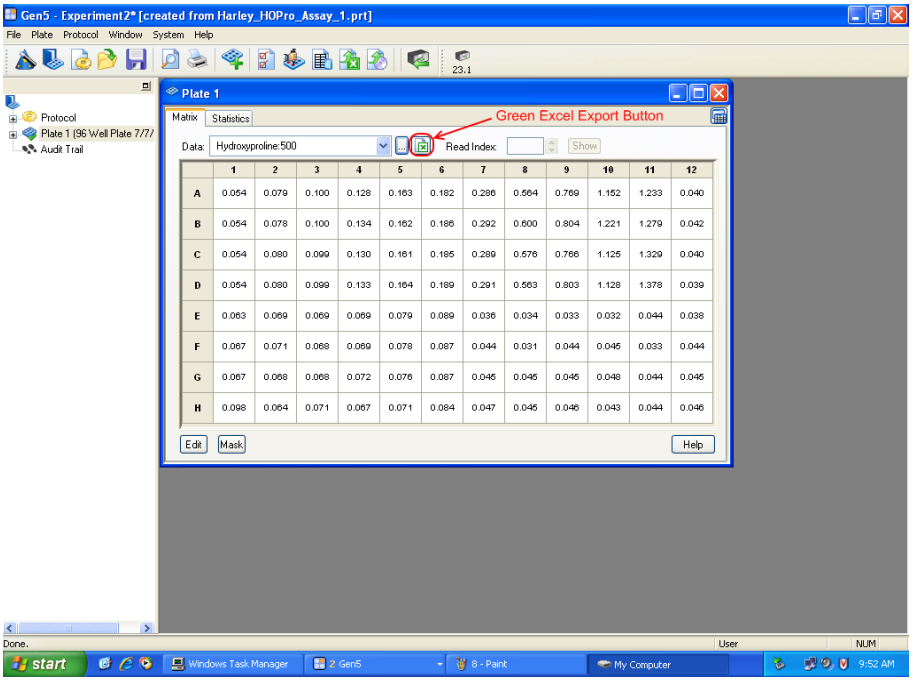

	1	2	3	4	5	6	7	8	9	10	11	12
A	0.054	0.079	0.100	0.128	0.163	0.182	0.286	0.564	0.769	1.152	1.233	0.040
B	0.054	0.078	0.100	0.134	0.162	0.186	0.292	0.600	0.804	1.221	1.279	0.042
C	0.054	0.080	0.099	0.130	0.161	0.185	0.289	0.578	0.766	1.125	1.329	0.040
D	0.054	0.080	0.099	0.133	0.164	0.189	0.291	0.563	0.803	1.128	1.378	0.039
E	0.063	0.069	0.069	0.069	0.079	0.089	0.036	0.034	0.033	0.032	0.044	0.038
F	0.067	0.071	0.068	0.069	0.078	0.087	0.044	0.031	0.044	0.045	0.033	0.044
G	0.067	0.068	0.068	0.072	0.076	0.087	0.045	0.045	0.045	0.048	0.044	0.045
H	0.098	0.064	0.071	0.067	0.071	0.084	0.047	0.045	0.046	0.043	0.044	0.046

14. Each wavelength (500nm, 525nm, 550nm, 558nm, 575nm, 600nm) will be exported to a separate excel book. It is recommended, for convenience, that you copy and paste all the data into one excel spread sheet and then back the data up.

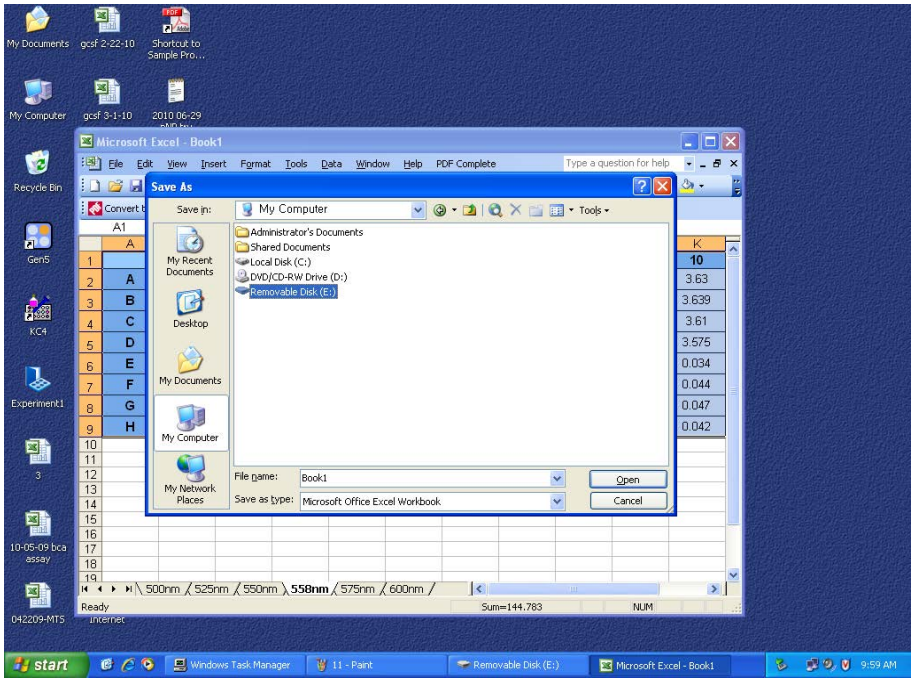

15. The Gen5 program can then be closed.

16. Do not turn off the computer, leave it on.

17. Close the spectrometer carrier, and turn the spectrometer off.

18. Turn off the room lights.

B.5 1,9-Dimethylmethylene Blue (DMMB) for Glycosaminoglycan Content

B.5.1 References

Barbosa, I.; Garcia, S.; Barbier-Chassefiere, V.; Caruelle, J.; Martelly, I.; Papy-Garcia, D. Improved and simple micro assay for sulfated glycosaminoglycans quantification in biological extracts and its use in skin and muscle tissue studies. *Glycobiology* **2003**, 13, 647-653.

B.5.2 Materials

- Ethanol
- Guanidine hydrochloride (GuHCl) (Sigma-Aldrich, G4630-1KG, $56.10)
- Sodium Formate (Sigma-Aldrich, 247596-100G, $37.70)
- 98% Formic Acid (Sigma-Aldrich, 94318-50ML-F, $33.20)
- DI H_2O
- 1,9-dimethylmethylene blue (DMMB) (Sigma-Aldrich, 341088-1G, $40.50)
- Sodium Acetate (Sigma-Aldrich, S2889-250G, $24.10)
- propan-1-ol (Sigma-Aldrich, 279544-100ML, $30.90)
- Chondroitin-6-Sulfate (GAG) (Sigma-Aldrich, C4384)

B.5.3 Procedure

1. Prepare a Formate Solution by mixing 25mL Ethanol, 100mL 1M GuHCl, 1g Sodium Formate, and 1mL 98% Formic Acid. Raise the total volume to 500mL using DI H_2O.

2. Prepare the DMMB Complexation Solution:

    a. Dissolve 16mg DMMB into 25mL Ethanol.
    b. Filter the resulting solution through filter paper.
    c. Add 100mL 1M GuHCl, 1g Sodium Formate, and 1mL 98% Formic Acid to the DMMB-Ethanol solution.
    d. Raise the total volume to 500mL using DI H_2O.
    e. Immediately dilute this DMMB solution with the Formate Solution (1:1). This is a time sensitive step.
    f. This solution may be stored for 4 months at room temperature in the dark.

3. Prepare a DMMB Decomplexation Solution by mixing a 50mM Sodium Acetate Solution (pH 6.8) with 10% propan-1-ol. Then dissolve GuHCl into the Sodium Acetate Solution to make a final concentration of 4M. This solution may be stored for 4 months at room temperature.

4. Prepare a 50ug/mL proteinase K in 100mM K_2HPO_4 solution.

5. Digest 6-8mm scaffold punches in the 1mL of the 50ug/mL proteinase K in 100mM K_2HPO_4 solution overnight at 56^{o}C. A plastic micro centrifuge tube is sufficient in size.

6. Deactivate the 50ug/mL proteinase K in 100mM K_2HPO_4 solution by heating it to 90^{o}C for 10min in the oven or equivalent.

7. Centrifuge the samples at 1400xg for 5min to separate the debris from extract.

8. Pipette the supernate (extract) from the precipitate (debris) carefully into a new vial. This will represent initially diluted sample (the scaffold was diluted in the 50ug/mL proteinase K in 100mM K_2HPO_4 solution).

9. Estimate the amount of gag present in the supernate (extract). For a 8mm punch from a 3"x3" scaffold using 24.6mL out of 300mL slurry digested in 1mL Proteinase K solution:

$$\frac{2.515g\_GAG\_in\_Slurry}{10^{-6}\,g/\mu g}\times\frac{24.6mL\_Slurry\_in\_Scaffold}{300mL\_Total\_Slurry}\times\frac{\pi(8mm/2)^2\_Punch\_Area}{(76.2mm)^2\_Scaffold\_Area}\times\frac{1}{1mL\_\mathrm{Pr}oteinase\_K\_Solution}$$

10. For each sample, make 2-3 dilutions using the estimated amount of gag present in the supernate. Dilute the samples to 10ug/mL, 20ug/mL, and/or 30ug/mL, if the amount of gag should be close to the expect amount. If amount of gag estimated is not expected to be similar, dilute samples to 10ug/mL, 30ug/mL, and/or 60ug/mL (a broader range). Thoroughly mix the samples after every dilution by vortexing.

11. For each of the diluted samples (10ug/mL, 20ug/mL, and/or 30ug/mL ect.) add 1mL DMMB complexation solution to an empty micro-centrifuge tube.

12. Add 100uL of the diluted samples (10ug/mL, 20ug/mL, and/or 30ug/mL ect.) to each of the micro-centrifuge tubes prepared in step 11. This will result in further diluted samples (1ug, 2ug, and/or 3ug for 10ug/mL, 20ug/mL, and/or 30ug/mL ect.) which are in the linear range (0-4ug).

13. Vortex all of the micro-centrifuge tubes for 30min. This allows adequate time for the GAG-DMMB complex to form.

14. Centrifuge all of the micro-centrifuge tubes at 14000xg for 30min.

15. Pipette out and discard the supernate (unused DMMB complexation solution) while carefully keeping any precipitate present in all of the micro-centrifuge tubes. Note: the precipitate is not visible below 4ug.

16. Add 1mL DMMB decomplexation solution to each of the micro-centrifuge tubes.

17. Vortex the micro-centrifuge tubes for 30min. This allows adequate time for the GAG-DMMB complex to be separated/destroyed.

18. It is recommended to pipette 0.2mL each samples into 4 wells in a 96 well plate for analysis with a spectrometer.

19. The wavelength of interest is at 656nm.

20. Standard curves are prepared in the same way as steps 9-19, the only difference being that a known amount of GAG was added to a 100mM K_2HPO_4 solution. Dilute the GAG down to 0ug, 0.2ug, 0.4ug, 0.6ug, 0.8ug, 1.0ug, 2.0ug, 4.0ug, 6.0ug, 8.0ug, 10.0ug. This accounts for the entire linear region and some none linear parts (8.0ug and 10.0ug).

B.5.4 Operation of the Spectrometer

This is identical to the operation of the spectrometer for the hydroxyproline assay, with the exception that the ‘Harley_DMMB_Assay_1.prt’ is used instead. Please see appendix B, section B.4, subsection B.4.4 for operating instructions.

B.6 Permeability of Hydrated Collagen-Glycosaminoglycan Scaffolds

B.6.1 Reference

O'Brien, F., Brendan, H., Waller, A., Yannas, I., Gibson, L., Prendergast, P. The effect of pore size on permeability and cell attachment in collagen scaffolds for tissue engineering. *Technology and Health Care*, 2007, 15, 3-17.

B.6.2 Supplies

- De-Ionized Water
- Food coloring

B.6.3 Equipment

- Permeability Rig
- Assorted gaskets, grommets, and spacers
- Container (dimensions exceeding 6"x6"x4")
- Ring stand

B.6.4 Procedure

1. Fill the container with De-Ionized water. The water level should be a minimum of 5.83cm or 2.3" (2" + 75% of sample height), the gasket/grommet being used must be completely submerged. This allows the samples to remain submerged and hydrated, but not float away in the event of poor hydration.

2. Assemble the rig. It is recommended that the rig is dried prior to assembly if previously used.

3. Thread bolts through the top half of the rig, use tape to ensure the bolts remain fixed.

4. Place desired spacers (dependent on desired compression and gasket used, the spacers must be at most 85% of the height of the gasket to ensure a good seal) on the bolts fixed in the top half of the rig.

5. Center gasket over the grating on the top half of the rig, use tape to ensure the gasket maintains this position.

6. Carefully submerge the top half of the rig (step 2), ensuring that there is no air bubbles trapped. It is necessary for the top half of the rig to be upside down (grating facing up) in the container filled with De-Ionized water (step 1).

7. Carefully place the sample into the container filled with De-Ionized water (step 1). Once the sample and hydration of the sample has been confirmed, maneuver the sample over the grating. This must be done such that the sample covers the grating completely and fills the gasket/grommet completely.

8. Carefully thread the bottom half of the rig onto the exposed bolts. It must be slowly moved down to prevent the bottom half of the rig from becoming stuck (due to uneven progression) and moving the sample out of the gasket.

9. Once the bottom half has been threaded onto the bolts completely (the sample should have been smoothly compressed into the gasket/grommet), wingnuts should be threaded onto the end of the bolts to secure the entire rig.

10. Slowly rotate the rig onto its side. This should cause the rig to be entirely submerged. There should be no air bubbles in the rig.

11. Remove the tap used to secure the bolts on the top of the rig. While completely submerged, use an adjustable wrench to tighten the bolts and wingnuts to ensure that only the spacer is separating top and bottom halves of the rig.

12. Rotate the wingnuts (approximately 30° or 60° with respect to the sides) so that they form a rough circle and fit into the ring stand.

13. Add the bottom cap to the permeability rig to prevent any flow of water during placement onto the ring stand.

14. Remove the bottom cap to allow water to flow through the rig. Be prepared to immediately add water to prevent the pressure head and water level from deviating from either 1.2” or 3.0” (experiment and rig dependent).

15. A pasture pipette is recommended, but in some cases this may not be sufficient enough.

16. Place a designated graduated cylinder under the permeability rig to collect water (10.0±0.2mL graduated cylinder is recommended, but the choice of graduated cylinder is dependent upon the permeability of the scaffold). Start the timer with the appearance of the first drop. Always stop the timer after the last drop.

17. Due to radical changes with compression, stopping measurements after set volume or time increments is difficult.

18. Make a note of:
    a. Volume of De-Ionized Water in graduate cylinder (mL).
    b. Time the measurement occurred over (s).
    c. Height of gasket/grommet used (mm).
    d. Height of spacers used (mm).
    e. Pressure head used (1.2” or 3.0”, experiment and rig dependent).
    f. Any other information that maybe relevant to experiment.

19. Repeat step 12 twice more for each sample (for a total of three measurements per sample).

20. Replace the rig in the container filled with De-Ionized water. Disassemble the rig, note carefully if there is an abnormality in sample hydration or placement.

21. Repeat steps 2-14 for different compressions, samples, or groups (experiment dependent).

22. Calculate the permeability of samples using Darcy’s Law:

$$\boldsymbol{K = \frac{Q \cdot l \cdot \mu}{\Delta P \cdot A} = \frac{V \cdot l \cdot \mu}{t \cdot \Delta P \cdot A}}$$

Where: **V** is the volume measured.

$\boldsymbol{l}$ is the distance the De-Ionized water travels, in this case the spacer distance.

$\boldsymbol{\mu}$ is the viscosity of water, which is 0.001 Pas.

$\boldsymbol{t}$ is the time the measurement occurs over.

$\boldsymbol{A}$ is the area through which the De-Ionized water travels.

$\boldsymbol{\Delta P = (pressure\ head) \cdot (density\ of\ water) \cdot (gravity)}$ is the pressure.

B.7 Sectioning the Embedded CG Scaffold Samples Protocol; Aniline Blue Staining Protocol

B.7.1 Reference

O'Brien, Harley, et al., 2004; O'Brien, Harley, et al., 2005

B.7.2 Supplies

- Aniline Blue
    - 2.5mg aniline blue (Cat. No. AC40118-0250, Fisher Scientific, Hanover Park, IL)
    - 2mL glacial acetic acid (Mallinckrodt Chemical Co., Paris, KY)
    - 100mL distilled water
    - Filter before use
- 1% Acetic Acid
    - 1mL glacial acetic acid (Mallinckrodt Chemical Co.)
    - 99mL distilled water
- 95%, 100% ethanol
- Cytoseal 60 (Cat. No. NC9472256, Fisher Scientific)

B.7.3 Equipment

- Leica RM2165 microtome (Mannheim, Germany)

B.7.4 Procedure

1. Serially section the embedded CG scaffold samples on a Leica RM2165 microtome (Mannheim, Germany) at a 5um thickness. Mount each section on a glass microscope slide.

2. Dip the slides in the Aniline Blue solution for 2-4 minutes.

3. Place the slides into a 1% acetic acid solution for 1 minute.

4. Dip each slide 5-10 times in 95% alcohol until most of background staining goes away.

5. Dip each slide 5-10 times 100% alcohol to complete the rinsing process.

6. Mount each sample with 4 drops of Cytoseal 60 (Fisher Scientific) and coverslip. Try to not introduce air bubbles when placing the coverslip onto the sample.

7. Dry the coverslipped samples laying flat in a chemical fume hood for at minimum 1 hour.

8. Continue to dry the coverslipped samples while laying flat for an additional 2 days on the bench top or in the chemical fume hood.

B.8 Complete α-MEM Media for MC3T3 Pre-Osteoblasts

B.8.1 Supplies

- 440mL of α-MEM Media without Ascorbic Acid (SCS CMF, RAL 491, UIUC)
- 50mL Fetal Bovine Serum, Qualified, Heat-Inactivated (16140-71, Invitrogen)
- 5mL Penicillin-Streptomycin, Liquid (15140-122, Invitrogen)
- 5mL L-Glutamine, 200 mM (25030-081, Invitrogen)

B.8.2 Equipment

- Automatic Pipette
- 2x 25mL Sterile Pipette Tips
- 2x 5mL Sterile Pipette Tips
- Sterile 500mL Sealable Bottle
- 37°C Water Bath
- Bio Safety Cabinet
- 70% Ethanol (30% DI H_2O)

B.8.3 Procedure

1. The Fetal Bovine Serum (FBS), Penicillin-Streptomycin (Pen-Strep), and L-Glutamine (L-Glu) are stored at -20°C. It is necessary to thaw these using a 37°C Water Bath. After thawing, make sure they are adequately mixed, vortexing or shaking is recommended.

2. Turn on the Bio Safety Cabinet (BSC). Allow adequate time for it to properly turn on.

3. Spray with 70% Ethanol two 25mL Pipette Tips, two 5mL Pipette Tips, the Sterile 500mL Bottle, the Automatic Pipette, the α-MEM Media without Ascorbic Acid, FBS, Pen-Strep, and L-Glu. After spraying each item, place them into the ready BSC.

4. Carefully Pipette 440mL (88%) of the α-MEM without Ascorbic Acid into the empty 500mL Sterile Bottle using a 25mL Pipette Tip. This will take 16x25mL+2x20mL.

5. Carefully Pipette 50mL (10%) FBS into the 500mL Sterile Bottle.

6. Carefully pipette, using a 5mL Pipette Tip, 5mL (1%) Pen-Strep into the 500mL Sterile Bottle.

7. Carefully pipette, using a 5mL Pipette Tip, 5mL (1%) L-Glu into the 500mL Sterile Bottle.

8. Mix all the components together by gently shaking the 500mL Sterile Bottle. This is the "Complete α-MEM Media." Store this at 4°C when not in use.

9. Clean up the BSC by removing any Pipette Tips and/or empty containers. These should be placed in the Biowaste.

B.8.4 Notes

- Once open, if any of the Pipette Tips touch any surface within the BSC, they should be replaced to avoid contaminating any of the solutions in use.
- If any of the FBS or Anti-Anti remains, they should be placed at -20°C for storage.

B.9 Complete Mesenchymal Stem Cell Media for Human Mesenchymal Stem Cell Culture

B.9.1 Supplies

- 450 mL of d-MEM Media (SCS CMF, RAL 491, UIUC)
- 50 mL Fetal Bovine Serum, Mesenchymal Stem Cell-Qualified (12662-029, Invitrogen)
- 5 mL Antibiotic-Antimycotic, 100X (15240-062, Invitrogen)

B.9.2 Equipment

- Automatic Pipette
- 2x 25mL Sterile Pipette Tips
- 1x 5mL Sterile Pipette Tips
- Sterile 500mL Sealable Bottle
- 37°C Water Bath
- Bio Safety Cabinet
- 70% Ethanol (30% DI H_2O)

B.9.3 Procedure

1. The Fetal Bovine Serum (FBS) and Antibiotic-Antimycotic (Anti-Anti) are stored at -20°C. It is necessary to thaw these using a 37°C Water Bath. After thawing, make sure they are adequately mixed, vortexing or shaking is recommended.

2. Turn on the Bio Safety Cabinet (BSC). Allow adequate time for it to properly turn on.

3. Spray with 70% Ethanol two 25mL Pipette Tips, one 5mL Pipette Tips, the Sterile 500mL Bottle, the Automatic Pipette, the d-MEM Media without Ascorbic Acid, FBS, and Anti-Anti. After spraying each item, place them into the ready BSC.

4. Carefully Pipette 450mL (90%) of the d-MEM into the empty 500mL Sterile Bottle using a 25mL Pipette Tip. This will take 18x25mL.

5. Carefully Pipette 50mL (10%) FBS into the 500mL Sterile Bottle.

6. Carefully pipette, using a 5mL Pipette Tip, 5mL Anti-Anti into the 500mL Sterile Bottle.

7. Mix all the components together by gently shaking the 500mL Sterile Bottle. This is the "Complete d-MEM Media." Store this at 4°C when not in use.

8. Clean up the BSC by removing any Pipette Tips and/or empty containers. These should be placed in the Biowaste.

B.9.4 Notes

- Once open, if any of the Pipette Tips touch any surface within the BSC, they should be replaced to avoid contaminating any of the solutions in use.
- If any of the FBS, Pen-Strep, or L-Glue remains, they should be placed at -20°C for storage.

B.10 Passaging MC3T3 Pre-Osteoblasts Cell Culture

B.10.1 Supplies

- Complete α-MEM Media for MC3T3 Pre-Osteoblasts
- 3mL per flask Trypsin, 0.05% (1X) with EDTA 4Na, liquid (925300-062, Invitrogen)
- 10mL per flask Sterile Phosphate Buffered Saline without Calcium and Magnesium (CLSL Stock Room, CLSL C107, UIUC)

B.10.2 Equipment

- 1 BD Falcon 50mL Conical Centrifuge Tubes per 4 flasks (14-432-22, Fisher Scientific)
- Centrifuge capable of 1200rpm
- 75mL Polystyrene Cell Culture Flasks (CLSL Stock Room, CLSL C107, UIUC)
- Glass Beaker (for waste)
- Automatic Pipette
- 3x 10mL Sterile Pipette Tips
- 1x 5mL Sterile Pipette Tip
- 1x 25mL Sterile Pipette Tip
- Hemocytometer or other equivalent device and capable microscope
- 37°C Water Bath
- 70% Ethanol (30% DI H_2O)
- Sterile Cell Incubator
- Micro-Pipette and associated Micro Pipette Tips

B.10.3 Procedure

1. Trypsin is normally stored at -20°C. It is necessary to thaw it using a 37°C Water Bath prior to use. After thawing, make sure the Trypsin is adequately mixed either by vortexing or shaking.

2. Because the Complete α-MEM Media is stored at 4°C, it is necessary to bring warm it up to 37°C prior to use. Again, this can be done using the 37°C Water Bath.

3. In the same manner as the Complete α-MEM Media, warm up the Sterile Phosphate Buffered Saline without Calcium and Magnesium (PBS) to 37°C.

4. Turn on the Bio Safety Cabinet (BSC) and allow adequate time for it to become ready prior to putting things in it.

5. Spray with 70% Ethanol the thawed Trypsin, the warmed up Complete α-MEM Media, the 50mL Conical Centrifuge Tubes, the Glass Beaker (for waste), three 10mL Sterile Pipette Tips, one 5mL Steril Pipette Tip, one 25mL Sterile Pipette Tip, the Automatic Pipette, and any new Cell Culture Flasks. After spraying each item, place them into the ready BSC.

6. Begin by using one 10mL Sterile Pipette Tip to remove any old media from the flasks. Pipette this media into the Glass Beaker (for waste). Cap each flask after the removal of the media. Be careful not to disturb the bottom of the flask (where the cells reside) with the pipette tip.

7. Using a clean 10mL Sterile Pipette, pipette 10mL PBS into the now empty flasks. Cap all the flasks and gently swish the PBS around inside. Then using the same 10mL Sterile Pipette Tip, pipette remove the 10mL PBS from each flask and pipette into the Glass Beaker.

8. Using a clean 5mL Sterile Pipette, pipette 3mL Trypsin into each of the Cell Culture Flasks. Afterwards, cap each flask and place into the cell incubator for 4min. Remember to spray each flask with 70% Ethanol prior to placing them into the Sterile Incubator.

9. After 4min, remove the flasks from the sterile incubator. Gently tap the sides of each flask to loosen any cells that are still attached. Using a microscope, verify that the cells are detached and floating. Then, after being sprayed with 70% Ethanol, the flasks can be placed back into the BSC.

10. Using a 10mL Sterile Pipette Tip, immediately add 6mL Complete α-MEM Media to each flask. Cap the flasks and gently swish any Media and Trypsin around inside. This deactivates the Trypsin.

11. Using the same 10mL Sterile Pipette Tip, pipette a majority of the 9mL Media and Trypsin in each flask up and then over the bottom of the flask. This washes any cells that are yet attached on the bottom of the flask. After repeating this twice, pipette all 9mL into a 50mL conical tube. Each conical tube will hold up to 45mL (or five flasks).

12. Thoroughly mix each cell solution using either a 10mL or 25mL Sterile Pipette. Remove 20µL of this mixed cell solution into a micro-centrifuge tube using a micro-pipette.

B.11 Operation of the DXA for Bone Mineral Density Analysis

B.11.1 Equipment

- Hologic QDR 4500A

B.11.2 Procedure

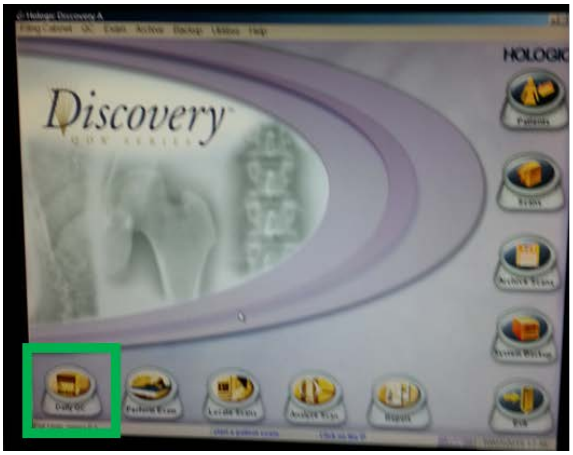

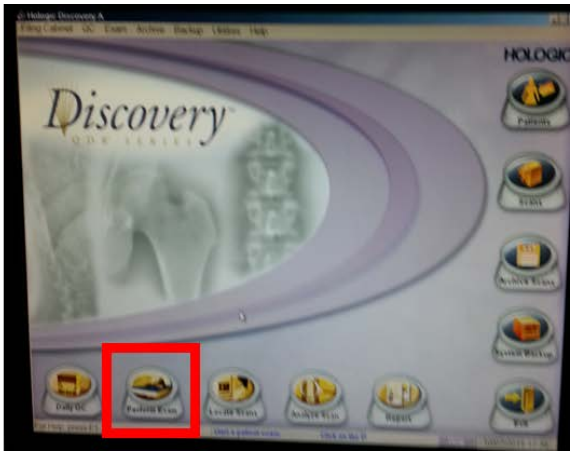

1. If you are the first user of the day, select “Daily OC” (green box), no other option will be available. This starts the daily calibration. If the instrument has already been calibrated, choose the “Perform Exam” (red box).

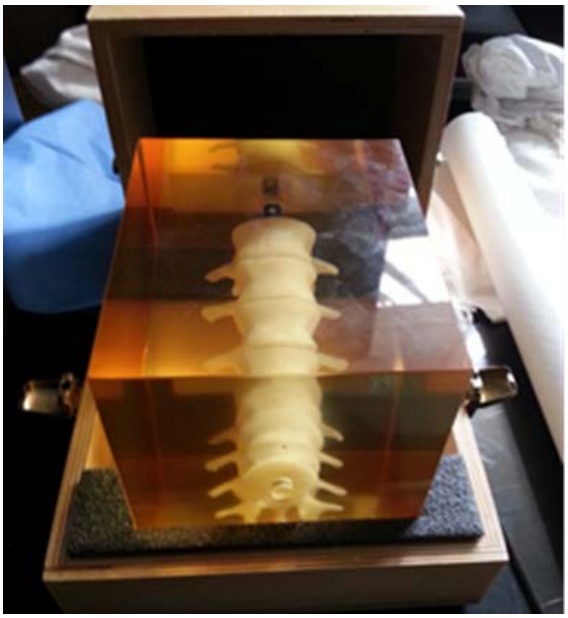

2. If you are performing the “Daily OC” follow the on screen instructions. When prompted for the calibration spine phantom, it is located in the wood box on the side of the room. CAREFULLY handle and maneuver it onto the bench and align it with the laser. To align: (1) have the crosshair centered on the circle within the black dot; (2) orient the phantom so that the spine is extending to the right of the crosshair; (3) position the right (as opposed to left, top, bottom) crosshair line such that while maintaining (1), so the line is situated in the center of the text. Place the phantom back in its case following completion of the scan.

3. If the crosshair disappears during calibration or sample positioning, you may reactivate by pressing the laser button on the console next to the apparatus.

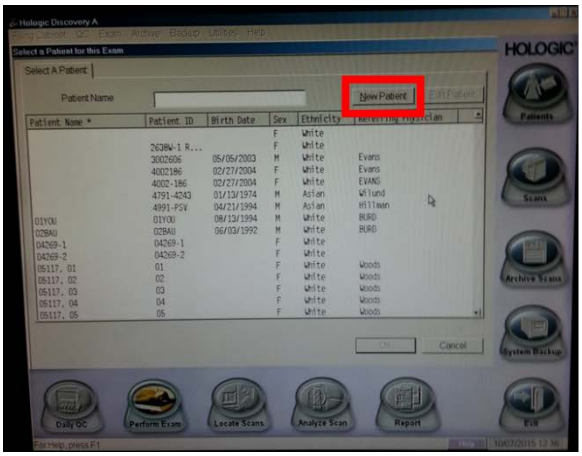

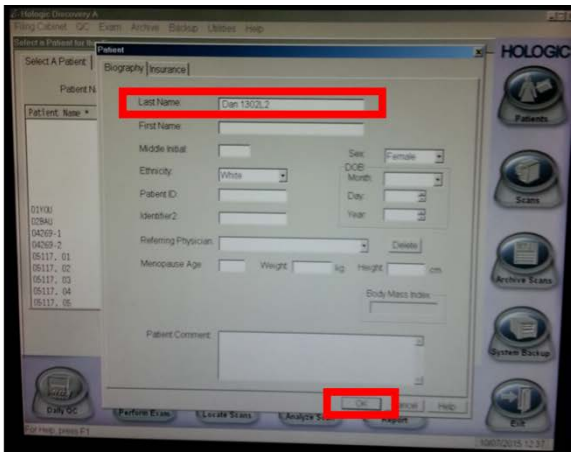

4. After pressing the “preform exam” button, select “new patient,” input your sample name, then click ok. Additional information is not necessary and maybe skipped.

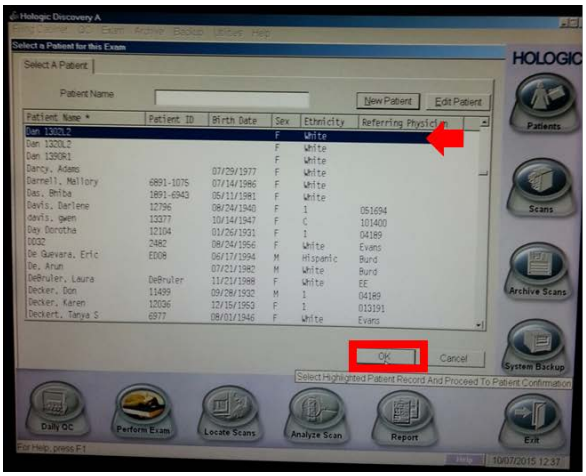
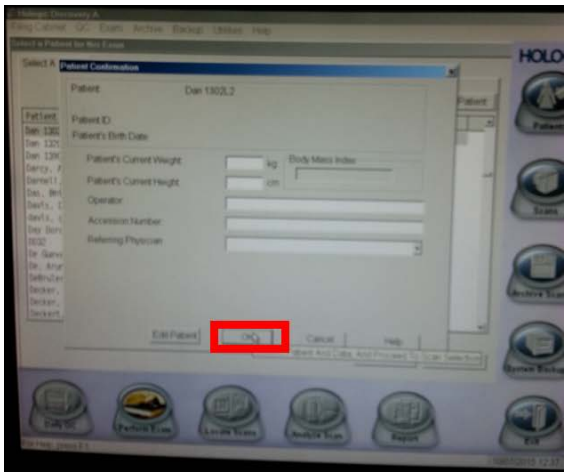

5. Ensure that after creation you have your sample (patient) selected and press ok. You will be prompted for additional information, skip this as it does not apply and click ok.

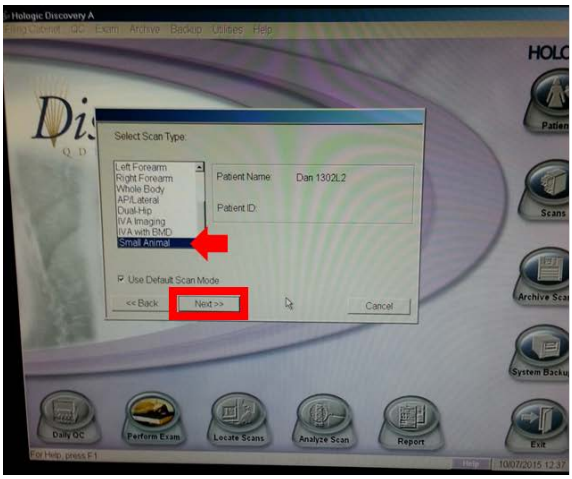
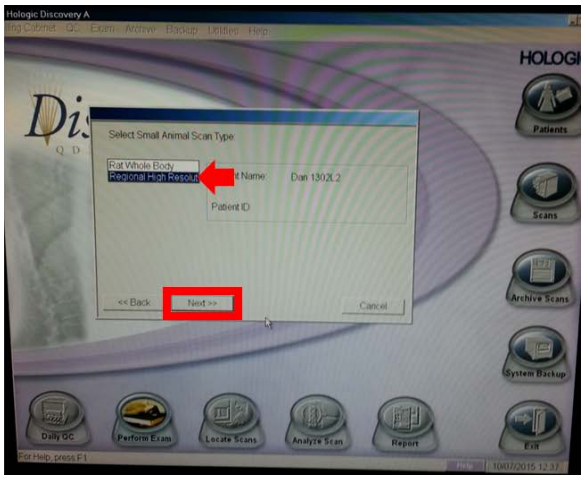

6. You will then be prompted to select your scan type. Select “small animal” (at the bottom of the list) and click next. Then select “regional high resolution.” If your sample is too large, you can select “rat whole body.” However, for best results use the “regional high resolution.”
7. You may now place the appropriate absorbent material on top of the bedding. It is recommended: (1) several paper towels; (2) two layers of bench paper (absorbent side face up); (3) more paper towels.

Remember, this apparatus is for human usage, ensure that there is no chance of chemical or biological contamination. Adequate preparation will allow for simple clean up once data collection is complete.

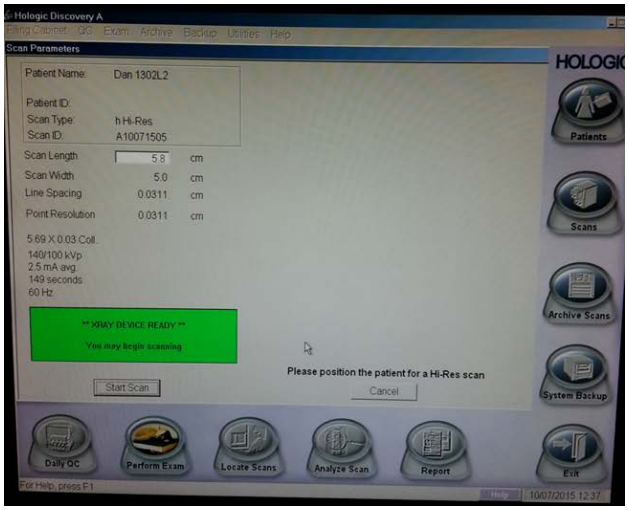

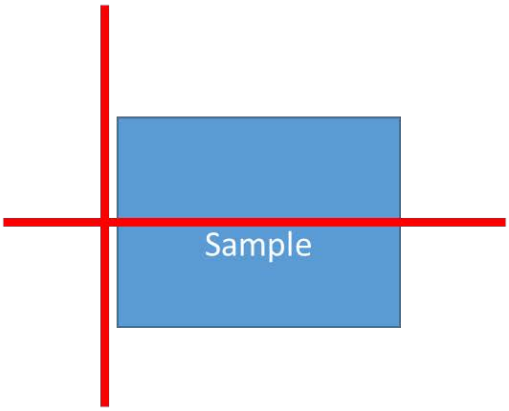

8. Place the sample to the right of the crosshair prior to starting the scan by hitting “start scan.”

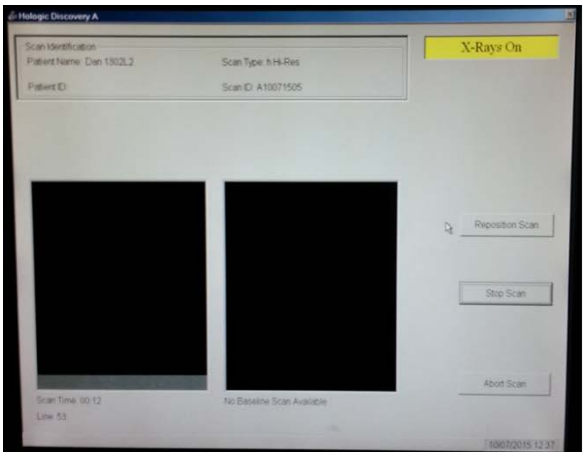

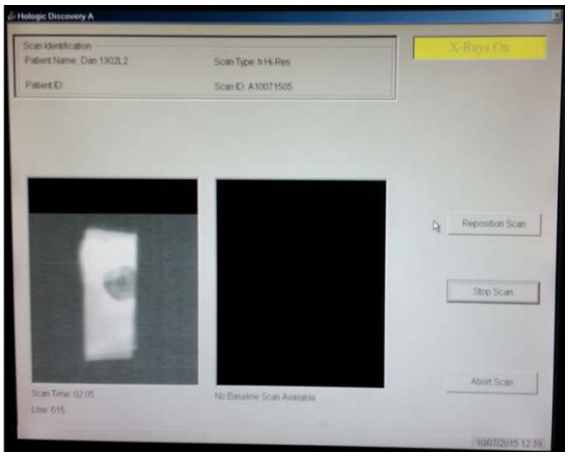

9. The scan will then commence. For a scan distance of 5.8cm, the total scan time was approximately 1.5-2min.

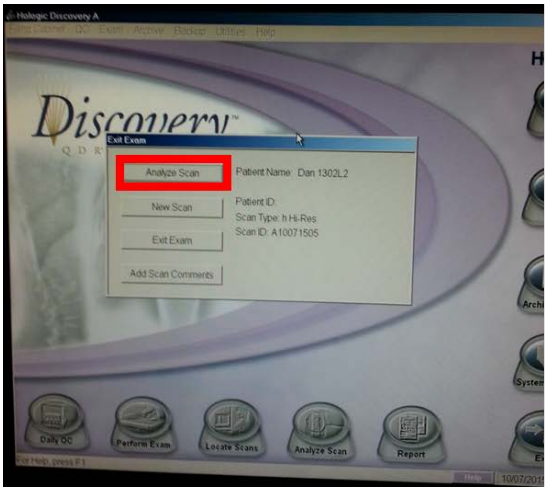

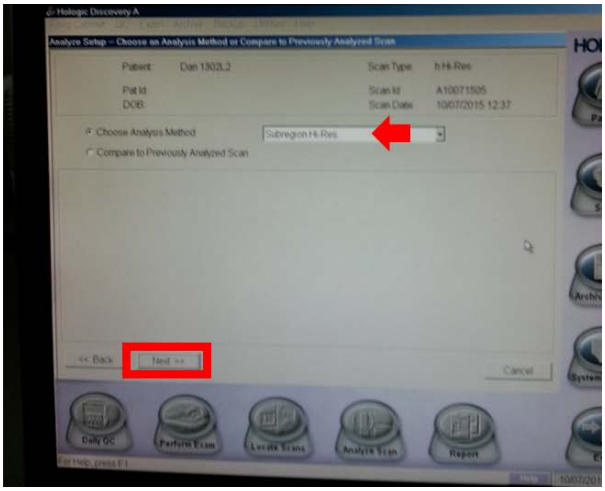

10. Following completion of the scan, select “analyze scan,” then select the analysis method of “subregion hi-res.”

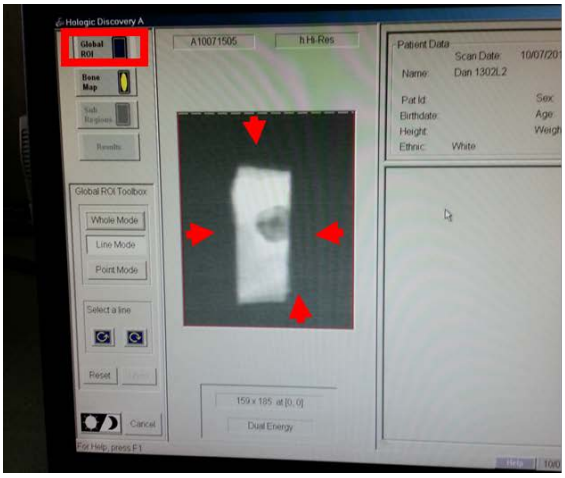

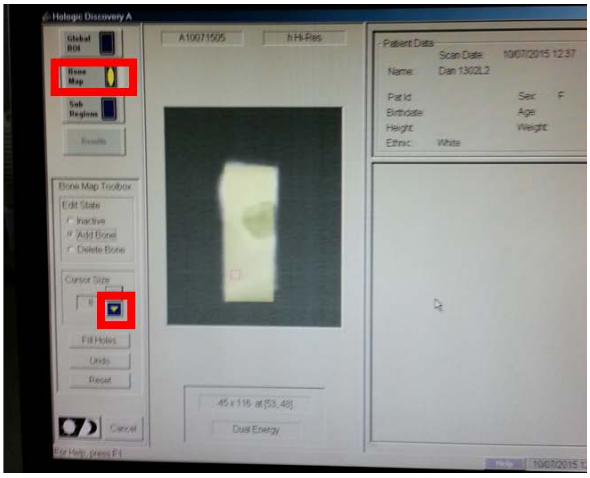

11. Analysis of the scan then consisted of selecting the global region of interest (ROI) by dragging the vertical and horizontal cutoff lines to outline the sample. Following this, ensure the “bone map” has properly highlighted all of the bone sample.

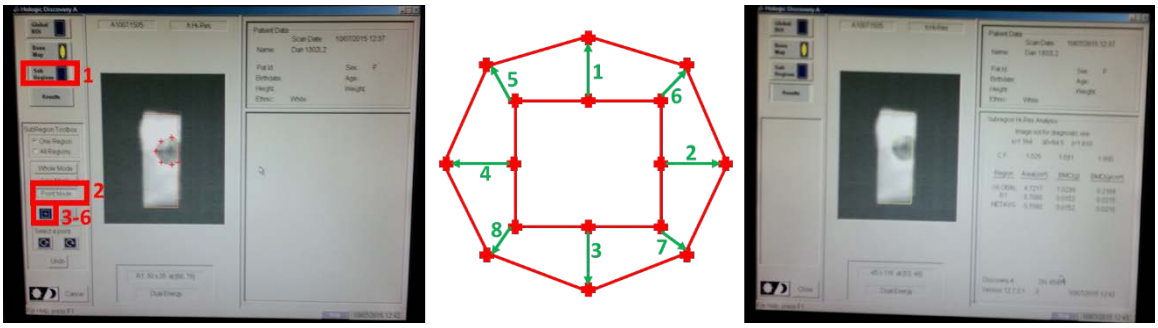

12. The next step in data analysis involved the selection of a sub region. Select the “sub region” step with “point mode.” The ROI sub-region will appear as a box, this box maybe selected and dragged to the center of your defect. With the sub-region selected, click the “+” button to add additional inflection points to the sub-region, for creating an octagon this requires four additional sub regions. Drag the corners to extend the sub-region to the approximation of an octagon. Once properly outlined, click on the “results” tab to access the scan output.

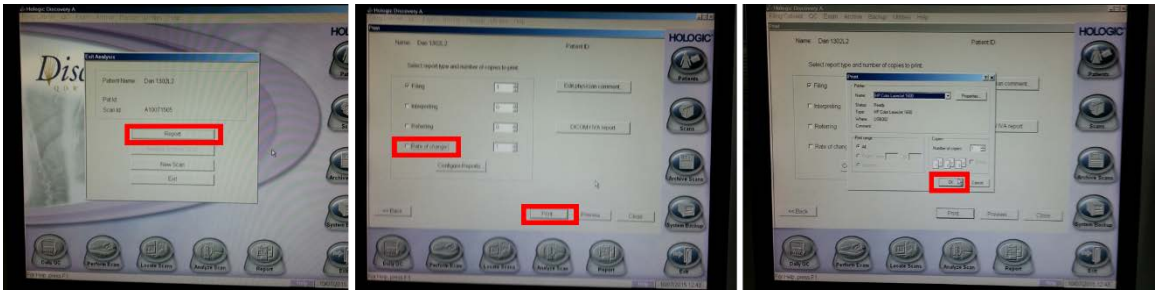

13. After analyzing the scan, click “close” to select “report.” Uncheck the rate of change option, then click print. The default printer should be the printer next to the computer, check the make and model to ensure that it is.
14. Select “perform exam” to scan another example.

Note: analysis can be performed a second time or retroactively, or printed, by selecting “scans” and locating the correct sample (patient) name within the database.

REFERENCES

1. Clarke, B., *Normal bone anatomy and physiology.* Clinical journal of the American Society of Nephrology : CJASN, 2008. **3 Suppl 3**: p. S131-9.
2. Wang, X. and Q. Ni, *Determination of cortical bone porosity and pore size distribution using a low field pulsed NMR approach.* Journal of orthopaedic research : official publication of the Orthopaedic Research Society, 2003. **21**(2): p. 312-9.
3. Kragstrup, J. and F. Melsen, *Three-dimensional morphology of trabecular bone osteons reconstructed from serial sections.* Metabolic bone disease & related research, 1983. **5**(3): p. 127-30.
4. Gilbert, S.F., *Developmental Biology*. 6th ed2000, Sunderland (MA): Sinauer Associates.
5. Mohsin, S., F.J. O'Brien, and T.C. Lee, *Microcracks in compact bone: a three-dimensional view.* Journal of anatomy, 2006. **209**(1): p. 119-24.
6. Marsell, R. and T.A. Einhorn, *The biology of fracture healing.* Injury, 2011. **42**(6): p. 551-5.
7. Einhorn, T.A. and L.C. Gerstenfeld, *Fracture healing: mechanisms and interventions.* Nature reviews. Rheumatology, 2015. **11**(1): p. 45-54.
8. Gaston, M.S. and A.H. Simpson, *Inhibition of fracture healing.* The Journal of bone and joint surgery. British volume, 2007. **89**(12): p. 1553-60.
9. Ponseti, I.V., *History of Orthopaedic Surgery*. The Iowa Orthopaedic Journal, 1991. **11**: p. 59-64.
10. Pollak, A.N., Watkins-Castillo, S.I. *BMUS: The Burden of Musculoskeletal Diseases in the United States*. 2014 [cited 2015 10/1/2015]; Available from: http://www.boneandjointburden.org/2014-report/vi0/injuries.
11. Yelin, E.H., Watkins-Castillo, S.I. *Economic Cost of Musculoskeletal Injuries*. 2014 [cited 2015 10/1/2015]; Available from: http://www.boneandjointburden.org/2014-report/vif0/economic-cost-musculoskeletal-injuries.
12. Parker, S.E., et al., *Updated National Birth Prevalence estimates for selected birth defects in the United States, 2004-2006.* Birth defects research. Part A, Clinical and molecular teratology, 2010. **88**(12): p. 1008-16.
13. (NBDPN), T.C.f.D.C.a.P.C.N.B.D.P.N. *Prevalence (Number of Cases) of Cleft Lip and Cleft Palate*. 2014 [cited 2015 10/1/2015]; Available from: http://www.nidcr.nih.gov/DataStatistics/FindDataByTopic/CraniofacialBirthDefects/PrevalenceCleft%20LipCleftPalate.htm.
14. Kraft, A., et al., *Craniomaxillofacial trauma: synopsis of 14,654 cases with 35,129 injuries in 15 years.* Craniomaxillofacial trauma & reconstruction, 2012. **5**(1): p. 41-50.
15. Handoll, H.H. and R. Madhok, *Closed reduction methods for treating distal radial fractures in adults.* The Cochrane database of systematic reviews, 2003(1): p. CD003763.
16. Fan, K., et al., *Top five craniofacial techniques for training in plastic surgery residency.* Plastic and reconstructive surgery, 2012. **129**(3): p. 477e-487e.
17. Burwell, R.G., *Studies in the Transplantation of Bone. Vii. The Fresh Composite Homograft-Autograft of Cancellous Bone; an Analysis of Factors Leading to Osteogenesis in Marrow Transplants and in Marrow-Containing Bone Grafts.* The Journal of bone and joint surgery. British volume, 1964. **46**: p. 110-40.
18. Boyne, P.J., *Autogenous cancellous bone and marrow transplants.* Clinical orthopaedics and related research, 1970. **73**: p. 199-209.
19. Nade, S. and R.G. Burwell, *Decalcified bone as a substrate for osteogenesis. An appraisal of the interrelation of bone and marrow in combined grafts.* The Journal of bone and joint surgery. British volume, 1977. **59**(2): p. 189-96.

20. Nade, S., *Clinical implications of cell function in osteogenesis. A reappraisal of bone-graft surgery.* Annals of the Royal College of Surgeons of England, 1979. **61**(3): p. 189-94.
21. Langer, R. and J.P. Vacanti, *Tissue engineering.* Science, 1993. **260**(5110): p. 920-6.
22. Mitragotri, S. and J. Lahann, *Physical approaches to biomaterial design.* Nature materials, 2009. **8**(1): p. 15-23.
23. Kohn, J., *New approaches to biomaterials design.* Nature materials, 2004. **3**(11): p. 745-7.
24. Drogset, J.O., et al., *Autologous patellar tendon and quadrupled hamstring grafts in anterior cruciate ligament reconstruction: a prospective randomized multicenter review of different fixation methods.* Knee surgery, sports traumatology, arthroscopy : official journal of the ESSKA, 2010. **18**(8): p. 1085-93.
25. Timmer, M.D., et al., *Fabrication of poly(propylene fumarate)-based orthopaedic implants by photo-crosslinking through transparent silicone molds.* Biomaterials, 2003. **24**(25): p. 4707-14.
26. Khiste, S.V., V. Ranganath, and A.S. Nichani, *Evaluation of tensile strength of surgical synthetic absorbable suture materials: an in vitro study.* Journal of periodontal & implant science, 2013. **43**(3): p. 130-5.
27. Chou, S.Y., C.M. Cheng, and P.R. LeDuc, *Composite polymer systems with control of local substrate elasticity and their effect on cytoskeletal and morphological characteristics of adherent cells.* Biomaterials, 2009. **30**(18): p. 3136-42.
28. Engler, A.J., et al., *Matrix elasticity directs stem cell lineage specification.* Cell, 2006. **126**(4): p. 677-89.
29. Pamula, E., et al., *The influence of pore size on colonization of poly(L-lactide-glycolide) scaffolds with human osteoblast-like MG 63 cells in vitro.* Journal of materials science. Materials in medicine, 2008. **19**(1): p. 425-35.
30. Hallab, N.J., et al., *Evaluation of metallic and polymeric biomaterial surface energy and surface roughness characteristics for directed cell adhesion.* Tissue engineering, 2001. **7**(1): p. 55-71.
31. Lutolf, M.P. and J.A. Hubbell, *Synthetic biomaterials as instructive extracellular microenvironments for morphogenesis in tissue engineering.* Nature Biotechnology, 2005. **23**(1): p. 47-55.
32. Tocce, E.J., et al., *Functionalization of reactive polymer multilayers with RGD and an antifouling motif: RGD density provides control over human corneal epithelial cell-substrate interactions.* Journal of biomedical materials research. Part A, 2012. **100**(1): p. 84-93.
33. Wei, G. and P.X. Ma, *Structure and properties of nano-hydroxyapatite/polymer composite scaffolds for bone tissue engineering.* Biomaterials, 2004. **25**(19): p. 4749-57.
34. Lee, K., E.A. Silva, and D.J. Mooney, *Growth factor delivery-based tissue engineering: general approaches and a review of recent developments.* Journal of the Royal Society, Interface / the Royal Society, 2011. **8**(55): p. 153-70.
35. Uchida, A., et al., *The use of ceramics for bone replacement. A comparative study of three different porous ceramics.* The Journal of bone and joint surgery. British volume, 1984. **66**(2): p. 269-75.
36. Kitsugi, T., et al., *Four calcium phosphate ceramics as bone substitutes for non-weight-bearing.* Biomaterials, 1993. **14**(3): p. 216-24.
37. Yuan, H., et al., *Osteoinductive ceramics as a synthetic alternative to autologous bone grafting.* Proceedings of the National Academy of Sciences of the United States of America, 2010. **107**(31): p. 13614-9.
38. Combes, C. and C. Rey, *Amorphous calcium phosphates: synthesis, properties and uses in biomaterials.* Acta biomaterialia, 2010. **6**(9): p. 3362-78.
39. Samavedi, S., A.R. Whittington, and A.S. Goldstein, *Calcium phosphate ceramics in bone tissue engineering: a review of properties and their influence on cell behavior.* Acta biomaterialia, 2013. **9**(9): p. 8037-45.

40. Suzawa, Y., et al., *Biomineral/Agarose Composite Gels Enhance Proliferation of Mesenchymal Stem Cells with Osteogenic Capability.* International journal of molecular sciences, 2015. **16**(6): p. 14245-58.
41. Wang, Y., et al., *[Effect of staining method and sintering temperature on the color of porcelain-fused-to-metal restorations].* Shanghai kou qiang yi xue = Shanghai journal of stomatology, 2004. **13**(6): p. 553-6.
42. Flauder, S., R. Sajzew, and F.A. Muller, *Mechanical properties of porous beta-tricalcium phosphate composites prepared by ice-templating and poly(epsilon-caprolactone) impregnation.* ACS applied materials & interfaces, 2015. **7**(1): p. 845-51.
43. Rogina, A., et al., *In Situ Hydroxyapatite Content Affects the Cell Differentiation on Porous Chitosan/Hydroxyapatite Scaffolds.* Annals of biomedical engineering, 2015.
44. Mottaghitalab, F., et al., *Silk as a potential candidate for bone tissue engineering.* Journal of controlled release : official journal of the Controlled Release Society, 2015. **215**: p. 112-28.
45. Villa, M.M., et al., *Improving the permeability of lyophilized collagen-hydroxyapatite scaffolds for cell-based bone regeneration with a gelatin porogen.* Journal of biomedical materials research. Part B, Applied biomaterials, 2015.
46. Furth, M.E., A. Atala, and M.E. Van Dyke, *Smart biomaterials design for tissue engineering and regenerative medicine.* Biomaterials, 2007. **28**(34): p. 5068-73.
47. Banerjee, A., et al., *The influence of hydrogel modulus on the proliferation and differentiation of encapsulated neural stem cells.* Biomaterials, 2009. **30**(27): p. 4695-9.
48. Weisgerber, D.W., et al., *The impact of discrete compartments of a multi-compartment collagen-GAG scaffold on overall construct biophysical properties.* Journal of the mechanical behavior of biomedical materials, 2013. **28**: p. 26-36.
49. Hannink, G. and J.J. Arts, *Bioresorbability, porosity and mechanical strength of bone substitutes: what is optimal for bone regeneration?* Injury, 2011. **42 Suppl 2**: p. S22-5.
50. Rho, J.Y., R.B. Ashman, and C.H. Turner, *Young's modulus of trabecular and cortical bone material: ultrasonic and microtensile measurements.* Journal of biomechanics, 1993. **26**(2): p. 111-9.
51. Reddi, A.H., *Regulation of cartilage and bone differentiation by bone morphogenetic proteins.* Current opinion in cell biology, 1992. **4**(5): p. 850-5.
52. Kirker-Head, C.A., *Potential applications and delivery strategies for bone morphogenetic proteins.* Advanced drug delivery reviews, 2000. **43**(1): p. 65-92.
53. Warnke, P.H., et al., *Growth and transplantation of a custom vascularised bone graft in a man.* Lancet, 2004. **364**(9436): p. 766-70.
54. Urist, M.R., *Bone: formation by autoinduction.* Science, 1965. **150**(3698): p. 893-9.
55. Johnson, E.E. and M.R. Urist, *One-stage lengthening of femoral nonunion augmented with human bone morphogenetic protein.* Clinical orthopaedics and related research, 1998(347): p. 105-16.
56. Quinlan, E., et al., *Development of collagen-hydroxyapatite scaffolds incorporating PLGA and alginate microparticles for the controlled delivery of rhBMP-2 for bone tissue engineering.* Journal of controlled release : official journal of the Controlled Release Society, 2015. **198**: p. 71-9.
57. Epstein, N.E., *Pros, cons, and costs of INFUSE in spinal surgery.* Surgical neurology international, 2011. **2**: p. 10.
58. Epstein, N.E., *Complications due to the use of BMP/INFUSE in spine surgery: The evidence continues to mount.* Surgical neurology international, 2013. **4**(Suppl 5): p. S343-52.
59. Brouillet, F., et al., *Biomimetic apatite-based composite materials obtained by spark plasma sintering (SPS): physicochemical and mechanical characterizations.* Journal of materials science. Materials in medicine, 2015. **26**(8): p. 223.

60. Przekora, A., K. Palka, and G. Ginalska, *Chitosan/beta-1,3-glucan/calcium phosphate ceramics composites--novel cell scaffolds for bone tissue engineering application.* Journal of biotechnology, 2014. **182-183**: p. 46-53.
61. Jin, Y., et al., *Bio-inspired mineralization of hydroxyapatite in 3D silk fibroin hydrogel for bone tissue engineering.* Colloids and surfaces. B, Biointerfaces, 2015. **134**: p. 339-45.
62. Palazzo, B., et al., *Fabrication, characterization and cell cultures on a novel composite chitosan-nano-hydroxyapatite scaffold.* International journal of immunopathology and pharmacology, 2011. **24**(1 Suppl 2): p. 73-8.
63. Kanungo, I., et al., *Influence of PCL on the material properties of collagen based biocomposites and in vitro evaluation of drug release.* Materials science & engineering. C, Materials for biological applications, 2013. **33**(8): p. 4651-9.
64. Patel, J.J., et al., *Dual Delivery of EPO and BMP2 from a Novel Modular Poly-varepsilon-Caprolactone Construct to Increase the Bone Formation in Prefabricated Bone Flaps.* Tissue engineering. Part C, Methods, 2015. **21**(9): p. 889-97.
65. Chwalek, K., et al., *In vitro bioengineered model of cortical brain tissue.* Nature protocols, 2015. **10**(9): p. 1362-73.
66. Cerri, F., et al., *Peripheral nerve morphogenesis induced by scaffold micropatterning.* Biomaterials, 2014. **35**(13): p. 4035-45.
67. Arora, A., A. Kothari, and D.S. Katti, *Pore orientation mediated control of mechanical behavior of scaffolds and its application in cartilage-mimetic scaffold design.* Journal of the mechanical behavior of biomedical materials, 2015. **51**: p. 169-83.
68. Zhao, X., et al., *Conditions for seeding and promoting neo-auricular cartilage formation in a fibrous collagen scaffold.* Journal of cranio-maxillo-facial surgery : official publication of the European Association for Cranio-Maxillo-Facial Surgery, 2015. **43**(3): p. 382-9.
69. Mullen, L.M., et al., *Bioactive IGF-1 release from collagen-GAG scaffold to enhance cartilage repair in vitro.* Journal of materials science. Materials in medicine, 2015. **26**(1): p. 5325.
70. Pang, Y., et al., *The temporal and spatial dynamics of microscale collagen scaffold remodeling by smooth muscle cells.* Biomaterials, 2009. **30**(11): p. 2023-31.
71. Zhao, W., et al., *Diaphragmatic muscle reconstruction with an aligned electrospun poly(epsilon-caprolactone)/collagen hybrid scaffold.* Biomaterials, 2013. **34**(33): p. 8235-40.
72. Serena, E., et al., *Electrophysiologic stimulation improves myogenic potential of muscle precursor cells grown in a 3D collagen scaffold.* Neurological research, 2008. **30**(2): p. 207-14.
73. Villa, M.M., et al., *Bone tissue engineering with a collagen-hydroxyapatite scaffold and culture expanded bone marrow stromal cells.* Journal of biomedical materials research. Part B, Applied biomaterials, 2015. **103**(2): p. 243-53.
74. Xia, Z., M.M. Villa, and M. Wei, *A Biomimetic Collagen-Apatite Scaffold with a Multi-Level Lamellar Structure for Bone Tissue Engineering.* Journal of materials chemistry. B, Materials for biology and medicine, 2014. **2**(14): p. 1998-2007.
75. Long, T., et al., *Fabrication of three-dimensional porous scaffold based on collagen fiber and bioglass for bone tissue engineering.* Journal of biomedical materials research. Part B, Applied biomaterials, 2015. **103**(7): p. 1455-64.
76. Williams, D., *Collagen: ubiquitous in nature, multifunctional in devices.* Medical device technology, 1998. **9**(6): p. 10-3.
77. Di Lullo, G.A., et al., *Mapping the ligand-binding sites and disease-associated mutations on the most abundant protein in the human, type I collagen.* The Journal of biological chemistry, 2002. **277**(6): p. 4223-31.
78. Yannas, I.V., et al., *Synthesis and characterization of a model extracellular matrix that induces partial regeneration of adult mammalian skin.* Proceedings of the National Academy of Sciences of the United States of America, 1989. **86**(3): p. 933-7.

79. Burke, J.F., et al., *Successful use of a physiologically acceptable artificial skin in the treatment of extensive burn injury.* Annals of surgery, 1981. **194**(4): p. 413-28.
80. Yannas, I.V. and J.F. Burke, *Design of an artificial skin. I. Basic design principles.* Journal of biomedical materials research, 1980. **14**(1): p. 65-81.
81. Yannas, I.V., et al., *Design of an artificial skin. II. Control of chemical composition.* Journal of biomedical materials research, 1980. **14**(2): p. 107-32.
82. Dagalakis, N., et al., *Design of an artificial skin. Part III. Control of pore structure.* Journal of biomedical materials research, 1980. **14**(4): p. 511-28.
83. Chamberlain, L.J., et al., *Collagen-GAG substrate enhances the quality of nerve regeneration through collagen tubes up to level of autograft.* Experimental neurology, 1998. **154**(2): p. 315-29.
84. Chamberlain, L.J., et al., *Near-terminus axonal structure and function following rat sciatic nerve regeneration through a collagen-GAG matrix in a ten-millimeter gap.* Journal of neuroscience research, 2000. **60**(5): p. 666-77.
85. Spilker, M.H., et al., *Contraction of collagen-glycosaminoglycan matrices by peripheral nerve cells in vitro.* Biomaterials, 2001. **22**(10): p. 1085-93.
86. Farrell, E., et al., *A collagen-glycosaminoglycan scaffold supports adult rat mesenchymal stem cell differentiation along osteogenic and chondrogenic routes.* Tissue engineering, 2006. **12**(3): p. 459-68.
87. Lynn, A.K., et al., *Design of a multiphase osteochondral scaffold. I. Control of chemical composition.* Journal of biomedical materials research. Part A, 2010. **92**(3): p. 1057-65.
88. Harley, B.A., et al., *Design of a multiphase osteochondral scaffold. II. Fabrication of a mineralized collagen-glycosaminoglycan scaffold.* Journal of biomedical materials research. Part A, 2010. **92**(3): p. 1066-77.
89. Harley, B.A., et al., *Design of a multiphase osteochondral scaffold III: Fabrication of layered scaffolds with continuous interfaces.* Journal of biomedical materials research. Part A, 2010. **92**(3): p. 1078-93.
90. Getgood, A.M., et al., *Evaluation of early-stage osteochondral defect repair using a biphasic scaffold based on a collagen-glycosaminoglycan biopolymer in a caprine model.* The Knee, 2012. **19**(4): p. 422-30.
91. O'Brien, F.J., et al., *Influence of freezing rate on pore structure in freeze-dried collagen-GAG scaffolds.* Biomaterials, 2004. **25**(6): p. 1077-86.
92. O'Brien, F.J., et al., *The effect of pore size on cell adhesion in collagen-GAG scaffolds.* Biomaterials, 2005. **26**(4): p. 433-41.
93. O'Brien, F.J., et al., *The effect of pore size on permeability and cell attachment in collagen scaffolds for tissue engineering.* Technology and health care : official journal of the European Society for Engineering and Medicine, 2007. **15**(1): p. 3-17.
94. Harley, B.A., et al., *Mechanical characterization of collagen-glycosaminoglycan scaffolds.* Acta biomaterialia, 2007. **3**(4): p. 463-74.
95. Harley, B.A., et al., *A new technique for calculating individual dermal fibroblast contractile forces generated within collagen-GAG scaffolds.* Biophysical journal, 2007. **93**(8): p. 2911-22.
96. Harley, B.A., et al., *Fabricating tubular scaffolds with a radial pore size gradient by a spinning technique.* Biomaterials, 2006. **27**(6): p. 866-74.
97. Caliari, S.R. and B.A. Harley, *The effect of anisotropic collagen-GAG scaffolds and growth factor supplementation on tendon cell recruitment, alignment, and metabolic activity.* Biomaterials, 2011. **32**(23): p. 5330-40.
98. Harley, B.A., et al., *Optimal degradation rate for collagen chambers used for regeneration of peripheral nerves over long gaps.* Cells, tissues, organs, 2004. **176**(1-3): p. 153-65.
99. Lynn, A.K., I.V. Yannas, and W. Bonfield, *Antigenicity and immunogenicity of collagen.* Journal of biomedical materials research. Part B, Applied biomaterials, 2004. **71**(2): p. 343-54.

100. Gonnerman, E.A., et al., *The promotion of HL-1 cardiomyocyte beating using anisotropic collagen-GAG scaffolds.* Biomaterials, 2012. **33**(34): p. 8812-21.
101. Caliari, S.R., et al., *The influence of collagen-glycosaminoglycan scaffold relative density and microstructural anisotropy on tenocyte bioactivity and transcriptomic stability.* Journal of the mechanical behavior of biomedical materials, 2012. **11**: p. 27-40.
102. Martin, T.A., et al., *The generation of biomolecular patterns in highly porous collagen-GAG scaffolds using direct photolithography.* Biomaterials, 2011. **32**(16): p. 3949-57.
103. Pence, J.C., et al., *Strategies to balance covalent and non-covalent biomolecule attachment within collagen-GAG biomaterials.* Biomaterials science, 2014. **2**(9): p. 1296-1304.
104. Alsop, A.T., et al., *Photopatterning of vascular endothelial growth factor within collagen-glycosaminoglycan scaffolds can induce a spatially confined response in human umbilical vein endothelial cells.* Acta biomaterialia, 2014. **10**(11): p. 4715-22.
105. Pence, J.C., K.B. Clancy, and B.A. Harley, *The induction of pro-angiogenic processes within a collagen scaffold via exogenous estradiol and endometrial epithelial cells.* Biotechnology and bioengineering, 2015. **112**(10): p. 2185-94.
106. Hortensius, R.A., et al., *The effect of glycosaminoglycan content on polyethylenimine-based gene delivery within three-dimensional collagen-GAG scaffolds.* Biomaterials science, 2015. **3**(4): p. 645-54.
107. Lynn, A.K. and W. Bonfield, *A novel method for the simultaneous, titrant-free control of pH and calcium phosphate mass yield.* Accounts of chemical research, 2005. **38**(3): p. 202-7.
108. Kanungo, B.P., et al., *Characterization of mineralized collagen-glycosaminoglycan scaffolds for bone regeneration.* Acta biomaterialia, 2008. **4**(3): p. 490-503.
109. Bloebaum, R.D., et al., *Determining mineral content variations in bone using backscattered electron imaging.* Bone, 1997. **20**(5): p. 485-90.
110. Pietrzak, W.S. and J. Woodell-May, *The composition of human cortical allograft bone derived from FDA/AATB-screened donors.* The Journal of craniofacial surgery, 2005. **16**(4): p. 579-85.
111. Sierpowska, J., et al., *Effect of human trabecular bone composition on its electrical properties.* Medical engineering & physics, 2007. **29**(8): p. 845-52.
112. Yeni, Y.N., C.U. Brown, and T.L. Norman, *Influence of bone composition and apparent density on fracture toughness of the human femur and tibia.* Bone, 1998. **22**(1): p. 79-84.
113. Al-Munajjed, A.A., J.P. Gleeson, and F.J. O'Brien, *Development of a collagen calcium-phosphate scaffold as a novel bone graft substitute.* Studies in health technology and informatics, 2008. **133**: p. 11-20.
114. Al-Munajjed, A.A., et al., *Development of a biomimetic collagen-hydroxyapatite scaffold for bone tissue engineering using a SBF immersion technique.* Journal of biomedical materials research. Part B, Applied biomaterials, 2009. **90**(2): p. 584-91.
115. Gleeson, J.P., N.A. Plunkett, and F.J. O'Brien, *Addition of hydroxyapatite improves stiffness, interconnectivity and osteogenic potential of a highly porous collagen-based scaffold for bone tissue regeneration.* European cells & materials, 2010. **20**: p. 218-30.
116. Curtin, C.M., et al., *Innovative collagen nano-hydroxyapatite scaffolds offer a highly efficient non-viral gene delivery platform for stem cell-mediated bone formation.* Advanced materials, 2012. **24**(6): p. 749-54.
117. Curtin, C.M., et al., *Combinatorial gene therapy accelerates bone regeneration: non-viral dual delivery of VEGF and BMP2 in a collagen-nanohydroxyapatite scaffold.* Advanced healthcare materials, 2015. **4**(2): p. 223-7.
118. Murphy, C.M., et al., *A collagen-hydroxyapatite scaffold allows for binding and co-delivery of recombinant bone morphogenetic proteins and bisphosphonates.* Acta biomaterialia, 2014. **10**(5): p. 2250-8.

119. Quinlan, E., et al., *Long-term controlled delivery of rhBMP-2 from collagen-hydroxyapatite scaffolds for superior bone tissue regeneration.* Journal of controlled release : official journal of the Controlled Release Society, 2015. **207**: p. 112-9.
120. Quinlan, E., et al., *Controlled release of vascular endothelial growth factor from spray-dried alginate microparticles in collagen-hydroxyapatite scaffolds for promoting vascularization and bone repair.* Journal of tissue engineering and regenerative medicine, 2015.
121. Lopez-Noriega, A., et al., *Thermally triggered release of a pro-osteogenic peptide from a functionalized collagen-based scaffold using thermosensitive liposomes.* Journal of controlled release : official journal of the Controlled Release Society, 2014. **187**: p. 158-66.
122. Weisgerber, D.W., S.R. Caliari, and B.A. Harley, *Mineralized collagen scaffolds induce hMSC osteogenesis and matrix remodeling.* Biomaterials science, 2015. **3**(3): p. 533-42.
123. Weisgerber, D.W., K. Erning, C. Flanagan, S. Hollister, B.A.C. Harley, *Adaptation of the mineralized collagen-glycosaminoglycan scaffold for in vivo implantation: formation of a multi-scale biomaterial composite.* In preparation, 2015.
124. Weisgerber, D.W., R.A. Hortensius, Milner D., Rubessa M., Lopez-Lake H., M. Wheeler, B.A.C. Harley, *In vivo implantation of the mineral polycaprolactone-collagen-glycosaminoglycan composite into a subcritical porcine mandibular ramus defect: assessment of in vivo efficacy.* In preparation, 2015.
125. Weisgerber, D.W., R.A. Hortensius, B.A.C. Harley, *Alterations in mineralized collagen-glycosaminoglycan scaffold composition: effect of mineral addition and protein constituents.* In preparation, 2015.
126. Siemionow, M., et al., *Near-total human face transplantation for a severely disfigured patient in the USA.* Lancet, 2009. **374**(9685): p. 203-9.
127. Nade, S., *Osteogenesis after bone and bone marrow transplantation. II. The initial cellular events following transplantation of decalcified allografts of cancellous bone.* Acta orthopaedica Scandinavica, 1977. **48**(6): p. 572-9.
128. Miller, M.J., et al., *Guided bone growth in sheep: a model for tissue-engineered bone flaps.* Tissue engineering, 1996. **2**(1): p. 51-9.
129. Christenson, E.M., et al., *Nanobiomaterial applications in orthopedics.* Journal of orthopaedic research : official publication of the Orthopaedic Research Society, 2007. **25**(1): p. 11-22.
130. Mountziaris, P.M. and A.G. Mikos, *Modulation of the inflammatory response for enhanced bone tissue regeneration.* Tissue engineering. Part B, Reviews, 2008. **14**(2): p. 179-86.
131. Krishnan, L., N.J. Willett, and R.E. Guldberg, *Vascularization strategies for bone regeneration.* Annals of biomedical engineering, 2014. **42**(2): p. 432-44.
132. DiCarlo, E.F. and P.G. Bullough, *The biologic responses to orthopedic implants and their wear debris.* Clinical materials, 1992. **9**(3-4): p. 235-60.
133. Landgraeber, S., et al., *The pathology of orthopedic implant failure is mediated by innate immune system cytokines.* Mediators of inflammation, 2014. **2014**: p. 185150.
134. Thomas, P., *[Allergic reactions to implant materials].* Der Orthopade, 2003. **32**(1): p. 60-4.
135. Kanungo, B.P. and L.J. Gibson, *Density-property relationships in mineralized collagen-glycosaminoglycan scaffolds.* Acta biomaterialia, 2009. **5**(4): p. 1006-18.
136. Dhankhar, P., *Homogenization Fundamentals.* IOSR Journal of Engineering, 2014. **4**(5): p. 1-8.
137. Kasper, J.C. and W. Friess, *The freezing step in lyophilization: physico-chemical fundamentals, freezing methods and consequences on process performance and quality attributes of biopharmaceuticals.* European journal of pharmaceutics and biopharmaceutics : official journal of Arbeitsgemeinschaft fur Pharmazeutische Verfahrenstechnik e.V, 2011. **78**(2): p. 248-63.
138. Yannas, I.V. and A.V. Tobolsky, *Cross-linking of gelatine by dehydration.* Nature, 1967. **215**(5100): p. 509-10.
139. Samuel, C.S., *Methods in Molecular Biology*. Vol. 466. 2009, Totowa, NJ: Kidney Research. Humana Press.

140. Barbosa, I., et al., *Improved and simple micro assay for sulfated glycosaminoglycans quantification in biological extracts and its use in skin and muscle tissue studies.* Glycobiology, 2003. **13**(9): p. 647-53.
141. Haugh, M.G., C.M. Murphy, and F.J. O'Brien, *Novel freeze-drying methods to produce a range of collagen-glycosaminoglycan scaffolds with tailored mean pore sizes.* Tissue engineering. Part C, Methods, 2010. **16**(5): p. 887-94.
142. Gibson, L.J., Ashby, M.F., Harley, B.A., *Cellular materials in nature and medicine*2010, Cambridge, UK: Cambridge University Press.
143. Dodson, T.B., et al., *Cranial bone graft to reconstruct the mandibular condyle in Macaca mulatta.* Journal of oral and maxillofacial surgery : official journal of the American Association of Oral and Maxillofacial Surgeons, 1997. **55**(3): p. 260-7.
144. Smith, M.H., et al., *Computed tomography-based tissue-engineered scaffolds in craniomaxillofacial surgery.* The international journal of medical robotics + computer assisted surgery : MRCAS, 2007. **3**(3): p. 207-16.
145. Zimmermann, G. and A. Moghaddam, *Allograft bone matrix versus synthetic bone graft substitutes.* Injury, 2011. **42 Suppl 2**: p. S16-21.
146. Laurencin, C., Y. Khan, and S.F. El-Amin, *Bone graft substitutes.* Expert review of medical devices, 2006. **3**(1): p. 49-57.
147. Lyons, F.G., et al., *Novel microhydroxyapatite particles in a collagen scaffold: a bioactive bone void filler?* Clinical orthopaedics and related research, 2014. **472**(4): p. 1318-28.
148. Hutmacher, D.W., *Scaffold design and fabrication technologies for engineering tissues--state of the art and future perspectives.* Journal of biomaterials science. Polymer edition, 2001. **12**(1): p. 107-24.
149. Xu, X.L., et al., *Evaluation of different scaffolds for BMP-2 genetic orthopedic tissue engineering.* Journal of biomedical materials research. Part B, Applied biomaterials, 2005. **75**(2): p. 289-303.
150. Place, E.S., N.D. Evans, and M.M. Stevens, *Complexity in biomaterials for tissue engineering.* Nature materials, 2009. **8**(6): p. 457-70.
151. Grayson, W.L., et al., *Engineering anatomically shaped human bone grafts.* Proceedings of the National Academy of Sciences of the United States of America, 2010. **107**(8): p. 3299-304.
152. Muller, P., et al., *Calcium phosphate surfaces promote osteogenic differentiation of mesenchymal stem cells.* Journal of cellular and molecular medicine, 2008. **12**(1): p. 281-91.
153. Nakamura, S., et al., *Effect of calcium ion concentrations on osteogenic differentiation and hematopoietic stem cell niche-related protein expression in osteoblasts.* Tissue engineering. Part A, 2010. **16**(8): p. 2467-73.
154. Hu, J., et al., *Porous nanofibrous PLLA scaffolds for vascular tissue engineering.* Biomaterials, 2010. **31**(31): p. 7971-7.
155. Musah, S., et al., *Glycosaminoglycan-binding hydrogels enable mechanical control of human pluripotent stem cell self-renewal.* ACS nano, 2012. **6**(11): p. 10168-77.
156. Liao, S.S., et al., *Hierarchically biomimetic bone scaffold materials: nano-HA/collagen/PLA composite.* Journal of biomedical materials research. Part B, Applied biomaterials, 2004. **69**(2): p. 158-65.
157. Kim, H.W., J.H. Song, and H.E. Kim, *Bioactive glass nanofiber-collagen nanocomposite as a novel bone regeneration matrix.* Journal of biomedical materials research. Part A, 2006. **79**(3): p. 698-705.
158. Massumi, M., et al., *The effect of topography on differentiation fates of matrigel-coated mouse embryonic stem cells cultured on PLGA nanofibrous scaffolds.* Tissue engineering. Part A, 2012. **18**(5-6): p. 609-20.
159. Sun, Y., et al., *Mechanics regulates fate decisions of human embryonic stem cells.* Plos One, 2012. **7**(5): p. e37178.

160. Pountos, I., et al., *The effect of bone morphogenetic protein-2, bone morphogenetic protein-7, parathyroid hormone, and platelet-derived growth factor on the proliferation and osteogenic differentiation of mesenchymal stem cells derived from osteoporotic bone.* Journal of orthopaedic trauma, 2010. **24**(9): p. 552-6.
161. Shen, W., et al., *The effect of incorporation of exogenous stromal cell-derived factor-1 alpha within a knitted silk-collagen sponge scaffold on tendon regeneration.* Biomaterials, 2010. **31**(28): p. 7239-49.
162. Lee, J.H., et al., *Osteogenic differentiation of human adipose tissue-derived stromal cells (hASCs) in a porous three-dimensional scaffold.* Biochemical and biophysical research communications, 2008. **370**(3): p. 456-60.
163. Shen, Y.H., M.S. Shoichet, and M. Radisic, *Vascular endothelial growth factor immobilized in collagen scaffold promotes penetration and proliferation of endothelial cells.* Acta biomaterialia, 2008. **4**(3): p. 477-89.
164. Caliari, S.R. and B.A. Harley, *Composite growth factor supplementation strategies to enhance tenocyte bioactivity in aligned collagen-GAG scaffolds.* Tissue engineering. Part A, 2013. **19**(9-10): p. 1100-12.
165. Caliari, S.R. and B.A. Harley, *Structural and biochemical modification of a collagen scaffold to selectively enhance MSC tenogenic, chondrogenic, and osteogenic differentiation.* Advanced healthcare materials, 2014. **3**(7): p. 1086-96.
166. Wang, H., et al., *Dexamethasone has variable effects on mesenchymal stromal cells.* Cytotherapy, 2012. **14**(4): p. 423-30.
167. Thomopoulos, S., et al., *Effect of several growth factors on canine flexor tendon fibroblast proliferation and collagen synthesis in vitro.* The Journal of hand surgery, 2005. **30**(3): p. 441-7.
168. Malladi, P., et al., *Effect of reduced oxygen tension on chondrogenesis and osteogenesis in adipose-derived mesenchymal cells.* American journal of physiology. Cell physiology, 2006. **290**(4): p. C1139-46.
169. Ren, X., et al., *Osteogenesis on nanoparticulate mineralized collagen scaffolds via autogenous activation of the canonical BMP receptor signaling pathway.* Biomaterials, 2015. **50**: p. 107-14.
170. Lee, J.C., et al., *Optimizing Collagen Scaffolds for Bone Engineering: Effects of Cross-linking and Mineral Content on Structural Contraction and Osteogenesis.* The Journal of craniofacial surgery, 2015. **26**(6): p. 1992-6.
171. Zhou, J., et al., *In vitro generation of osteochondral differentiation of human marrow mesenchymal stem cells in novel collagen-hydroxyapatite layered scaffolds.* Acta biomaterialia, 2011. **7**(11): p. 3999-4006.
172. Tseng, P.C., et al., *Resveratrol promotes osteogenesis of human mesenchymal stem cells by upregulating RUNX2 gene expression via the SIRT1/FOXO3A axis.* Journal of bone and mineral research : the official journal of the American Society for Bone and Mineral Research, 2011. **26**(10): p. 2552-63.
173. Frank, O., et al., *Real-time quantitative RT-PCR analysis of human bone marrow stromal cells during osteogenic differentiation in vitro.* Journal of Cellular Biochemistry, 2002. **85**(4): p. 737-46.
174. Pauly, S., et al., *Characterization of tendon cell cultures of the human rotator cuff.* European cells & materials, 2010. **20**: p. 84-97.
175. Brydone, A.S., D. Meek, and S. Maclaine, *Bone grafting, orthopaedic biomaterials, and the clinical need for bone engineering.* Proceedings of the Institution of Mechanical Engineers. Part H, Journal of engineering in medicine, 2010. **224**(12): p. 1329-43.
176. Langer, R. and D.A. Tirrell, *Designing materials for biology and medicine.* Nature, 2004. **428**(6982): p. 487-92.
177. Agrawal, C.M. and R.B. Ray, *Biodegradable polymeric scaffolds for musculoskeletal tissue engineering.* Journal of biomedical materials research, 2001. **55**(2): p. 141-50.

178. Wettergreen, M.A., et al., *Computer-aided tissue engineering of a human vertebral body.* Annals of biomedical engineering, 2005. **33**(10): p. 1333-43.
179. Lipner, J., et al., *The mechanics of PLGA nanofiber scaffolds with biomimetic gradients in mineral for tendon-to-bone repair.* Journal of the mechanical behavior of biomedical materials, 2014. **40**: p. 59-68.
180. Temple, J.P., et al., *Engineering anatomically shaped vascularized bone grafts with hASCs and 3D-printed PCL scaffolds.* Journal of biomedical materials research. Part A, 2014. **102**(12): p. 4317-25.
181. Przekora, A. and G. Ginalska, *Addition of 1,3-beta-D-glucan to chitosan-based composites enhances osteoblast adhesion, growth, and proliferation.* International journal of biological macromolecules, 2014. **70**: p. 474-81.
182. Chen, L., et al., *Preparation and evaluation of an Arg-Gly-Asp-modified chitosan/hydroxyapatite scaffold for application in bone tissue engineering.* Molecular medicine reports, 2015.
183. Xie, J., et al., *Osteogenic differentiation and bone regeneration of the iPSC-MSCs supported by a biomimetic nanofibrous scaffold.* Acta biomaterialia, 2015.
184. Mobasseri, S.A., G. Terenghi, and S. Downes, *Micro-structural geometry of thin films intended for the inner lumen of nerve conduits affects nerve repair.* Journal of materials science. Materials in medicine, 2013. **24**(7): p. 1639-47.
185. O'Brien, F.J., et al., *The effect of pore size on permeability and cell attachment in collagen scaffolds for tissue engineering.* Technol Health Care, 2007. **15**(1): p. 3-17.
186. Woodard, J.R., et al., *The mechanical properties and osteoconductivity of hydroxyapatite bone scaffolds with multi-scale porosity.* Biomaterials, 2007. **28**(1): p. 45-54.
187. Suarez-Gonzalez, D., et al., *Controllable mineral coatings on PCL scaffolds as carriers for growth factor release.* Biomaterials, 2012. **33**(2): p. 713-21.
188. Patel, J.J., C.L. Flanagan, and S.J. Hollister, *Bone Morphogenetic Protein-2 Adsorption onto Poly-varepsilon-caprolactone Better Preserves Bioactivity In Vitro and Produces More Bone In Vivo than Conjugation Under Clinically Relevant Loading Scenarios.* Tissue engineering. Part C, Methods, 2015. **21**(5): p. 489-98.
189. Hu, W.W., et al., *The use of reactive polymer coatings to facilitate gene delivery from poly (epsilon-caprolactone) scaffolds.* Biomaterials, 2009. **30**(29): p. 5785-92.
190. Jeong, C.G., H. Zhang, and S.J. Hollister, *Three-dimensional poly(1,8-octanediol-co-citrate) scaffold pore shape and permeability effects on sub-cutaneous in vivo chondrogenesis using primary chondrocytes.* Acta biomaterialia, 2011. **7**(2): p. 505-14.
191. Patel, J.J., et al., *Dual Delivery of EPO and BMP2 from a Novel Modular Poly-varepsilon-Caprolactone Construct to Increase the Bone Formation in Prefabricated Bone Flaps.* Tissue engineering. Part C, Methods, 2015.
192. Smith, M.H., et al., *Computed tomography-based tissue-engineered scaffolds in craniomaxillofacial surgery.* Int J Med Robot, 2007. **3**(3): p. 207-16.
193. Hollister, S.J., et al., *Engineering craniofacial scaffolds.* Orthod Craniofac Res, 2005. **8**(3): p. 162-73.
194. Kuhne, J.H., et al., *Bone formation in coralline hydroxyapatite. Effects of pore size studied in rabbits.* Acta Orthop Scand, 1994. **65**(3): p. 246-52.
195. Hulbert, S.F., et al., *Potential of ceramic materials as permanently implantable skeletal prostheses.* J Biomed Mater Res, 1970. **4**(3): p. 433-456.
196. Lipowiecki, M., et al., *Permeability of rapid prototyped artificial bone scaffold structures.* Journal of biomedical materials research. Part A, 2014. **102**(11): p. 4127-35.
197. Karam, G.N. and L.J. Gibson, *Biomimicking of animal quills and plant stems - natural cylindrical-shells with foam cores.* Mater. Sci. Eng. C Biomim. Mater. Sens. Syst., 1994. **2**(1-2): p. 113-132.

198. Olde Damink, L.H., et al., *Cross-linking of dermal sheep collagen using a water-soluble carbodiimide.* Biomaterials, 1996. **17**(8): p. 765-73.
199. Pontius, J.S., *Estimation of the mean in line intercept sampling.* Environmental and Ecological Statistics, 1998. **5**(4): p. 371-379.
200. Tierney, C.M., M.J. Jaasma, and F.J. O'Brien, *Osteoblast activity on collagen-GAG scaffolds is affected by collagen and GAG concentrations.* Journal of biomedical materials research. Part A, 2009. **91**(1): p. 92-101.
201. Hannink, G. and J.J.C. Arts, *Bioresorbability, porosity and mechanical strength of bone substitutes: What is optimal for bone regeneration?* Injury-International Journal of the Care of the Injured, 2011. **42**: p. S22-S25.
202. Harley, B.A.C. and L.J. Gibson, *In vivo and in vitro applications of collagen-GAG scaffolds.* Chem Eng J, 2008. **137**(1): p. 102-121.
203. Caliari, S.R., et al., *Collagen Scaffolds Incorporating Coincident Gradations of Instructive Structural and Biochemical Cues for Osteotendinous Junction Engineering.* Advanced healthcare materials, 2015. **4**(6): p. 831-7.
204. Caliari, S.R. and B.A. Harley, *Collagen-GAG scaffold biophysical properties bias MSC lineage choice in the presence of mixed soluble signals.* Tissue engineering. Part A, 2014. **20**(17-18): p. 2463-72.
205. Kurtz, S.M. and J.N. Devine, *PEEK biomaterials in trauma, orthopedic, and spinal implants.* Biomaterials, 2007. **28**(32): p. 4845-69.
206. Bonfield, W., *Composites for bone replacement.* Journal of biomedical engineering, 1988. **10**(6): p. 522-6.
207. Jungreuthmayer, C., et al., *A comparative study of shear stresses in collagen-glycosaminoglycan and calcium phosphate scaffolds in bone tissue-engineering bioreactors.* Tissue engineering. Part A, 2009. **15**(5): p. 1141-9.
208. Amoroso, N.J., et al., *Microstructural manipulation of electrospun scaffolds for specific bending stiffness for heart valve tissue engineering.* Acta biomaterialia, 2012. **8**(12): p. 4268-77.
209. Argento, G., et al., *Multi-scale mechanical characterization of scaffolds for heart valve tissue engineering.* Journal of biomechanics, 2012. **45**(16): p. 2893-8.
210. Wust, S., R. Muller, and S. Hofmann, *3D Bioprinting of complex channels-Effects of material, orientation, geometry, and cell embedding.* Journal of biomedical materials research. Part A, 2015. **103**(8): p. 2558-70.
211. Yodmuang, S., et al., *Silk microfiber-reinforced silk hydrogel composites for functional cartilage tissue repair.* Acta biomaterialia, 2015. **11**: p. 27-36.
212. Rizkalla, A.S. and D.W. Jones, *Indentation fracture toughness and dynamic elastic moduli for commercial feldspathic dental porcelain materials.* Dental materials : official publication of the Academy of Dental Materials, 2004. **20**(2): p. 198-206.
213. Tarafder, S. and S. Bose, *Polycaprolactone-coated 3D printed tricalcium phosphate scaffolds for bone tissue engineering: in vitro alendronate release behavior and local delivery effect on in vivo osteogenesis.* ACS applied materials & interfaces, 2014. **6**(13): p. 9955-65.
214. Hak, D.J., et al., *Use of carbon-fiber-reinforced composite implants in orthopedic surgery.* Orthopedics, 2014. **37**(12): p. 825-30.
215. Nganga, S., et al., *Multi-layer porous fiber-reinforced composites for implants: in vitro calcium phosphate formation in the presence of bioactive glass.* Dental materials : official publication of the Academy of Dental Materials, 2012. **28**(11): p. 1134-45.
216. Alberti, K., et al., *Functional immobilization of signaling proteins enables control of stem cell fate.* Nature methods, 2008. **5**(7): p. 645-50.
217. Watarai, A., et al., *TGFbeta functionalized starPEG-heparin hydrogels modulate human dermal fibroblast growth and differentiation.* Acta biomaterialia, 2015. **25**: p. 65-75.

218. Sakiyama-Elbert, S.E. and J.A. Hubbell, *Development of fibrin derivatives for controlled release of heparin-binding growth factors.* Journal of controlled release : official journal of the Controlled Release Society, 2000. **65**(3): p. 389-402.
219. Sakiyama-Elbert, S.E. and J.A. Hubbell, *Controlled release of nerve growth factor from a heparin-containing fibrin-based cell ingrowth matrix.* Journal of controlled release : official journal of the Controlled Release Society, 2000. **69**(1): p. 149-58.
220. Hudalla, G.A., et al., *Harnessing endogenous growth factor activity modulates stem cell behavior.* Integrative biology : quantitative biosciences from nano to macro, 2011. **3**(8): p. 832-42.
221. Paschoa, A.F., *Heparin: 100 years of pleiotropic effects.* Journal of thrombosis and thrombolysis, 2015.
222. Gama, C.I., et al., *Sulfation patterns of glycosaminoglycans encode molecular recognition and activity.* Nature chemical biology, 2006. **2**(9): p. 467-73.
223. Raman, R., V. Sasisekharan, and R. Sasisekharan, *Structural insights into biological roles of protein-glycosaminoglycan interactions.* Chemistry & Biology, 2005. **12**(3): p. 267-77.
224. Kisiel, M., et al., *Complexation and sequestration of BMP-2 from an ECM mimetic hyaluronan gel for improved bone formation.* Plos One, 2013. **8**(10): p. e78551.
225. Kanzaki, S., et al., *Heparin inhibits BMP-2 osteogenic bioactivity by binding to both BMP-2 and BMP receptor.* Journal of cellular physiology, 2008. **216**(3): p. 844-50.
226. Hortensius, R.A. and B.A. Harley, *The use of bioinspired alterations in the glycosaminoglycan content of collagen-GAG scaffolds to regulate cell activity.* Biomaterials, 2013. **34**(31): p. 7645-52.
227. Thomopoulos, S., G.M. Genin, and L.M. Galatz, *The development and morphogenesis of the tendon-to-bone insertion - what development can teach us about healing.* Journal of musculoskeletal & neuronal interactions, 2010. **10**(1): p. 35-45.
228. Cimino, F., B.S. Volk, and D. Setter, *Anterior cruciate ligament injury: diagnosis, management, and prevention.* American family physician, 2010. **82**(8): p. 917-22.
229. Buckwalter, J.A., H.J. Mankin, and A.J. Grodzinsky, *Articular cartilage and osteoarthritis.* Instructional course lectures, 2005. **54**: p. 465-80.
230. Genin, G.M., et al., *Functional grading of mineral and collagen in the attachment of tendon to bone.* Biophysical journal, 2009. **97**(4): p. 976-85.
231. Woo, S.L., et al., *Injury and repair of ligaments and tendons.* Annual review of biomedical engineering, 2000. **2**: p. 83-118.
232. Wopenka, B., et al., *The tendon-to-bone transition of the rotator cuff: a preliminary Raman spectroscopic study documenting the gradual mineralization across the insertion in rat tissue samples.* Applied spectroscopy, 2008. **62**(12): p. 1285-94.
233. Butler, D.L., et al., *Functional tissue engineering for tendon repair: A multidisciplinary strategy using mesenchymal stem cells, bioscaffolds, and mechanical stimulation.* Journal of orthopaedic research : official publication of the Orthopaedic Research Society, 2008. **26**(1): p. 1-9.
234. Vitale, M.A., et al., *Rotator cuff repair: an analysis of utility scores and cost-effectiveness.* Journal of shoulder and elbow surgery / American Shoulder and Elbow Surgeons ... [et al.], 2007. **16**(2): p. 181-7.
235. Boileau, P., et al., *Arthroscopic repair of full-thickness tears of the supraspinatus: does the tendon really heal?* The Journal of bone and joint surgery. American volume, 2005. **87**(6): p. 1229-40.
236. Galatz, L., et al., *Development of the supraspinatus tendon-to-bone insertion: localized expression of extracellular matrix and growth factor genes.* Journal of orthopaedic research : official publication of the Orthopaedic Research Society, 2007. **25**(12): p. 1621-8.
237. Klepps, S., et al., *Prospective evaluation of the effect of rotator cuff integrity on the outcome of open rotator cuff repairs.* The American journal of sports medicine, 2004. **32**(7): p. 1716-22.

238. Millar, N.L., et al., *Open versus two forms of arthroscopic rotator cuff repair.* Clinical orthopaedics and related research, 2009. **467**(4): p. 966-78.
239. Li, X., et al., *Nanofiber scaffolds with gradations in mineral content for mimicking the tendon-to-bone insertion site.* Nano letters, 2009. **9**(7): p. 2763-8.
240. Chan, V., et al., *Three-dimensional photopatterning of hydrogels using stereolithography for long-term cell encapsulation.* Lab on a chip, 2010. **10**(16): p. 2062-70.
241. Feinberg, S.E., et al., *Image-based biomimetic approach to reconstruction of the temporomandibular joint.* Cells, tissues, organs, 2001. **169**(3): p. 309-21.
242. Khanarian, N.T., et al., *A functional agarose-hydroxyapatite scaffold for osteochondral interface regeneration.* Biomaterials, 2012. **33**(21): p. 5247-58.
243. Moffat, K.L., et al., *Orthopedic interface tissue engineering for the biological fixation of soft tissue grafts.* Clinics in sports medicine, 2009. **28**(1): p. 157-76.